Petrogenesis of the Melba Flats Ni-Cu-PGE Deposit in Western Tasmania: Insights from a Geochemical and Geochronological Investigation

Author:
Marcus PHUA

Supervisors:
Prof. Reid KEAYS
Prof. David PHILLIPS

A thesis submitted in partial fulfilment of the requirements for the degree of Master of Science

in the

School of Earth Sciences
The University of Melbourne

October 2015

THE UNIVERSITY OF MELBOURNE

Declaration of Authorship

I, Marcus PHUA, declare that this thesis titled, 'Petrogenesis of the Melba Flats Ni-Cu-PGE Deposit in Western Tasmania: Insights from a Geochemical and Geochronological Investigation' contains less than 25,000 words.

Signed: _____

Date: _____

THE UNIVERSITY OF MELBOURNE

Abstract

Faculty of Science
School of Earth Sciences

Master of Science

Petrogenesis of the Melba Flats Ni-Cu-PGE Deposit in Western Tasmania: Insights from a Geochemical and Geochronological Investigation

by Marcus PHUA

Since its discovery in 1893, the Melba Flats Ni-Cu-PGE deposit has produced 10,000 tons of Ni and Cu at an average grade of 9.7% and 4.7% respectively. It is a magmatic sulphide deposit located 8 km north-east of the township of Zeehan, along the eastern margin of the Dundas Trough in Western Tasmania. The deposit is associated with a suite of bifurcating mafic intrusions hosting magmatic Ni-Cu-PGE sulphides intruded into a sequence of volcaniclastic lithic greywackes, which are correlated to the Crimson Creek Formation. U-Pb detrital zircon geochronology was utilized to show that the Melba Flats sediments have a maximum depositional age of *c.* 582 Ma. The Melba Flats mafic intrusions were formed by primitive magmas with 13 to 16 wt% MgO and a sub-alkaline tholeiitic affinity. ^{40}*Ar/^{39}Ar hornblende geochronology was employed to establish that the mafic intrusions were emplaced at *c.* 568 Ma, along an attenuated continental margin characterized by a transitional rift setting, analogous to the early Paleogene break-up margin of East Greenland. Melba Flats Ni-Cu-PGE sulphides are characterized by massive-to-semi-massive sulphides that possess high Ni, Cu and PGE tenors and mantle-like δ^{34}S values and S/Se ratios and disseminated sulphides that have low Ni, Cu and PGE tenors, along with crustal δ^{34}S values and S/Se ratios. Geochemical data indicates that the massive-to-semi-massive sulphides were formed at depth before being transported to their current sites, whilst the disseminated sulphides were formed during transport as the primitive magma interacted with the S-bearing crustal rocks.

Acknowledgements

Firstly, I would like to express my greatest appreciation to Professor Reid Keays and Professor David Phillips, my research supervisors, for their patience, guidance and useful critiques of this research work. Specifically, I would like to extend a special thanks to Professor Reid Keays for his unfailing support, enthusiastic encouragement and his countless coffee and beer shouts at Trotters and Jimmy Watson's throughout this time.

This research would not have been possible without the generous sponsorship from MMG Limited, the student support initiative by the Association of Applied Geochemistry (AAG) and the analytical support by Bureau Veritas, Perth, Australia.

Special thanks are also extended to Roland Maas, Erin Matchin, Steve Boger, Malcolm Wallace, Janet Hergt, Jon Woodhead, Abaz Alimanovic, Alan Greig, Stan Szczepanski and Graham Hutchinson for their technical and analytical assistance and support.

It has been an absolute pleasure completing my research alongside the most brilliant and diverse bunch of Masters students. I am grateful to all of you for not only turning the Masters office into a work sanctuary, but a refuge away from work where constant laughter and bickers prevail. Morning teas and beer-o'clocks with every single one of you will be sorely missed. A special thanks to Malcolm and John for our mid-Masters adventure in the Land of the Golden Pagodas, Burma and for keeping me on track every step of the way.

Lastly, a massive shout-out to my friends and family back home in Singapore who have constantly offered kind words of encouragement. To Dad, Mum and Joyce, my deepest gratitude for your unwavering support and encouragement, without which, the completion of this research would have been impossible.

Contents

Declaration of Authorship i

Abstract ii

Acknowledgements iii

Contents iv

List of Figures viii

List of Tables xi

1 Introduction & Aims 1
- 1.1 Introduction . . . 1
- 1.2 Research Aims . . . 3
- 1.3 Thesis Outline . . . 4

2 Background 5
- 2.1 Exploration History . . . 5
- 2.2 Regional Tectonics . . . 7
  - 2.2.1 Cambrian . . . 9
  - 2.2.2 Devonian . . . 10
  - 2.2.3 Carboniferous-Jurassic . . . 10
- 2.3 Regional Geology . . . 10
  - 2.3.1 Neoproterozoic . . . 11
  - 2.3.2 Cambrian . . . 11
  - 2.3.3 Ordovician-Quaternary . . . 12
- 2.4 Local Geology . . . 12
  - 2.4.1 Melba Flats Sediments . . . 12
  - 2.4.2 Previous Work . . . 14
    - 2.4.2.1 Sediment Affiliation . . . 14
    - 2.4.2.2 Depositional Age . . . 14
  - 2.4.3 Melba Flats Mafic Intrusions . . . 14
  - 2.4.4 Previous Work . . . 15
    - 2.4.4.1 Geochemistry . . . 15
    - 2.4.4.2 Magmatic Affiliation . . . 16

2.4.4.3 Tectonic Implications . . . 16
2.4.4.4 Emplacement Age . . . 16
2.4.5 Melba Flats Ni-Cu-PGE Sulphides . . . 17
2.4.6 Previous Work . . . 17
2.4.6.1 Geochemistry . . . 17
2.4.6.2 Potential Genetic Models . . . 17

3 Methodology 18
3.1 Overview . . . 18
3.2 Whole Rock Geochemistry . . . 18
3.2.1 Sample Preparation . . . 18
3.2.2 Analytical Procedures . . . 18
3.2.2.1 Major Elements . . . 18
3.2.2.2 Trace Elements . . . 19
3.2.2.3 Platinum Group Elements . . . 20
3.3 Sulphur Isotope Geochemistry . . . 20
3.3.1 Sample Preparation . . . 20
3.3.2 Analytical Procedures . . . 20
3.4 U-Pb Geochronology . . . 21
3.4.1 Sample Preparation . . . 21
3.4.2 Analytical Procedures . . . 23
3.4.2.1 U-Pb Detrital Zircon . . . 23
3.5 $^{40}Ar^*/^{39}Ar$ Geochronology . . . 23
3.5.1 Sample Preparation . . . 23
3.5.2 Analytical Procedures . . . 25
3.5.2.1 $^{40}Ar^*/^{39}Ar$ Detrital Muscovite . . . 25
3.5.2.2 $^{40}Ar^*/^{39}Ar$ Hornblende . . . 26

4 Age Dating & Geochemistry of the Melba Flats Sediments 27
4.1 U-Pb Dating of Detrital Zircons . . . 28
4.1.1 Results: U-Pb Dating of Detrital Zircons . . . 28
4.1.2 Comparison of Detrital Age Spectra by Kernel Function Estimation . . . 36
4.2 $^{40}Ar^*/^{39}Ar$ Dating of Detrital Muscovite . . . 39
4.2.1 Results: $^{40}Ar^*/^{39}Ar$ Detrital Muscovite . . . 39
4.2.2 Implication of $^{40}Ar^*/^{39}Ar$ Detrital Muscovite Cooling Ages . . . 44
4.3 Trace Element Geochemistry . . . 45
4.3.1 Results: Trace Element Geochemistry . . . 45
4.3.2 Comparison of Trace Element Geochemistry Data . . . 49

5 Age Dating & Geochemistry of the Melba Flats Mafic Intrusions 52
5.1 $^{40}Ar^*/^{39}Ar$ Dating of Hornblende . . . 53
5.1.1 Results: $^{40}Ar^*/^{39}Ar$ Hornblende . . . 53
5.1.2 Implication of $^{40}Ar^*/^{39}Ar$ Hornblende Ages . . . 57
5.2 Whole Rock Geochemistry . . . 58
5.2.1 Results: Whole Rock Geochemistry . . . 58
5.2.1.1 Major Element Geochemistry . . . 61
5.2.1.2 Trace Element Geochemistry . . . 65

5.2.2 Suitability of Geochemical Data for Interpretation 69
5.2.3 Rock Classification Discrimination 72
5.2.4 Magmatic Affinity Discrimination 76
5.2.5 Tectonic Setting Discrimination 78
5.2.5.1 Approach to Tectonic Discrimination 80
5.2.5.2 Suggested Tectonic Setting 82
5.3 Comparison to Possible Stratigraphic Equivalents 83

6 Geochemistry of the Melba Flats Ni-Cu-PGE Sulphides 86
6.1 Platinum Group Element Geochemistry 86
6.1.1 Results: Platinum Group Element Geochemistry 89
6.1.2 Comparison of Unmineralized to Mineralized Intrusions 91
6.1.3 S-Saturation Status of Magma 93
6.1.4 Source of S in Melba Flats Ni-Cu-PGE Sulphides 94
6.2 Sulphur Isotope Geochemistry 96
6.2.1 Results: Sulphur Isotope Geochemistry 96
6.2.2 Significance of Sulphur Isotope Values in relation to S/Se Ratios . . . 97

7 Synthesis & Future Work 99
7.1 Correlation & Age of the Melba Flats Sediments 99
7.1.1 Future Work 100
7.2 Petrogenesis, Age & Tectonic Setting of the Melba Flats Mafic Intrusions . . 101
7.2.1 Future Work 102
7.3 Origin of the Melba Flats Ni-Cu-PGE Sulphides 103
7.3.1 Future Work 104

8 Conclusion 106

A Petrographic Descriptions 108
A.1 Representative Melba Flats Sediments 108
A.2 Representative Melba Flats Mafic Intrusions 110

B Dating Methods 114
B.1 The U-Pb Dating Method 114
B.2 The $^{40}Ar^*/^{39}Ar$ Dating Method 117
B.2.1 Minerals used for $^{40}Ar^*/^{39}Ar$ Dating 118

C Whole Rock Geochemical Data 119
C.1 Major Elements Geochemical Data 119
C.1.1 Melba Flats Mafic Intrusions 119
C.2 Trace Elements Geochemical Data 123
C.2.1 Melba Flats Sediments 123
C.2.2 Melba Flats Mafic Intrusions 128
C.3 Platinum Group Elements Geochemical Data 139
C.3.1 Melba Flats Mafic Intrusions 139

D $^{40}Ar^*/^{39}Ar$ Analytical Data 142

D.1 ARGUS-VI $^{40}Ar^*/^{39}Ar$ Detrital Muscovite Analytical Data 142
D.2 VG3600 $^{40}Ar^*/^{39}Ar$ Hornblende Analytical Data 161

E U-Pb Analytical Data **166**
E.1 LA-ICPMS U-Pb Detrital Zircon Analytical Data 166

Bibliography **176**

List of Figures

1.1 Location of the Melba Flats Ni-Cu-PGE deposit in Western Tasmania. 2

2.1 Geology of the area surrounding the Melba Flats Ni-Cu-PGE deposit. 6
2.2 Locality map of the Melba Flats area. 7
2.3 Strato-tectonic map of Tasmania. 8
2.4 Structural history of the Cambrian Tyennan Orogeny in Western Tasmania. . 9
2.5 Geological map of Melba Flats and its surrounding area. 13

3.1 Photomicrographs of samples selected for $^{40}Ar^*/^{39}Ar$ geochronology. 24

4.1 Detrital zircon morphology, internal textures and U-Pb detrital zircon age data for sample MF23 - 44.6 m. 30
4.2 Detrital zircon morphology, internal textures and U-Pb detrital zircon age data for sample MF40 - 56.3 m. 32
4.3 Detrital zircon morphology, internal textures and U-Pb detrital zircon age data for sample MF83 - 152.0 m. 34
4.4 Kernel density plots for samples MF23 - 44.6 m, MF40 - 56.3 m and MF83 - 152.0 m. 35
4.5 Detrital zircon age spectra and functional distance dendrogram for selected sedimentary spectra from Avebury and Melba Flats. 37
4.6 $^{40}Ar^*/^{39}Ar$ step-heating spectra for 4 single muscovite grains (MF40-1, MF40-2, MF40-4 and MF40-5). 42
4.7 $^{40}Ar^*/^{39}Ar$ step-heating spectra for 2 single muscovite grains (MF40-3 and MF40-6). 43
4.8 Kernel density plot comparing $^{40}Ar^*/^{39}Ar$ detrital muscovite ages and U-Pb detrital zircon ages for sample MF40 - 56.3 m. 44
4.9 C1 chondrite-normalized lithophile element plot for the Melba Flats sediments. 48
4.10 C1 chondrite-normalized REE plot for the Melba Flats sediments. 48
4.11 C1 chondrite-normalized lithophile element plot comparing the Melba Flats sediment samples to the Avebury sediment samples. 50
4.12 C1 chondrite-normalized REE plot comparing the Melba Flats sediment samples to the Avebury sediment samples. 51

5.1 $^{40}Ar^*/^{39}Ar$ step-heating spectra for 2 aliquots of hornblende (MF103-1 and MF103-2). 56
5.2 Bivariate plot of Mg# vs. MgO for the unmineralized Melba Flats mafic intrusions. 61
5.3 Major element bivariate plots for the unmineralized Melba Flats mafic intrusions. 62
5.4 Bivariate plot of Mg# vs. MgO for the mineralized Melba Flats mafic intrusions. 63

5.5 Major element bivariate plots for the mineralized Melba Flats mafic intrusions. 64
5.6 Primitive mantle-normalized lithophile element plot for the unmineralized samples from the Melba Flats mafic intrusions. 66
5.7 Primitive mantle-normalized REE plot for the unmineralized samples from the Melba Flats mafic intrusions. 66
5.8 Primitive mantle-normalized lithophile element plot for the mineralized samples from the Melba Flats mafic intrusions. 68
5.9 Primitive mantle-normalized REE plot for the mineralized samples from the Melba Flats mafic intrusions. 68
5.10 Elements mobility plots for the Melba Flats mafic intrusions. 71
5.11 Major element rock classification of the Melba Flats mafic intrusions. 73
5.12 Trace element rock classification by Hallberg (1984) for the Melba Flats mafic intrusions.. 74
5.13 Trace element rock classification by Winchester & Floyd (1977) for the Melba Flats mafic intrusions. 75
5.14 Trace element rock classification by Pearce (1996) for the Melba Flats mafic intrusions. 75
5.15 Major element magmatic affiliation of the Melba Flats mafic intrusions. . . . 76
5.16 Trace element magmatic affiliation discrimination by Floyd & Winchester (1975) for the Melba Flats mafic intrusions. 77
5.17 Trace element magmatic affiliation discrimination by MacLean & Barrett (1993) for the Melba Flats mafic intrusions. 78
5.18 Graphical representation for the tectonic discrimination of igneous rocks. . . 79
5.19 Tectonic discrimination using Ti-Zr-Y plot for the Melba Flats mafic intrusions. 81
5.20 Tectonic discrimination using Hf-Th-Ta plot for the Melba Flats mafic intrusions. 82
5.21 Primitive mantle-normalized lithophile element plot comparing Melba Flats mafic intrusions to possible stratigraphic equivalents. 84
5.22 Primitive mantle-normalized REE plot comparing Melba Flats mafic intrusions to possible stratigraphic equivalents. 84

6.1 Primitive mantle-normalized Ni-Cu-PGE plot for the average values of unmineralized samples from the Melba Flats mafic intrusions. 89
6.2 Primitive mantle-normalized Ni-Cu-PGE plot for the average values of mineralized samples from the Melba Flats mafic intrusions. 90
6.3 Bivariate plot of Cu vs. Ni comparing unmineralized to mineralized Melba Flats mafic intrusions. 92
6.4 Bivariate plot of Pd vs. Pt comparing unmineralized to mineralized Melba Flats mafic intrusions. 92
6.5 Bivariate plot of Pd vs. Pt comparing unmineralized to mineralized Melba Flats mafic intrusions. 93
6.6 Plot of $(Pt + Pd)_{100\% \text{ Sulphides}}$ vs. S/Se comparing unmineralized to mineralized Melba Flats mafic intrusions. 95
6.7 Plot of $\delta^{34}S$ ‰ vs. VCDT vs. S/Se comparing massive-to-semi-massive to disseminated sulphide-rich mineralized Melba Flats mafic intrusions. 98

A.1 Photomicrographs of representative Melba Flats greywacke sample - MF40 - 56.3 m. 109
A.2 Photomicrographs of representative Melba Flats mafic intrusion sample - MF93 - 332.0 m. 111

A.3 Photomicrographs of representative Melba Flats mafic intrusion sample - MF93 - 365.4 m. 112
A.4 Photomicrographs of representative Melba Flats mafic intrusion sample - MF103 - 101.4 m. 113

B.1 U-Th-Pb decay chains. 116

List of Tables

3.1 Drill cores sampled at Melba Flats for geochronology. 21
3.2 Samples selected at Melba Flats for U-Pb and $^{40}Ar^*/^{39}Ar$ dating. 22

4.1 Summary of $^{40}Ar^*/^{39}Ar$ age data for single muscovite grains. 40
4.2 Summary of trace element analytical data for the Melba Flat sediments. . . . 46

5.1 Summary of $^{40}Ar^*/^{39}Ar$ age data for multiple hornblende aliquots. 54
5.2 Representative major elements geochemical data for the unmineralized Melba Flats mafic intrusions. 59
5.3 Representative major elements geochemical data for the mineralized Melba Flats mafic intrusions. 60

6.1 Representative PGE elements geochemical data for the unmineralized Melba Flats mafic intrusions. 87
6.2 Representative PGE elements geochemical data for the mineralized Melba Flats mafic intrusions. 88
6.3 Summary of S isotope values for the sulphide-rich samples from the mineralized Melba Flats mafic intrusions. 97

C.1 Major elements geochemical data for the Melba Flats Mafic Intrusions. . . . 120
C.2 Trace elements geochemical data for the Avebury and Melba Flats Sediments. 124
C.3 Lithophile elements geochemical data for the Melba Flats mafic intrusions. . 129
C.4 REE geochemical data for the Melba Flats mafic intrusions. 136
C.5 PGE geochemical data for the Melba Flats mafic intrusions. 140

D.1 ARGUS-VI $^{40}Ar^*/^{39}Ar$ analytical data for single muscovite grains. 143
D.2 ARGUS-VI $^{40}Ar^*/^{39}Ar$ raw analytical data for single muscovite grains. 149
D.3 ARGUS-VI $^{40}Ar^*/^{39}Ar$ blank values for single muscovite grains. 155
D.4 VG3600 $^{40}Ar^*/^{39}Ar$ analytical data for multiple aliquots of hornblende. . . . 162
D.5 VG3600 $^{40}Ar^*/^{39}Ar$ raw analytical data for multiple aliquots of hornblende. . 164

E.1 LA-ICPMS U-Pb detrital zircon analytical data. 167

Chapter 1

Introduction & Aims

1.1 Introduction

A broad group of deposits containing anomalous concentrations of magmatic Ni-Cu-PGE sulphides occur in association with mafic-ultramafic bodies within a variety of tectonic settings (Eckstrand & Hulbert 2007; Groves & Bierlein 2007; Maier & Groves 2011; Naldrett 2004a). Among these deposits, two major types are distinguishable: (1) the Ni-Cu deposits associated with sulphide-rich ores that typically occur within differentiated mafic-ultramafic dykes and sills, and (2) the PGE deposits associated with sulphide-poor ores that usually occur within mafic-ultramafic layered intrusions (Eckstrand & Hulbert 2007; Naldrett 1999, 2004a). Together, these magmatic sulphide deposit types constitute the world's largest source of Ni, as well as being a major source of Cu and PGE (Eckstrand & Hulbert 2007). On account of their significance, considerable effort has been directed at unravelling the controls of genesis.

Key aspects in the genesis of a magmatic Ni-Cu-PGE deposit (Keays & Lightfoot 2010; Maier & Groves 2011; Naldrett 2004b) include: (1) the assimilation of crustal sulphur that drives the host magma to sulphide saturation, (2) the segregation of immiscible sulphides from the sulphide saturated host magma, (3) the interaction of sulphides with the host magma to concentrate chalcophile elements to an economic level, and (4) the concentration of sufficient sulphides within a restricted locality to constitute an ore body. Broadly speaking, these key genetic characteristics are certainly accurate, however, the manifestation of other unaccounted variables in the formation of many magmatic Ni-Cu-PGE deposits suggest a far more complex genetic process is evident.

This research project is concerned with the first type of magmatic Ni-Cu-PGE sulphide deposits, with particular focus on Melba Flats, a magmatic sulphide deposit associated with mafic intrusions. Melba Flats is a well endowed magmatic Ni-Cu-PGE deposit located near the township of Zeehan in Western Tasmania, one of the richest and most diversely mineralized provinces in the world (Corbett *et al.* 2014b; Crawford & Keays 2010). A petrogenetic investigation of the mafic intrusions, and their associated mineralization is essential to better understand the controls for the genesis of the highly mineralized Melba Flats Ni-Cu-PGE deposit, and the potential for further Ni-Cu-PGE mineralization in the wider region.

FIGURE 1.1: *Location of the Melba Flats Ni-Cu-PGE deposit in Western Tasmania.*

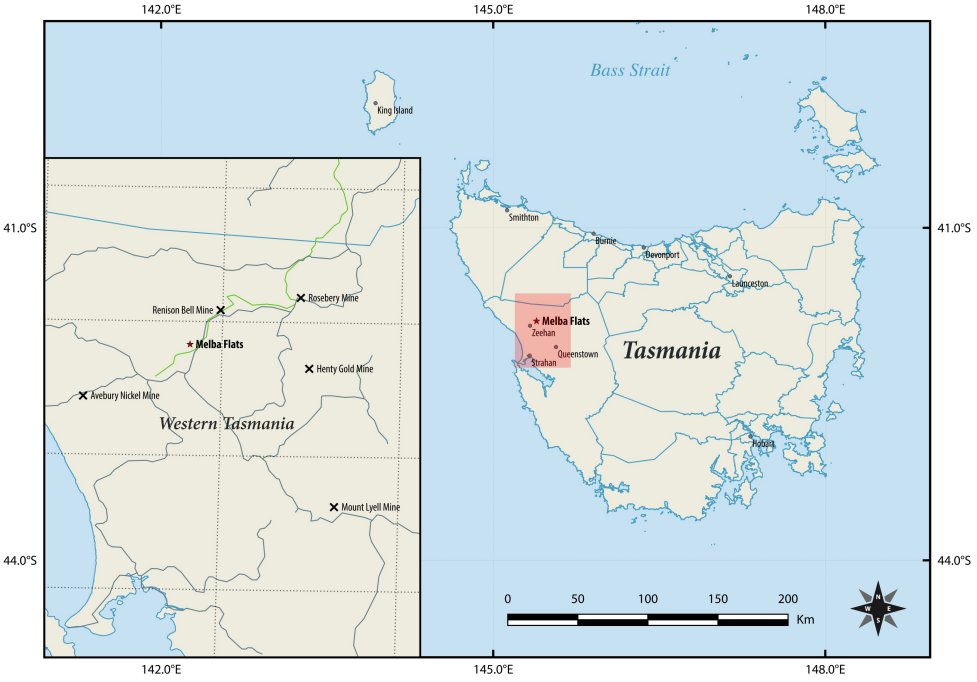

1.2 Research Aims

Historically, a significant amount of exploration and geological work has been undertaken at Melba Flats and its surrounding area. However, the Melba Flats mafic intrusions hosting magmatic Ni-Cu-PGE sulphides, along with their host sedimentary rocks, continue to be poorly understood. Consequently, in order to unravel the petrogenesis of the Melba Flats Ni-Cu-PGE deposit, 4 primary aims will be addressed in this research project:

1. Ascertain the sediment affiliation, and depositional age of the host sedimentary rocks;
2. Establish the magmatic affiliation, and emplacement age of the mafic intrusions;
3. Determine the emplacement tectonic setting of the mafic intrusions; and
4. Establish if the magmatic Ni-Cu-PGE sulphides were formed *in situ* or at depth.

1.3 Thesis Outline

The geochemical and geochronological investigation of the petrogenesis of the Melba Flats mafic intrusions has presented new data for the host sedimentary rocks, the mafic intrusions and their associated magmatic Ni-Cu-PGE sulphides. Included are:

- U-Pb detrital zircon and $^{40}Ar^*/^{39}Ar$ detrital muscovite ages from the Melba Flats sediments, which are useful tools to help establish the maximum depositional age of the Melba Flats sediments and to determine the potential correlations between the Melba Flats sediments and other sedimentary sequences;
- Trace element geochemical data that can also be used to establish correlations between the Melba Flats sediments and their potential stratigraphic equivalents;
- $^{40}Ar^*/^{39}Ar$ hornblende ages, which is an excellent tool to help establish the emplacement age of the Melba Flats mafic intrusions;
- Major and trace element geochemical data that allows for the discrimination of the rock classification, magmatic affiliation and emplacement tectonic setting of the Melba Flats mafic intrusions;
- Platinum element geochemical data for the Melba Flats Ni-Cu-PGE sulphides that can help provide important constraints for sulphides-forming processes;
- S isotopic data for the Melba Flats Ni-Cu-PGE sulphides, which can help to determine the source of S for the magmatic sulphides.

Chapter 2: Background will provide the geological background to the Melba Flats Ni-Cu-PGE deposit and Chapter 3: Methodology will present all the analytical methods that were utilized for this study.

Data is presented in the following chapters:

- Chapter 4: Age Dating & Geochemistry of the Melba Flats Sediments
- Chapter 5: Age Dating & Geochemistry of the Melba Flats Mafic Intrusions
- Chapter 6: Geochemistry of the Melba Flats Ni-Cu-PGE Sulphides

Chapter 7: Synthesis & Future Work will present a synthesis of the results and a discussion of the future work beyond this study.

Chapter 2

Background

The Melba Flats Ni-Cu-PGE deposit lies within one the richest and most diversely mineralized provinces in the world. It is located about 8 km northeast of the historic Zeehan mineral field and approximately 30 km northeast of the township of Strahan in Western Tasmania, Australia (Fig. 2.1; Corbett *et al.* (2014b); Keays & Jowitt (2013)). Specifically, the Melba Flats Ni-Cu-PGE deposit consists of mafic intrusions hosting magmatic Ni-Cu-PGE sulphide mineralization intruded within a sedimentary sequence that forms part of the Zeehan Basin, which is situated near the eastern margin of the northeast-trending Dundas Trough (Calver *et al.* 2014; Keays & Jowitt 2013).

2.1 Exploration History

The Melba Flats Ni-Cu-PGE deposit was previously known as the Five-Mile deposit (Taylor & Burger 1952) or the Cuni deposit (Greenhill 1995). This deposit underwent five major periods of development in the time between its discovery in 1893 and 1948 (Greenhill 1995), during which, eight historical workings (Fig. 2.2) were established (Reid 1925; Nye & Blake 1938; Taylor & Burger 1952). A protracted period of exploration inactivity followed, and it was not until the 'nickel boom' years between 1966 and 1971 (Hoatson *et al.* 2006) that the Melba Flats Ni-Cu-PGE deposit attracted renewed interest (Crawford & Keays 2010). Following discovery of the Avebury Ni deposit nearby, interest in further deposits in the broader region led to targeted exploration work at Melba Flats (Corbett *et al.* 2014b).

FIGURE 2.1: *Geology of the area surrounding the Melba Flats Ni-Cu-PGE deposit, also showing the location of the Avebury Ni deposit and Zeehan mineral field. The Melba Flats deposit is located about 30 km to the north of the township Strahan.*

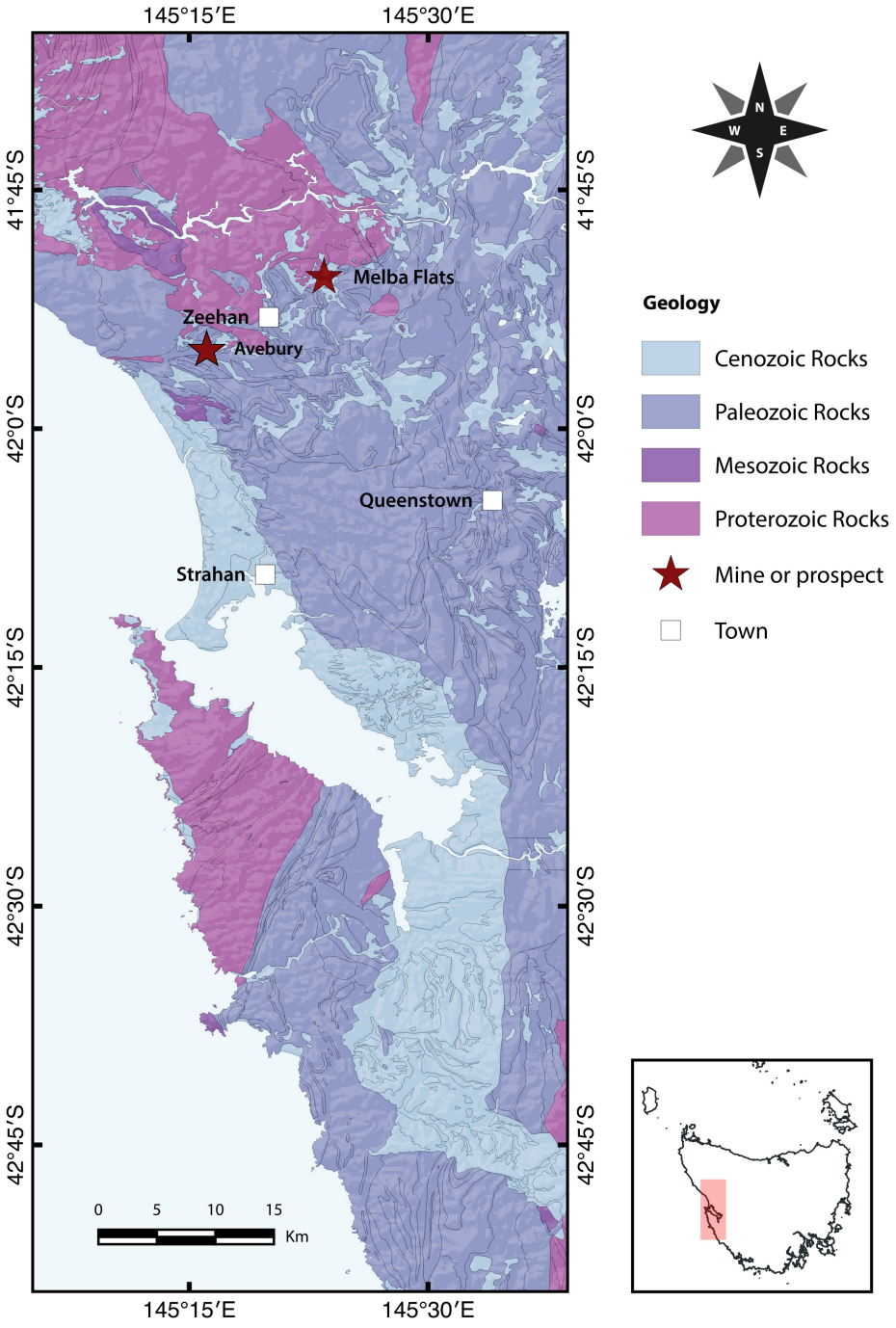

FIGURE 2.2: *Locality map of the Melba Flats area showing 8 historically-active mine workings: Deverearux, Nickel Reward, Vaudeau, Mosquito, Blowfly, South Cuni, North Cuni and Genets Winze.*

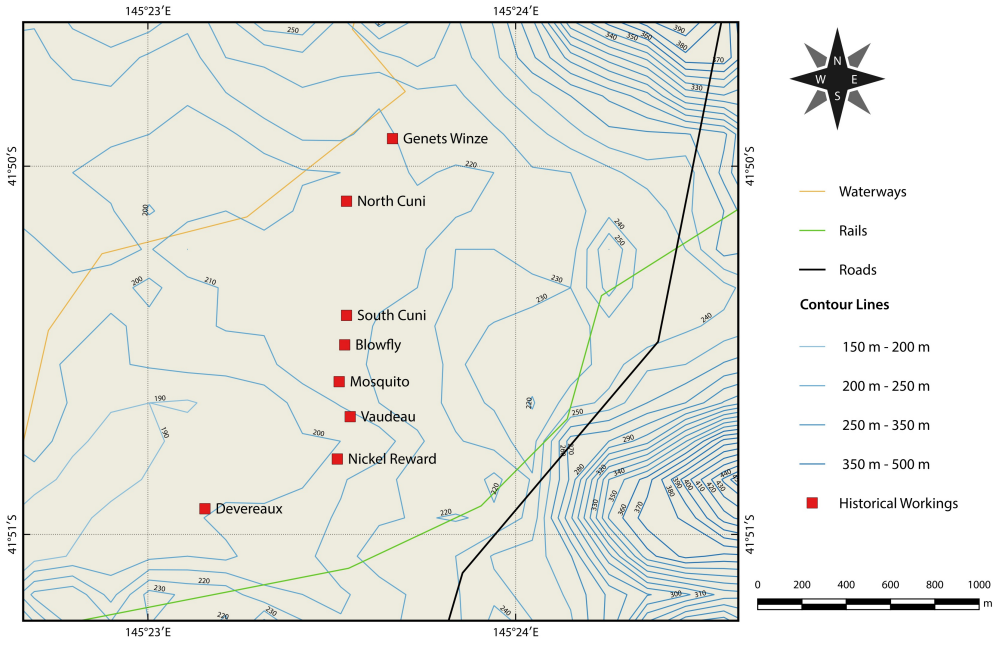

2.2 Regional Tectonics

Geologically, Tasmania is commonly divided into two major strato-tectonic terranes: 1) Eastern Tasmanian Terrane and 2) Western Tasmanian Terrane. These major strato-tectonic terranes are further sub-divided into 8 separate strato-tectonic elements as shown in Fig. 2.3. Specifically, the highly complex Western Tasmanian Terrane, which is characterized by a structural history that involves 2 major tectono-metamorphic events, known as the Cambrian Tyennan Orogeny and the Devonian Tabberabberan Orogeny (Corbett 2014; Berry & Bull 2012; Stacey & Berry 2004) is of particular interest. These major orogenic events have been recognized to occur within the Melba Flats area, and the wider region within the Dundas Trough strato-tectonic element (DT; Fig. 2.3).

FIGURE 2.3: *Strato-tectonic map of Tasmania showing the 2 major strato-tectonic terranes: Eastern Tasmanian Terrane and Western Tasmanian Terrane and the 8 stratotectonic elements: Adamsfield-Jubilee (AJ), Dundas Trough (DT), Eastern Tasmania (ET), King Island (KI), Rocky Cape Region (RC), Smithton Basin (SB), Sheffield-Ulverstone (SU) and Tyennan Region (TY).*

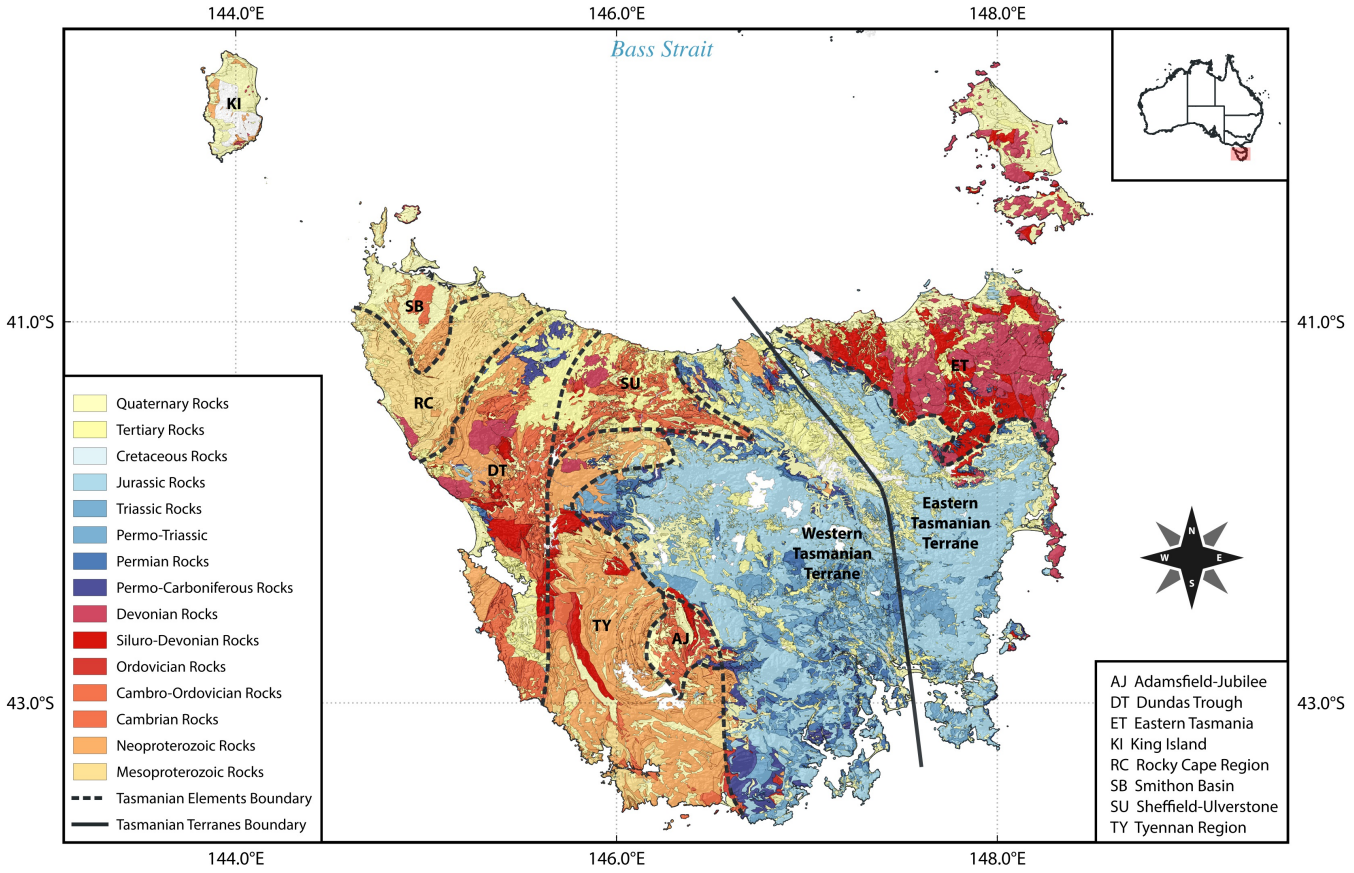

2.2.1 Cambrian

The Tyennan Orogeny was the first major tectono-metamorphic event that affected the Western Tasmanian Terrane. Typified by rapid changes in the locus and style of deformation, the Tyennan Orogeny was a complex Cambrian deformation event, with three discrete orogenic phases (Fig. 2.4; Corbett *et al.* (2014a); Stacey & Berry (2004)). The first phase resulted in the obduction of mafic-ultramafic complexes into the Dundas Trough, and across Western Tasmania, when the east-facing Tasmanian passive continental margin collided with an oceanic arc during the Lower Cambrian (Berry & Crawford 1988; Corbett *et al.* 2014a; Crawford & Berry 1992). The second phase was characterized by a Middle Cambrian extensional event that resulted in active syn-orogenic deposition and extensive post-collisional felsic-intermediate volcanism of the Mount Read Volcanics within the Dundas Trough (Berry & Crawford 1988; Corbett *et al.* 2014a; Crawford & Berry 1992). The final phase was typified by a basin inversion event during the Upper Cambrian that resulted in the tectonic uplift of the Tyennan region, with syn-orogenic sediments accumulating in a half graben (Stacey & Berry 2004; Seymour *et al.* 2013).

FIGURE 2.4: *Structural history of the Cambrian Tyennan Orogeny in Western Tasmania. Modified from Seymour* et al. *(2013).*

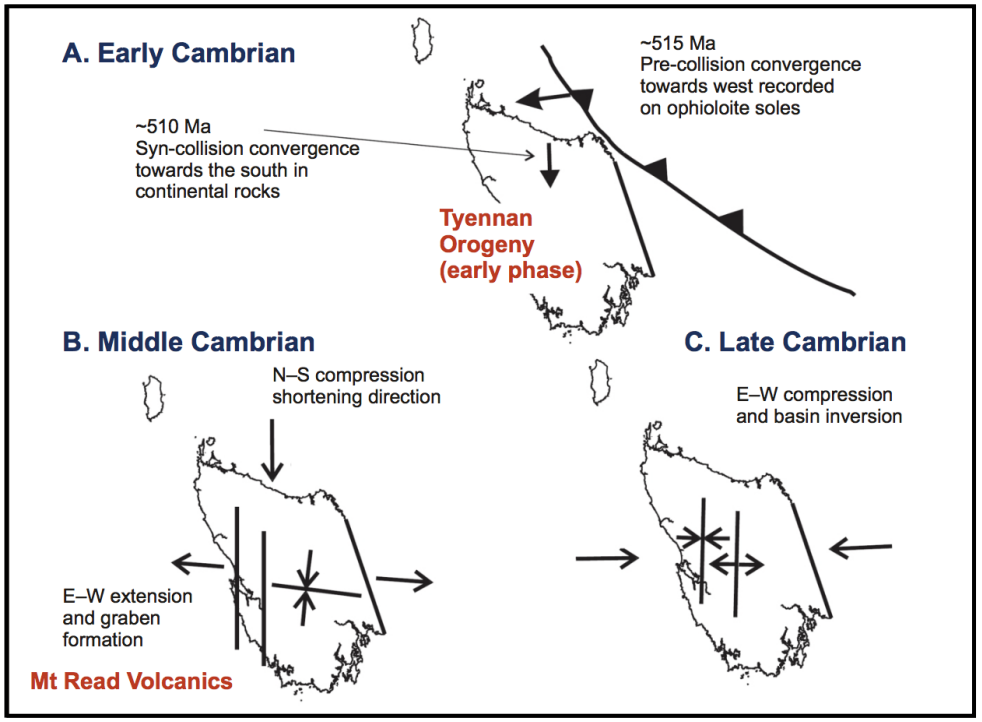

2.2.2 Devonian

A new cycle of deposition followed the Tyennan Orogeny, and continued until the Middle Devonian, when the second major tectonometamorphic event, the Tabberabberan Orogeny, occurred in the Western Tasmanian Terrane (Seymour *et al.* 2013; Stacey & Berry 2004). Characterized by a complexity of fold orientations, the Tabberabberan Orogeny was a polyphase Devonian deformation event, with two major orogenic phases (Seymour *et al.* 2013, 2014; Williams *et al.* 1989). The earlier phase was typified by a compressional event that caused the tightening of pre-existing north-trending Cambrian folds in the Dundas region (Seymour *et al.* 2013, 2014). The later phase was dominated by a second main phase of compression that produced northwest to west-northwest-trending folds and thrusts in the Dundas region (Seymour *et al.* 2013, 2014). The Tabberabberan Orogeny was also responsible for the widespread emplacement of Devonian granites (e.g. Meredith Batholith and Heemskirk Granite) in Western Tasmania (Seymour & Calver 1995; Seymour *et al.* 2014).

2.2.3 Carboniferous-Jurassic

Major structures that developed in Western Tasmania following the Tabberabberan Orogeny are attributed to the break-up of the supercontinent Gondwana. However, this tectonometamorphic event did not significantly affect the Melba Flats area, or the wider Dundas region (Corbett 2014; Greenhill 1995).

2.3 Regional Geology

The mafic intrusions hosting magmatic Ni-Cu-PGE sulphides at Melba Flats are located within the northeast-trending Dundas Trough strato-tectonic element in Western Tasmania (Fig. 2.3). Formed as a result of the extension of the Proterozoic basement, the Dundas Trough lies between two major divisions of polydeformed Mesoproterozoic metasediments characterized by siliciclastics and carbonates of the Rocky Cap Massif to the west and quartz-chlorite pelites and schist-quartzite amphibolites of the Tyennan Massif to the east (Brown & Jenner 1989; Calver *et al.* 2014; Turner *et al.* 1989).

2.3.1 Neoproterozoic

The Oonah Formation, which comprises multiply deformed, quartzwacke turbidites, formed the basement of the Dundas Trough during the Lower Tonian (*c.* 1070 - 750 Ma), when sedimentation was initiated within early rift basins along a passive continental margin (Brown *et al.* 1989; Calver *et al.* 2014; Seymour & Calver 1995). Following a hiatus in sedimentation, deposition of siliciclastics and carbonates of the Success Creek Group continued in the rift basins during the Middle Cryogenian (*c.* 750 - 640 Ma) (Brown *et al.* 1989; Calver *et al.* 2014; Seymour & Calver 1995). Crustal attenuation along the passive margin persisted from the Upper Cryogenian to the Middle Ediacaran (*c.* 640 - 570 Ma), and resulted in the accumulation of the Crimson Creek Formation, a succession of siliciclastics, volcaniclastics, and mafic rift volcanics (Brown *et al.* 1989; Calver *et al.* 2014; Seymour & Calver 1995).

2.3.2 Cambrian

Following deposition of the Crimson Creek Formation in the Dundas Trough, a series of mafic-ultramafic complexes were formed during the Middle Cambrian (*c.* 515 - 510 Ma) within an intra-oceanic arc offshore from the passive margin (Corbett *et al.* 2014a; Crawford & Berry 1992; Keays & Jowitt 2013). Represented by the Serpentine Hill mafic-ultramafic complex in the Melba Flats area, these mafic-ultramafic complexes are composed of a series of high magnesium boninites, low titanium tholeiites, and ultramafics (Corbett *et al.* 2014a; Crawford & Berry 1992; Seymour & Calver 1995). The Serpentine Hill mafic-ultramafic complex was subsequently obducted and emplaced high into the Crimson Creek Formation (Corbett *et al.* 2014a; Crawford & Berry 1992; Keays & Jowitt 2013).

Emplacement of the mafic-ultramafic complexes was followed by an extended period of sedimentation and volcanism through the Middle and Upper Cambrian (*c.* 510 - 500 Ma) that resulted in the deposition of the Dundas Group and Mount Read Volcanics (Brown *et al.* 1989; Brown & Jenner 1989; Corbett *et al.* 2014a). The Dundas Group is characterized by fossiliferous flysch-type successions that interdigitate with, and are partly derived from the Mount Read Volcanics (Brown & Jenner 1989; Corbett *et al.* 2014a; Seymour & Calver 1995). The Mount Read Volcanics occur as a belt of felsic-intermediate volcanics along the eastern margin of the Dundas Trough and are host to a number of world-class polymetallic volcanic-hosted massive sulphide deposits, for example Mount Lyell and Rosebery (Corbett *et al.* 2014a; Crawford *et al.* 1992; Greenhill 1995).

2.3.3 Ordovician-Quaternary

In the Lower Ordovician (*c.* 500 - 485 Ma), siliceous conglomerate and sandstone successions of the Owen Group overlain the interdigitated Dundas Group and Mount Read Volcanics in the Dundas Trough (Banks *et al.* 1989; Brown & Jenner 1989; Corbett *et al.* 2014a). Continued deposition in the trough until the lower Devonian (*c.* 485 - 420 Ma) formed a thick succession of limestone, siliceous sandstone, and siltstone-mudstone of the Gordon and Eldon Group (Banks *et al.* 1989; Brown & Jenner 1989; Corbett *et al.* 2014a). Following this, several granites bodies were emplaced in the Middle Devonian (Seymour & Calver 1995; Seymour *et al.* 2014). Rocks of Carboniferous to Neogene age are generally not well represented in the Dundas Trough, but erosion of the overlying rock sequences has led to the development of a shallow cover of Quaternary sands and gravels within the Dundas region (Greenhill 1995; Seymour *et al.* 2013).

2.4 Local Geology

2.4.1 Melba Flats Sediments

Host rocks to the mafic intrusions at Melba Flats (Fig. 2.5) include an interbedded succession of grey and red volcaniclastic lithic greywackes, and grey carbonaceous siltstones-mudstones, commonly interpreted as the Crimson Creek Formation (Blissett 1962; Brown 1986; Calver *et al.* 2014; Crawford & Keays 2010). Mafic fragments typified by basaltic lava, devitrified glass and detrital fragments of polycrystalline quartz are characteristic of the detritus dominant in these greywackes (Calver *et al.* 2014; Crawford & Keays 2010). A depositional environment characterized by a developing rift setting is implied by the detritus material, which was probably derived from the metasediments of the Rocky Cape Group and the mafics associated with the Crimson Creek Formation (Crawford & Keays 2010).

FIGURE 2.5: *Geological map of Melba Flats and its surrounding area.*

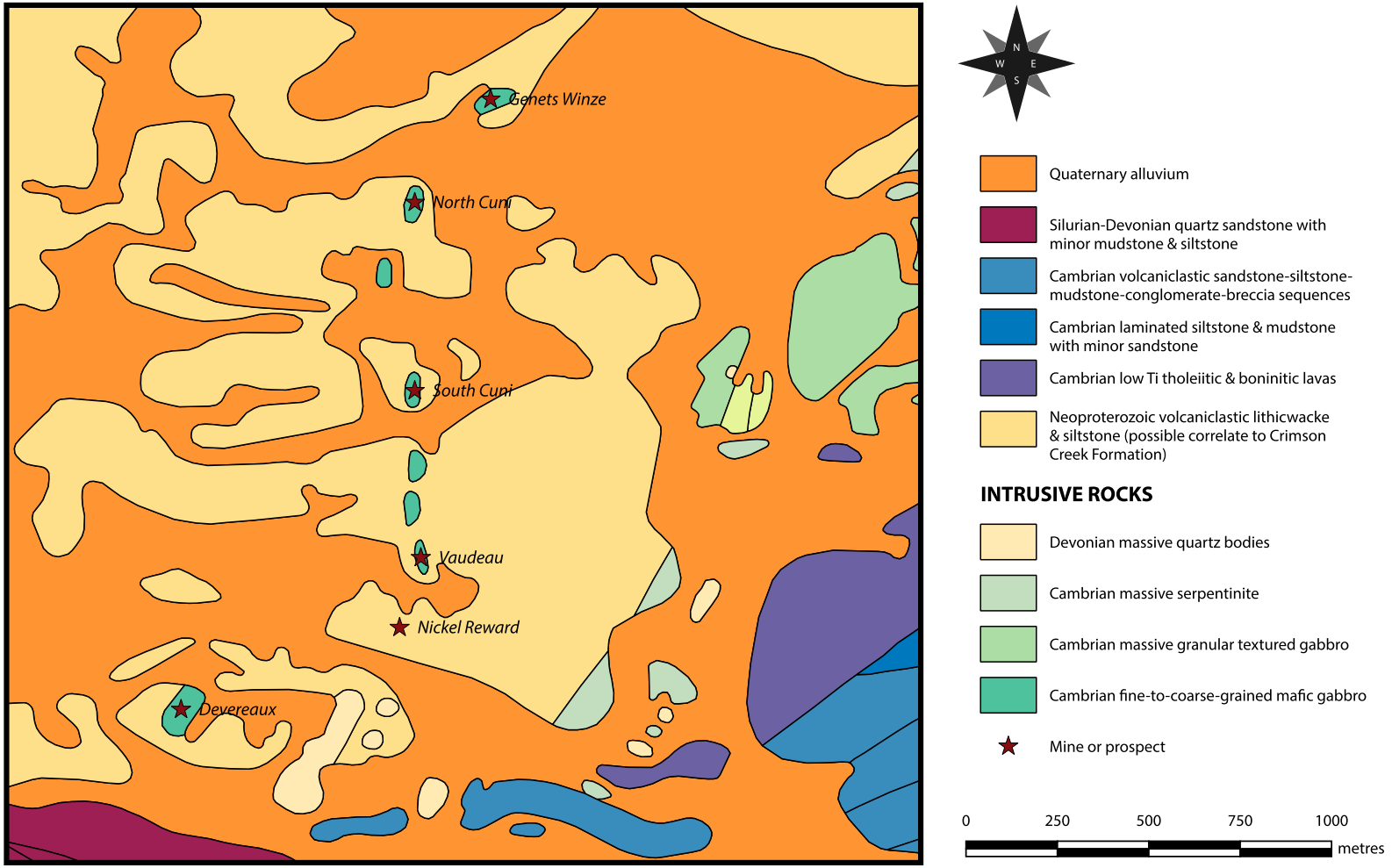

2.4.2 Previous Work

2.4.2.1 Sediment Affiliation

The provenance of the Melba Flats sediments is assumed to be the same as the other Crimson Creek Formation sediments located within the Dundas Trough (Crawford & Keays 2010). However, literature concerning the affiliation of the Melba Flats sediments has presented conflicting evidence (Greenhill 1995; Corbett *et al.* 2014a). Brown (1991) differentiated the Melba Flats host rocks as a separate, unassigned Cambrian unit and suggested an affiliation to the Dundas Group based on the presence of felsic detritus within the sediments. Conversely, Greenhill (1995) and Crawford & Keays (2010) precluded the Melba Flats host rocks from being a part of the Dundas Group or Mount Read Volcanics, due to the occurrence of mafic detritus, and the absence ophiolitic chromites. Consequently, correlation between the Melba Flats sediments and the Crimson Creek Formation remains highly ambiguous.

2.4.2.2 Depositional Age

The depositional age range of the Crimson Creek Formation is inferred to be between Upper Cryogenian to Middle Ediacaran (*c.* 650 - 580 Ma) on the basis of carbon isotope chemostratigraphy by (Adabi 1997). However, a more precise depositional age range between 579 ± 16 Ma and 582 ± 4 Ma was indirectly implied based on the dating of an intrusive volcanic of the Togari Group on King Island (Meffre *et al.* 2004) and a rhyodacite of the Kanunnah Subgroup in the Smithton Basin (Calver 1998; Calver *et al.* 2004). Consequently, the depositional age of the Crimson Creek Formation remains largely unresolved.

2.4.3 Melba Flats Mafic Intrusions

The mafic intrusions at Melba Flats (Fig. 2.5) are both concordant and disconcordant to the host rocks, and are regarded as a combination of sills and dykes (Corbett *et al.* 2014a; Crawford & Keays 2010) that often branch and bifurcate, typical of tholeiitic intrusions emplaced in a developing rift setting (Kattenhorn 1994; Crawford & Keays 2010). These intrusions occur as pods of gabbro that appear to be limited at depth, but persist as discontinuous bodies over a 2 km north-south strike length (Fig. 2.5).

Most of the intrusions appear to be between 5 to 20 m thick at Melba Flats (Crawford & Keays 2010). The narrower intrusions have been described as aphyric, with typical subophitic textures, and the thicker intrusions have been described as phyric, with typical subophitic textures (Crawford & Keays 2010). These intrusions share the same primary mineralogy, dominated by clinopyroxene and plagioclase, with minor iron-titanium oxides and hornblende (Corbett *et al.* 2014a; Crawford & Keays 2010). Little primary olivine was preserved, but pseudomorphs after olivine are often present (Greenhill 1995; Crawford & Keays 2010).

The alteration mineralogy of these intrusions is composed of lower greenschist facies metamorphic assemblages dominated by: albite, sericite, and carbonate after plagioclase, chlorite, quartz, epidote, and actinolite after clinopyroxene, and leucoxene after iron-titanium oxides (Greenhill 1995; Crawford & Keays 2010). Crawford & Keays (2010) observed that the mineralized intrusions appear to be far more intensely altered compared to the unmineralized intrusions and attributed this intense alteration to the interaction of late stage reactive fluids with the disseminated sulphides.

2.4.4 Previous Work

2.4.4.1 Geochemistry

The Melba Flats mafic intrusions were previously interpreted to have formed by sub-alkaline tholeiitic magmas, with 12 to 13% MgO content (Greenhill 1995; Crawford & Keays 2010). This interpretation is consistent with the consensus that magmatic Ni-Cu-PGE deposits are largely hosted by primitive magmas (Arndt *et al.* 2005; Simon & Ripley 2011). It was also demonstrated that the Melba Flats magma was initially S-undersaturated, before being subjected to significant crustal contamination (Crawford & Keays 2010). Such S-undersaturated magma with a crustal S component is generally required to form magmatic Ni-Cu-PGE deposits, thus highlighting the ore-forming potential of the Melba Flats magma (Keays 1995; Keays & Lightfoot 2010). Crawford & Keays (2010) suggested that the magma was highly dynamic and turbulent in nature due to the strong homogeneity of the magma with its crustal contaminant. Evidence of homogeneity and crustal contamination are important characteristics commonly associated with the formation of magmatic Ni-Cu-PGE deposits. Although these conclusions may be tentative (Crawford & Keays 2010), it was argued that the Melba Flats magma possessed a strong disposition to generate an economic Ni-Cu-PGE deposit.

2.4.4.2 Magmatic Affiliation

There appear to be conflicting interpretations regarding the magmatic affiliation of the Melba Flats mafic intrusions based on a variety of geochemical indicators. Crawford *et al.* (1992) proposed an affinity to the Miners Ridge tholeiites based on the similarly weakly LREE-enriched REE patterns. Greenhill (1995) tentatively suggested affinities to the rift tholeiites of the Crimson Creek Formation basalts (Crawford & Berry 1992) and the mafic rocks of the Henty Dyke Swarm (Crawford *et al.* 1992) based on similar major and trace element abundances. More recently, Crawford & Keays (2010) suggested that the intrusions might not be genetically associated with the Crimson Creek Formation basalts, as the Melba Flats mafic rocks possesses a notably higher magnesium content. Consequently, the magmatic affiliation of the Melba Flats mafic intrusions remains highly ambiguous.

2.4.4.3 Tectonic Implications

The emplacement of the Melba Flats mafic intrusions was interpreted to have occurred along a *c.* 600 to 570 Ma passive continental margin, immediately prior to the rifting of the Tasmanian craton (Varne & Foden 1987; Crawford & Berry 1992; Crawford & Keays 2010). Direen & Crawford (2003) further substantiated this interpretation by showing that Neoproterozoic mafic volcanics emplaced in Western New South Wales, Western Victoria and Western Tasmania, all formed part of a passive continental margin analogous to the early Paleogene break-up margin of East Greenland. Crawford & Keays (2010) argued in support that the geochemical similarity between the Melba Flats intrusions and the seaward-dipping reflector basalts of East Greenland, reflects a similarity in the tectonic setting.

2.4.4.4 Emplacement Age

The Melba Flats mafic intrusions has not been dated previously. However, the literature lists a variety of inferred age based on stratigraphic correlations. Reid (1925) and Nye & Blake (1938) suggested a middle Palaeozoic age range, between the upper Silurian and Devonian. Blissett (1962) proposed a middle upper Cambrian age range for the intrusions. More recently, Varne & Foden (1987) and Crawford & Berry (1992) suggested an upper Neoproterozoic age range. Speculation surrounding the age of the Melba Flats mafic intrusions remains highly contentious in the literature today.

2.4.5 Melba Flats Ni-Cu-PGE Sulphides

Since its discovery in 1893, historical production for the Melba Flats Ni-Cu-PGE deposit is estimated to be approximately 10,000 tonnes at an average grade of 9.7% Ni and 4.7% Cu (Greenhill 1995). The Ni-Cu-PGE mineralization at Melba Flats is typically hosted throughout the gabbroic intrusions as disseminated sulphides, and along the basal sections of the intrusions as massive sulphides (Greenhill 1995; Taylor & Burger 1952). These Ni-Cu-PGE sulphides are principally dominated by pyrrhotite, chalcopyrite, pentlandite, millerite, and minor pyrite (Greenhill 1995; Nye & Blake 1938).

2.4.6 Previous Work

2.4.6.1 Geochemistry

Crawford & Keays (2010) previously determined that two types of Ni-Cu-PGE sulphides appear to be present at the Melba Flats deposit: (1) sulphides with lower PGE and Cu tenors and (2) sulphides with higher PGE and Cu tenors. Crawford & Keays (2010) concluded on the basis of the PGE contents of the sulphides that they were magmatic in origin; furthermore, they noted that the Melba Flats sulphides had similar tenors to those of the Sudbury Ni-Cu-PGE ores. Some of the sulphides possess high S/Se ratios that suggest a crustal origin for the sulphur (Crawford & Keays 2010). These conclusions are, however, considered tentative due to the small sample size of the study.

2.4.6.2 Potential Genetic Models

Crawford & Keays (2010) suggested three models for the origin of the Melba Flats sulphides: (1) they were formed *in situ* within the mafic intrusions, (2) they were formed at depth and transported to their current sites with the same sulphide tenors and (3) they were formed at depth as low tenor sulphides, but evolved into high tenor sulphides during transport. The PGE geochemistry of primitive magma has been established as a powerful indicator of Ni-Cu-PGE sulphides-forming processes (Fiorentini *et al.* 2010). Based on this approach, Crawford & Keays (2010) proposed that the third genetic model best explains the origin of the Melba Flats sulphides. The identification of the genetic process for the Melba Flats Ni-Cu-PGE sulphides is key to determining if significant mineralization lies at depth.

Chapter 3

Methodology

3.1 Overview

A wide range of analytical techniques including whole rock geochemistry (major, trace and PGE), sulphur isotope geochemistry, U-Pb geochronology and $^{40}Ar^*/^{39}Ar$ geochronology were employed in order to acquire the necessary data for this study. All sample preparation and data acquisition procedures are summarized below. Results have been compiled, representative samples presented in tables, detailed analytical results reported in the appendices and are referred to in the text where appropriate.

3.2 Whole Rock Geochemistry

3.2.1 Sample Preparation

Samples for whole rock geochemical analyses were prepared for at the School of Earth Sciences, the University of Melbourne. Samples were first broken into hand-sized pieces using a hydraulic splitter, further crushed using a jaw crusher and then rinsed in deionised water. The crushed material was then pulverized using a bench-top agate ball mill (Retsch Mixer Mill MM 400). The whole rock powder produced for each sample was subsequently divided into aliquots of ~ 25 g for major and trace elements and ~ 50 g for platinum group elements.

3.2.2 Analytical Procedures

3.2.2.1 Major Elements

Melba Flats Mafic Intrusions

Whole rock major element analyses for the Melba Flats mafic intrusion samples were conducted in the Mineral Laboratory at Bureau Veritas, Perth, Australia. Prepared whole rock powder were fused with 12:22 lithium borate flux into glass discs and then analysed using X-ray fluorescence spectrometry (XRF). International standard reference materials SARM-2 (Syenite), SARM-3 (Lujavrite), NCD DS 14006A (Siderite) and OREAS 24B (Granodiorite) were ran as standards. Corrections were made for inter-element and matrix effects to achieve results of the highest quality.

3.2.2.2 Trace Elements

Melba Flats Sediments

Whole rock trace element analyses for the Melba Flats sediment samples were conducted in the Isotope Geochronology and Geochemistry Laboratory at the School of Earth Sciences, the University of Melbourne. Preparation for solution-based whole rock trace element analyses were carried out in a class 350 HEPA-filtered clean air chemical laboratory. Prepared whole rock powder were digested with HF-HNO_3 mixtures in Krogh-type PTFE high pressure bombs placed within an oven at 180°C for 60 hours. The dissolved solutions were then evaporated to dryness and redissolved in HCl for 24 hours in an oven. Following which, the samples were refluxed twice with concentrated HNO_3 and dissolved in sealed Teflon pressure vessels overnight. Dilutions were spiked with a 1.8% HNO_3 solution containing an internal standard mixture and then analysed using an Agilent 7700x quadrupole inductively coupled plasma mass spectrometer (Q-ICPMS). Digests of international standard reference materials from the United States Geological Survey (USGS) AGV-2 (Andesite), BCR-2 (Basalt) and GSP-2 (Granodiorite) were ran as standards. Analytical and drift correction procedures comprehensively described in Eggins *et al.* (1997) were adopted for the analysis.

Melba Flats Mafic Intrusions

Whole rock trace element analyses for the Melba Flats mafic intrusion samples were conducted in the Mineral Laboratory at Bureau Veritas, Perth, Australia. Prepared whole rock powder were fused with 12:22 lithium borate flux into glass discs and then analysed using laser ablation inductively coupled plasma mass spectrometry (LA-ICPMS), during which, the glass discs were ablated using a 193 nm ArF excimer laser. International standard reference materials SARM-2 (Syenite), SARM-3 (Lujavrite), NCD-DS-14006A (Siderite) and OREAS-24B (Granodiorite) were ran as standards. Corrections were made for inter-element and matrix effects to achieve results of the highest quality.

3.2.2.3 Platinum Group Elements

Melba Flats Mafic Intrusions

Whole rock platinum group element (PGE) analyses for the Melba Flats mafic intrusions were conducted in the Mineral Laboratory at Bureau Veritas, Perth, Australia. Prepared whole rock powder were fused with a mixture of soda ash and borax using NiS as a collector to produce NiS buttons. The NiS buttons were dissolved in a mixture of acids and the subsequent solution analysed for PGE by inductively coupled plasma mass spectrometry (ICPMS). International standard reference materials AMIS-0151 (Platinum) and AMIS-0165 (Platinum Concentrate) were ran as standards. Corrections were made for inter-element and matrix effects to achieve results of the highest quality.

3.3 Sulphur Isotope Geochemistry

3.3.1 Sample Preparation

Samples for whole rock sulphur isotope analyses were prepared at the School of Earth Sciences, the University of Melbourne. Samples were first broken into hand-sized pieces using a hydraulic splitter, further crushed using a jaw crusher and then rinsed in deionised water. The crushed material was then pulverized using a bench-top agate ball mill (Retsch Mixer Mill MM 400). The whole rock powder produced was subsequently split into aliquots of ~ 15 for whole rock sulphur isotopes analyses.

3.3.2 Analytical Procedures

Sulphur isotope analysis of the Melba Flats Ni-Cu-PGE sulphides were conducted by the Stable Isotope Lab of Queen's Facility for Isotope Research (QFIR) at Queen's University, Ontario, Canada. Prepared whole rock powder were weighed and placed into tin capsules and the sulphur isotopic composition measured using a MAT 252 Stable Isotope Ratio Mass Spectrometer coupled to a Carlo Erba NCS 2500 Elemental Analyzer. $\delta^{34}S$ values were calculated by normalizing the $^{34}S/^{32}S$ ratios of the sample relative to the Vienna Cañon Diablo Troilite (VCDT) international reference standard. Values are reported using the delta (δ) notation in units of permil (‰) and are reproducible to ± 0.2 ‰.

3.4 U-Pb Geochronology

3.4.1 Sample Preparation

Polished thin sections were prepared for the sediments and mafic intrusions sampled at Melba Flats (Table. 3.1) for the purpose of U-Pb geochronology in order to determine the samples that would yield the fresh, unaltered mineral phases necessary for the application of the U-Pb dating method. A total of 8 thin sections were examined using a scanning electron microscope (SEM) at the School of Earth Sciences, the University of Melbourne and 3 samples were selected for U-Pb dating (Table. 3.2) as they contained the most abundant and suitable zircon mineral phases required.

TABLE 3.1: *Drill cores sampled at Melba Flats for geochronology.*

Drill Hole	**Sample**	**Lithology**	**Coordinates**	
			Latitude	**Longtitude**
Genets Winze				
MF93	MF93 - 324.25 m	Gabbro	41° 49' 48.8" S	145° 23' 39.6" E
MF93	MF93 - 332.0 m	Gabbro	41° 49' 48.8" S	145° 23' 39.6" E
North Cuni				
MF40	MF40 - 56.3 m	Greywacke	41° 49' 44.7" S	145° 23' 31.5" E
MF103	MF103 - 108.6 m	Gabbro	41° 49' 54.9" S	145° 23' 31.2" E
MF103	MF103 - 112.4 m	Gabbro	41° 49' 54.9" S	145° 23' 31.2" E
MF103	MF103 - 149.8 m	Greywacke	41° 49' 54.9" S	145° 23' 31.2" E
Nickel Reward				
MF23	MF23 - 44.6 m	Greywacke	41° 50' 49.3" S	145° 23' 27.7" E
MF81A	MF81A - 165.8 m	Gabbro	41° 50' 51.4" S	145° 23' 28.0" E
Devereaux				
MF83	MF83 - 152.0 m	Greywacke	41° 51' 1.40" S	145° 22' 50.9" E

TABLE 3.2: *Samples selected at Melba Flats for U-Pb and $^{40}Ar^*/^{39}Ar$ dating.*

Drill Hole	Sample	Mineral	Dating Method	Grain Size µm	Coordinates Latitude	Longtitude
North Cuni						
MF40	MF40 - 56.3 m	Muscovite	$^{40}Ar^*/^{39}Ar$	250-350	41° 49' 44.7" S	145° 23' 31.5" E
		Zircon	U-Pb	250-500		
MF103	MF103 - 112.4 m	Hornblende	$^{40}Ar^*/^{39}Ar$	250-350	41° 49' 54.9" S	145° 23' 31.2" E
Nickel Reward						
MF23	MF23 - 44.6 m	Zircon	U-Pb	250-500	41° 50' 49.3" S	145° 23' 27.7" E
Devereaux						
MF83	MF93 - 152.0 m	Zircon	U-Pb	250-500	41° 51' 1.40" S	145° 22' 50.9" E

Zircon Extraction

Mineral separation of the selected samples were processed in the Mineral Separation Laboratory at the School of Earth Sciences, the University of Melbourne. Selected samples were first broken into hand-sized pieces using a hydraulic splitter and then crushed using a jaw crusher. The crushed material was further pulverized to ~500 µm size fractions using a disc mill and subsequently filtered through a Wilfley Table. Only the heavy fractions from the water-based gravity separation process were used for further investigation. The heavy fractions were washed with deionised water, dried under a heat lamp and then sieved using a 250 µm mesh to produce separates ~250 - 500 µm in size. A vertical Frantz Isodynamic Magnetic Separator was used to remove the most ferromagnetic minerals before the separates were subjected to further magnetic separation using the horizontal Frantz Isodynamic Magnetic Separator to produce fractions of paramagnetic (magnetic) and diamagnetic (non-magnetic) material. Only the diamagnetic fractions were further separated through heavy liquid separation techniques using sodium polytungstate (SPT) with a maximum density of ~2.89 g/cm^3 followed by Di-idomethane (DIM) with a maximum density of ~3.31 g/cm^3.

Well-preserved (alteration- and inclusion-free) zircon grains (from heavier fraction of DIM) were subsequently handpicked in ethanol solution. Cleaning of the handpicked grains were conducted in individual glass vials where the zircon separates were immersed in ethanol solution and then placed within an ultrasonic bath for 15 minutes in order to remove any surface contamination. The zircon grains were then mounted in epoxy, grounded down to expose the core of the grains and finally polished to a flat and even surface.

3.4.2 Analytical Procedures

3.4.2.1 U-Pb Detrital Zircon

U-Pb detrital zircon analysis was conducted in the Isotope Geochronology and Geochemistry Laboratory at the School of Earth Sciences, the University of Melbourne, generally following analytical procedures analogous to those described by Paton *et al.* (2010). U-Pb ages of individual zircon grains were obtained by laser ablation inductively coupled plasma mass spectrometry (LA-ICPMS) using a Laurin Technic HelEx ablation system constructed around a Complex 110, Coherent, 193 nm ArF excimer laser coupled to an Agilent 7700x quadrupole ICP-MS. A detailed description of the laser instrumentation has been previously provided by Woodhead *et al.* (2004). Individual zircon grains were ablated within a Laurin Technic HelEx cell saturated with a mixture of He and Ar gases and the laser operated with an energy density of ~2 J/cm^2 at a repetition rate of 5 Hz using a 26 μm spot size.

A typical data acquisition sequence consisted of 2 - 3 spot analyses of the zircon reference standards interspersed between sets of 10 - 12 spot analyses of zircon unknowns. Each analytical measurement in the sequence consisted of an ablation time of 40 s followed by a further 20 s of background measurement. Corrections for instrument drift, mass bias and laser-induced elemental fractionation (LIEF), as well as U-Pb age calculations, relative to primary zircon reference standard 91500 (1062.4 ± 0.4 Ma; Wiedenbeck *et al.* (1995)) and secondary reference standards Temora 2 (416.8 ± 0.33 Ma; Black *et al.* (2004)) and Plesovice (337.1 ± 0.37 Ma; Sláma *et al.* (2008)) were performed using the Iolite software package for data deconvolution and reduction. A detailed description of Iolite and the built-in U-Pb data reduction scheme employed has been previously provided by Paton *et al.* (2011).

3.5 ^{40}Ar*/^{39}Ar Geochronology

3.5.1 Sample Preparation

Polished thin sections were prepared for the sediments and mafic intrusions sampled at Melba Flats (Table. 3.1) for the purpose of ^{40}Ar*/^{39}Ar geochronology in order to determine the samples that would yield the appropriate fresh, unaltered mineral phases necessary for the application of the ^{40}Ar*/^{39}Ar dating method. A total of 9 thin sections were examined using a petrographic microscope and 2 samples were selected for irradiation and ^{40}Ar*/^{39}Ar dating (Table. 3.2) as they contained the most abundant and suitable muscovite and hornblende phases required. Photomicrographs of the selected samples can be seen in Fig. 3.1 below.

FIGURE 3.1: *Photomicrographs of samples selected for $^{40}Ar^*/^{39}Ar$ geochronology - samples MF40 - 56.3 m and MF103 - 112.4 m. (**a**) - (**c**) hornblende grains under plane polarized light (PPL), (**d**) muscovite grain under plain polarized light (PPL) and (**e**) - (**f**) muscovite grains under cross polarized light, exhibiting distinctive mottled extinction.*

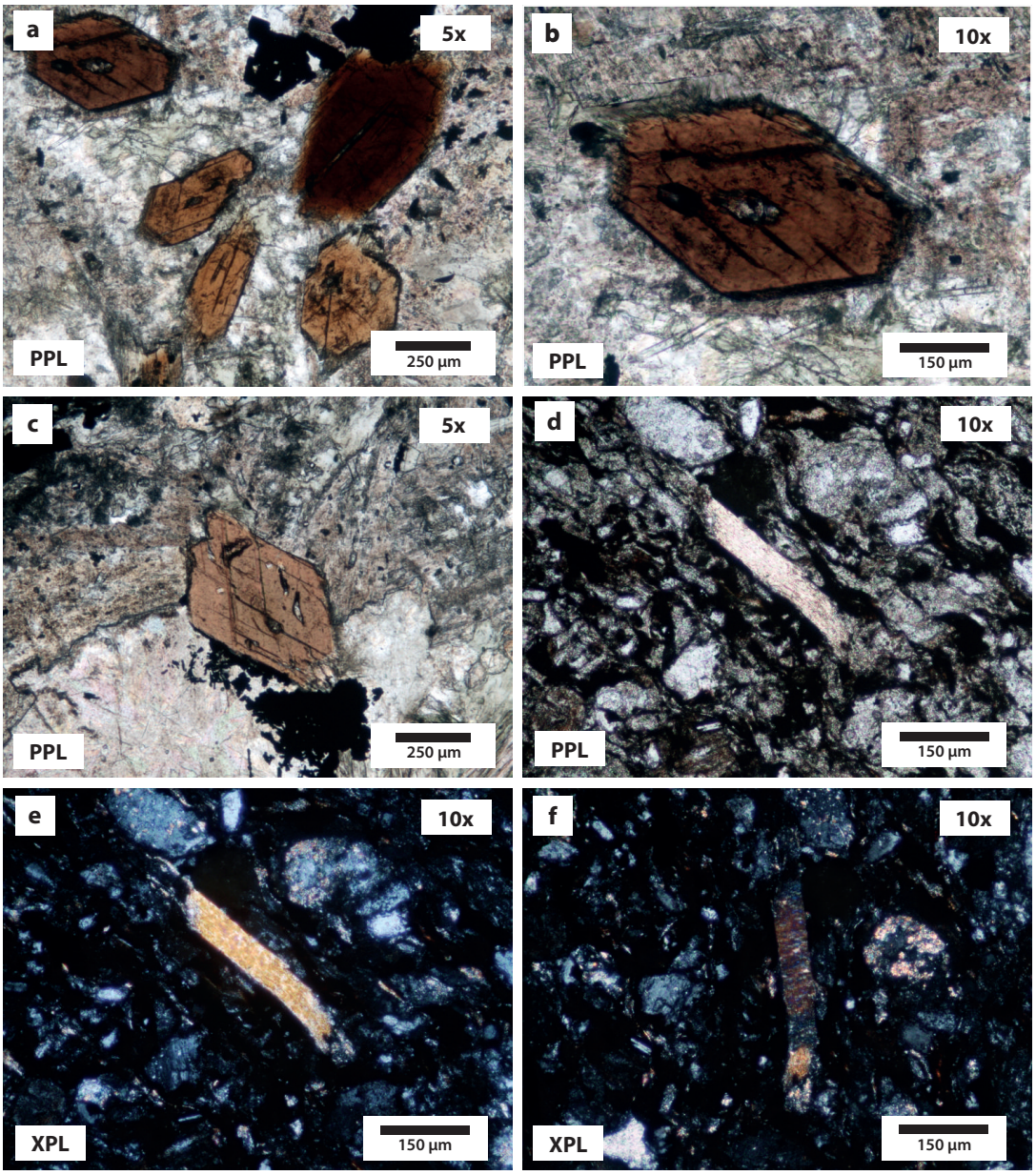

Muscovite & Hornblende Extraction

Mineral separation of the selected samples were processed in the Mineral Separation Laboratory at the School of Earth Sciences, the University of Melbourne. Selected samples were first broken into hand-sized pieces using a hydraulic splitter and then crushed into rock chips ~2 cm in size using a jaw crusher. Individual rock chips were further crushed to ~500 μm size fractions using a disc mill and then washed with deionised water; dried under a heat lamp; and sieved using a 250 μm mesh to produce separates ~250 - 500 μm in size. A vertical Frantz Isodynamic Magnetic Separator was used to remove the most ferromagnetic material from both separates. Only the mafic rock separate was subjected to further magnetic separation using the horizontal Frantz Isodynamic Magnetic Separator. To minimise possible argon loss and extraneous argon contributions, only muscovite and hornblende of grain-sizes ~250 - 350 μm were handpicked from the separates using a binocular microscope, avoiding surface alterations and inclusions where possible. Approximately 50 grains of each separate were handpicked. Cleaning of the grains was conducted in individual glass vials where the separates were immersed in 5% HNO_3 for 10 minutes in order to remove any surface contamination and then thoroughly rinsed with acetone for 5 minutes in an ultrasonic bath.

Separates were subsequently weighed, loaded into aluminium-foil packets and then placed into the centre of a silica glass tube (#UM64) along with packages of the flux monitor Fish Canyon Tuff sanidine (28.02 ± 0.14 Ma (1σ); Renne *et al.* (1998)). Can #UM64 was irradiated for 75 hours in the cadmium-shielded CLIC-IT irradiation facility of the Oregon State TRIGA Reactor at the Oregon State University, Oregon.

3.5.2 Analytical Procedures

3.5.2.1 $^{40}Ar^*/^{39}Ar$ Detrital Muscovite

$^{40}Ar^*/^{39}Ar$ muscovite laser step-heating analysis was conducted in the Noble Gas Geochronology and Geochemistry Laboratory at the School of Earth Sciences, the University of Melbourne, generally following analytical procedures analogous to those described by Phillips & Matchan (2013). Six irradiated muscovite grains were loaded into a custom-made circular copper sample holder with 6 mm wide slots. $^{40}Ar^*/^{39}Ar$ laser step-heating analyses of the individual muscovite grains were carried out using a new generation, multi-collector Thermo Fisher Scientific ARGUS-VI mass spectrometer coupled with a stainless steel gas extraction/purification line and a Photon Machines Fusions 10.6 CO_2 laser system. Decay constants and atmospheric $^{40}Ar/^{36}Ar$ ratio recommended by Steiger & Jäger (1977) and Lee *et al.* (2006) were adopted for the analyses respectively.

3.5.2.2 $^{40}Ar^*/^{39}Ar$ Hornblende

$^{40}Ar^*/^{39}Ar$ hornblende furnace step-heating analysis was conducted in the Noble Gas Geochronology and Geochemistry Laboratory at the School of Earth Sciences, the University of Melbourne, generally following analytical procedures analogous to those described by Phillips *et al.* (2007). The irradiated hornblende separate was split into two aliquots of ~ 170 mg each and loaded into tin-foil packets. $^{40}Ar^*/^{39}Ar$ step-heating analyses of the hornblende aliquots were carried out using a double vacuum tantalum furnace connected to a VG3600 mass spectrometer equipped with a Daly detector. Mass discrimination was monitored through analyses of multiple purified air aliquots from a Dorflinger pipette that yielded a weighted mean of 1.0104 ± 0.20% (1σ). Isotope interference corrections adopted for age calculations are $(^{36}Ar/^{37}Ar)_{Ca}$ = 2.58 (± 0.07) X 10^{-4}; $(^{39}Ar/^{37}Ar)_{Ca}$ = 6.56 (± 0.25) X 10^{-4}; $(^{40}Ar/^{39}Ar)_{K}$ = 1.00 (± 5.00) X 10^{-10}; and $(^{38}Ar/^{39}Ar)_{K}$ = 1.22 (± 0.23) X 10^{-2}. Decay constants and atmospheric $^{40}Ar/^{36}Ar$ ratio recommended by Steiger & Jäger (1977) and Lee *et al.* (2006) were adopted for the analyses respectively.

Apparent Age Spectra

Apparent age spectra were plotted from the corrected data using ISOPLOT (Ludwig 2012) and two age types (plateau age; and weighted mean age) were derived from the apparent age spectra of the muscovite and hornblende aliquots. The plateau age is derived from three or more contiguous gas fractions within an age spectrum that together represent at least 50% of the total ^{39}Ar released from the sample (Fleck *et al.* 1977). Usually reported at the 2σ level, the plateau ages takes into account the uncertainties in the neutron flux constant J, but exclude errors associated with the decay constants and the age of the flux monitor. Weighted mean ages were calculated for the age spectra that did not satisfy the criteria for plateau ages, with errors quoted at the 95% confidence level (Phillips *et al.* 2007). Inverse isochron diagrams were also plotted; however, due to a clustering of results near the $^{39}Ar/^{40}Ar$ axis, no reliable conclusions may be drawn, and therefore, not referred to herein.

Chapter 4

Age Dating & Geochemistry of the Melba Flats Sediments

Prior to the commencement of this research project it was unclear if the Melba Flats sediments belonged to the Crimson Creek Formation or other sedimentary formations/groups such as the Luina Group (or formerly Cleveland-Waratah Association) and Dundas Group. Consequently, a primary aim of this project was to establish the sediment affiliation and depositional age of the host sediments to the mafic intrusions at Melba Flats. A related aim was to establish the relationship between the host sedimentary rocks at Melba Flats with the hanging-wall sediments at the Avebury Ni mine; the latter had been assigned to the Crimson Creek Formation. These aims were addressed using methods that include U-Pb detrital zircon geochronology, ^{40}Ar-^{39}Ar detrital muscovite geochronology and whole rock trace element geochemistry, which are powerful tools for determining the correlation and maximum depositional age of sedimentary units. U-Pb ages of detrital zircon populations present in sedimentary rocks are compared to evaluate possible linkages between different sedimentary units in order to establish their correlation, whilst the youngest age component of a detrital zircon population generally provides the maximum depositional age of the sedimentary rock. ^{40}Ar*/^{39}Ar cooling ages of detrital muscovite help provide constraints on the maximum depositional age of sedimentary rocks, whilst trace element geochemistry provides an avenue to establish correlations between sedimentary rock units.

4.1 U-Pb Dating of Detrital Zircons

U-Pb dating of detrital zircons by laser ablation inductively coupled plasma mass spectroscopy (LA-ICPMS) is a proven technique commonly used in provenance and correlation studies of sedimentary rocks. The LA-ICPMS method is efficient and yields ages with a precision and accuracy of 1 to 2% (Gehrels 2011). Zircon ($ZrSiO_4$) is a common accessory mineral that occurs in a wide variety of rocks that form the proto-sources of sedimentary rocks. Zircon usually contains up to a percent of radioactive U and Th that decays into various Pb isotopes; it is the radioactive decay of U and Th that forms the basis of the U-Th-Pb geochronometer. Zircon is a very durable mineral that is highly resistant to chemical alteration and mechanical abrasion, therefore, the ubiquity of zircon grains in sedimentary rocks is regarded as a critical link in the understanding of the igneous and metamorphic histories of their proto-sources (Fedo *et al.* 2003; Vermeesch 2012). U-Pb dating of detrital zircons was conducted on 3 samples from the Melba Flats sediments and then compared to 3 samples from the Crimson Creek Formation sediments at Avebury, a possible correlate of the Melba Flats sediments.

4.1.1 Results: U-Pb Dating of Detrital Zircons

U-Pb detrital zircon data obtained for sediment samples MF23 - 44.6 m, MF40 - 56.3 m and MF83 - 152.0 m were visualized with Python 2.7.10 through the Anaconda Scientific Python Distribution interface, using a collection of python functions proposed by Noda (2015) to produce concordia diagrams (Fig. 4.1-4.3) for U-Pb age analysis. Kernel density plots (Fig. 4.4) were produced with DensityPlotter using the Kernel Density Estimator function of Vermeesch (2012). Only U-Pb detrital zircon ages concordant within ±15% were plotted in the concordia diagrams and kernel density plots. $^{206}Pb/^{238}U$ ages were used for detrital zircons younger than 1.2 Ga and $^{207}Pb/^{206}Pb$ ages were quoted for detrital zircons older than 1.2 Ga. All age errors quoted in the text are reported at the 2σ level. Age results and isotopic data are detailed in Table. E.1 of Appendix. E.

Sample MF23 - 44.6 m

Detrital zircon grains from sediment sample MF23 - 44.6 m form a heterogenous mix of colourless and brown translucent grains. The zircon grains are characterized by a mixture of rounded (2%), sub-rounded (34%) and euhedral (64%) zircon morphologies, aspect ratios ranging between 1:1 and 2:1, and grain widths mostly between 50 and 150 μm (Fig. 4.1a). A total of 122 zircon grains were analysed, of which 102 yield concordant ages (Table. E.1). Of these, 97 concordant analyses (95%) plot on or near concordia between 637 ± 26 Ma and 752 ± 22 Ma (Fig. 4.1c) and a further 5 concordant analyses (5%) plot within ±15% of concordia yielding ages between 1474 ± 52 Ma and 1932 ± 22 Ma (Fig. 4.1b). The remaining 20 analyses plot outside ±15% of concordia and were excluded.

The Cryogenian to Ediacaran aged detrital zircons define the youngest population consisting of mostly complete sub-rounded to euhedral zircon grains that exhibit a range of oscillatory and sector zoning textures, with mostly homogeneous cathodoluminescence (CL) response (see analyses MF23-9, MF23-77 and MF23-110; Fig. 4.1a). 67% of analyses for this population had Th/U between 0.5 and 1.1 and 33% had Th/U $<$ 0.5 (Table. E.1). A weighted mean $^{206}Pb/^{238}U$ age of 666 ± 3 Ma (2σ; MSWD = 3.0) is obtained when combining all 97 analyses. This age coincides with the largest kernel density peak observed for this sample (Fig. 4.4a). The scatter for this age is considered excessive and a statistically more robust age is obtained using a subset of 94 analyses to produce an improved weighted mean $^{206}Pb/^{238}U$ age of 665 ± 2 Ma (2σ; MSWD = 1.8). The youngest 7 analyses of this age population constrain a maximum depositional age of 644 ± 7 Ma (2σ; n = 7; MSWD = 0.12) for the sediment sample MF23 - 44.6 m.

The Paleoproterozoic to Mesoproterozic aged detrital zircons define another population consisting of mostly complete rounded zircon grains that display complex growth zoning textures, with generally darker homogeneous catholuminescence (CL) response (see analyses MF23-8, MF23-50 and MF23-89; Fig. 4.1a). The Th/U ratios for these zircon grains vary between 0.4 and 1.6 (Table. E.1). This population of zircons can be further grouped into 2 age populations: a population that yield Mesoproterozoic ages at *c.* 1474, *c.* 1585 and *c.* 1596; and another population that contains the 2 oldest zircons of the sample with Paleoproterozoic ages at 1856 ± 22 Ma and 1932 ± 22 Ma.

FIGURE 4.1: *Detrital zircon morphology, internal textures and U-Pb detrital zircon age data for sample MF23 - 44.6 m. (**a**) CL images of representative zircons showing location of the laser beam spot, along with the corresponding $^{206}Pb/^{238}U$ ages reported at the 1σ level. (**b**) Wetherill concordia plot for all concordant detrital zircon ages. (**c**) Wetherill concordia plot for concordant detrital zircon ages between 0.5 Ga and 0.8 Ga. Error ellipses are plotted at the 2σ level for all concordia diagrams. N = X/Y (Z) where X = number of concordant analyses shown on the plot, Y = total number of concordant analyses and Z = total number of analysed detrital zircon grains for sample MF23 - 44.6 m.*

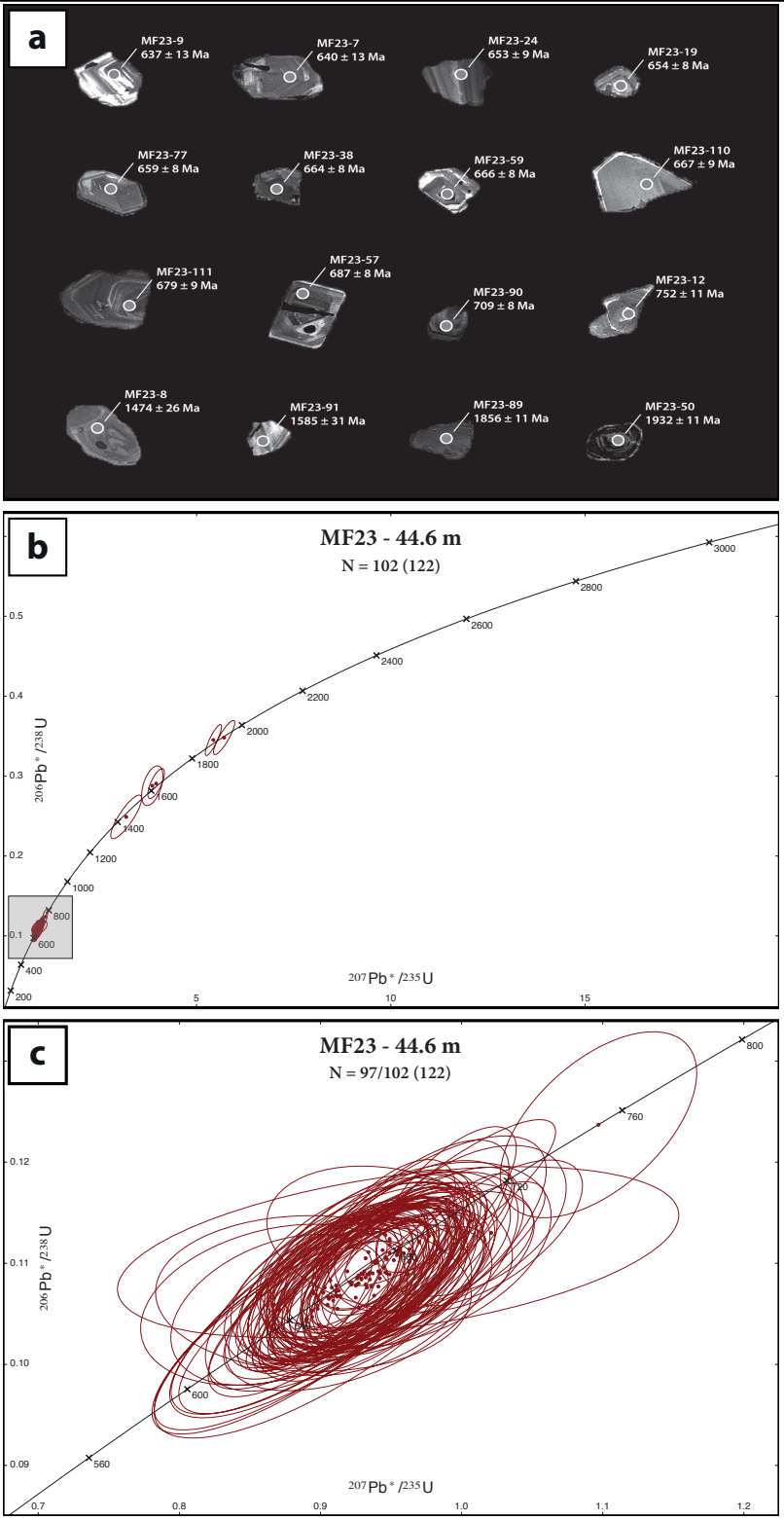

Sample MF40 - 56.3 m

Detrital zircon grains from sediment sample MF40 - 56.3 m form a heterogenous mix of colourless and brown translucent grains. These zircon grains are characterized by a mixture of rounded (3%), sub-rounded (29%) and euhedral (68%) zircon morphologies, aspect ratios ranging between 1:1 and 2:1, and grain widths generally between 100 and 200 μm (Fig. 4.2a). A total of 143 zircon grains were analysed, of which 130 yield concordant ages within ±15% (Table. E.1). The concordant dataset is multimodal with a cluster of 104 analyses (80%) plotting on or near concordia between 576 ± 15 Ma and 701 ± 19 Ma (Fig. 4.2c) and another cluster of 26 analyses (20%) yielding ages between 1421 ± 38 Ma and 2685 ± 24 Ma (Fig. 4.3b). The remaining 13 analyses plot outside ±15% of concordia and were excluded.

The youngest population is represented by Cryogenian to Ediacaran aged detrital zircons that are mostly complete sub-rounded to euhedral zircon grains that display a range of oscillatory and sector zoning textures, with a mixture of bright and dark homogeneous cathodoluminescence (CL) response (see analyses MF40-6, MF40-8 and MF40-111; Fig. 4.2a). 62.5% of analyses for this population had Th/U ratios between 0.5 and 0.8 and 32.5% had Th/U $<$ 0.5 (Table. E.1). A weighted mean $^{206}Pb/^{238}U$ age of 660 ± 5 Ma (2σ; MSWD = 8.0) is obtained when combining all 104 analyses. This age coincides with the largest kernel density peak observed for this sample (Fig. 4.4b). The scatter for this age is considered excessive and a statistically more robust age is obtained using a subset of 100 analyses to produce an improved weighted mean $^{206}Pb/^{238}U$ age of 663 ± 4 Ma (2σ; MSWD = 5.1). The youngest 2 analyses of this age population constrain a maximum depositional age of 582 ± 11 Ma (2σ; n = 2; MSWD = 1.2) for sediment sample MF40 - 56.3 m.

The next population is defined by Archean to Mesoproterozic aged detrital zircons that are mostly complete rounded to sub-rounded zircon grains that display complex and patchy growth zoning textures, with generally darker homogeneous cathodoluminescence (CL) response (see analyses MF40-9, MF40-28 and MF40-44; Fig. 4.2a). The Th/U ratio for these zircon grains vary between 0.1 and 1.2 (Table. E.1). This population of zircons can be further grouped into 2 age populations: one of which is a population that yield Paleoproterozoic to Mesoproterozoic ages between *c.* 1421 and *c.* 2013 Ma, within which a subset of 9 analyses can be grouped to give a weighted mean $^{207}Pb/^{206}Pb$ age of 1749 ± 10 Ma (2σ; MSWD = 18). This age coincides with the second largest probability density peak observed for this sample (Fig. 4.4b); and the other contains the oldest zircons of the sample with Archean ages between *c.* 2523 and *c.* 2685 Ma and are characterized by relatively high Th/U (0.4-0.8).

FIGURE 4.2: *Detrital zircon morphology, internal textures and U-Pb detrital zircon age data for sample MF40 - 56.3 m. (**a**) CL images of representative zircons showing location of the laser beam spot, along with the corresponding $^{206}Pb/^{238}U$ ages reported at the 1σ level. (**b**) Wetherill concordia plot for all concordant detrital zircon ages. (**c**) Wetherill concordia plot for concordant detrital zircon ages between 0.5 Ga and 0.8 Ga. Error ellipses are plotted at the 2σ level for all concordia diagrams. N = X/Y (Z) where X = number of concordant analyses shown on the plot, Y = total number of concordant analyses and Z = total number of analysed detrital zircon grains for sample MF40 - 56.3 m.*

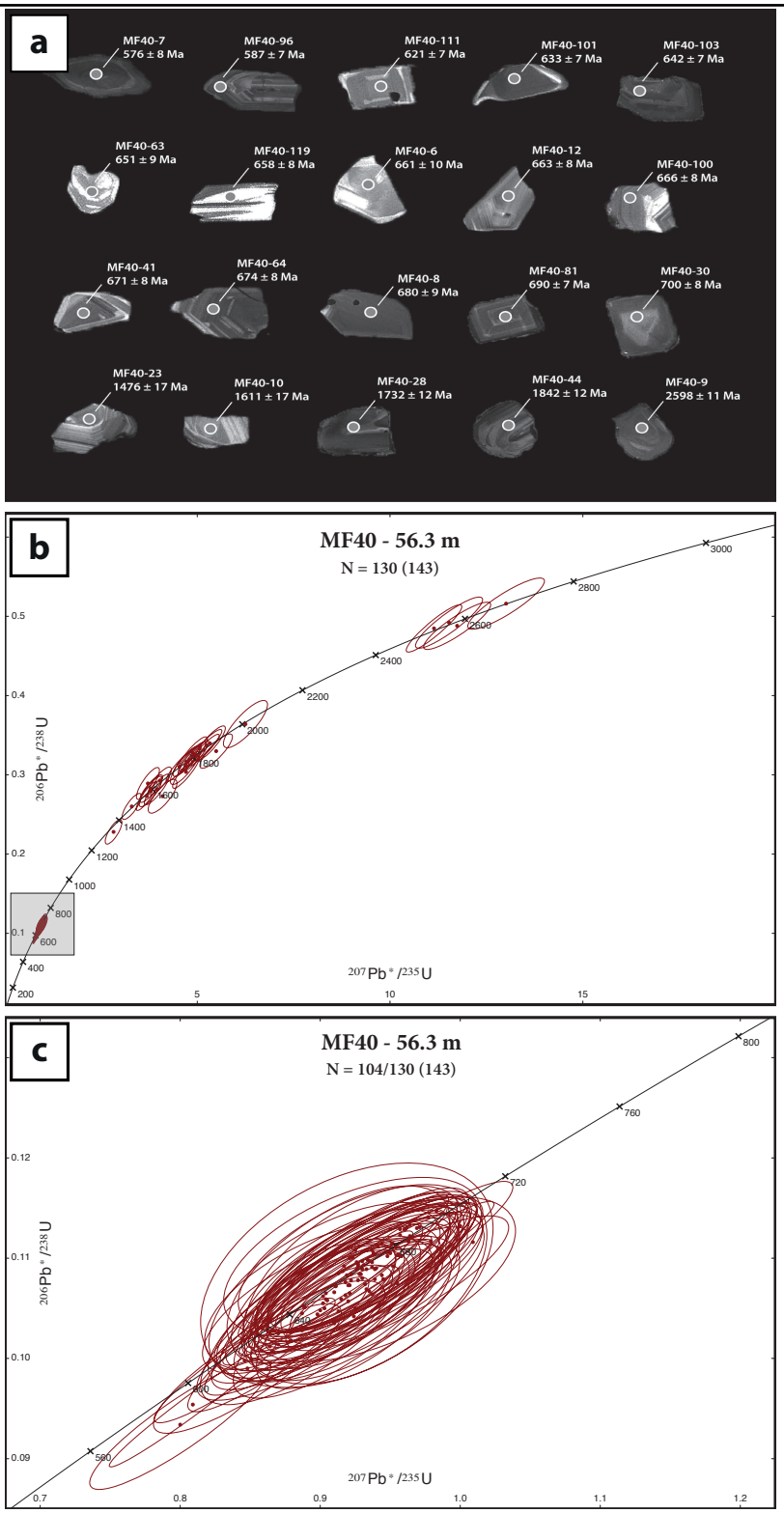

Sample MF83 - 152.0 m

Detrital zircon grains from sediment sample MF83 - 152.0 m form a heterogenous mix of colourless and brown translucent grains. The zircon grains are characterized by a mixture of rounded (2%), sub-rounded (30%) and euhedral (68%) zircon morphologies, aspect ratios ranging between 1:1 and 2:1, and grain widths generally between 50 and 150 μm (Fig. 4.3a). A total of 105 zircon grains were analysed, of which 86 yield concordant ages within ±15% (Table. E.1). One concordant zircon analysis was excluded due to irregular ablation signals. The concordant dataset is multimodal with a cluster of 72 analyses (84%) plotting on or near concordia between 597 ± 15 Ma and 702 ± 20 Ma (Fig. 4.3c) and another cluster of 14 analyses (16%) yielding ages between 1616 ± 34 Ma and 2609 ± 56 Ma (Fig. 4.3b). The remaining 19 analyses plot outside ±15% of concordia and were excluded.

The youngest population is represented by Cryogenian to Ediacaran aged detrital zircons that are mostly complete sub-rounded to euhedral zircon grains that display a range of oscillatory and sector zoning textures, with a mixture of bright and dark homogeneous cathodoluminescence (CL) response (see analyses MF83-25, MF83-38 and MF83-63; Fig. 4.3a). 67% of analyses for this population had Th/U ratios between 0.5 and 1.2 and 33% had Th/U $<$ 0.5 (Table. E.1). A weighted mean $^{206}Pb/^{238}U$ age of 660 ± 5 Ma (2σ; MSWD = 7.2) is obtained when combining all 72 analyses. This age coincides with the largest kernel density peak observed for this sample (Fig. 4.4c). The scatter for this age is considered excessive and a statistically more robust age is obtained using a subset of 70 analyses to produce an improved weighted mean $^{206}Pb/^{238}U$ age of 662 ± 5 Ma (2σ; MSWD = 5.8). The youngest two analyses of this age population constrain a maximum depositional age of 603 ± 11 Ma (2σ; n = 2; MSWD = 1.4) for the greywacke sample MF83 - 152.0 m.

The Archean to Paleoproterozic aged detrital zircons define another population consisting of mostly complete rounded to sub-rounded zircon grains that display complex and patchy growth zoning textures, with generally darker homogeneous catholuminescence (CL) response (see analyses MF83-71, MF83-74 and MF83-111; Fig. 4.3a). The Th/U ratios for these zircon grains vary between 0.1 and 1.3 (Table. E.1). This population of zircons can be classified into 2 age populations: one of which is a population that yield Paleoproterozoic ages between *c.* 1616 and *c.* 2444 Ma, within which a subset of 9 analyses can be grouped to give a weighted mean $^{207}Pb/^{206}Pb$ age of 1752 ± 14 Ma (2σ; MSWD = 3.8). This age coincides with the second largest probability density peak observed for this sample (Fig. 4.4c); and the other contains the oldest zircon of the sample with an Archean age at *c.* 2609 Ma.

FIGURE 4.3: *Detrital zircon morphology, internal textures and U-Pb detrital zircon age data for sample MF83 - 152.0 m. (**a**) CL images of representative zircons showing location of the laser beam spot, along with the corresponding $^{206}Pb/^{238}U$ ages reported at the 1σ level. (**b**) Wetherill concordia plot for all concordant detrital zircon ages. (**c**) Wetherill concordia plot for concordant detrital zircon ages between 0.5 Ga and 0.8 Ga. Error ellipses are plotted at the 2σ level for all concordia diagrams. N = X/Y (Z) where X = number of concordant analyses shown on the plot, Y = total number of concordant analyses and Z = total number of analysed detrital zircon grains for sample MF83 - 152.0 m.*

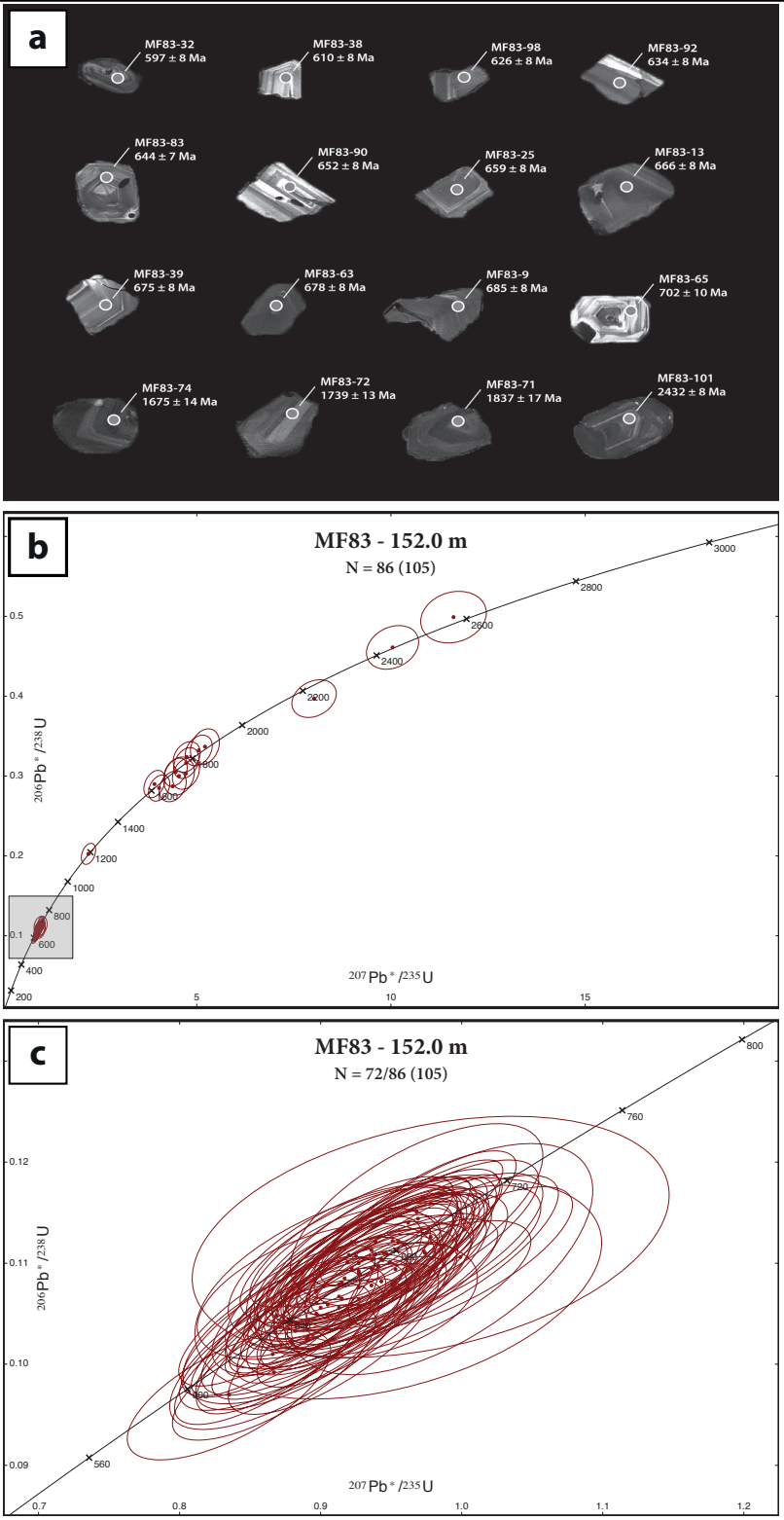

FIGURE 4.4: *Kernel density plots (Vermeesch 2012) for the dated Melba Flats sediment samples. (**a**) Kernel density plot for the detrital zircons from sample MF23 - 44.6 m. (**b**) Kernel density plot for the detrital zircons from sample MF40 - 56.3 m. (**c**) Kernel density plot for the detrital zircons from sample MF83 - 152.0 m. For detrital zircon analyses younger than 1.2 Ga, $^{206}Pb/^{238}U$ ages are used. For detrital zircon analyses older than 1.2 Ga, $^{207}Pb/^{206}Pb$ ages are used. n = total number of analyses concordant within ±15%.*

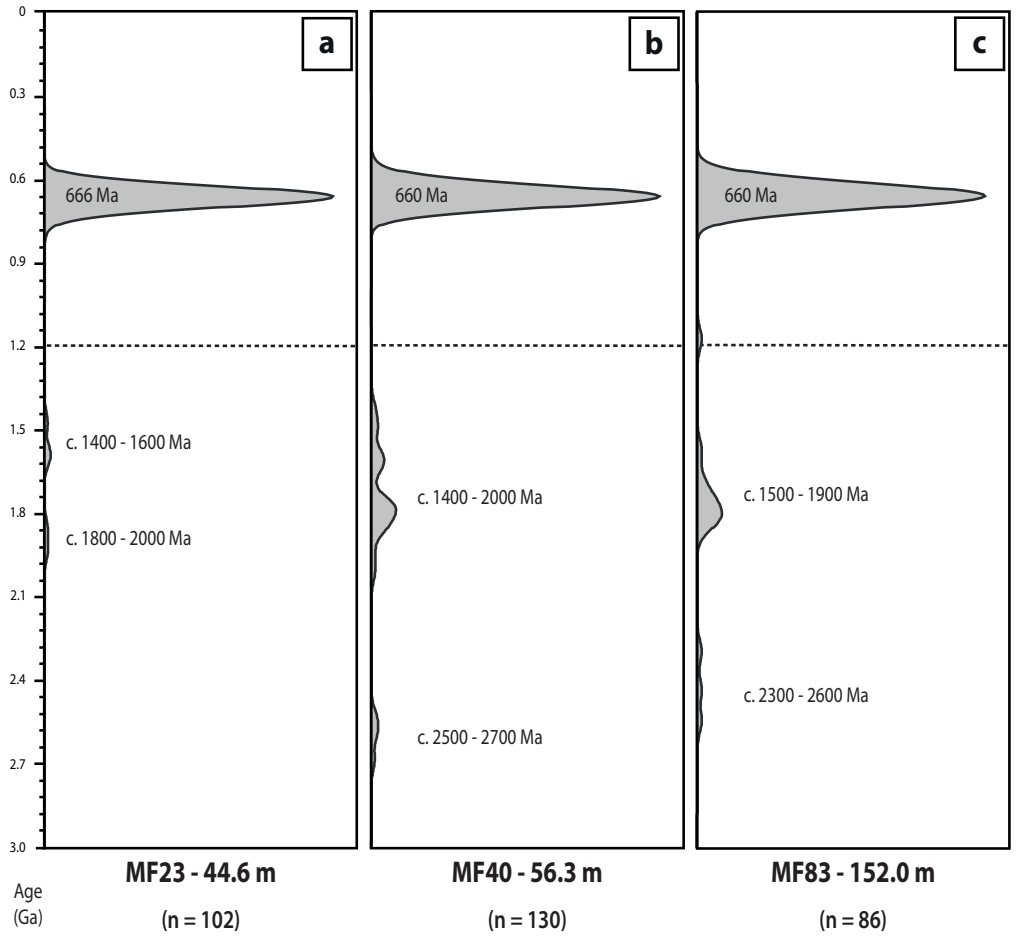

4.1.2 Comparison of Detrital Age Spectra by Kernel Function Estimation

Detrital zircons of 3 Crimson Creek Formation samples (A150B - 156.4 m; A207 - 40.4 m; and A231 - 279.6 m) from Avebury were also dated. These sediments are considered possible correlates to the Melba Flats sediments (Calver *et al.* 2014). U-Pb detrital zircons yielded major age modes at 625 - 745 Ma (85%) and 1571 - 1851 Ma (15%) for sample A150B - 156.4 m; 635 - 714 Ma (95%), 1586 - 1806 Ma (4%) and 2610 Ma (1%) for sample A207 - 40.4 m; and 634 - 704 Ma (80%), 1442 - 1864 Ma (10%) and 2037 - 3074 Ma (10%) for sample A231 - 279.6 m.

(Sircombe & Hazelton 2004) reported a method for assessing and statistically testing the similarity of U-Pb detrital zircon age spectra for the purpose of provenance analysis, correlation and tectonic reconstructions. This method takes into account the intrinsic uncertainties of age measurements by constructing kernel functional estimates for each set of age data in order to compensate for the different degrees of measurement error through the application of varying levels of smoothing. Consequently, the dissimilarity between these estimates can be quantified to provide a meaningful and valid mode of comparison between detrital age spectra (Sircombe & Hazelton 2004). This is a statistically more robust alternative to other methods of comparison such as a probability density plot, which lacks any theoretical basis as a probability density estimator (Vermeesch 2012).

U-Pb detrital zircon results for each sample are presented as individual kernel density plots on the left hand side of Figure. 4.5 in order to facilitate comparison of the detrital age spectra. While the human eye is adept in the recognition of similarities in these univariate age distributions, interpretation is always prone to subjective bias. Consequently, in order to quantify the similarities in detrital zircon age spectra, kernel functional distance estimates are calculated for each sample following the methodology proposed by Sircombe & Hazelton (2004). The dendrogram on the right hand side of Figure. 4.5 is used to graphically illustrate the dissimilarity between the samples. The cophenetic correlation is a measure of how faithfully a dendrogram preserves the pair-wise distances between the original data points.

FIGURE 4.5: *Detrital zircon age spectra and functional distance dendrogram for selected sedimentary spectra from Avebury and Melba Flats. Age kernel density in the left hand column Vermeesch (2012) have band widths and bins widths set at 20 and 50. Top right of each plot is the number of individual measurements with ages concordant within ± 15%. Inset right show the calculated matrix of comparison Sircombe & Hazelton (2004) on which the dendrogram is based. Values in the lower left half of the matrix are the calculated functional estimate distances (x 10^3). The values in the upper right half are P-values for testing the equality of age distributions. Cophenetic correlation coefficient = 0.97.*

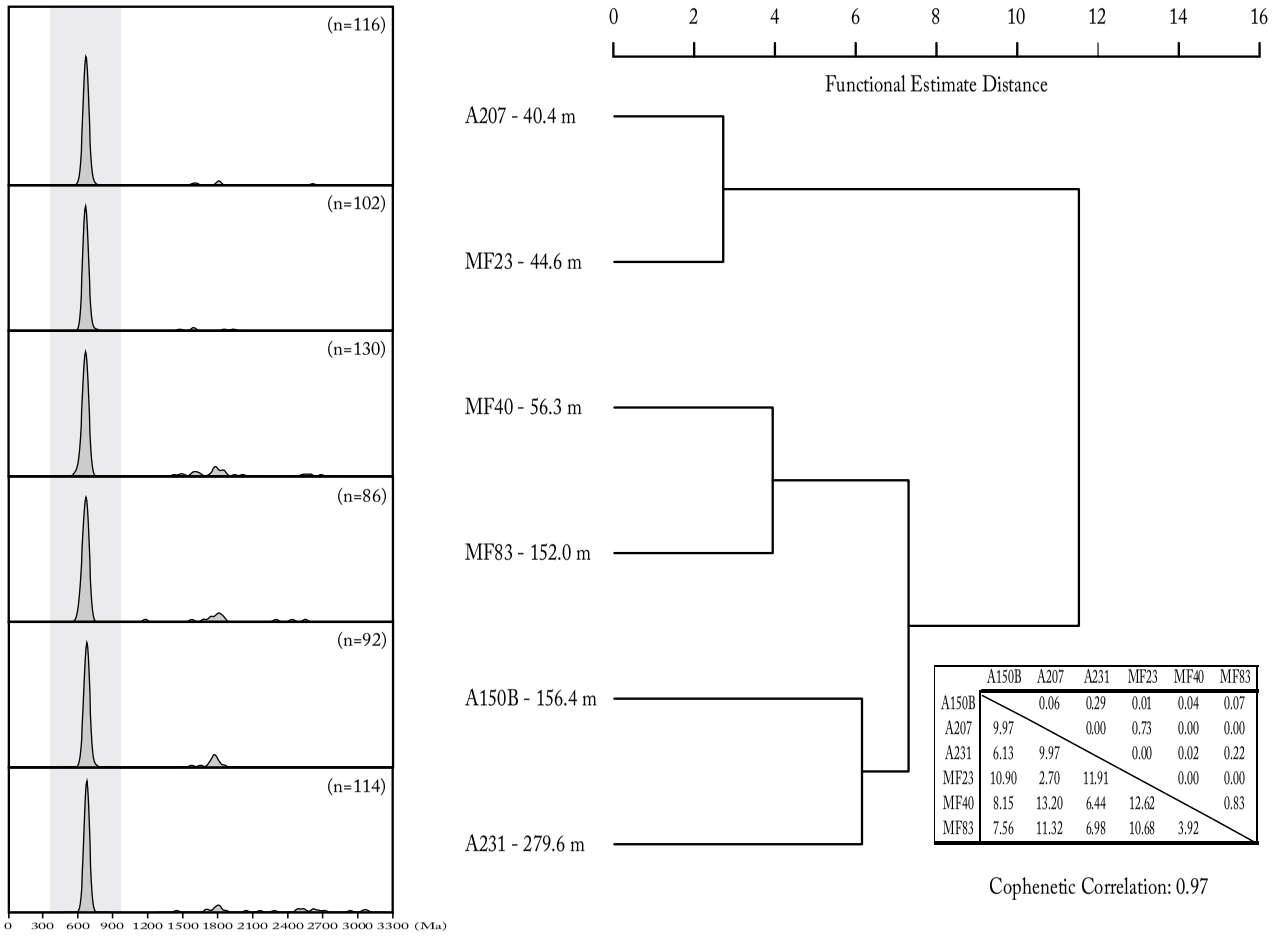

	A150B	A207	A231	MF23	MF40	MF83
A150B		0.06	0.29	0.01	0.04	0.07
A207	9.97		0.00	0.73	0.00	0.00
A231	6.13	9.97		0.00	0.02	0.22
MF23	10.90	2.70	11.91		0.00	0.00
MF40	8.15	13.20	6.44	12.62		0.83
MF83	7.56	11.32	6.98	10.68	3.92	

Strong spectral similarities exist between the 3 sediment samples from Melba Flats and the 3 Crimson Creek Formation samples from Avebury (Fig. 4.5). Common to all these samples is a dominant model age peak at c. 666 ma, although with the exception of samples MF23 - 40.4 m and A207 - 40.4 m, the other samples contain a higher proportion of zircons older than 800 Ma. Of the 6 samples, MF23 - 40.4 m and A207 - 40.4 m have the strongest correlation as illustrated by the dendrogram, with a calculated functional estimate distance of 2.7. Initially, it is perhaps surprising that Melba Flats sample MF23 - 40.4 m is more closely related to Avebury sample A207 - 40.4 m compared to the samples collected from their respective localities. However, on closer inspection it is determined that this is a direct result of the lower proportion of detrital zircons older than 800 Ma in these samples compared to the rest. All samples collected from Melba Flats and Avebury are unsurprisingly correlated with each other within their respective localities. Samples MF23 40.4 m and A231 - 279.6 share the largest functional estimation distance and hence, are the least correlated samples amongst the six that were compared. The dissimilarity relationship between all 6 samples (functional estimate distance < 12) is very much comparable to the unequivocally related sedimentary units (functional estimate distance $= 12$) observed along the east coast of Australia (Sircombe & Hazelton 2004). It is clear that there are very strong similarities between the detrital age spectra of the sedimentary rocks from Melba Flats and Avebury. Consequently, it can be argued that the Melba Flats sediments are likely to be correlates of the Crimson Creek Formation sediments at Avebury and that the Melba Flats sediments are also likely to a part of the Crimson Creek Formation.

The youngest age of a sedimentary unit can be determined from the weighted mean of 3 or more youngest zircon grains that are overlapping statistically in age at 2σ within a U-Pb detrital zircon dataset (Dickinson & Gehrels 2009; Gehrels 2011). This measure of the youngest age is considered the most statistically robust method where the derived youngest age is the most consistently compatible with maximum depositional ages of sedimentary units (Dickinson & Gehrels 2009). Following this method, the youngest ages determined for each of the Melba Flats samples MF23 - 40.4 m, MF40 - 56.3 m and MF83 - 152.0 m are 644 ± 7 Ma, 582 ± 11 Ma and 603 ± 11 Ma respectively; and for each of the Avebury samples A150B - 156.4 m, A207 - 40.4 m and A231 - 279.6 m are 634 ± 15 Ma, 623 ± 10 Ma and 641 ± 9 Ma respectively. These data demonstrate that the maximum age of deposition for the Melba Flats sediments is *c.* 582 Ma whilst the maximum age of deposition for the Avebury Crimson Creek Formation sediments is *c.* 632 Ma. These maximum depositional ages of the correlated Melba Flats sediments and the Avebury Crimson Creek Formation sediments corroborates with the interpretation of Calver *et al.* (2014); Moore *et al.* (2015) that the deposition of these sedimentary units probably occurred at or before *c.* 582 - 575 Ma (Calver *et al.* 2004; Meffre *et al.* 2004).

The detrital age spectra of the Melba Flats sediments and the Crimson Creek Formation sediments from Avebury are similar enough that it could be strongly argued that these sediments are correlates. Furthermore, the maximum depositional age for the Melba Flats sediments inferred based on the method demonstrated by Dickinson & Gehrels (2009) is coincident with the depositional age suggested by Calver *et al.* (2014) and Moore *et al.* (2015). Although the older detrital zircon age spectra of the samples were not the focus of discussion, the level of similarity as determined by the kernel function estimation method proposed by Sircombe & Hazelton (2004) suggests that these sediments may have been sourced from the same general region. Further analysis of the detrital zircon age data is required before any other interpretation with regards to their provenance may be made.

4.2 $^{40}Ar^*/^{39}Ar$ Dating of Detrital Muscovite

$^{40}Ar^*/^{39}Ar$ dating of detrital muscovite by the ARGUS-VI laser step-heating method is a technique that is far less utilized for detrital studies as compared to the U-Pb dating method. In recent years, however, has gained importance in this field as a technique that provides different but complimentary information about the source provenance of sediments in a multi-faceted approach to detrital studies. Muscovite (or white mica) is a detrital mineral commonly associated with low grade, regionally metamorphosed sediments that typically retains original cooling ages during physical processes of weathering, transport and diagenesis (Haines *et al.* 2004) These cooling ages are imparted as its source terrain cooled through the Ar closure temperature of ~425°C (Harrison *et al.* 2009) and have been demonstrated by Najman *et al.* (1997) to provide at least a maximum estimate of the depositional age of a sedimentary unit. $^{40}Ar^*/^{39}Ar$ dating of detrital muscovite was conducted on a sample from the Melba Flats sediments (MF40 - 56.3 m) where six single grain detrital muscovite underwent laser step-heating experiments.

4.2.1 Results: $^{40}Ar^*/^{39}Ar$ Detrital Muscovite

ARGUS-VI laser step-heating analyses were conducted for 6 single detrital muscovite grain (MF40-1 to MF40-6). The $^{40}Ar^*/^{39}Ar$ detrital muscovite data obtained from the analyses were visualized using ISOPLOT 3.75 (Ludwig 2012) to produce step-heating spectra (Fig. 4.6 and Fig. 4.7) for $^{40}Ar^*/^{39}Ar$ age analysis. All error box heights presented in the step-heating spectra are plotted at the 1σ level, whilst all age errors quoted in the text are reported at the 2σ level. Age results are summarized in Table. 4.1 and isotopic data detailed in Tables. D.1 to D.3 of Appendix. D.

TABLE 4.1: *Summary of $^{40}Ar^*/^{39}Ar$ age data for single muscovite grains - MF40-1 to MF40-6.*

Sample	Aliquot		Mineral	Analysis Type	No. of Steps	Total Gas Age[a] (Ma)	Plateau Age[a] (Ma)	^{39}Ar (%)	MSWD	Weighted Mean Age[a] (Ma)	^{39}Ar (%)	MSWD
MF40 - 56.3 m	MF40-1	1 Grain	Muscovite	ARGUS-VI Laser Step-heating	5	638.2 ± 0.4	No Plateau	-	-	642.4 ± 0.6	91.5	3.9
MF40 - 56.3 m	MF40-2	1 Grain	Muscovite	ARGUS-VI Laser Step-heating	5	643.5 ± 0.4	644.1 ± 0.5	85.9	1.8	644.1 ± 0.6	85.9	1.8
MF40 - 56.3 m	MF40-3	1 Grain	Muscovite	ARGUS-VI Laser Step-heating	5	744.0 ± 0.6	No Plateau	-	-	748.8 ± 0.7	85.9	5.1
MF40 - 56.3 m	MF40-4	1 Grain	Muscovite	ARGUS-VI Laser Step-heating	6	629.7 ± 0.4	No Plateau	-	-	644.9 ± 0.5	51.8	11.5
MF40 - 56.3 m	MF40-5	1 Grain	Muscovite	ARGUS-VI Laser Step-heating	6	642.4 ± 0.4	No Plateau	-	-	644.0 ± 0.6	60.0	5.5
MF40 - 56.3 m	MF40-6	1 Grain	Muscovite	ARGUS-VI Laser Step-heating	7	745.1 ± 0.6	No Plateau	-	-	746.7 ± 0.7	73.0	14.0

[a] Ages calculated relative to an assumed age of 28.02 ± 0.28 Ma (2σ) for the Fish Canyon Tuff sanidine (Renne et al. 1998) and errors associated include the J-value uncertainty.

Samples MF40-1, MF40-2, MF40-4 & MF40-5

Muscovite from sample MF40-1 produced a slightly discordant age spectrum that did not define a plateau age. A weighted mean age of 642.4 ± 0.6 Ma (MSWD = 3.9; Fig. 4.6a) for the sample was calculated from 91.5% of released ^{39}Ar gas over three contiguous steps (steps 2-4). Muscovite from samples MF40-2, MF40-4 and MF40-5 produced relatively concordant age spectra with step-like profiles that did not define plateau ages, except for sample MF40-2 that defined a plateau age of 644.1 ± 0.5 Ma (MSWD = 1.8; Fig. 4.6b) from 85.9% of released ^{39}Ar gas over three contiguous steps (steps 2-4). A weighted mean age of 644.1 ± 0.6 Ma (MSWD = 1.8; Fig. 4.6b) for the sample was also calculated from 85.9% of released ^{39}Ar gas over the same contiguous steps. Calculated weighted mean ages for the remaining samples with insufficient steps to constitute an age plateau were 644.9 ± 0.5 Ma (MSWD = 11.5; Fig. 4.6c) for sample MF40-4 from 51.8% of released ^{39}Ar gas over three contiguous steps (steps 3-5) and 644.0 ± 0.6 Ma (MSWD = 5.5; Fig. 4.6d) for sample MF40-5 from 60.0% of released ^{39}Ar gas over three contiguous steps (steps 3-5). Samples MF40-1, MF40-2, MF40-4 and MF40-5 generated weighted mean ages within error of one another, with a weighted mean of 644.0 ± 0.3 Ma (2σ; MSWD = 14). However, the scatter for this age is considered excessive and a statistically more robust age is obtained using a subset of three analyses (MF40-2, MF40-4 and MF40-5) to produce an improved weighted mean age of 644.4 ± 0.3 Ma (2σ; MSWD = 3.4).

Samples MF40-3 & MF40-6

Muscovite from sample MF40-3 produced a slightly discordant age spectrum that did not define a plateau age. A weighted mean age of 748.8 ± 0.7 Ma (MSWD = 5.1; Fig. 4.7a) for the sample was calculated from 85.9% of released ^{39}Ar gas over three contiguous steps (steps 2-4). Muscovite from sample MF40-6 produced a relatively concordant age spectrum with a step-like profile that did not define a plateau age. A weighted mean age of 746.7 ± 0.7 Ma (MSWD = 14; Fig. 4.7b) for the sample was calculated from 73.0% of released ^{39}Ar gas over three contiguous steps (steps 2-4). Samples MF40-3 and MF40-6 generated weighted mean ages that were within error of one another, with a weighted mean of 747.8 ± 0.5 Ma (2σ; MSWD = 18).

Discordance in ^{40}Ar/^{39}Ar Age Spectra*

Discordance observed in the age spectra in each of these samples may be a result of possible ^{39}Ar loss or relocation during irradiation of the muscovite grains commonly as a by-product of ^{39}Ar recoil and/or microscopic chlorite and actinolite alteration that may have existed within the mineral crystal lattice (Hodges *et al.* 2005; Faure & Mensing 2005a).

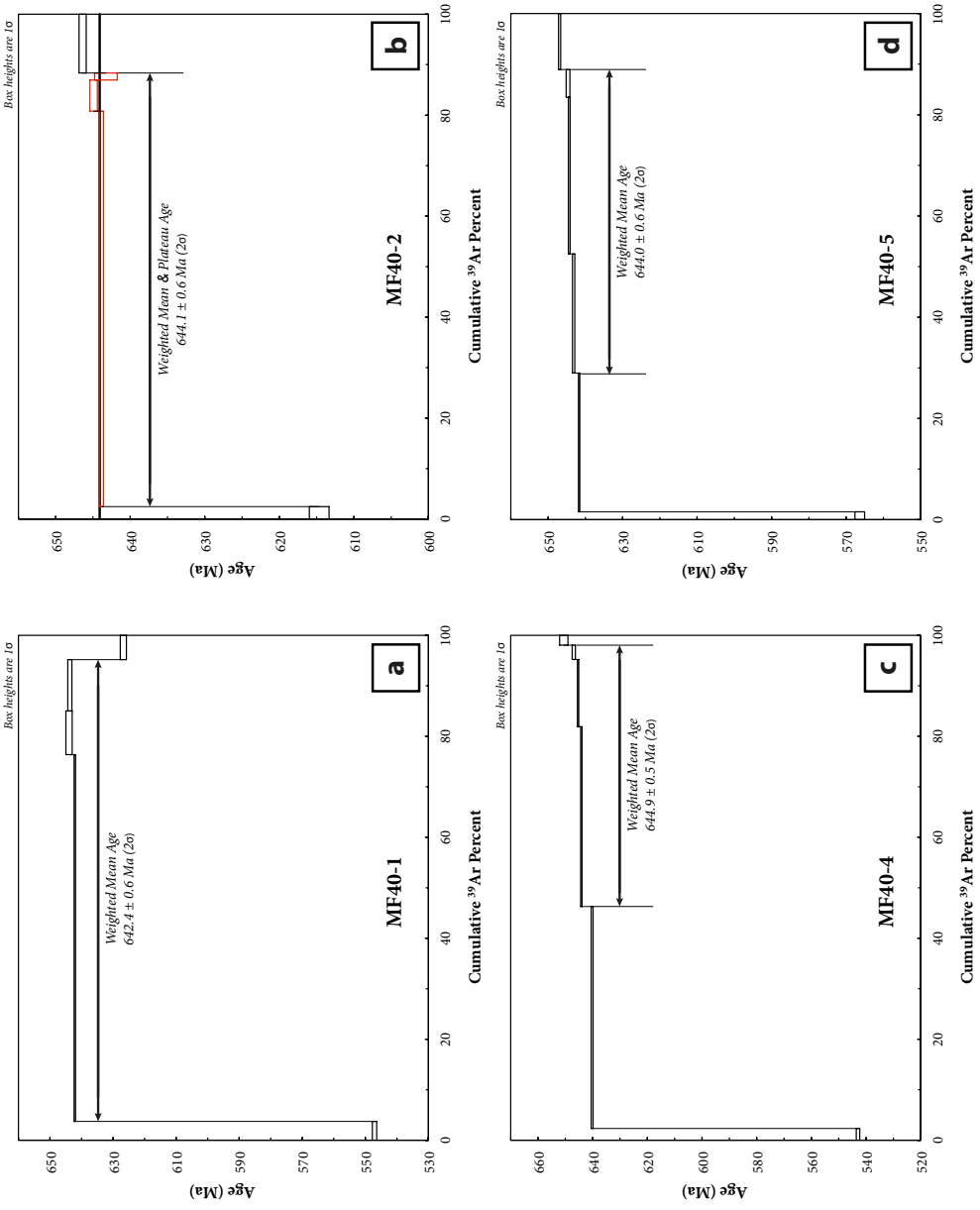

FIGURE 4.6: $^{40}Ar^*/^{39}Ar$ *step-heating spectra for four single muscovite grains (MF40-1, MF40-2, MF40-4 and MF40-5).* (**a**) $^{40}Ar^*/^{39}Ar$ *step-heating spectra for MF40-1.* (**b**) $^{40}Ar^*/^{39}Ar$ *step-heating spectra for MF40-2.* (**c**) $^{40}Ar^*/^{39}Ar$ *step-heating spectra for MF40-4.* (**d**) $^{40}Ar^*/^{39}Ar$ *step-heating spectra for MF40-5. Steps highlighted in red are included in plateau ages. All ages are reported at the 2σ level.*

FIGURE 4.7: *$^{40}Ar^*/^{39}Ar$ step-heating spectra for two single muscovite grains (MF40-3 and MF40-6). (**a**) $^{40}Ar^*/^{39}Ar$ step-heating spectra for MF40-3. (**b**) $^{40}Ar^*/^{39}Ar$ step-heating spectra for MF40-6. All ages are reported at the 2σ level.*

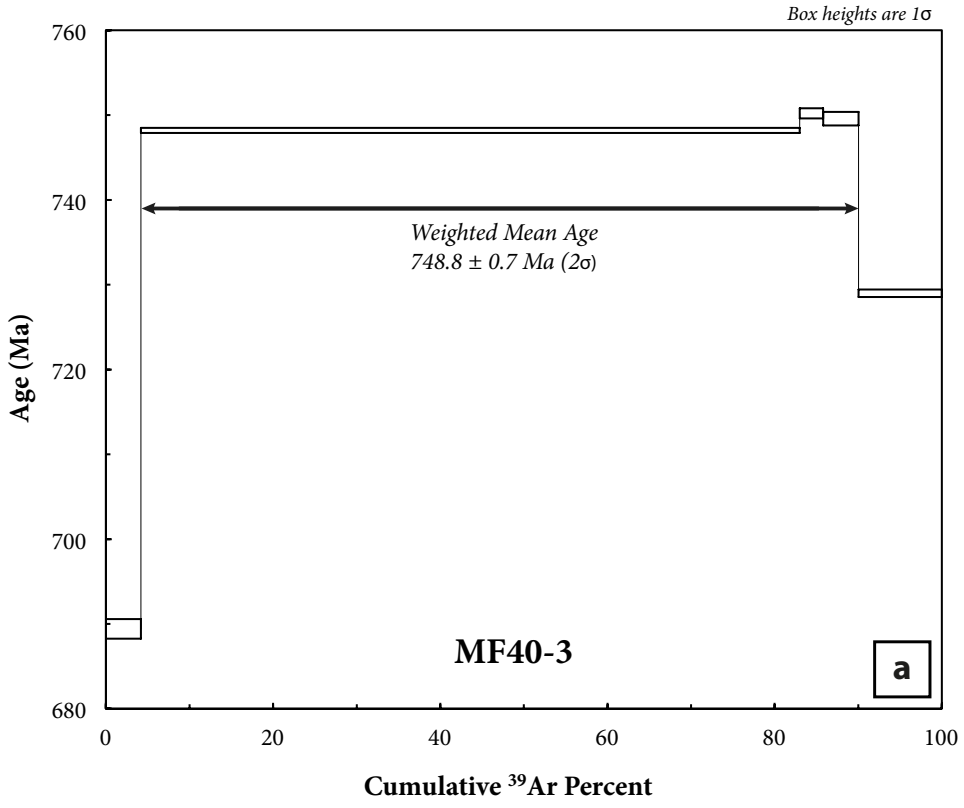

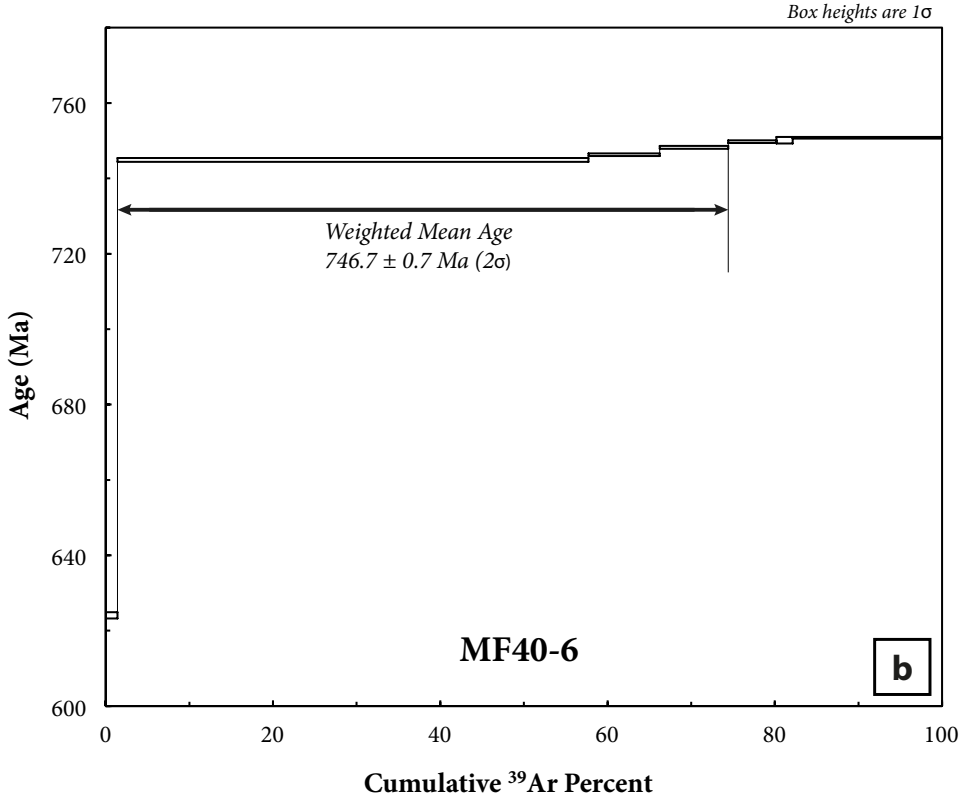

4.2.2 Implication of $^{40}Ar^*/^{39}Ar$ Detrital Muscovite Cooling Ages

Vermeesch (2004) indicated that if it is desired that no fraction of a detrital mineral age population comprising more than 0.05 of the total is missed at the 95% confidence level, at least 117 detrital mineral grains should be dated. Considering this, the fact that only 6 single grain detrital muscovite grains were dated strongly suggests that that the required level of statistical adequacy is insufficient for any definitive conclusions to be drawn from these cooling ages. However, the ARGUS-VI laser step-heating technique have produced detrital muscovite ages of high precision and accuracy; consequently, it is argued that some general inferences can be made about the implication of the $^{40}Ar^*/^{39}Ar$ cooling ages. $^{40}Ar^*/^{39}Ar$ detrital muscovite cooling ages obtained are presented as a kernel density plot and then overlain upon the U-Pb detrital zircon age spectra for the equivalent sample (MF40 - 56.3 m) from Melba Flats in Fig. 4.8.

FIGURE 4.8: *Kernel density plot comparing $^{40}Ar^*/^{39}Ar$ detrital muscovite ages and U-Pb detrital zircon ages for sample MF40 - 56.3 m from the Melba Flats sediments.*

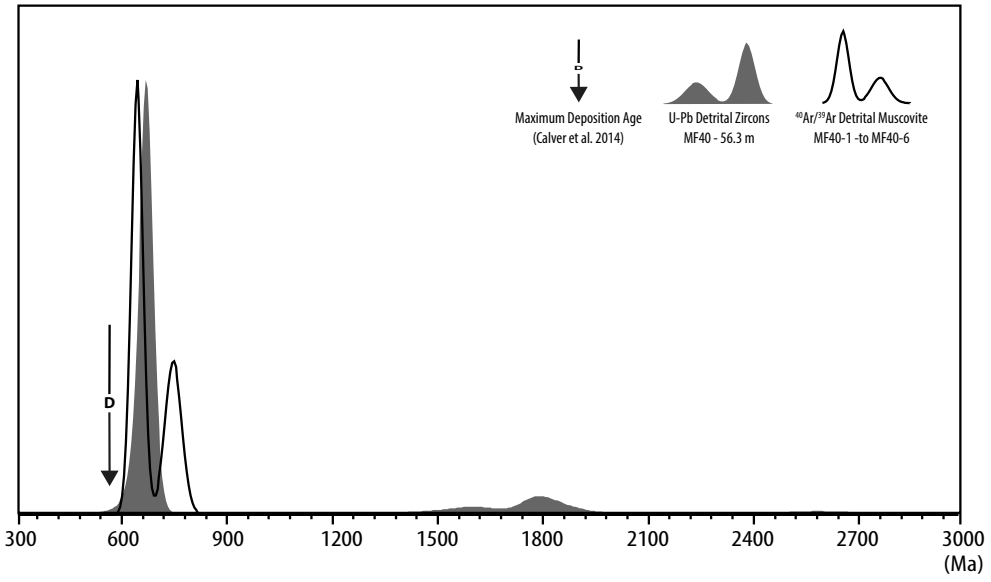

6 single muscovite grains produced a tight cluster of ages between *c.* 642 and *c.* 749 Ma. Age spectra defined by these cooling ages displays an overall bimodal distribution, comprising a double kernel density peak of *c.* 644 Ma and *c.* 748 Ma. The U-Pb zircon ages display a major age peak in the range between *c.* 576 and *c.* 701 Ma, close to the maximum age of deposition (Calver *et al.* 2014) and an older peak centred around *c.*1749 ma. The Melba Flats detrital muscovite $^{40}Ar^*/^{39}$ primary cooling age peak of *644* Ma are closely coincident with the main zircon age peak of *c.* 663 Ma, but interestingly, the centre of the secondary cooling age peak of *748* Ma is slightly older than that the oldest zircon of the main zircon U-Pb age peak. According to Haines *et al.* (2004), this might suggest that most of the zircons were derived from contemporaneous volcanism rather than being of plutonic/metamorphic

origin. It can also be argued that the $^{40}Ar^*/^{39}Ar$ cooling ages provide a constraint on the maximum deposition age of the Melba Flats sediments; they are younger than the detrital muscovite ages that record the cooling of the mineral through 425°C in the source region, which strongly corroborates with the youngest age component (*c. 582 Ma*) of the U-Pb detrital zircon spectra.

The muscovite cooling ages have provided complimentary information that validated and strengthened the interpreted maximum depositional age of the Melba Flats sediments provided by the U-Pb detrital zircon ages. Nevertheless, as a consequence of the small sampling size, the inferences made should be interpreted with care as they are not supported by the required level of statistical adequacy.

4.3 Trace Element Geochemistry

Trace element geochemistry of sedimentary rocks has been shown to be another excellent tool in the correlation of sedimentary rocks. Numerous authors have demonstrated correlation between sedimentary rocks by comparing the relative abundance of trace elements and rare earth elements (REE) in sedimentary rocks (Do Campo & Ribeiro Guevara 2005; Floyd *et al.* 1991; Winchester & Max 1989). Trace element geochemistry analyses were conducted for 5 samples from the Melba Flats sediments and then compared to 4 samples from the Crimson Creek Formation sediments at Avebury, a possible correlate of the Melba Flats sediments.

4.3.1 Results: Trace Element Geochemistry

Solution mode laser ablation inductively coupled plasma mass spectrometry (LA-ICPMS) was conducted for 5 whole rock samples from 5 drill holes that intersected sediments at Melba Flats. All standard results are within error. The trace element analytical data is summarized in Table. 4.2 and detailed in Table. C.2 of Appendix. C.

TABLE 4.2: *Summary of trace element analytical data for the Melba Flat sediments.*

	Melba Flats Sediments						
	MF23-44.6	**MF40-56.3**	**MF83-152.0**	**MF93-123.55**	**MF103-149.8**	**Mean**	**S.D.**
	Lithophile Elements (ppm)						
Cs	13.9	30.5	3.8	23.8	38.1	22.0	12.1
Rb	71.2	98.8	14.0	108.8	217.4	102.0	66.5
Ba	267.9	337.4	525.0	207.4	472.6	362.1	120.1
Th	8.8	9.1	8.6	10.0	12.1	9.7	1.3
U	2.4	2.8	2.3	2.7	3.0	2.6	0.3
Nb	39.9	45.4	38.5	41.0	40.9	41.2	2.3
Ta	2.2	2.8	2.4	2.8	2.7	2.6	0.2
K	20497.5	22308.9	4232.7	17858.6	56207.0	24220.9	17208.4
La	44.5	50.4	46.9	54.8	57.8	50.9	4.9
Ce	99.3	112.6	100.3	121.4	122.1	111.1	9.8
Pb	14.4	10.1	14.0	8.6	5.8	10.6	3.2
Pr	12.4	13.7	12.4	15.2	15.1	13.8	1.2
Sr	75.6	111.5	108.5	50.4	46.5	78.5	27.6
P	8747.9	9985.0	8554.6	7877.3	9922.7	9017.5	817.6
Nd	49.5	54.2	48.2	60.2	59.9	54.4	5.0
Zr	335.7	446.2	304.2	339.0	322.2	349.4	49.9
Sm	10.6	11.5	10.1	13.1	13.0	11.7	1.2
Eu	2.6	2.9	2.4	3.0	2.3	2.6	0.3
Ti	41484.7	53425.9	38098.0	40679.0	40451.8	42827.9	5417.7
Dy	9.0	9.6	8.2	11.0	12.3	10.0	1.5
Y	44.9	47.2	40.1	54.7	61.0	49.6	7.4
Yb	4.1	4.4	3.7	4.6	5.3	4.4	0.5
Lu	0.6	0.6	0.5	0.6	0.7	0.6	0.1
	Rare Earth Elements (ppm)						
La	44.5	50.4	46.9	54.8	57.8	50.9	5.5
Ce	99.3	112.6	100.3	121.4	122.1	111.1	11.0
Pr	12.4	13.7	12.4	15.2	15.1	13.8	1.4
Nd	49.5	54.2	48.2	60.2	59.9	54.4	5.6
Sm	10.6	11.5	10.1	13.1	13.0	11.7	1.4
Eu	2.6	2.9	2.4	3.0	2.3	2.6	0.3
Gd	10.2	11.0	9.4	12.3	13.6	11.3	1.7
Tb	1.6	1.7	1.4	1.9	2.2	1.7	0.3
Dy	9.0	9.6	8.2	11.0	12.3	10.0	1.6
Ho	1.8	1.9	1.6	2.1	2.4	1.9	0.3
Er	4.7	5.0	4.3	5.5	6.2	5.1	0.8
Tm	0.7	0.7	0.6	0.8	0.9	0.7	0.1
Yb	4.1	4.4	3.7	4.6	5.3	4.4	0.6
Lu	0.6	0.6	0.5	0.6	0.7	0.6	0.1
Σ REE	251.5	280.1	250.0	306.4	313.9	280.4	29.8
	Element Ratios						
$(Nd/Lu)_{C1}$	4.68	4.76	5.01	5.04	4.38	4.8	0.3
$(La/Yb)_{C1}$	7.8	8.2	9.0	8.6	7.8	8.3	0.5
$(La/Sm)_{C1}$	2.7	2.8	3.0	2.7	2.9	2.8	0.1
$(Gd/Yb)_{C1}$	2.1	2.1	2.1	2.2	2.1	2.1	0.1
Eu/Eu*	0.75	0.77	0.74	0.70	0.53	0.70	0.1

(Nd/Lu)C1, (La/Yb)C1, (Gd/Yb)C1 are C1 chondrite-normalized ratios; chondrite REE abundances from Sun and McDonough (1989).

Eu/Eu* = 2(Eu)C1/[(Sm)C1+(Gd)C1] from Maas and McCulloch (1991).

Lithophile Elements

C1 chondrite-normalized lithophile element patterns for the Melba Flats sediment samples are relatively parallel (Fig. 4.9), with the more compatible elements (Cs to P) exhibiting more variation in lithophile element enrichment patterns in comparison to the less compatible elements (Nd to Lu). These incompatible elements are characterized by strongly fractionated element patterns, with a $(Nd/Lu)_{C1}$ average of ~ 4.8. Relative to C1 chondrite (Sun & McDonough 1989), the sediments are variably depleted in Rb, K, Pb, Sr and P relative to the other lithophile elements, with enrichment factors in these elements ranging from 2 to about 90. The sediments are also characterized by varied enrichment in Ba, Th, U and Ti, with enrichment factors in these elements ranging from 100 to about 500. There are some significant variation in the enrichment factors between samples for the elements Cs, Rb and K. These elements are known to be fluid mobile and most probably reflect element mobility during post-depositional processes. There are no systematic differences in the lithophile element patterns between the sediment samples at Melba Flats.

Rare Earth Elements

C1 chondrite-normalized REE patterns for the Melba Flats sediments are almost identical (Fig. 4.10), with the LREE displaying strongly enriched patterns in comparison to the MREE and HREE. Relative to C1 chondrite (Sun & McDonough 1989), the sediments are enriched in LREE relative to the MREE, with a $(La/Sm)_{C1}$ average of ~ 2.8; and strongly enriched in LREE relative to the HREE, with a $(La/Yb)_{C1}$ average of ~ 8.3. The sediments are also characterized by weakly fractioned HREE, with a $(Gd/Yb)_{C1}$ average of ~ 2.1 and pronounced negative Eu anomalies where the $(Eu/Eu^*)_{C1}$ average is ~ 0.70 (Maas & McCulloch 1991). There is little dissimilarity in the REE patterns between the sediment samples at Melba Flats.

FIGURE 4.9: *C1 chondrite-normalized lithophile element plot for the Melba Flats sediment samples MF23-44.6, MF40-56.3, MF83-152.0, MF93-123.55 and MF103-149.8.*

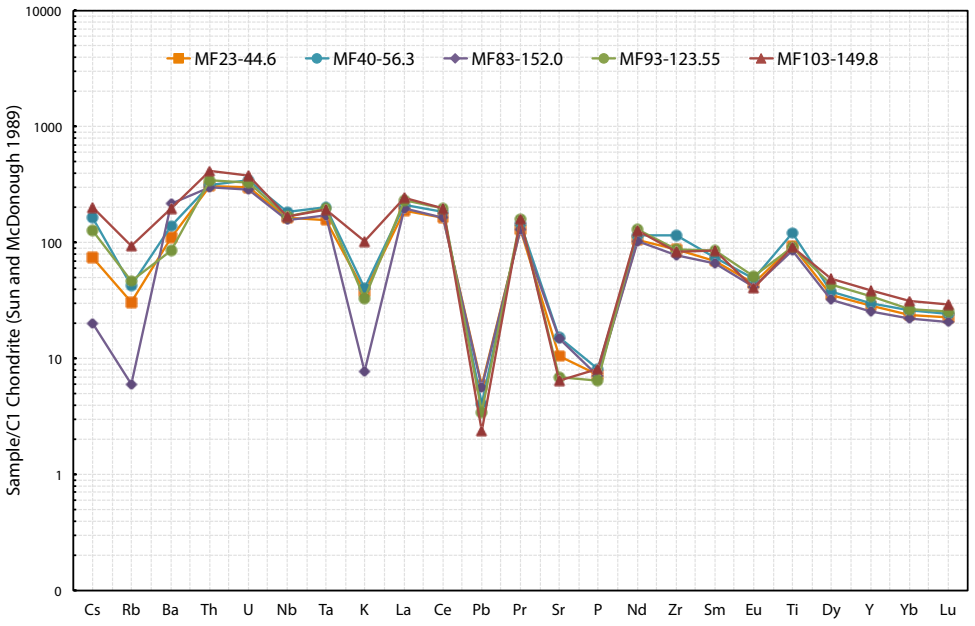

FIGURE 4.10: *C1 chondrite-normalized REE plot for the Melba Flats sediment samples MF23-44.6, MF40-56.3, MF83-152.0, MF93-123.55 and MF103-149.8.*

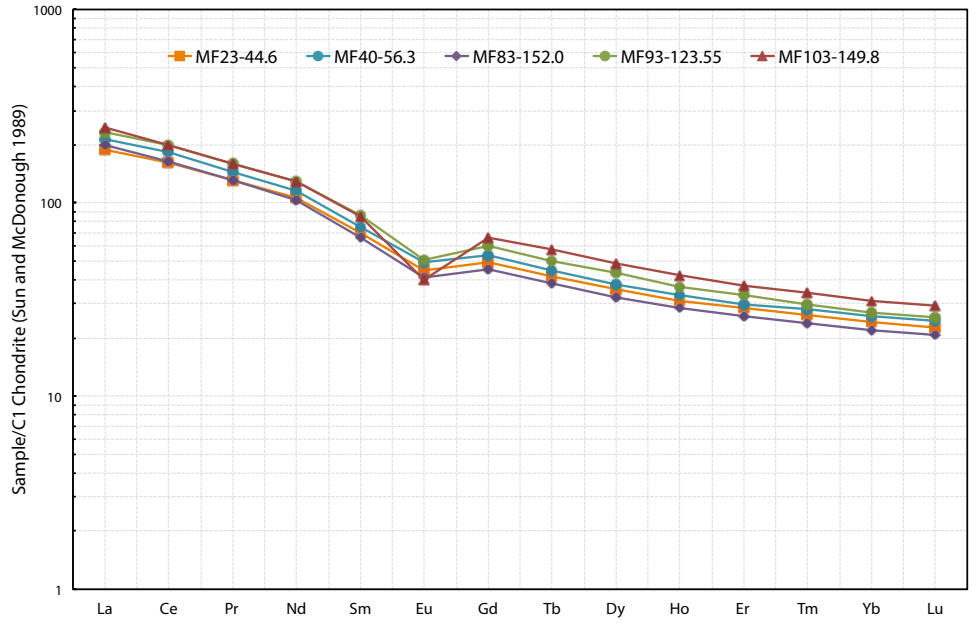

4.3.2 Comparison of Trace Element Geochemistry Data

Trace element compositions were determined in sediment samples A150-144.7, A150B-156.4, A207-40.4, and A231-279.6 from Avebury (refer to Table. C.2 of Appendix. C); all of which are believed to belong to Crimson Creek Formation. These sediments are considered possible correlates to the Melba Flats sediments (Calver *et al.* 2014). In general, the trace element geochemistry results show similar lithophile element and REE patterns between 4 four samples, with variable enrichment factors for most of the lithophile elements and REE ranging from 2 to approximately 800. Comparison between the Melba Flats and Avebury sediments for lithophile element and REE patterns are shown below in Fig. 4.11 and Fig. 4.12 respectively.

Lithophile Elements

C1 chondrite-normalized lithophile element patterns for all the Melba Flats and Avebury sediment samples appear to be relatively parallel (Fig. 4.11), with the more compatible elements (Cs to P) exhibiting more variation in lithophile element enrichment patterns in comparison to the less compatible elements (Nd to Lu). These incompatible elements are characterized by strongly fractionated element patterns, with similar $(Nd/Lu)_{C1}$ average of ~ 4.8 for the Melba Flats sediments and $(Nd/Lu)_{C1}$ average of ~ 4.0 for the Avebury sediments. Relative to C1 chondrite (Sun & McDonough 1989), both sedimentary groups also share similarly varied depletion in Rb, K, Pb, Sr and P relative to the other lithophile elements and similar enrichment in Ba, Th, U and Ti. These sedimentary groups also share significant variation in the enrichment factors between samples for the same elements Cs, Rb and K. The lithophile element patterns for both sedimentary groups are largely similar in most respectives and therefore, it can be argued that they are likely to be correlates.

Rare Earth Elements

C1 chondrite-normalized REE patterns for all the Melba Flats and Avebury sediment samples are almost identical (Fig. 4.12), with the LREE displaying strongly enriched patterns in comparison to the MREE and HREE. However, the extent of REE enrichment is greater for the Melba Flats sediments (average $\sum$ REE = 280) in comparison to the Avebury sediments (average $\sum$ REE = 187). Relative to C1 chondrite (Sun & McDonough 1989), both sedimentary groups are enriched in LREE relative to the MREE, with a $(La/Sm)_{C1}$ average of ~ 2.8 for the Melba Flats sediments and a $(La/Sm)_{C1}$ average of ~ 2.6 for the Avebury sediments; and strongly enriched in LREE relative to the HREE, with a $(La/Yb)_{C1}$ average of ~ 8.3 for the Melba Flats sediments and a $(La/Yb)_{C1}$ average of ~ 6.8 for the Avebury sediments. Both sedimentary groups are also characterized by weakly fractionated HREE, with a $(Gd/Yb)_{C1}$ average of ~ 2.0 for the Melba Flats sediments and a $(Gd/Yb)_{C1}$ average of ~ 2.1 for the Avebury sediments. The Avebury sediments (average $(Eu/Eu^*)_{C1}$ = ~ 0.82) exhibit less pronounced negative Eu anomalies in comparison to the Melba Flats sediments (average $(Eu/Eu^*)_{C1}$ = 0.70). Although the extent of REE enrichment for the Crimson Creek Formation sediments from Avebury is lower compared to the Melba Flats sediments, both sedimentary groups largely share identical REE patterns and similar REE C1 chondrite-normalized elemental ratios. Consequently, it can be argued that these sediments are likely to be correlates.

FIGURE 4.11: *C1 chondrite-normalized lithophile element plot comparing Melba Flats sediment samples MF23-44.6, MF40-56.3, MF83-152.0, MF93-123.55 and MF103-149.8 to the Avebury sediment samples A150-144.7, A150-156.4, A207-40.4 and A231-279.6.*

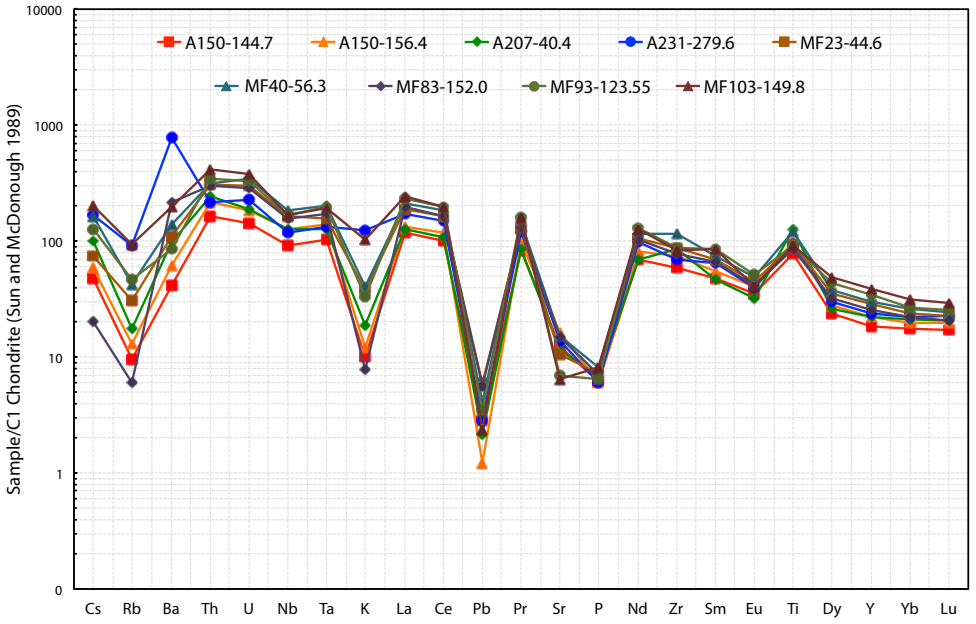

FIGURE 4.12: *C1 chondrite-normalized REE plot comparing the Melba Flats sediment samples MF23-44.6, MF40-56.3, MF83-152.0, MF93-123.55 and MF103-149.8 to Avebury sediment samples A150-144.7, A150-156.4, A207-40.4 and A231-279.6.*

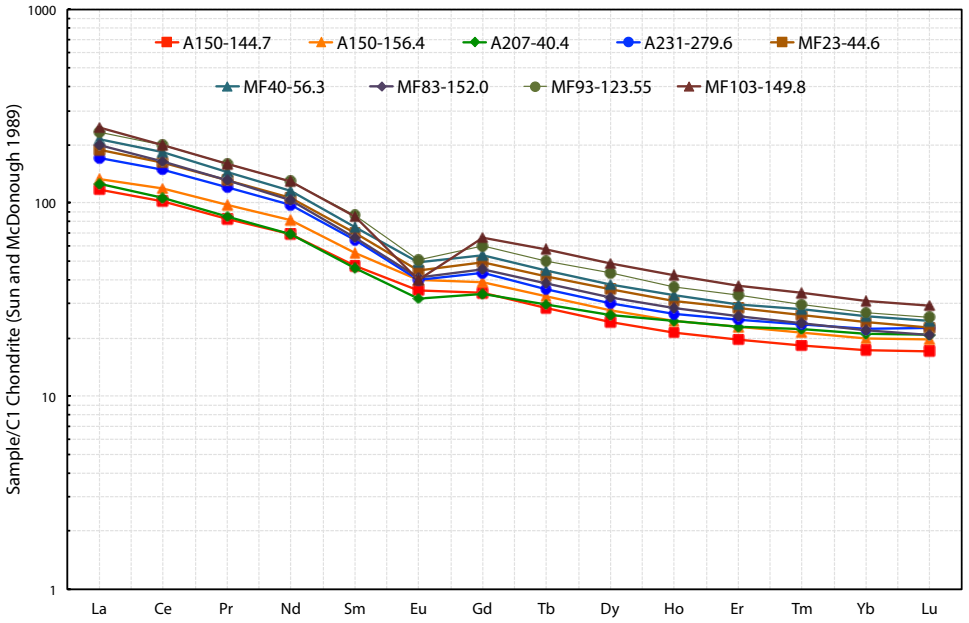

Based on the highly similar lithophile element and REE patterns observed in Fig. 4.11 and Fig. 4.12 respectively, it is argued that the Melba Flats sediments are probably correlates of the Crimson Creek Formation sediments from Avebury. This interpretation is consistent with the U-Pb detrital zircon studies conducted for the both sedimentary groups, which established that the Melba Flats sediments and the Avebury Crimson Creek Formation sediments are likely correlates based on highly similar detrital zircon age spectra.

Chapter 5

Age Dating & Geochemistry of the Melba Flats Mafic Intrusions

Petrogenetic studies of igneous rocks involve the characterization of the unique chemical features igneous rocks inherit from the source regions of the magmas and from the processes that modify the magmas during their transport and evolution prior to emplacement or eruption. In particular, the petrogenesis of the mafic intrusions at Melba Flats have been the subject of much geological interest, in part due to the highly endowed Ni-Cu-PGE mineralization associated with the mafic intrusions and its close proximity to the Avebury Ni mine nearby, which drew interest in the wider region. Consequently, a primary aim of this research project was to unravel the petrogenesis of the Melba Flats mafic intrusions and a related aim was to define the relationship between the mafic intrusions at Melba Flats and the intrusives at the Avebury Ni mine. These aims were addressed using methods that include ^{40}Ar-^{39}Ar hornblende geochronology and whole rock major and trace element geochemistry, which are powerful tools in petrogenetic studies of igneous rocks. ^{40}Ar*/^{39}Ar cooling ages of hornblende help provide constraints on the emplacement/eruption age of igneous bodies. Whilst major and trace element geochemistry provides compositional data that can be used to determine the rock classification, establish the magmatic affinity and identify the tectonic setting of emplacement/eruption of igneous bodies.

5.1 $^{40}Ar^*/^{39}Ar$ Dating of Hornblende

$^{40}Ar^*/^{39}Ar$ dating of hornblende by VG3600 laser step-heating is a technique extensively used in the dating of igneous and metamorphic rocks, either as a complementary geochronometer to the U-Pb dating method or as an alternative to the U-Pb geochronometer in the absence of suitable heavy minerals, especially in mafic-ultramafic rocks. Hornblende is a commonly occurring mineral in a wide range of igneous and metamorphic rocks and it has a general formula of $(Ca,Na,K)_{2\text{-}3}(Mg,Fe,Al)_5(Si_7AlO_{22})(OH)_2$. Hornblene has excellent radiogenic $^{40}Ar^*$ retention properties, minimal atmospheric argon content, and relatively high closure temperature (T_c) of ~500°C (Harrison 1981; Villa *et al.* 1996), which allows the mineral to retain original age information as it cools through the closure temperature. $^{40}Ar^*/^{39}Ar$ dating of hornblende was conducted on a sample from the Melba Flats mafic intrusions (MF103 - 112.4 m) where two aliquots of hornblende underwent furnace step-heating experiments to determine the emplacement age of the mafic intrusions.

5.1.1 Results: $^{40}Ar^*/^{39}Ar$ Hornblende

$^{40}Ar^*/^{39}Ar$ hornblende data obtained from the VG3600 furnace step-heating analyses were visualized using ISOPLOT 3.75 (Ludwig 2012) to produce step-heating spectra (Fig. 5.1) for $^{40}Ar^*/^{39}Ar$ age analysis. All error box heights presented in the step-heating spectra are plotted at the 1σ level, whilst all age errors quoted in the text are reported at the 2σ level. Age results are summarized in Table. 5.1 and isotopic data detailed in Tables. D.4 to D.5 of Appendix. D.

TABLE 5.1: *Summary of $^{40}Ar^*/^{39}Ar$ age data for hornblende aliquots MF103-1 and MF103-2.*

Sample	Aliquot		Mineral	Analysis Type	No. of Steps	Total Gas Age[a] (Ma)	Plateau Age[a] (Ma)	^{39}Ar (%)	MSWD	Weighted Mean Age[a] (Ma)	^{39}Ar (%)	MSWD
MF103 - 112.4 m	MF103-1	184 mg	Hornblende	VG3600 Furnace Step-heating	14	536.9 ± 12.6	560.4 ± 13.0	47.8	1.5	560.7 ± 9.8	56.4	0.9
MF103 - 112.4 m	MF103-2	156 mg	Hornblende	VG3600 Furnace Step-heating	11	574.5 ± 11.6	569.6 ± 5.2	100.0	1.6	569.2 ± 9.0	77.2	1.3

[a] Ages calculated relative to an assumed age of 28.02 ± 0.28 Ma (2σ) for the Fish Canyon Tuff sanidine (Renne et al. 1998) and errors associated include the J-value uncertainty.

Samples MF103-1 & MF103-2

Hornblende from sample MF103-1 produced a fairly discordant age spectrum that defined a plateau age of 560.4 ± 13.0 Ma (MSWD = 1.5; Fig. 5.1a) from 47.8% of released ^{39}Ar gas over seven contiguous steps (steps 4-10). ~90% of ^{39}Ar gas released had occurred above 1070°C and significant ^{39}Ar gas was not released until the higher temperature steps between 1170°C to 1250°C. A weighted mean age of 560.7 ± 9.8 Ma (MSWD = 0.9; Fig. **??**a) for the sample was also calculated from 56.4% of released ^{39}Ar gas over four higher temperature steps (steps 9-13, excluding step 11). Hornblende from sample MF103-2 produced a relatively concordant age spectrum with some discordance in the younger age steps, which defined a plateau age of 569.6 ± 5.2 Ma (MSWD = 1.6; Fig. 5.1b) from 100% of released ^{39}Ar gas over eleven contiguous steps (steps 1-11). ~90% of ^{39}Ar gas released had occurred above 1030°C and significant ^{39}Ar gas was not released until the higher temperature steps between 1100°C to 1250°C. A weighted mean age of 569.2 ± 9.0 Ma (MSWD = 1.3; Fig. **??**b) for the sample was also calculated from 77.2% of released ^{39}Ar gas over five contiguous steps (steps 5-9). Samples MF103-1 and MF103-2 generated plateau ages that were within error of one another, with a weighted mean of 568.3 ± 4.8 Ma (2σ; MSWD = 1.7).

Discordance in ^{40}Ar/^{39}Ar Age Spectra*

Discordance observed in the age spectra for these samples may be attributed to variable argon diffusivities due to the likely presence of compositional domains within the hornblende grains as a result of the optically discontinuous nature of larger grains and/or ^{39}Ar loss or relocation due to ^{39}Ar recoil as a result of microscopic chlorite and actinolite alteration that is likely to exist within the mineral crystal lattices (Faure & Mensing 2005a; Ely *et al.* 2014).

FIGURE 5.1: *$^{40}Ar^*/^{39}Ar$ step-heating spectra for 2 aliquots of hornblende (MF103-1 and MF103-2). (**a**) $^{40}Ar^*/^{39}Ar$ step-heating spectra for MF103-1. (**b**) $^{40}Ar^*/^{39}Ar$ step-heating spectra for MF103-1. Steps highlighted in red are included in plateau ages. All ages are reported at the 2σ level.*

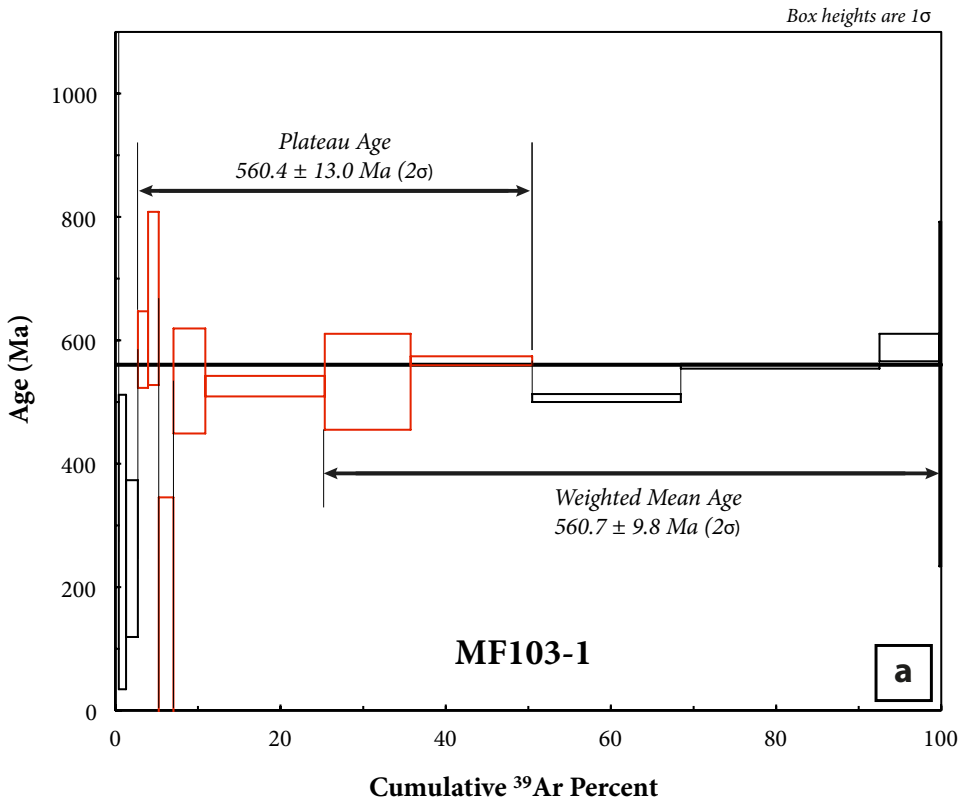

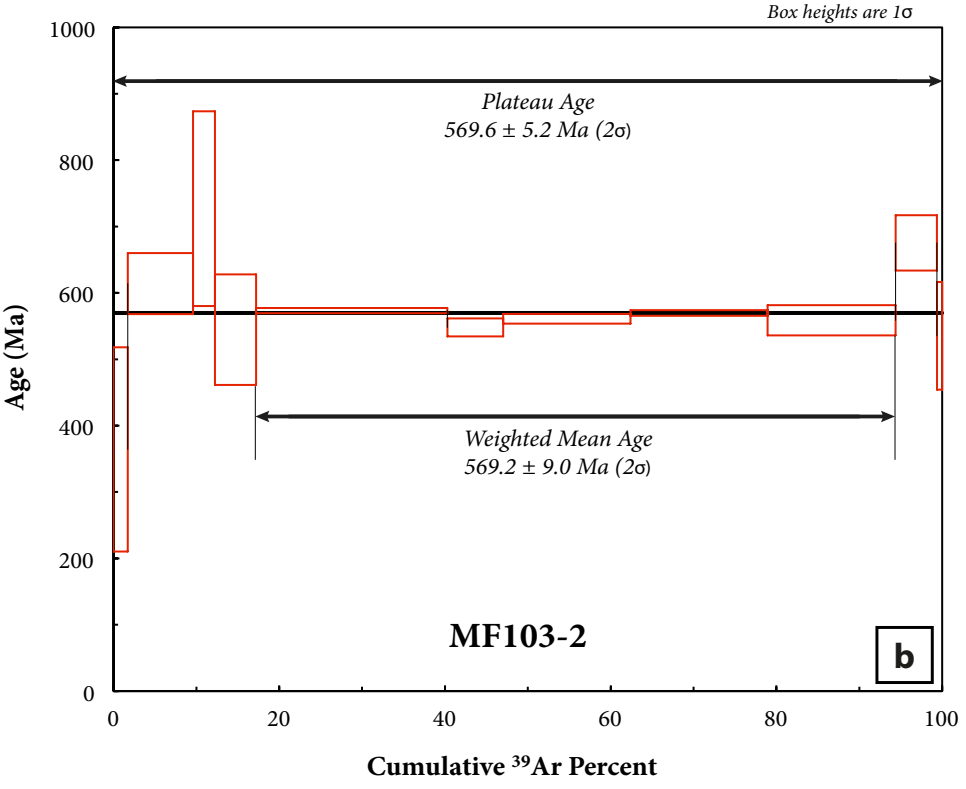

5.1.2 Implication of $^{40}Ar^*/^{39}Ar$ Hornblende Ages

Age spectra for this group of hornblendes are inferred to constrain a maximum cooling age estimate, where it can be assumed that the cooling of these hornblende below ~500°C (Harrison 1981; Villa *et al.* 1996) occurred after the age of *c.* 568 Ma. This cooling age is likely to reflect an age younger than the emplacement of the Melba Flats mafic intrusions and consequently, it may be interpreted as the geological age closest to the emplacement age of the mafic intrusions at Melba Flats. This is supported by the fact that the Melba Flats mafic intrusions are very likely to have cooled rapidly upon emplacement as the intrusions are made up of a combination of very narrow (between 5 to 20 m) sills and dykes (Crawford & Keays 2010). If this is the case, a higher rate of cooling for the associated hornblende is expected and therefore, it is likely to retain an age close to the emplacement age as it cools rapidly through the closure temperature.

The inferred *c.* 568 Ma emplacement age satisfies the principle of relative chronology (Jacques & Galeotti 2008) where the age of the intrusive mafic intrusions is younger than the maximum depositional age of the Melba Flats sediments, which were dated *c.* 582 Ma (see Chapter. 6). The close proximity in the emplacement age of the Melba Flats mafic intrusions and the maximum depositional age of the Melba Flats sediments strongly suggests that the emplacement of the mafic intrusions have occurred immediately after the deposition of the Melba Flats sediments or perhaps even contemporaneous with the deposition of the Melba Flats sediments. Furthermore, the emplacement age of 568 ± 5 Ma is also largely coincident with the stratigraphic equivalents of the Melba Flats mafic intrusions in the Smithton Basin and on King Island, where the rift tholeiitic basalts of the Spinks Creek Volcanics in the Smithton Basin and the MORB tholeiitic basalts of the Grassy Group on King Island were dated 575 ± 3 Ma and 582 ± 4 ma respectively (Calver *et al.* 2004; Meffre *et al.* 2004; Moore *et al.* 2015). Consequently, in the absence of U-Pb ages due to the lack of suitable heavy minerals in the mafic intrusions of Melba Flats, the $^{40}Ar^*/^{39}Ar$ hornblende cooling age of *c.* 568 Ma provides the maximum age constraint and the geological age closest to the emplacement age of the Melba Flats mafic intrusions.

5.2 Whole Rock Geochemistry

Whole rock major and trace element geochemistry of igneous rocks has been shown to be a powerful tool to establish their rock classification and magmatic affinity. Numerous authors have demonstrated that the relative abundance of major and trace elements in igneous rocks are relatively representative of their rock and magma type (Cox *et al.* 1979; Irvine & Baragar 1971; Winchester & Floyd 1977). Major and trace element geochemistry analyses were conducted on 73 samples from the Melba Flats mafic intrusions and then compared to 5 other samples from the Avebury mafic intrusions and other possible correlates of the mafic intrusions at Melba Flats.

5.2.1 Results: Whole Rock Geochemistry

X-ray fluorescence spectrometry (XRF) and laser ablation inductively coupled plasma mass spectrometry (LA-ICPMS) were conducted for 73 whole rock samples from drill holes that intersected Melba Flats mafic intrusions. Major and trace elements geochemical data obtained for the mafic intrusions were divided into two different groups: 1) unmineralized samples (less than 1 wt% S) and 2) mineralized samples (more than 1 wt% S) and analysed accordingly, in order to facilitate an equitable interpretation process. Approximately 30% of the 73 samples analysed are classified as mineralized and the remaining 70% constitute 50 unmineralized samples. All major element data have been recalculated to 100% on a volatile-free basis to facilitate comparisons of variably altered samples. Representative concentrations of the recalculated major elements for the Melba Flats mafic intrusions are summarized in Table. 5.2 and Table. 5.3 and detailed in Table. C.1 of Appendix. C. Trace elements abundances of the Melba Flats intrusions are detailed in Table. C.3 and Table. C.4 of Appendix. C.

TABLE 5.2: *Representative major elements geochemical data for the unmineralized Melba Flats mafic intrusions.*

Unmineralized Major Elements (wt %)												
Sill	MF17 Sill 1	MF23 Sill 1	MF81A Sill 1	MF83 Sill 1	MF93 Sill 1	MF93 Sill 2	MF93 Sill 3	MF93 Sill 4	MF95 Sill 1	MF95 Sill 2	MF97 Sill 1	MF103 Sill 1
Sample	MF17-70.8	MF23-48.35	MF81A-164.2	MF83-143.2	MF93-128.55	MF93-159.0	MF93-310.55	MF93-323.3	MF95-126.4	MF95-212.15	MF97-215.9	MF103-101.4
Lab	**BV**	**ACME**	**GEO**	**BV**	**GEO**	**GEO**	**GEO**	**GEO**	**GEO**	**BV**	**BV**	**BV**
Al_2O_3	15.87	16.87	16.22	15.69	16.88	15.94	15.68	15.43	15.22	16.17	16.29	15.31
CaO	4.47	4.51	5.69	5.24	5.44	4.47	7.40	7.66	5.16	7.20	5.10	6.52
Cr_2O_3	0.10	0.06	0.09	0.09	0.08	0.10	0.10	0.05	0.13	0.08	0.11	0.14
FeO_T	12.47	12.21	11.92	13.01	11.56	12.34	12.14	15.32	13.72	12.11	12.22	11.25
K_2O	0.15	1.23	0.52	0.64	1.18	1.04	2.42	0.61	1.30	1.09	0.93	0.91
MgO	15.43	13.41	12.61	14.57	13.03	13.70	12.75	7.86	15.72	12.33	14.60	17.89
MnO	0.18	0.26	0.24	0.18	0.25	0.28	0.23	0.25	0.37	0.35	0.25	0.22
Na_2O	2.01	1.65	3.29	2.24	2.77	2.21	1.80	3.30	1.01	2.25	2.59	1.57
P_2O_5	0.08	0.04	0.08	0.08	0.07	0.08	0.08	0.07	0.08	0.08	0.08	0.07
SiO_2	48.38	48.83	48.38	47.42	47.82	48.97	46.51	48.42	46.44	47.42	46.94	45.51
TiO_2	0.85	0.93	0.96	0.84	0.92	0.88	0.89	1.02	0.86	0.92	0.89	0.61

TABLE 5.3: *Representative major elements geochemical data for the mineralized Melba Flats mafic intrusions.*

Mineralized Major Elements (wt %)										
Sill	MF19 Sill 1	MF23 Sill 2	MF81A Sill 1	MF83 Sill 1	MF93 Sill 2	MF93 Sill 3	MF93 Sill 4	MF95 Sill 1	MF97 Sill 1	MF103 Sill 1
Sample	MF19-34.25	MF23-64.8	MF81A-171.5	MF83-139.0	MF93-151.55	MF93-304.0	MF93-335.2	MF95-123.35	MF97-207.7	MF103-146.0
Lab	BV	ACME	ACME	BV	GEO	GEO	ACME	GEO	BV	BV
Al_2O_3	17.78	16.50	14.68	13.93	12.20	17.00	15.91	12.18	17.74	16.72
CaO	16.60	3.17	7.00	2.82	7.36	3.15	4.29	4.31	2.88	4.66
Cr_2O_3	0.11	0.09	0.13	0.18	0.25	0.00	0.00	0.15	0.03	0.11
FeO_T	9.13	32.07	13.67	19.69	16.29	11.52	28.55	25.64	14.40	13.43
K_2O	4.86	0.01	0.08	0.02	0.02	0.91	0.15	0.18	0.67	0.89
MgO	8.20	12.33	14.74	18.96	19.56	4.91	10.44	15.21	10.86	14.03
MnO	0.43	0.25	0.23	0.14	0.34	0.19	0.27	0.38	0.16	0.18
Na_2O	1.11	0.02	1.61	0.04	0.06	5.52	0.80	0.06	3.69	2.54
P_2O_5	0.09	0.04	0.05	0.07	0.07	0.39	0.08	0.06	0.10	0.08
SiO_2	40.73	34.62	46.97	43.48	43.14	54.66	37.29	41.18	48.24	46.52
TiO_2	0.95	0.92	0.86	0.69	0.71	1.75	2.21	0.63	1.23	0.84

5.2.1.1 Major Element Geochemistry

Unmineralized Samples

The major element composition of the unmineralized samples from 12 different intrusions are variable. Box plots of MgO and Mg # indicate a highly primitive magma source, with inter-quartile values (25% to 75%) ranging from 13.1 to 16.2 wt% and 66 to 71 respectively (Fig 5.2). A bivariate plot of SiO_2 versus MgO correlates negatively, with concentrations ranging from 38.3 to 50.8 wt% and 6.9 to 27.3 wt% respectively (Fig. 5.3a). Both TiO_2 and Al_2O_3 show broad negative correlation with MgO and are markedly different in abundance (TiO_2: 0.4 to 1.4 wt%; Al_2O_3: 9.7 to 18.7 wt%; Fig. 5.3b; Fig. 5.3c). Cr_2O_3 exhibits a strong positive correlation with MgO (Fig. 5.3d), ranging from 0.001 wt% in the most evolved samples to 0.647 wt% in the most primitive samples. A bivariate plot of FeO_T versus MgO shows little correlation (Fig. 5.3e), with FeO_T concentrations ranging from 9.0 to 18.6 wt%. Alkali elements (CaO, K_2 and Na_2O) show a general scatter, along with a broad negative correlation and varied abundance ranges (CaO: 3.4 to 12.7 wt%; K_2: 0.05 to 3.46 wt%; Na_2O: 0.11 to 3.45 wt%; Fig. 5.3f; Fig. 5.3g; Fig. 5.3h). This is consistent with the possible effects of post-magmatic processes or a consequence of crustal contamination of the mafic intrusions. Specifically, major element composition of MF93 Sill 4 is the most varied and scattered, whilst the major element profile of MF103 Sill 1 appears to be vertically differentiated.

FIGURE 5.2: *Bivariate plot of Mg# vs. MgO for the unmineralized Melba Flats mafic intrusions, along with box plots representing the total spread of Mg# and MgO. Box height is defined by the 25th and 75th quartile, whilst the upper and lower whiskers mark the minimum and maximum concentrations of the dataset.*

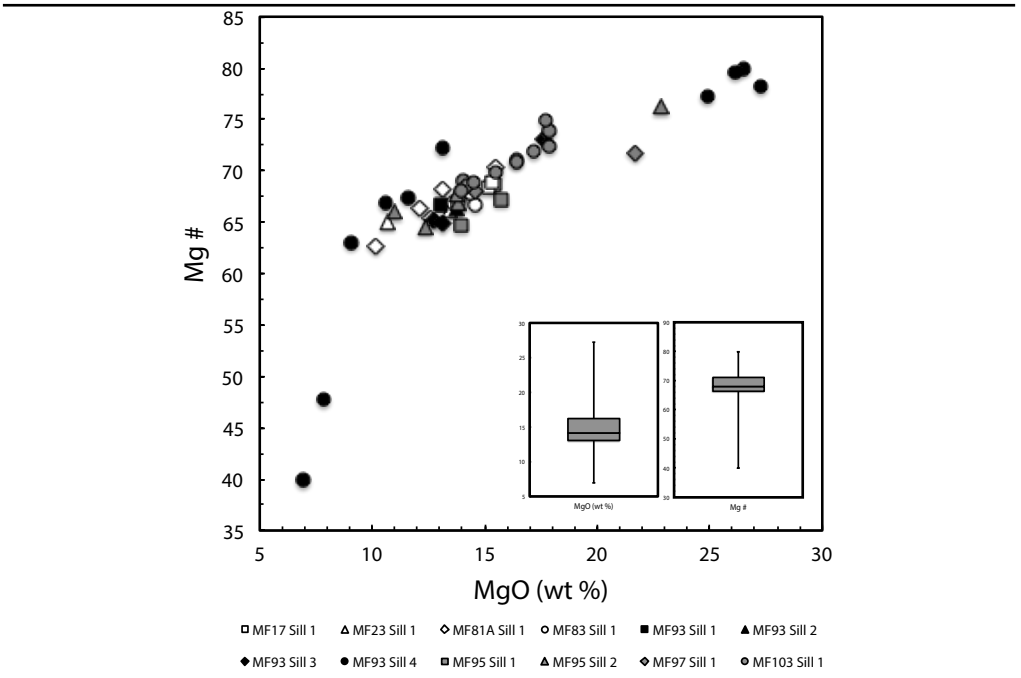

FIGURE 5.3: *Major element bivariate plots of (a) SiO_2 vs. MgO, (b) TiO_2 vs. MgO, (c) Al_2O_3 vs. MgO, (d) $Cr_2O_{(}3$ vs. MgO, (e) FeO_T vs. MgO, (f) CaO vs. MgO, (g) K_2O vs. MgO and (h) Na_2O vs. MgO for the unmineralized Melba Flats mafic intrusions.*

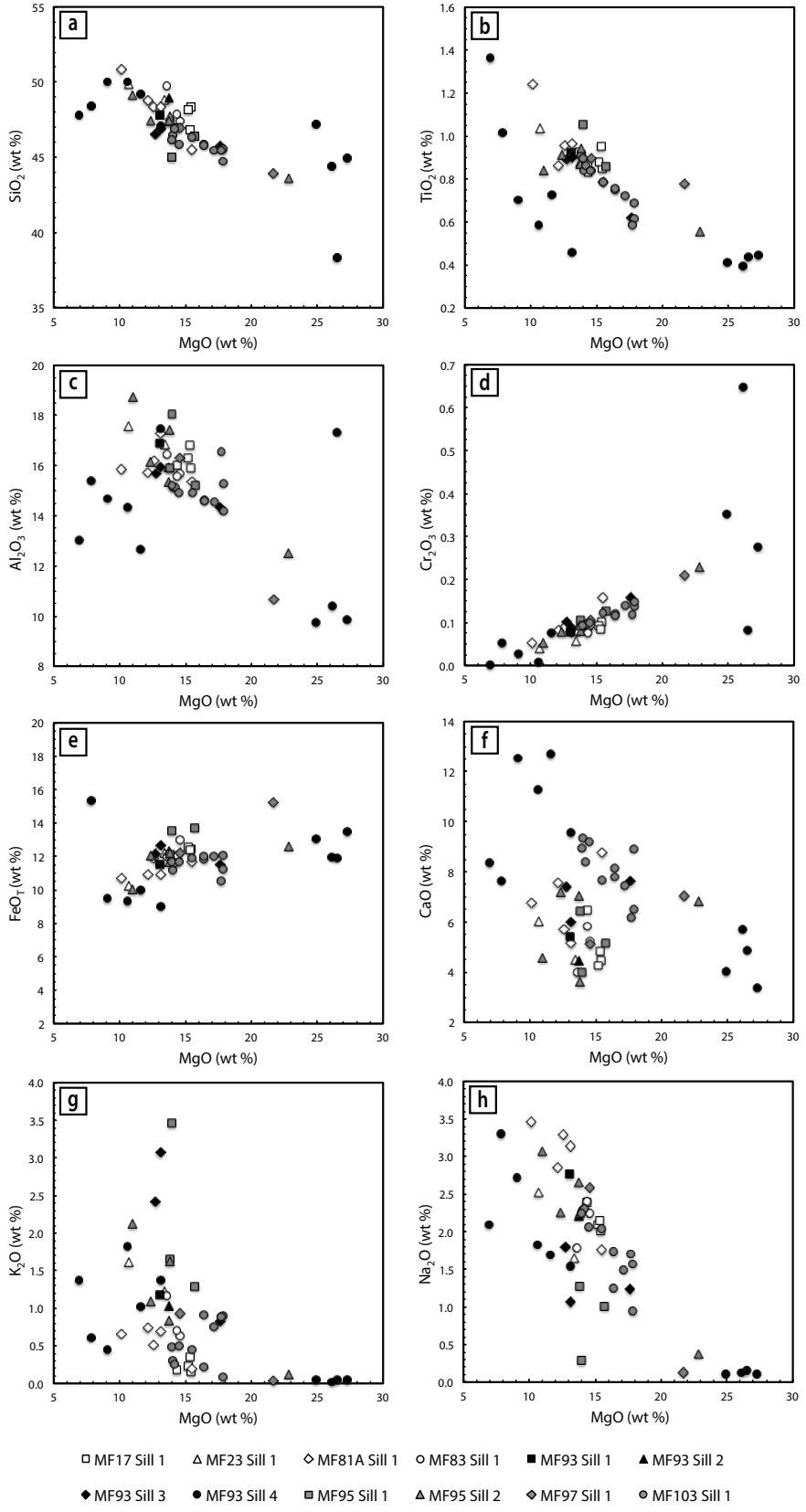

Mineralized Samples

The major element composition of the mineralized samples from 10 different intrusions are highly variable. Box plots of MgO and Mg # generally indicate a highly primitive magma source, although the inter-quartile values (25% to 75%) exhibit varied ranges from 3.0 to 15.0 wt% and 7 to 59 respectively (Fig. 5.4). Bivariate plots of SiO_2 versus MgO, TiO_2 versus MgO, Al_2O_3 versus MgO and FeO_T versus MgO discriminate two unique groups of correlated mineralized intrusions, with six samples from MF19 Sill 1, MF23 Sill 2 and MF81A Sill 2 forming Group I and the remaining samples forming Group II (Fig. 5.5a - Fig. 5.5d). Samples from Group I share similar abundance ranges for SiO_2, TiO_2 and Al_2O_3 (~0.1 to ~ 5.6 wt%) and FeO_T concentrations ranging from 86.5 to 95.2 wt%. Whilst mineralized intrusions from Group II exhibit general scatter and little to no correlation for SiO_2, TiO_2, Al_2O_3 and FeO_T, with abundances ranging from 24.9 to 54.6 wt%, 0.6 to 2.2 wt%, 11.5 to 17.8 wt% and 9.1 to 62.7 wt% respectively. Bivariate plots of Cr_2O_3 versus MgO, CaO versus MgO, K_2O versus MgO and Na_2O versus MgO exhibit general scatter, little to no correlation and concentrations ranging from 0.05 to 16.60 wt%, 0.001 to 0.250 wt%, 0.01 to 4.80 wt% and 0.01 to 5.50 wt% respectively (Fig. 5.5e - Fig. 5.5h). Major element composition of Group I appear to correlate with massive sulphides-bearing mineralized intrusions with high S content, whilst the major element profile for Group II seem to be coincident with disseminated sulphides-bearing mineralized intrusions with a much lower S content.

FIGURE 5.4: *Bivariate plot of Mg# vs. MgO for the mineralized Melba Flats mafic intrusions, along with box plots representing the total spread of Mg# and MgO. Box height is defined by the 25th and 75th quartile, whilst the upper and lower whiskers mark the minimum and maximum concentrations of the dataset.*

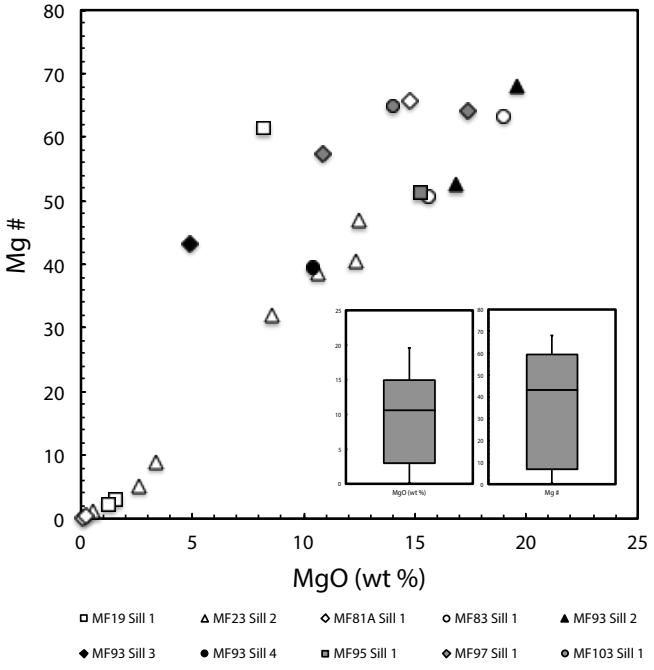

FIGURE 5.5: *Major element bivariate plots of (a) SiO_2 vs. MgO, (b) TiO_2 vs. MgO, (c) Al_2O_3 vs. MgO, (d) $Cr_2O_(3$ vs. MgO, (e) FeO_T vs. MgO, (f) CaO vs. MgO, (g) K_2O vs. MgO and (h) Na_2O vs. MgO for the mineralized Melba Flats mafic intrusions.*

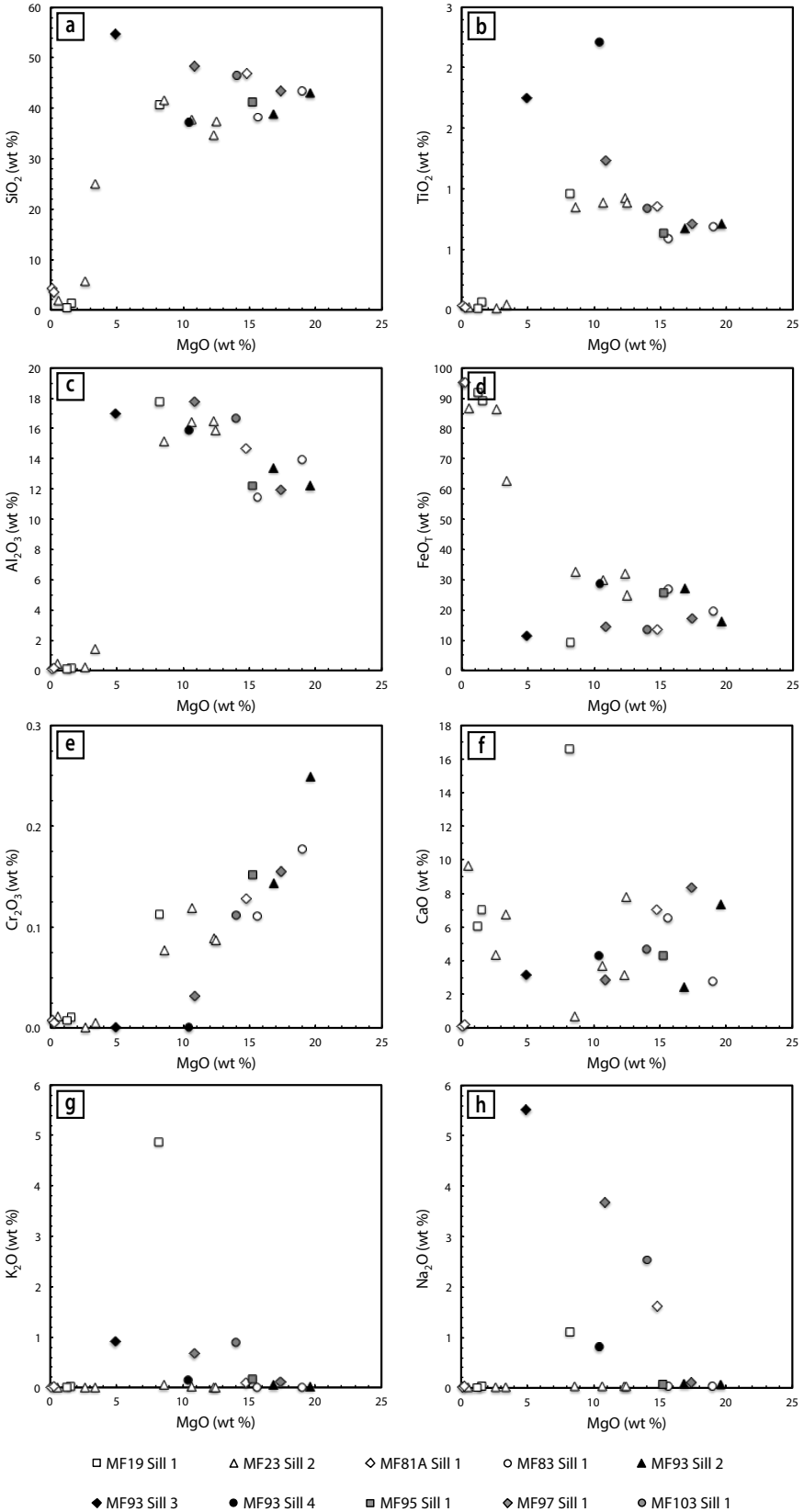

5.2.1.2 Trace Element Geochemistry

Unmineralized Samples

Lithophile Elements

Primitive mantle-normalized lithophile element patterns for the unmineralized samples from 12 different intrusions are relatively parallel (Fig. 5.6), with the more compatible elements (Cs to Sr) exhibiting more variation in lithophile element enrichment patterns in comparison to the less compatible elements (P to Lu). These incompatible elements are characterized by relatively unfractionated element patterns, with a $(P/Lu)_{PM}$ average of ~ 0.8. Relative to primitive mantle (McDonough *et al.* 1992), the unmineralized intrusions are variably enriched in Cs, Rb, Ba, K, Pb and Sr relative to other lithophile elements, with enrichment factors in these elements ranging from 10 to more than a 1000. These elements are known to be chemically mobile and the enrichment most probably reflect an upper crustal contamination of these mafic intrusions. The unmineralized intrusions are also characterized by a minor depletion in Nb relative to La (average $(La/Nb)_{PM}$ of ~ 1.5), which is consistent with clear signs of crustal contamination. There appears to be no systematic differences in the lithophile element patterns for the unmineralized samples.

Rare Earth Elements

Primitive mantle-normalized REE patterns for the twelve unmineralized intrusions are relatively similar (Fig. 5.7), with the LREE exhibiting relatively flat to very weakly-enriched patterns in comparison to the MREE and HREE. Relative to primitive mantle (McDonough *et al.* 1992), the unmineralized intrusions are very weakly-enriched in LREE relative to the MREE, with a $(La/Sm)_{PM}$ average of ~ 1.3; and weakly enriched in LREE relative to the HREE, with a $(La/Yb)_{PM}$ average of ~ 1.5, except for MF93 Sill 4 and MF97 Sill 1. These outliers are very weakly-depleted in LREE relative to the MREE, with a $(La/Sm)_{PM}$ average of ~ 1.0; and weakly-depleted relative to the HREE with a $(La/Yb)_{PM}$ average of ~ 1.0. Apart from this, there is little dissimilarity in the REE patterns for the unmineralized samples.

FIGURE 5.6: *Primitive mantle-normalized lithophile element plot for the unmineralized samples from the Melba Flats mafic intrusions.*

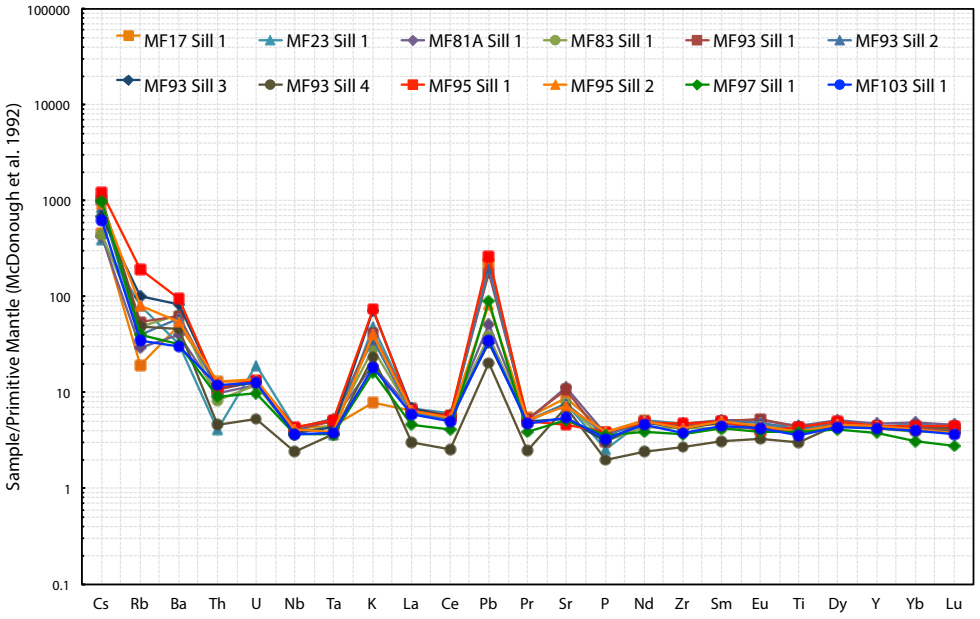

FIGURE 5.7: *Primitive mantle-normalized REE plot for the unmineralized samples from the Melba Flats mafic intrusions.*

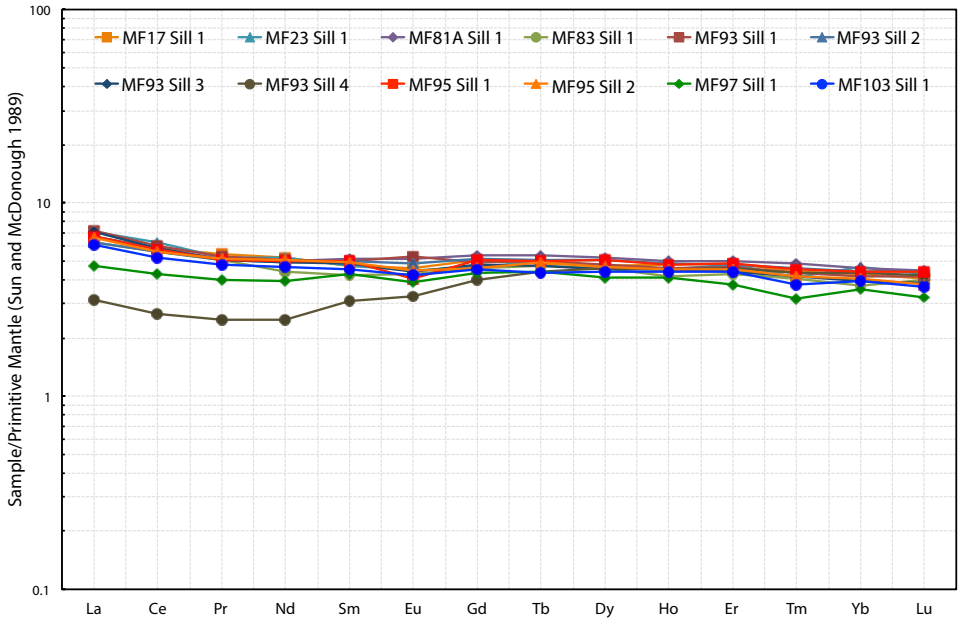

Mineralized Samples

Lithophile Elements

Primitive mantle-normalized lithophile element patterns for the mineralized samples from 10 different intrusions are relatively sub-parallel (Fig. 5.8), with the more compatible elements (Cs to Sr) exhibiting more variation in lithophile element enrichment patterns in comparison to the less compatible elements (P to Lu). These incompatible elements are characterized by relatively unfractionated element patterns, with a $(P/Lu)_{PM}$ average of ~ 1.2. Relative to primitive mantle (McDonough *et al.* 1992), the mineralized intrusions are variably enriched in Cs, Rb, and Pb, with enrichment factors in these elements ranging from 10 to about 4000, whilst Ba, K, and Sr are variably enriched in some mineralized intrusions and variably depleted in others. These elements are known to be chemically mobile and the variations most probably reflect an upper crustal contamination of these mafic intrusions. The mineralized intrusions are also characterized by a depletion in Nb relative to La (average $(La/Nb)_{PM}$ of ~ 2.1), which consistent with clear signs of crustal contamination. There are no distinctive differences in the lithophile element patterns for the mineralized samples.

Rare Earth Elements

Primitive mantle-normalized REE patterns for the 10 mineralized intrusions are relatively sub-parallel (Fig. 5.9), with the LREE exhibiting relatively flat to very weakly-enriched patterns in comparison to the MREE and HREE. Relative to primitive mantle (McDonough *et al.* 1992), the mineralized intrusions are very weakly-enriched in LREE relative to the MREE, with a $(La/Sm)_{PM}$ average of ~ 1.3; and weakly-enriched in LREE relative to the HREE, with a $(La/Yb)_{PM}$ average of ~ 1.5, except for MF19 Sill 1, MF23 Sill 2 and MF81A Sill 1. These three samples are particularly more depleted in REE (average $\sum$ REE = 26) compared to rest of the intrusions (average $\sum$ REE = 66) and are depleted in LREE relative to the MREE, with a $(La/Sm)_{PM}$ average of ~ 2.7; and strongly depleted in LREE relative to the HREE with a $(La/Yb)_{PM}$ average of ~ 5.0. Apart from the three intrusions, there appears to be little dissimilarity in the REE patterns for the mineralized samples.

FIGURE 5.8: *Primitive mantle-normalized lithophile element plot for the mineralized samples from the Melba Flats mafic intrusions.*

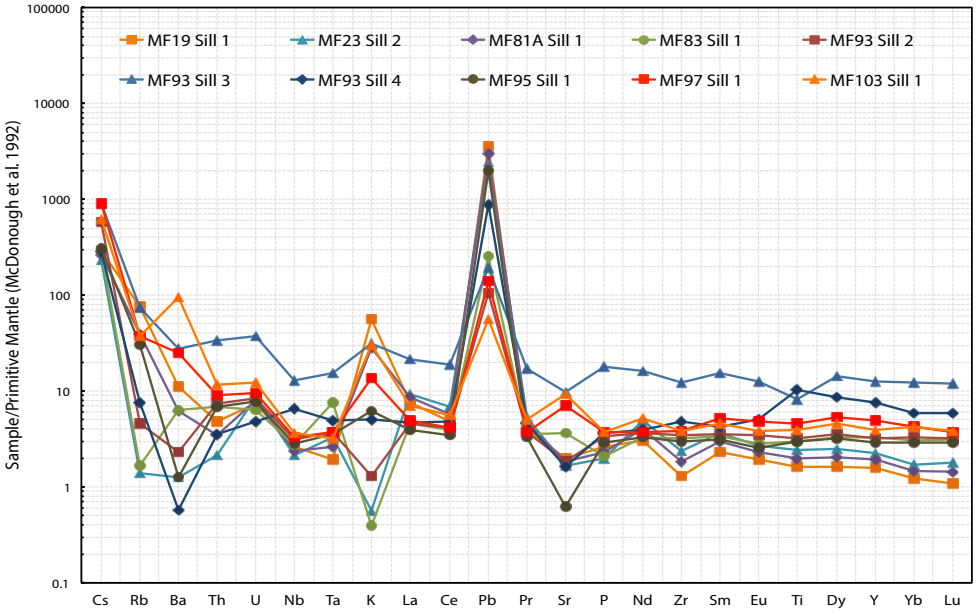

FIGURE 5.9: *Primitive mantle-normalized REE plot for the mineralized samples from the Melba Flats mafic intrusions.*

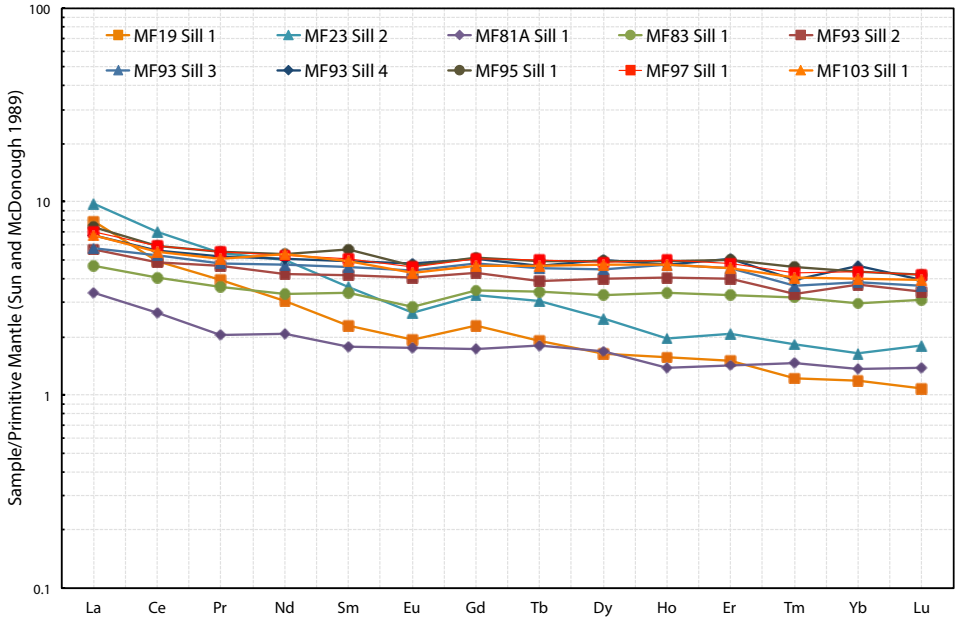

5.2.2 Suitability of Geochemical Data for Interpretation

Mafic intrusions at Melba Flats have undergone regional sub-greenschist facies metamorphism (Calver *et al.* 2014; Greenhill 1995) and consequently, possible mobilization of elements during post-magmatic processes must be considered prior to further interpretation of the geochemical data. Post-magmatic processes such as alteration and metamorphism can potentially affect the geochemical composition of igneous rocks and lead to a misinterpretation of geochemical data. Published studies on igneous rocks by Floyd & Winchester (1978) and Rollinson (1993) suggest that large ion lithophile elements (LILE) such as K, Rb and Ba are more chemically mobile than high field strength elements (HFSE) such as Ti, Zr, Y, Nb and REE during low grade metamorphism. However, similar studies by Gélinas *et al.* (1982) and Hynes (1980) have led to conflicting results that indicate the necessity of a case-by-base assessment. An effective method to assess element mobility following post-magmatic processes is to plot mobile trace elements (LILE) against immobile trace elements (HFSE) on bivariate diagrams (Godel *et al.* 2011; Seat *et al.* 2011). Positive correlations between these trace elements is likely to indicate that the samples are unlikely to have been affected by post-magmatic processes and will therefore, act as effective tools towards unraveling the petrogenesis of the mafic intrusions at Melba Flats.

Bivariate plots of Ti versus Zr and Y versus Zr exhibit strong positive correlations (Fig. 5.10a; Fig. 5.10b) for all samples considered, except for a limited degree of scatter observed for the mineralized samples in comparison to the unmineralized samples. Ti, Y and Zr are considered relatively immobile (Blundy & Wood 2003) during post-magmatic processes and hence, indicates that HFSE have remained relatively unaffected by low grade metamorphism in all the samples considered. Similarly, La and Ce show a positive correlation with Zr (Fig. 5.10c; Fig. 5.10d) for all samples considered, except for some degree of scatter observed for the mineralized samples. Zr is immobile, whereas La and Ce are considered to be more mobile during post-magmatic processes (Blundy & Wood 2003), therefore, this suggests that LREE have largely remained immobile during the low grade metamorphism that has affected the Melba Flats mafic intrusions for the unmineralized samples. Furthermore, Ba and K show a weak positive correlation (Fig. 5.10e; Fig. 5.10f) with Zr for all samples considered. However, a high degree of scatter is observed for the mineralized samples. Both Ba and K are considered highly mobile (Blundy & Wood 2003) during post-magmatic processes and consequently, this indicates that the mineralized samples have been affected by the low grade metamorphism, whereas post-magmatic geochemical modification is limited in the unmineralized samples. Significantly, if the typically highly mobile elements such as Ba and K may be considered immobile, then the other major and trace elements would more than likely have been immobile during post-magmatic processes.

Specifically, it is also observed that of the mineralized samples, samples with low sulphide contents (those with $>$ 20 ppm Zr) plot in tight clusters with the unmineralized samples in all the bivariate plots. Hence, this indicates that these samples may be also considered immobile during post-magmatic processes. It is worthwhile pointing out that the considerable mobility of elements in the mineralized samples with high sulphide contents (those with $<$ 10 ppm Zr) would suggest that it is probable that the presence sulphides in the rocks have acted as a catalyst for chemical reactions that have encouraged element mobility during post-magmatic processes. In summary, these observations support the fact that the unmineralized samples, along with the mineralized samples associated with low sulphide content analyzed in this study have not been greatly affected by post-magmatic processes, whereas the mineralized samples associated with high sulphide content have exhibited HFSE mobility during post-magmatic processes. Consequently, only the unmineralized samples are deemed suitable for subsequent major and trace element discrimination of the rock classification, magmatic affiliation and tectonic setting of the Melba Flats mafic intrusions.

FIGURE 5.10: *Element mobility plots of (a) Ti vs. Zr (b) Y vs. Zr, (c) La vs. Zr, (d) Ce vs. Zr, (e) Ba vs. Zr and (f) K vs. Zr for the mafic intrusions at Melba Flats.*

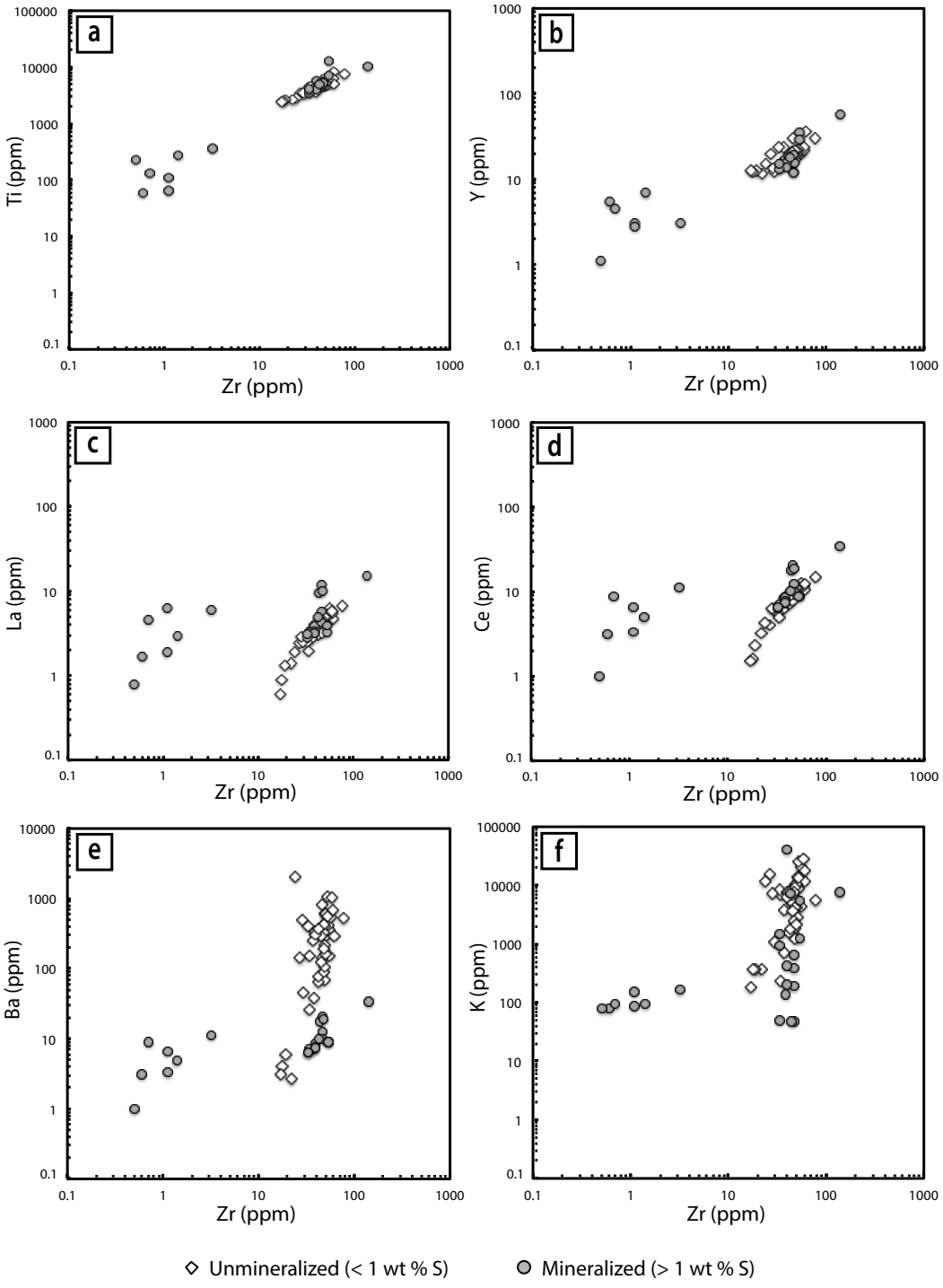

5.2.3 Rock Classification Discrimination

Major Elements

Following the method outline by Wilson (1989) in Rollinson (1993) for the major element discrimination of plutonic igneous rock classification, a total alkali-silica (TAS) diagram was generated to differentiate and classify the mafic intrusions at Melba Flats. Based upon an earlier version developed for volcanic rocks by Cox *et al.* (1979), the TAS diagram is one of the most useful rock classification schemes available that utilizes major oxides chemical data by plotting the sum of Na_2O + K_2O content against the SiO_2 content of the rock. The TAS diagram primarily utilizes SiO_2 as a parameter for distinguishing between ultrabasic, basic, intermediate and acid groups of igneous rock and total alkalis (Na_2O + K_2O) as a secondary parameter to further subdivide these four groups of igneous rocks into their sub-classes (Le Bas *et al.* 1992). Fig. 5.11 shows that the mafic rocks of the Melba Flats intrusions are gabbroic rocks that are sub-alkaline in nature, with abundances clustering within 2 to 4 wt% of Na_2O + K_2O and 45 to 50 wt% of SiO_2. There is also an observed trend towards alkalinity (Na_2O + $K_2O > 4$ wt%), which is likely to be a result of an enrichment in alkali elements as a consequence of crustal contamination. Although it has been determined that these unmineralized samples have not been affected by post-magmatic processes, it is considered prudent to still utilize rock classification schemes that employ immobile trace elements (HFSE) to verify the rock classification determined by the major oxides to ensure there is no misinterpretation of the geochemical data.

FIGURE 5.11: *Major element rock classification of the mafic intrusions at Melba Flats. TAS plutonic diagram, along with curved line (Irvine & Baragar 1971) sub-dividing the alkaline from the sub-alkaline rocks shows that the majority of the mafic intrusions plot in the gabbroic and sub-alkaline field.*

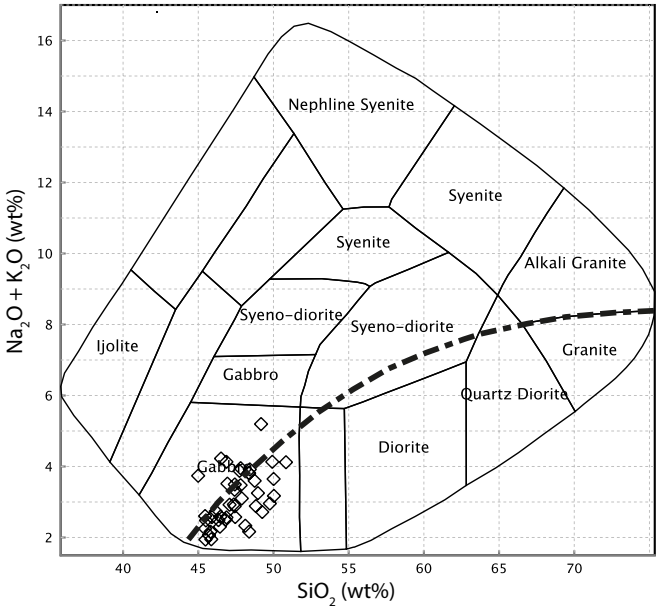

Trace Elements

A study based on the analysis of more than 9000 samples collected in the north-eastern Yilgarn Craton by Hallberg (1984) led to the development of a trace element rock classification diagram as a geochemical aid to rock-type identification, using immobile elements Ti and Zr to define compositional fields for the major plutonic igneous rock types: 1) gabbro, 2) diorite, 3) granodiorite and 4) granite. This method is based on Ti/Zr ratios, which have been shown to be relatively unaffected by post-magmatic process including hydrothermal alteration and low grade metamorphism (Blundy & Wood 2003; Hallberg 1984). The bivariate plot of Ti versus Zr shown in Fig. 5.12 indicates that the Melba Flats mafic intrusions plot well within the gabbroic field of the diagram, with the majority of the samples plotting wihtin a relatively narrow range of Ti/Zr ratios of ~ 40 to 120.

FIGURE 5.12: *Trace element rock classification of the Melba Flats mafic intrusions.Ti vs. Zr plot showing tight ranges in the Zr/Ti ratio for the mafic intrusions, field boundaries from Hallberg (1984).*

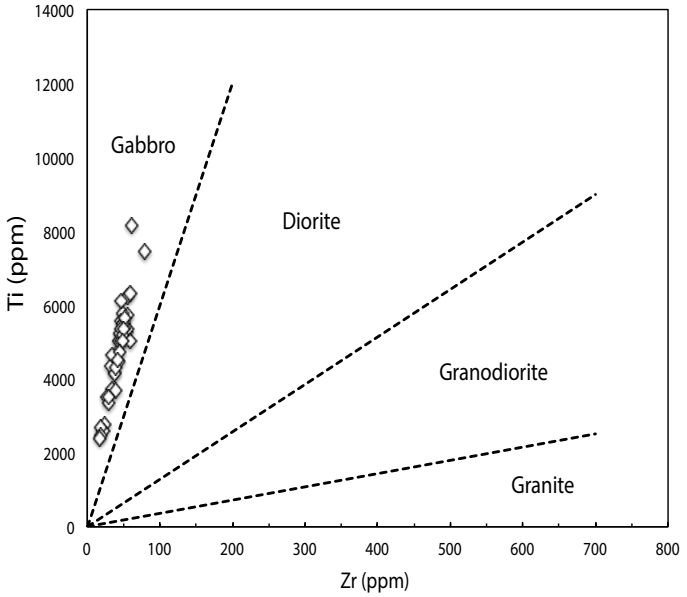

Winchester & Floyd (1977) developed a immobile trace element rock classification diagram based on the determination that selected immobile trace elements (Ti, Zr, Y and Nb) are more suitable for the classification of igneous rocks in a manner similar to the major element indices, but with a greater degree of confidence. The same diagram was later refined by Pearce (1996) to produce another set of compositional field boundaries that are far less convoluted and much more straightforward for wider use. Based on the use of a Zr/Ti versus Nb/Y plot, igneous rocks compositional field boundaries determined by both authors are shown in Fig. 5.13 and 5.14 respectively. Melba Flats mafic intrusions plot well within the gabbroic and sub-alkaline compositional field of the discrimination plots, with similar Zr/Ti ratio of ~ 0.001 and Nb/Y ratio of ~ 0.01.

FIGURE 5.13: *Trace element rock classification of the Melba Flats mafic intrusions. Zr/Ti vs. Nb/Y plot showing the majority of the mafic intrusions fall into the gabbroic and sub-alkaline field of the plot, field boundaries from Winchester & Floyd (1977).*

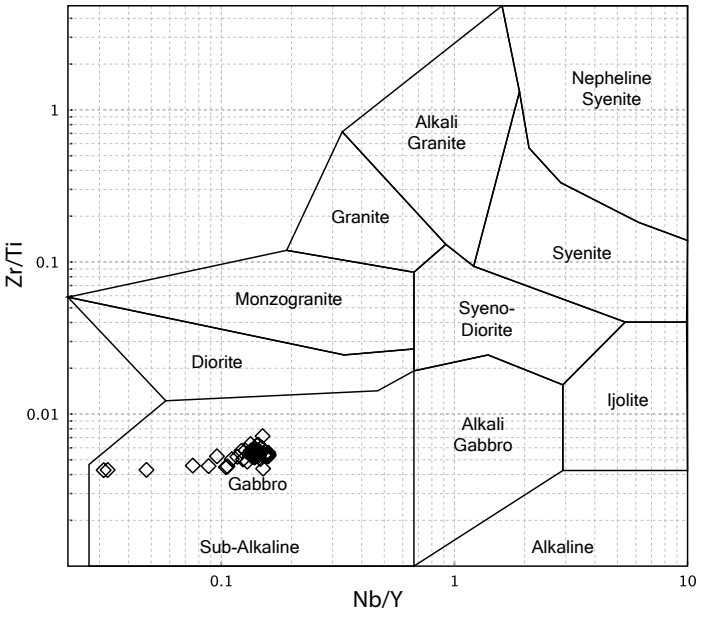

FIGURE 5.14: *Trace element rock classification of the Melba Flats mafic intrusions. Zr/Ti vs. Nb/Y plot showing the majority of the mafic intrusions fall into the gabbroic and sub-alkaline field of the plot, field boundaries from Pearce (1996).*

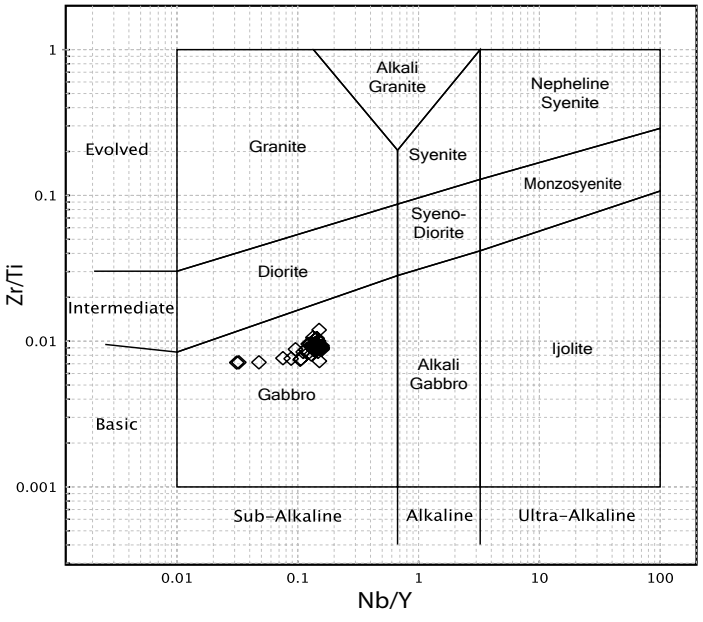

5.2.4 Magmatic Affinity Discrimination

Major Elements

An AFM ternary plot is a conventional three component variation diagram that displays the relative proportions of the major oxides - sum of Na_2O + K_2O, FeO_{Total} and MgO. This ternary plot is commonly used in conjunction with the discriminating curve line presented by Irvine & Baragar (1971), which differentiates igneous rock of calc-alkaline magmatic affinity from igneous rocks of tholeiitic magmatic affinity. Numerous authors have attested to the effectiveness of the AFM ternary plot as a tool in the discrimination of magmatic affinities of sub-alkaline rocks (Middlemost 1994; Rollinson 1993; Wilson 1989). Fig. 5.15 demonstrates that the mafic intrusions at Melba Flats largely follow a tholeiitic trend in the AFM plot shown with the magmatic affinity discrimination curve line from Irvine & Baragar (1971). Although some of the mafic intrusion samples from Melba Flats plot away from the primary cluster, they largely continue to follow the tholeiitic trend. The AFM plot clearly discerns the tholeiitic magmatic affiliation of the mafic intrusions from Melba Flats, however, it is still advisable for the application of magmatic affinity discrimination using immobile elements (HFSE) in order to corroborate the magmatic affiliation determined by the major oxides of the Melba Flats mafic intrusions. This will act as safeguard against the misinterpretation of geochemical data caused by any potential effects from post-magmatic processes, however unlikely it is.

FIGURE 5.15: *Major element magmatic affiliation of the mafic intrusions at Melba Flats. AFM plot, along with the curve line (Irvine & Baragar 1971) sub-dividing calc-alkaline from tholeiitic affinity shows the majority of the mafic intrusions plot along the tholeiitic trend.*

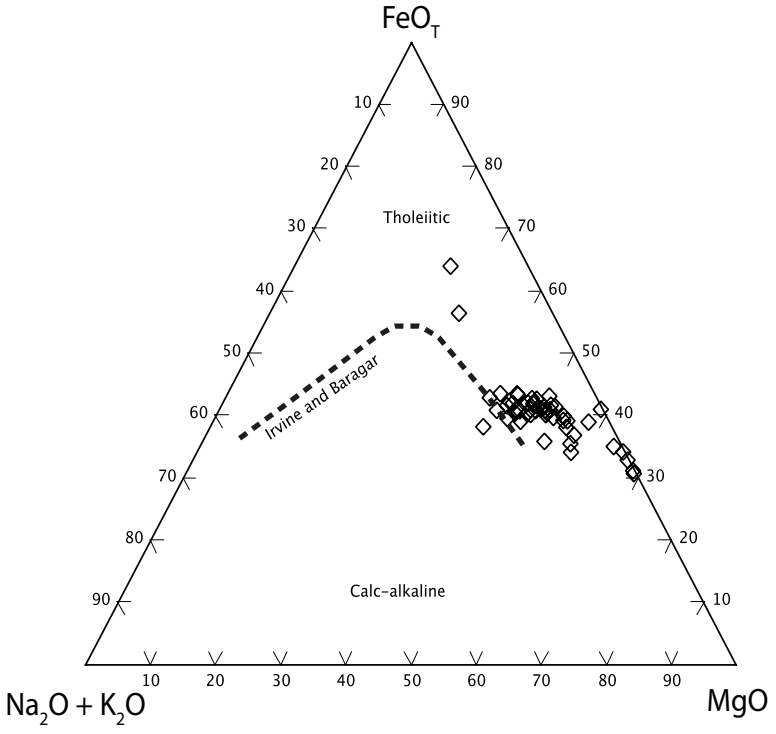

Trace Elements

Floyd & Winchester (1975) determined that a clear discrimination between alkaline and tholeiitic rocks that may have been subjected to post-magmatic process may be obtained from a set of bivariate plots produced with the use of selected immobile trace elements (Ti, Zr Y, Nb and P). Specifically, a P_2O_5 versus Zr plot developed by Floyd & Winchester (1975) and shown in Fig. 5.16, clearly distinguishes the mafic intrusions at Melba Flats as gabbroic rocks formed from magma with a tholeiitic affinity, with abundances clustering within 30 to 50 ppm Zr and 0.3 to 0.4 wt% P_2O_5.

FIGURE 5.16: *Trace element magmatic affiliation of the Melba Flats mafic intrusions. P_2O_5 vs. Zr plot showing showing a well-defined cluster of mafic intrusions plotting within the tholeiitic field from Floyd & Winchester (1975).*

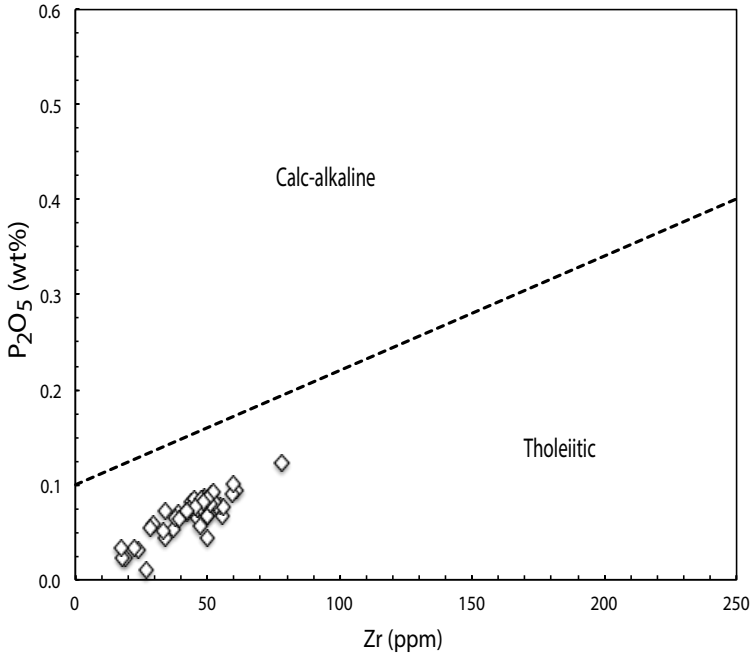

MacLean & Barrett (1993) recognised that gradients of chemical trends varied according to magmatic affinity, and that samples from different magmatic suites produce separate linear trends of magmatic enrichment. In particular, Zr versus Y plots can be used to separate magma affinities in rocks affected by post-magmatic processes, with Y/Zr ratio used as a differentiation index: 1) tholeiite from 2 to 4.5, 2) transitional from 4.5 to 7 and 3) calc-alkaline from 7 to 25. This dicrimination plot is generated and shown in Fig. 5.17 where the mafic intrusions at Melba Flats plot close to and well within the tholeiitic field, with a tholeiite differentiation index ranging from ~ 1.8 to ~ 2.4.

FIGURE 5.17: *Trace element magmatic affiliation of the Melba Flats mafic intrusions. Y vs. Zr plot showing the mafic intrusions clustering close to and well within the tholeiitic field from MacLean & Barrett (1993).*

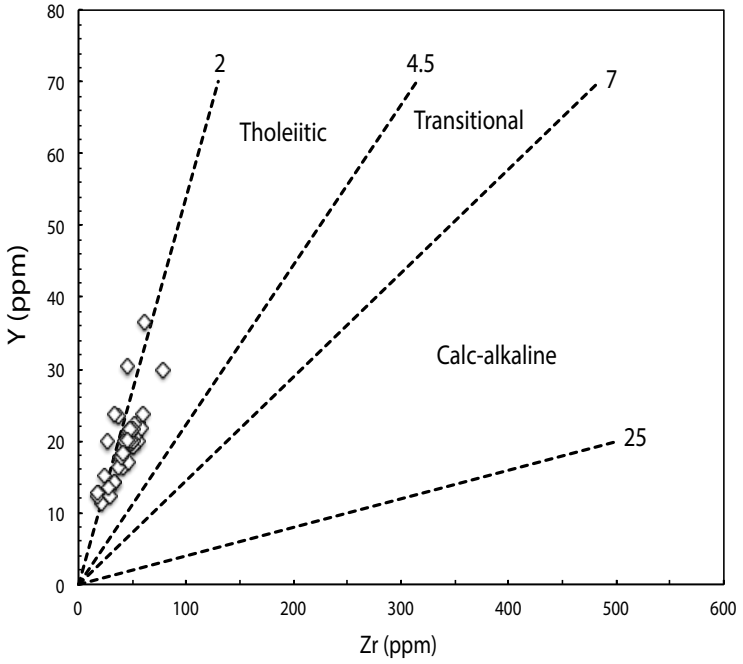

5.2.5 Tectonic Setting Discrimination

Whole rock trace element geochemistry of igneous rocks has not only been shown to be an excellent discriminant of rock classification and magmatic affinity, but it has also been demonstrated as a powerful discriminant of the tectonic environment of emplacement or eruption for igneous rocks. Numerous authors have shown that the compositional features, especially trace element geochemical signatures inherited by igneous rocks, tend to vary depending on the tectonic setting in which the magmas form (Rollinson 1993; Wilson 1989).

High field strength elements (HFSE) are especially useful in trace element studies of tectonic discrimination for igneous rocks due to their immobility. The suite of HFSE that are widely considered to remain immobile throughout post-magmatic processes such as hydrothermal alteration and low grade metamorphism includes Ti, Zr, Y, Nb, Hf, Ta, Th, REE and to a lesser extent, the transition elements V, Cr and Sc (Floyd & Winchester 1978; Rollinson 1993). Immobility of these elements permits the preservation of unique and primitive geochemical signatures often closely associated with the specific tectonic environment in which an igneous rock was emplaced or erupted. Consequently, numerous tectonic discrimination diagrams were developed based on the utilization of these chemically immobile elements.

Unfortunately, ambiguities often arise in the use of these tectonic discrimination diagrams and in an attempt to eradicate this complication, Pearce (1996) developed a protocol that is represented in the form of a ternary diagram shown in Fig. 5.18, Pearce (1996) proposed the tectonic classification of basalts that treated the end-members as three, tectonically defined basalt types: (1) Mid-oceanic ridge basalts (MORB), erupted at divergent plate margins; (2) volcanic arc basalts (VAB), erupted at convergent plate margins; and (3) within-plate basalts (WPB), erupted away from any plate margin. Pearce (1996) further proposed that basalts with complex geochemical signature typical of between-end-members basalts would represent an emplacement or eruptive environment within a complex tectonic setting. The approach described by Pearce (1996) to identify tectonic environments is based on the use of immobile elements discrimination diagrams and relies closely upon the classification protocol represented in Fig. 5.18 to minimize ambiguities in discrimination results and to help elucidate complex tectonic settings. The same approach will be undertaken in order to constrain the tectonic setting in which the Melba Flats mafic intrusions were emplaced in the Ediacaran.

FIGURE 5.18: *Graphical representation for the tectonic discrimination of igneous rocks (Pearce 1996). The three major basalt types are represented by the corners of the ternary plot and the common transitions in between by the edges of the plot. Eruptive/Emplacement settings in which the magma types are located are shown inside the ternary plot.*

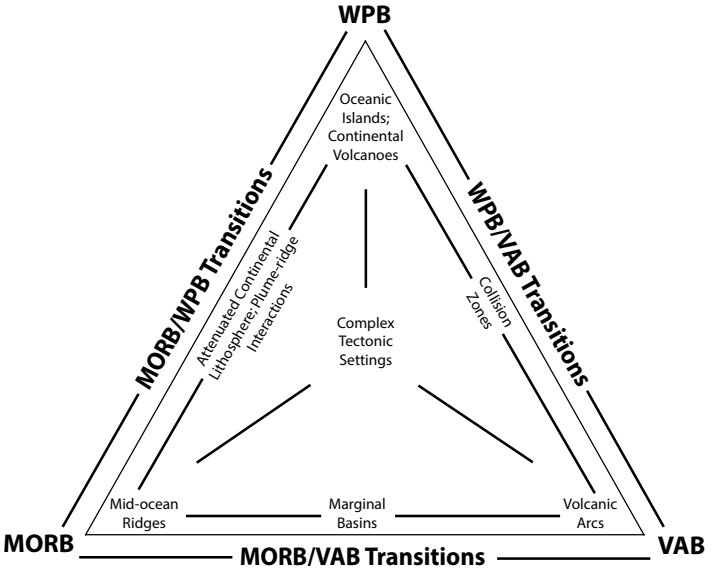

5.2.5.1 Approach to Tectonic Discrimination

Following the method outlined by Pearce (1996) for trace element discrimination of tectonic setting for igneous rocks, the following discrimination plots have been generated.

- Ti-Zr-Y
- Hf-Th-Ta

As determined previously, only the unmineralized samples from the Melba Flats mafic intrusions have been utilized for these discrimination plots in order to minimize any effects post-magmatic processes may have had on the mafic intrusions. It is important to note that these discrimination plots should be interpreted with caution; they are simply designed to highlight potential tectonic setting and any one plot cannot be taken alone as an indicator of a tectonic setting. The tectonic environments in which emplacement or eruption of igneous rocks occur are very often complex and are typified by mixed geochemical signatures.

Ti-Zr-Y

The Ti-Zr-Y ternary plot is primarily designed to identify WPB from MORB and VAB magma types, consequently, it can be used to distinguish marginal basins from collisional zones and attenuated continental lithosphere tectonic settings (Pearce 1996). The Ti-Zr-Y ternary plot was developed by Pearce & Cann (1973) and has been show to be successful in the separation of over 95% of WPB from other magma types and also achieves partial separation of MORB and VAB. The WPB type magma is characterized by an enrichment in Ti and Zr and similar Y values relative to MORB type magma. Consequently, these elements are the ideal indicators to differentiate the WAB magma from the other types. Fig. 5.19 shows the analysed samples, the magma type fields after Pearce & Cann (1973) and the tectonic setting fields after Pearce (1996). Mafic intrusions at Melba Flats plot mainly in the MORB + VAB magma type field and the overlapping tectonic fields of marginal basins and attenuated continental lithosphere on the Ti-Zr-Y plot (Fig. 5.19). This suggests that the tholeiitic intrusions are likely to have emplaced in a complex transitional environment with characteristics dominated by a mixture of MORB and VAB magma type.

FIGURE 5.19: *Ti-Zr-Y discrimination diagram used to identify the emplacement tectonic setting of the mafic intrusions at Melba Flats (after Pearce & Cann (1973)). Note that: on the Ti-Zr-Y diagram, MORB plot in field B, calc-alkaline VAB plot in fields B and C, tholeiitic VAB plot in fields A and C and WPB plot in field D.*

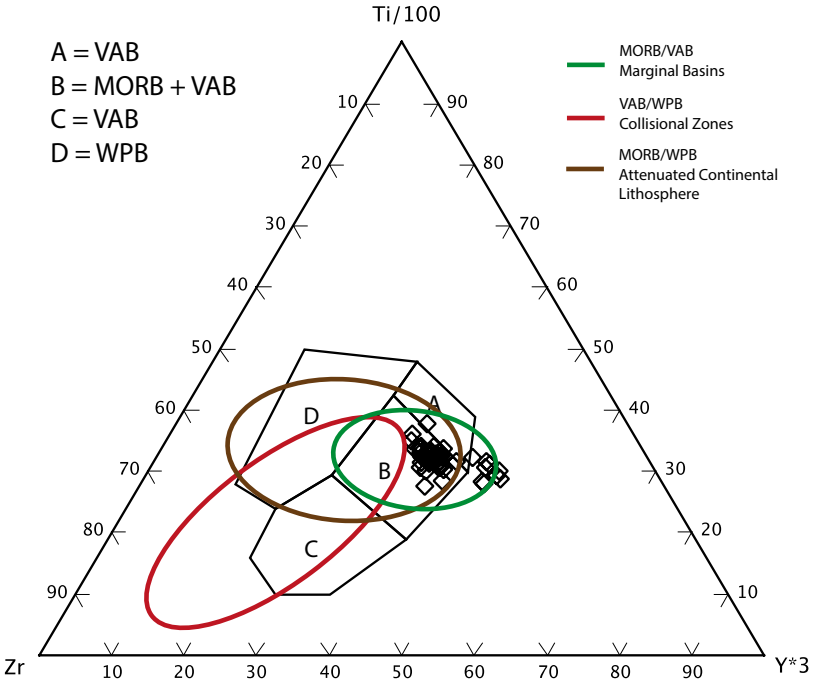

Hf-Th-Ta

The Hf-Th-Ta ternary plot is designed to discriminate VAB from other magma types and particularly from MORB, consequently, it can be used to specifically distinguish attenuated continental lithosphere from the other tectonic settings (Pearce 1996). The Hf-Th-Ta ternary plot was developed by Wood (1980) and has been show to be successful in the partial separation of MORB and WPB and a distinct separation of VAB relative to other magma types. The VAB type magma is characterized by selective enrichment of Th and the depletion of Hf and Ta relative to MORB type magma. Consequently, these elements are the ideal indicators to differentiate the VAB magma from other types. Fig. 5.20 shows the analysed samples, the magma type fields after Wood (1980) and the tectonic setting fields after Pearce (1996). Mafic intrusions at Melba Flats plot mainly in the VAB + MORB magma type field and the overlapping tectonic fields of collision zones and attenuated continental lithosphere on the Hf-Th-Ta plot (Fig. 5.20). This suggests that the tholeiitic intrusions are likely to have emplaced in a complex transitional environment with characteristics dominated by a mixture of VAB and MORB magma type.

FIGURE 5.20: *Hf-Th-Ta discrimination diagram used to identify the emplacement tectonic setting of the mafic intrusions at Melba Flats (after Wood (1980)). Note that: on the Th-Hf-Ta diagram, tholeiitic MORB plot in field A, E-MORB and tholeiitic WPB plot in field field B, alkalic WPB plot in field C and VAB in field D.*

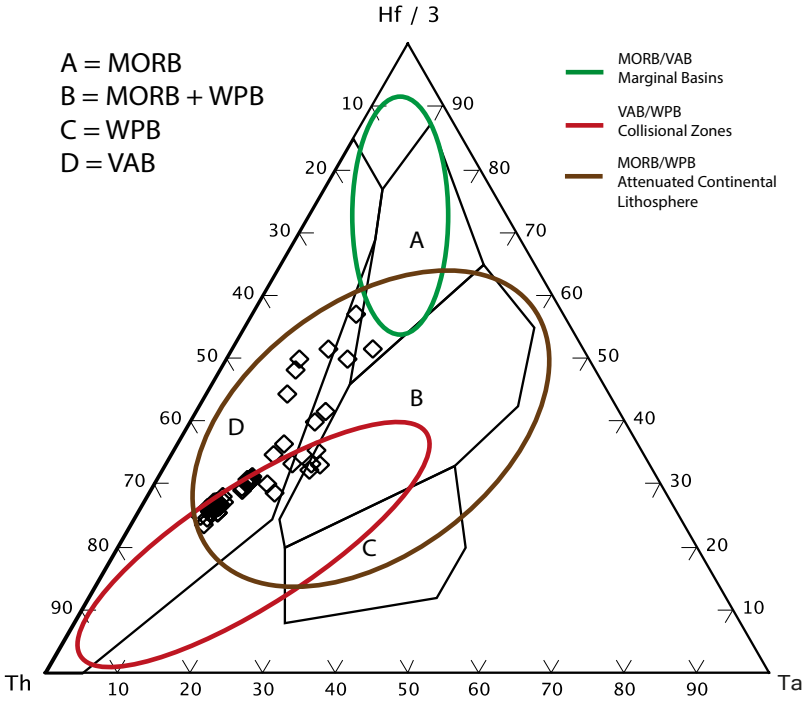

5.2.5.2 Suggested Tectonic Setting

Tectonic discrimination plots utilizing trace element signatures have been used to determine the emplacement setting of the mafic intrusions at Melba Flats. The Melba Flats mafic intrusions plotted in the MORB + VAB fields in both the Ti-Zr-Y and Th-Ta-Hf diagrams and this suggests that these tholeiitic intrusions are likely to have emplaced either at some marginal basin spreading axes (those at intermediate distances from a subduction zone) or within some attenuated continental settings (those in which the degree of attenuation was large and there was extensive interaction between magma and crust). However, based on the overlapping fields of tectonic settings in which the Melba Flats intrusions have plotted in the discrimination plots, one can exclude marginal basins as a potential tectonic setting of emplacement for the tholeiitic intrusions at Melba Flats. Consequently, it is argued that the emplacement setting for the Melba Flats intrusions is likely to be an attenuated continental lithosphere tectonic setting. Coincidentally, this assertion is consistent with the consensus that emplacement of the Melba Flats mafic intrusions occurred in the Ediacaran (*c.* 580 Ma) within rift basins that developed on thinning continental crust, along a volcanic passive margin (Calver *et al.* 2014; Crawford & Berry 1992; Direen & Crawford 2003).

5.3 Comparison to Possible Stratigraphic Equivalents

Geochemical data of possible stratigraphic equivalents to the Melba Flats mafic intrusions have been collated from the mafic intrusives within the Crimson Creek Formation Sediments at Avebury (A254 Sill 1); the Grimes Suite Intrusives of the Grassy Group on King Island (GIS); the Spinks Creek Volcanics of the Togari Group in the Smithton Basin (SCV); and the basalts within the Crimson Creek Formation Sediments at Zeehan (CCKB). These data are compared to the lithophile and REE compositional patterns described here for the Melba Flats mafic intrusions. In general terms, trace element geochemistry results of the Spinks Creek Volcanics basalts appears to be the most similar to the Melba Flats mafic intrusions, whilst the mafic intrusives from Avebury appears to be the most dissimilar, with significant depletion in compatible elements compared to the Melba Flats mafic intrusions. Comparison between the Melba Flats mafic intrusions and its possible stratigraphic equivalents are shown below in the lithophille element and REE plots of Fig. 5.21 and Fig. 5.22 respectively.

Lithophile Elements

Primitive mantle-normalized lithophile element patterns appear to be rather similar for the Melba Flats mafic intrusions in comparison to the Grimes Suite Intrusives, Spinks Creek Volcanics and Crimson Creek Formation Basalts, albeit with a slightly more enriched lithophile element patterns. However, the Melba Flats mafic intrusions are significantly dissimilar to the mafic intrusives at Avebury, which are represented by a more depleted lithophile element pattern and in particular, a 'U'-shaped lithophile element pattern characteristic of boninites. Relative to primitive mantle (McDonough *et al.* 1992), the Melba Flats mafic intrusions are depleted in Nb, La, Ce, Nd, Zr and Sm relative to GIS, SCV and CCKB and enriched in the same suite of elements relative to mafic intrusives at Avebury. Consequently, the Melba Flats mafic intrusions are interpreted to be vastly different from the mafic intrusives at Avebury, but fairly similar to GIS, SCV and CCKB in terms of lithophile element patterns, in spite of the slightly more enriched overall lithophile element patterns.

Rare Earth Elements

Primitive mantle-normalized REE patterns appear to be fairly similarly for the Melba Flats mafic intrusions in comparison to the Grimes Suite Intrusives, Spinks Creek Volcanics and Crimson Creek Formation Basalts, although the latter three are characterized by slighted more enriched LREE patterns relative to HREE, with a $(La/Yb)_{PM}$ average of ~ 4.1 in comparison to the mafic intrusions at Melba Flats, with a $(La/Yb)_{PM}$ average of ~ 1.5. However, the Melba Flats mafic intrusions are significantly dissimilar to the mafic intrusives at Avebury, which are represented by a more depleted LREE pattern relative to HREE, with a $(La/Yb)_{PM}$ average of ~ 0.1. Generally, the extent of REE enrichment is greater for the Melba Flats mafic intrusions (average $\sum$ REE = 30) in comparison to the intrusives at Avebury (average

$\sum$ REE = 11); and smaller for the Melba Flats mafic intrusions as compared to GIS, SCV and CCKB (average $\sum$ REE = 82). Consequently, the Melba Flats mafic intrusions can be interpreted as vastly different from the mafic intrusives at Avebury, but are more similar to GIS, SCV and CCKB in terms of REE patterns, in spite of the slightly more enriched overall REE patterns.

FIGURE 5.21: *Primitive mantle-normalized lithophile element plot, with Avebury Intrusives (A254 Sill 1), Grimes Intrusive Suite (GIS), Sprinks Creek Volcanics (SCV) and Crimson Creek Basalt (CCKB) plotted for comparison. Collated data from Calver* et al. *(2014).*

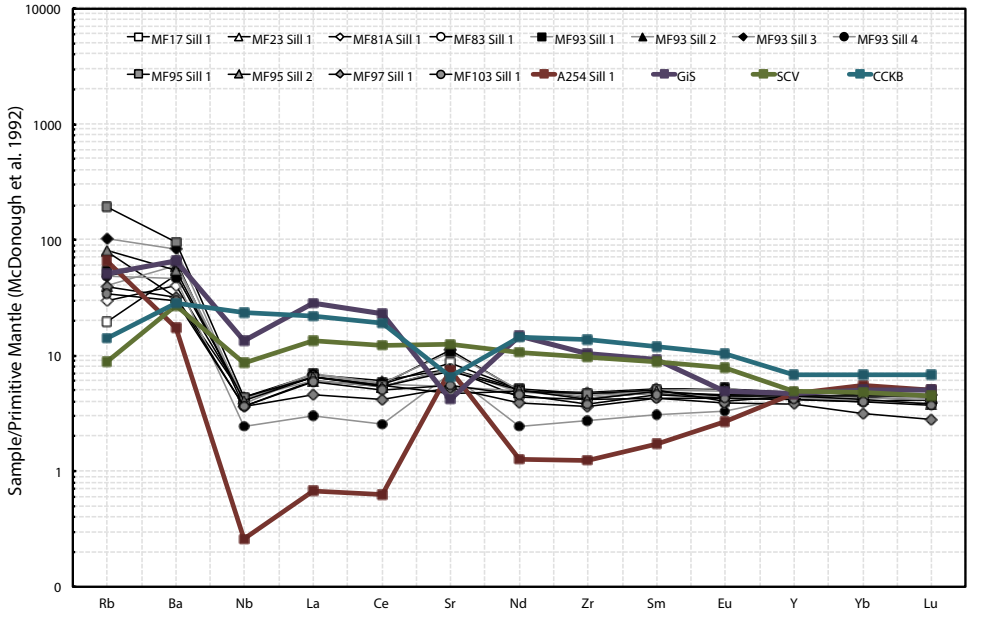

FIGURE 5.22: *Primitive mantle-normalized REE plot, with Avebury Intrusives (A254 Sill 1), Grimes Intrusive Suite (GIS), Sprinks Creek Volcanics (SCV) and Crimson Creek Basalt (CCKB) plotted for comparison. Collated data from Calver* et al. *(2014).*

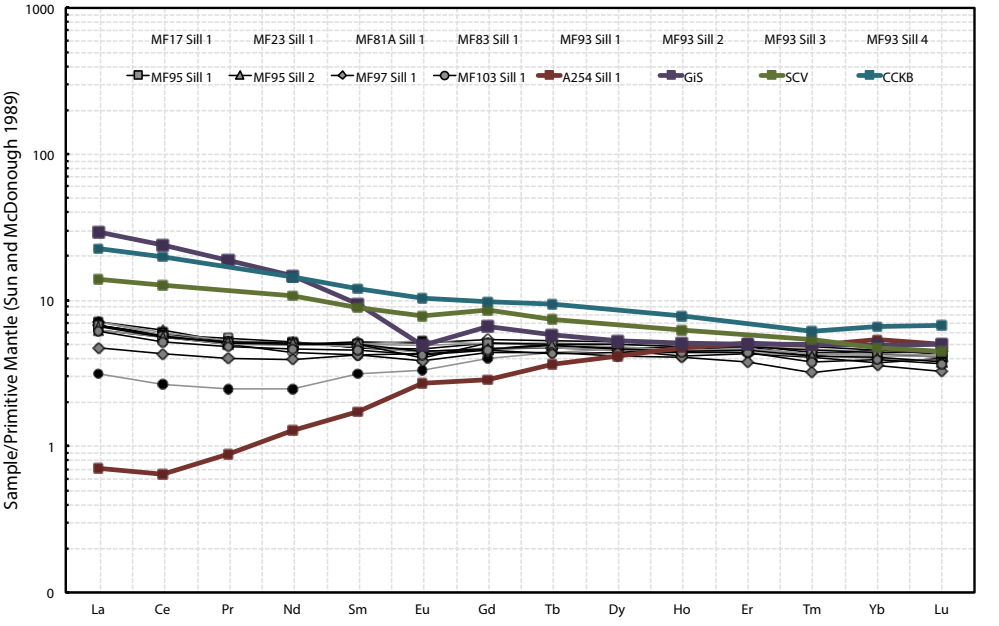

Based on the lithophile element and REE patterns observed in Fig. 5.21 and Fig. 5.22 respectively, it is argued that the Melba Flats sediments is most similar geochemically to the Spinks Creek Volcanics and geochemically most different from the mafic intrusions at Avebury. This likely correlation to Spinks Creek Volcanics is supported by numerous authors (Brown 1986; Varne & Foden 1987). It is also interesting that mafic intrusions at Avebury are so distinctive dissimilar to the Melba Flats mafic intrusions in spite of the fact that both intrusives have intruded sedimentary rocks that were described and correlated previously.

Chapter 6

Geochemistry of the Melba Flats Ni-Cu-PGE Sulphides

A primary aim of this research project was to determine if the Ni-Cu-PGE sulphide mineralization at Melba Flats was formed *in situ* or at depth. To accomplish this aim, it would require an understanding of the relationship between the different forms of sulphide mineralization associated with the deposit, the S-saturation status of the magma prior to the ore-forming event and the origin of the S component that makes up the associated magmatic sulphides. Considering these, powerful indicators of magmatic Ni-Cu-PGE sulphides-forming processes in the form of various analytical methods including platinum group element geochemistry of the primitive magma, along with trace element geochemistry (specifically S and Se) and sulphur isotope geochemistry of magmatic sulphides are adopted to address this aim.

6.1 Platinum Group Element Geochemistry

Solution-based laser ablation inductively coupled plasma mass spectrometry (LA-ICPMS) was conducted to determine the platinum group element (PGE) geochemistry for a subset of 57 from 73 whole rock samples of the Melba Flats mafic intrusions that were analysed for major and trace element geochemistry. Platinum group element (PGE) geochemical data obtained for the mafic intrusions were also sub-divided into unmineralized (less than 1 wt% S) and mineralized samples (more than 1 wt% S) samples and analysed accordingly, in order to facilitate an equitable interpretation process. About 37% of the 57 samples analysed are classified as mineralized and the remaining 63% constitute 36 unmineralized samples. Representative concentrations of PGE, along with selected trace element abundances in these samples from the Melba Flats mafic intrusions are summarized in Table. 6.1 and Table. 6.2 and detailed in Table. C.5 of Appendix. C.

TABLE 6.1: *Representative PGE elements geochemical data for the unmineralized Melba Flats mafic intrusions.*

Unmineralized PGE							
Sill	MF17 Sill 1	MF93 Sill 1	MF93 Sill 3	MF93 Sill 4	MF95 Sill 2	MF97 Sill 1	MF103 Sill 1
Sample	MF17-69.6	MF93-128.55	MF93-310.55	MF93-365.2	MF95-212.15	MF97-215.9	MF103-111.2
Lab	***BV***	***GEO***	***GEO***	***GEO***	***BV***	***BV***	***BV***
Ni (ppm)	361.48	267.20	370.30	312.80	337.91	762.26	534.36
Pt (ppb)	0.05	0.26	0.62	0.33	0.05	6.90	1.20
Pd (ppb)	0.05	0.27	0.73	0.45	0.05	5.50	0.05
Au (ppb)	0.90	0.49	1.14	0.46	1.90	3.90	0.90
Cu (ppm)	103.85	65.40	106.30	47.80	119.83	431.38	127.81

TABLE 6.2: *Representative PGE elements geochemical data for the mineralized Melba Flats mafic intrusions.*

Mineralized PGE									
Sill	MF19 Sill 1	MF23 Sill 2	MF81A Sill 1	MF83 Sill 1	MF93 Sill 2	MF93 Sill 3	MF93 Sill 4	MF95 Sill 1	MF103 Sill 1
Sample	MF19-39.5	MF23-65.5	MF81A-174.44	MF83-139.55	MF93-155.21	MF93-304.0	MF93-335.2	MF95-123.35	MF103-146.0
Lab	***ACME***	***ACME***	***ACME***	***ACME***	***GEO***	***GEO***	***ACME***	***GEO***	***BV***
Ni (ppm)	59800.00	200160.00	144700.00	23200.00	20241.68	16.30	35.00	20320.46	416.49
Pt (ppb)	794.00	885.00	3323.00	343.60	308.00	0.48	0.70	238.00	0.05
Pd (ppb)	1971.00	1361.00	1022.00	541.20	625.00	0.49	1.40	322.00	0.05
Au (ppb)	607.00	961.00	513.00	401.90	122.00	2.44	3.00	156.00	2.60
Cu (ppm)	59800.00	6422.40	24400.00	15200.00	13230.04	139.00	266.10	12102.85	71.90

6.1.1 Results: Platinum Group Element Geochemistry

Unmineralized

Ni-Cu-PGE metal concentrations vary widely in the unmineralized samples, with some containing Ni-Cu-PGE abundances up to 2877 ppm Ni, 5698 ppm Cu, 100 ppb Pt, 121 ppb Pd and 34 ppb Au; while others contain concentrations as low as 25 ppm Ni, 3 ppm Cu, 0.05 ppb Pt, 0.05 Pd and 0.1 ppb Au. With the exception of MF93 Sill 4 and MF97 Sill 1, primitive mantle-normalized Ni-Cu-PGE metal patterns for the unmineralized samples are relatively similar (Fig. 6.1), with variations in enrichment factors ranging from 1.5 to approximately 20 for Cu and Au; and variations in depletion factors ranging between 0.1 and 0.01 for Ni, Pt and Pd. MF93 Sill 4 and MF97 Sill 1 are generally more enriched in Ni-Cu-PGE metal content (average $\sum$ Ni & Cu = 1100 ppm; average $\sum$ Pt, Pd & Au = 33 ppb) relative to the rest of the unmineralized samples (average $\sum$ Ni & Cu = 522 ppm; average $\sum$ Pt, Pd & Au = 2 ppb). Notwithstanding the outliers, the remaining samples are characterized by PGE that are strongly depleted relative to Ni and Cu as indicated by their average $(Ni/Pd)_{PM}$ and $(Cu/Pt)_{PM}$ ratios of 5.2 and 74.5 respectively. Furthermore, Ni is weakly fractionated from Cu as indicated by the Ni/Cu ratio averaging 3.0 and there is little to no fractionation between Pt and Pd as shown by Pt/Pd ratio averaging 0.7 for the unmineralized samples. With the exception of MF93 Sill 4 and MF97 Sill 1, there is little dissimilarity in the Ni-Cu-PGE metal patterns between the unmineralized samples.

FIGURE 6.1: *Primitive mantle-normalized Ni-Cu-PGE plot for the average values of unmineralized samples from the Melba Flats mafic intrusions.*

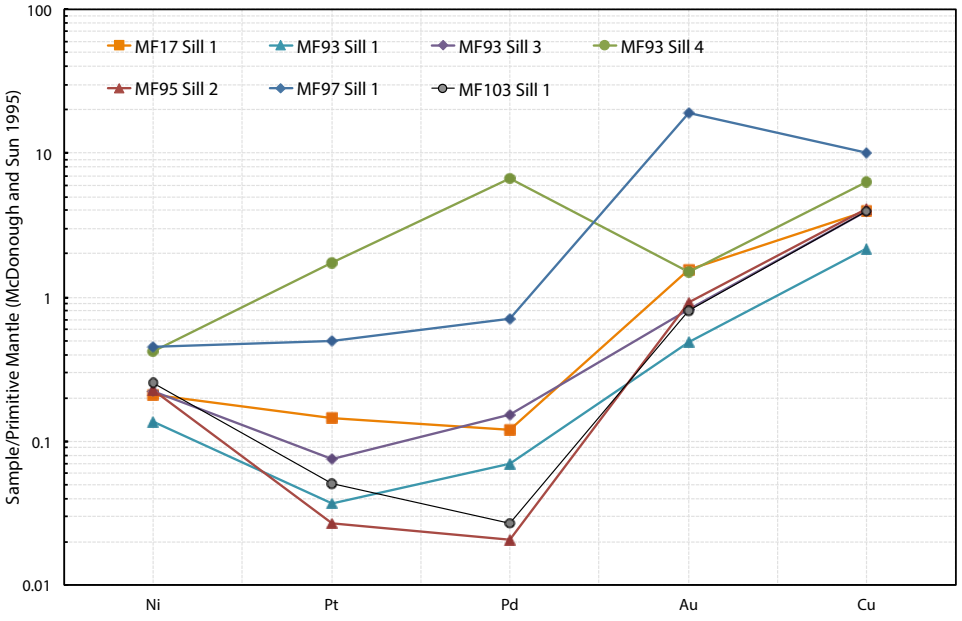

Mineralized

Ni-Cu-PGE metal concentrations also vary widely in the mineralized samples, with some containing Ni-Cu-PGE abundances up to 200,600 ppm Ni, 66,900 ppm Cu, 3323 ppb Pt, 1917 ppb Pd and 961 ppb Au, while others contain concentrations as low as 16 ppm Ni, 72 ppm Cu, 0.05 ppb Pt, 0.05 Pd and 2 ppb Au. With the exception of MF93 Sill 3, MF93 Sill 4 and MF103 Sill 1, the primitive mantle-normalized Ni-Cu-PGE metal patterns for the mineralized samples are almost identical (Fig. 6.2), with variations in enrichment factors ranging between 6 and about 1400 and increasing factors of enrichment from Ni to Cu. MF93 Sill 3, MF93 Sill 4 and MF103 Sill 1 are significantly depleted in Ni-Cu-PGE metal content (average $\sum$ Ni-Cu = 314 ppm; average $\sum$ PGE = 4 ppb) relative to the rest of the mineralized samples (average $\sum$ Ni-Cu = 60,110 ppm; average $\sum$ PGE = 1310 ppb). Notwithstanding the outliers, the Ni-Cu-PGE metal patterns of the remaining samples are relatively flat, characterized by very weak fractionation of Ni from Cu as indicated by the average Ni/Cu ratio of ~ 2.2 and little to no fractionation between Pt and Pd as shown by the average Pt/Pd ratio of ~ 0.9. With the exception of MF93 Sill 3, MF93 Sill 4 and MF103 Sill 1 that are characterized by significantly depleted Ni-Cu-PGE metal patterns, there are no systematic differences in the Ni-Cu-PGE metal patterns between the mineralized samples. Although it is likely that this represents the existence of two contrasting groups of Ni-Cu-PGE sulphide mineralization within the mineralized intrusions.

FIGURE 6.2: *Primitive mantle-normalized Ni-Cu-PGE plot for the average values of mineralized samples from the Melba Flats mafic intrusions.*

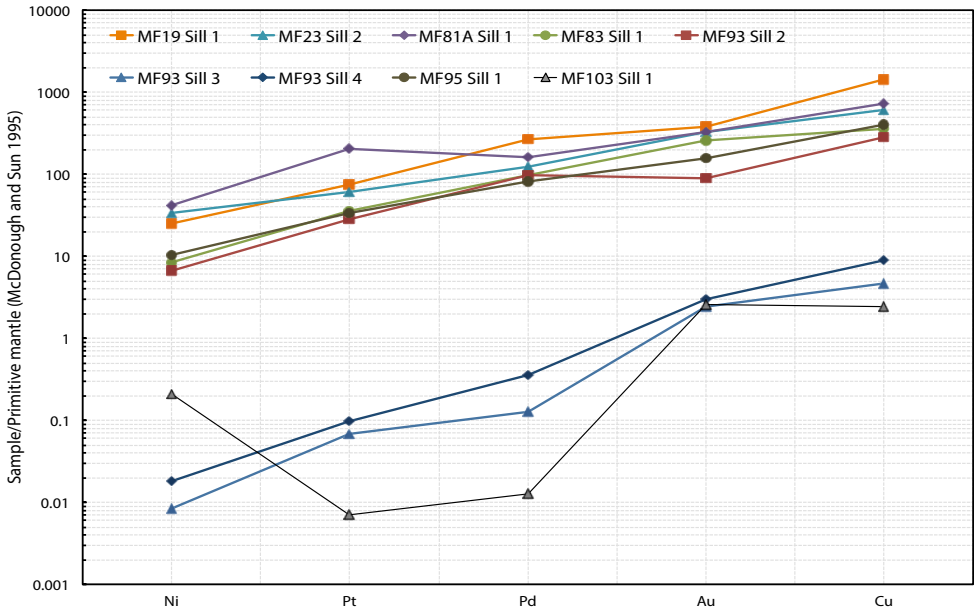

6.1.2 Comparison of Unmineralized to Mineralized Intrusions

Average Ni-Cu-PGE abundances for each of the 13 Melba Flats mafic intrusions (unmineralized and mineralized) were tabulated (Table. **??**) and then plotted on Cu versus Ni and Pd versus Pt bivariate diagrams shown in Fig. 6.3 and Fig. 6.4 respectively, in order to compare and contrast these individual intrusions. The bivariate plot of Cu versus Ni shows positive correlation between Cu and Ni, with a Pearson correlation coefficient (R^2) of about 0.81 (Fig. 6.3). This reasonable correlation between Cu and Ni might suggest that the Ni-Cu-PGE-rich and Ni-Cu-PGE-poor sulphides in these intrusions are correlated and that the unmineralized and mineralized intrusions are essentially co-magmatic. This is assertion is strongly supported by the bivariate plot of Pd versus Pt, which displays a strong positive correlation between Pd and Pt, with a Pearson correlation coefficient (R^2) of approximately 0.97 (Fig. 6.4). Consequently, it is argued that the Ni-Cu-PGE-rich and Ni-Cu-PGE-poor sulphides are correlated and the unmineralized and mineralized intrusions are co-magmatic.

Interestingly, the mineralized intrusions associated with disseminated sulphides plot in a cluster with the unmineralized intrusions, rather than the rest of the mineralized intrusions associated with massive-to-semi-massive sulphides in both bivariate diagrams (Fig. 6.3; Fig. 6.4). This strongly implies that the two forms of Ni-Cu-PGE sulphide mineralization observed by Crawford & Keays (2010) in the Melba Flats mafic intrusions are geochemically distinctive. This is consistent with the two unique primitive mantle-normalized Ni-Cu-PGE metal patterns previously described in Fig. 6.2, which can be implied to represent the massive-to-semi-massive sulphides (strongly enriched Ni-Cu-PGE metal patterns) and the disseminated sulphides (strongly depleted Ni-Cu-PGE metal patterns) in the Melba Flats mafic intrusions. Consequently, it is argued that two types of Ni-Cu-PGE mineralization exists in the mafic intrusions at Melba Flats: 1) massive-to-semi-massive sulphides that are rich in Ni, Cu and PGE and 2) disseminated sulphides that are poor in Ni, Cu and PGE.

FIGURE 6.3: *Bivariate plot of Cu vs. Ni comparing unmineralized to mineralized Melba Flats mafic intrusions.*

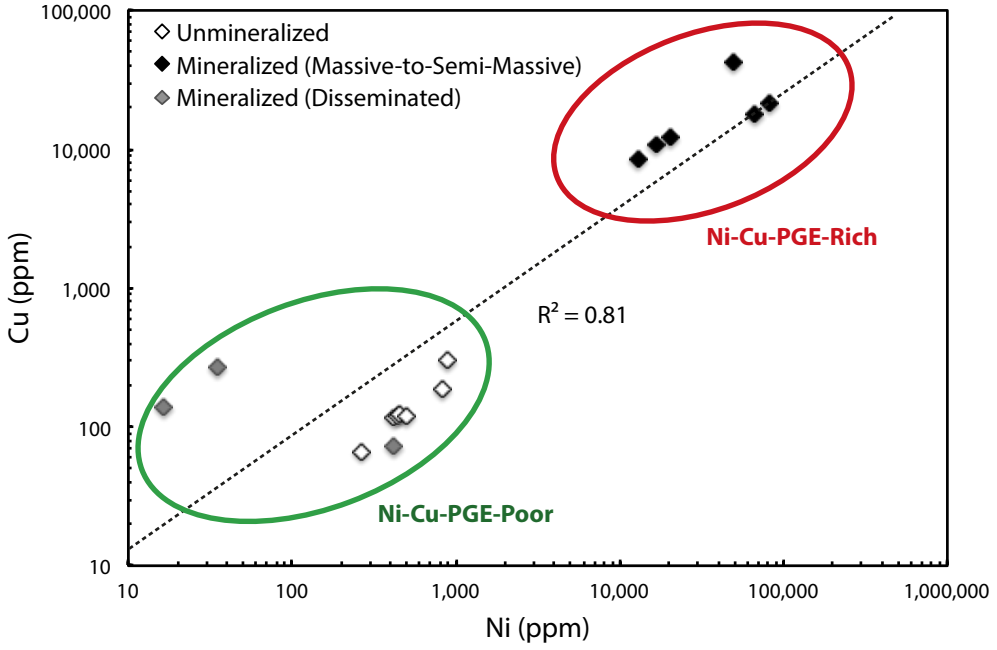

FIGURE 6.4: *Bivariate plot of Cu vs. Ni comparing unmineralized to mineralized Melba Flats mafic intrusions.*

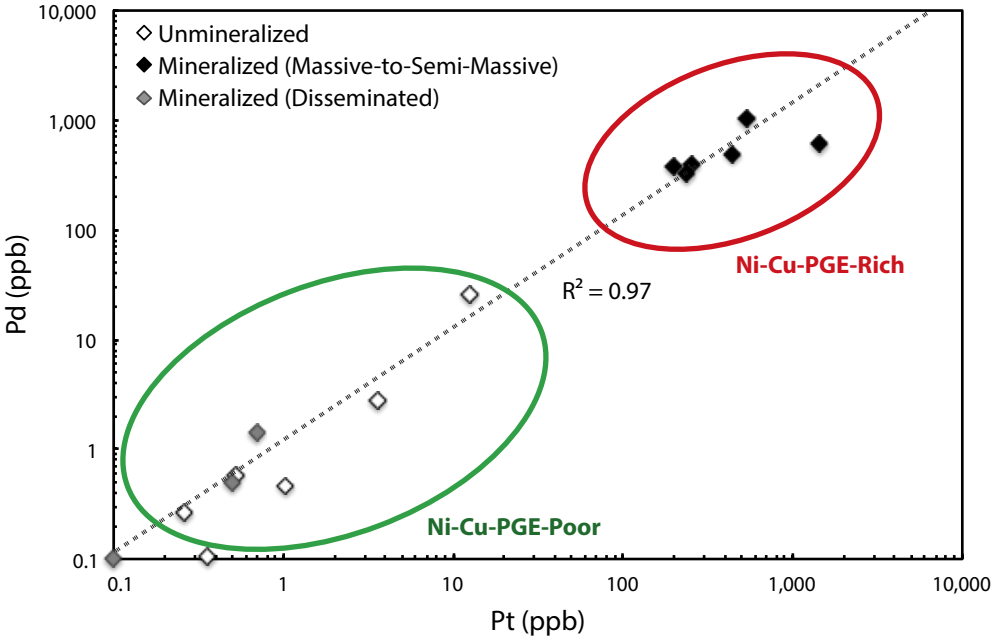

6.1.3 S-Saturation Status of Magma

The role of S-saturation (or sulphur saturation) of mafic magma has long been identified as one of the key processes in the formation of magmatic Ni-Cu-PGE deposits. Specifically, Keays (1995) and Keays & Lightfoot (2010) have argued that S-undersaturated magmas are generally required prior to an ore-forming event in order to form magmatic Ni-Cu-PGE deposits of significance. Vogel & Keays (1997) indicated that the relative behaviour of Pd and Cu is inversely controlled by the S-saturation status of the magma due to the significantly higher sulphide/silicate partition coefficient for Pd (~ 43,000; Peach *et al.* (1994)) relative to Cu (245-1383; Peach *et al.* (1990)). Consequently, the discrimination between S-undersaturated and S-saturated status of a magma is possible using a Pd versus Cu bivariate plot. A Pd versus Cu discrimination plot for the Melba Flats intrusions is shown in Fig. 6.5, along with the dashed line from Vogel & Keays (1997) separating fields of S-undersaturation in magma and S-saturation in magma.

FIGURE 6.5: *Bivariate plot of Cu vs. Ni comparing unmineralized to mineralized Melba Flats mafic intrusions. Dashed line separating S-undersaturated and S-saturated fields from Vogel & Keays (1997).*

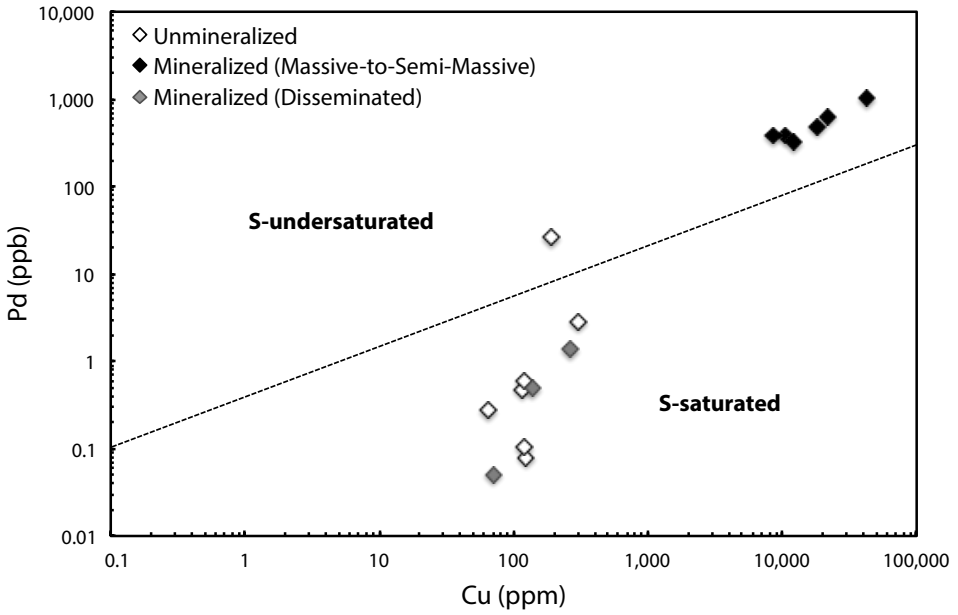

The Pd vs. Cu discrimination plot clearly shows that the unmineralized intrusions, along with the mineralized intrusions associated with disseminated sulphides (Ni-Cu-PGE-poor) are mostly plot in the field of S-saturated magmas and are largely characterized by a varied depletion in Pd and Cu. These intrusions may have been variably depleted in Pd and Cu as a result of the scavenging by magmatic sulphides, which have likely segregated from the magma. On the other hand, the mineralized intrusions associated with massive-to-semi-massive sulphides (Ni-Cu-PGE-rich) plot in the field of S-undersaturated magmas and are characterized by varied enrichment in Pd and Cu. The sulphide melts of these mineralized intrusions may have interacted with larger volumes of silicate magma as compared to the others, consequently, giving rise to the more enriched Cu/Pd ratios. Furthermore, it is also observed that the trend line defined by the mineralized intrusions associated with massive-to-semi-massive sulphides is vastly different from the trendline defined by the mineralized intrusions associated with disseminated sulphides. The correlation between the mineralized intrusions associated with massive-to-semi-massive sulphides (Ni-Cu-PGE-rich) and S-undersaturation is consistent with Keays (1995) who argued that S-undersaturated magma is crucial to the formation of Ni-Cu-PGE-rich ores.

6.1.4 Source of S in Melba Flats Ni-Cu-PGE Sulphides

S/Se ratios have commonly been employed in many studies of magmatic Ni-Cu-PGE deposits as a tool to determine the source (crustal, mantle or mixture) of S in magmatic sulphides and consequently, as a petrogenetic indicator of ore-forming processes (Eckstrand *et al.* 1989; Peck & Keays 1990; Thériault & Barnes 1998). S/Se ratios in these magmatic deposits vary from 100 to 100,000. Eckstrand & Hulbert (1987) estimated that the S/Se ratio of the mantle is between 2850 and 4350 and most igneous rocks have a S/Se ratio close to the mantle, as in the case of Merensky Reef of the Bushveld Complex (Godel *et al.* 2007), which suggests that S that saturated the mafic magma had a mantle origin. S/Se ratios greater than mantle values have been interpreted to signify a substantial S contribution from the country rock (Maier & Barnes 2010). In contrast, S/Se ratios less than the mantle values are taken to indicate either a S-loss due to low temperature alteration or resorption of sulphides into S-undersaturated magmas during their transport (Holwell *et al.* 2014). Specifically, plots of $(Pt + Pd)_{100\% \text{ Sulphides}}$ versus S/Se have been shown by Queffurus & Barnes (2015) to be a powerful tools in identifying the source of S and the characterization of petrogenetic processes involved in the formation of magmatic of Ni-Cu-PGE sulphide deposits. Fig. 6.6 shows the $(Pt + Pd)_{100\% \text{ Sulphides}}$ versus S/Se plot for the Melba Flats mafic intrusions.

FIGURE 6.6: *Plot of (Pt + Pd)$_{100\%\ Sulphides}$ vs. S/Se comparing unmineralized to mineralized Melba Flats mafic intrusions. Mantle domain values from Eckstrand & Hulbert (1987). R-factors from Queffurus & Barnes (2015).*

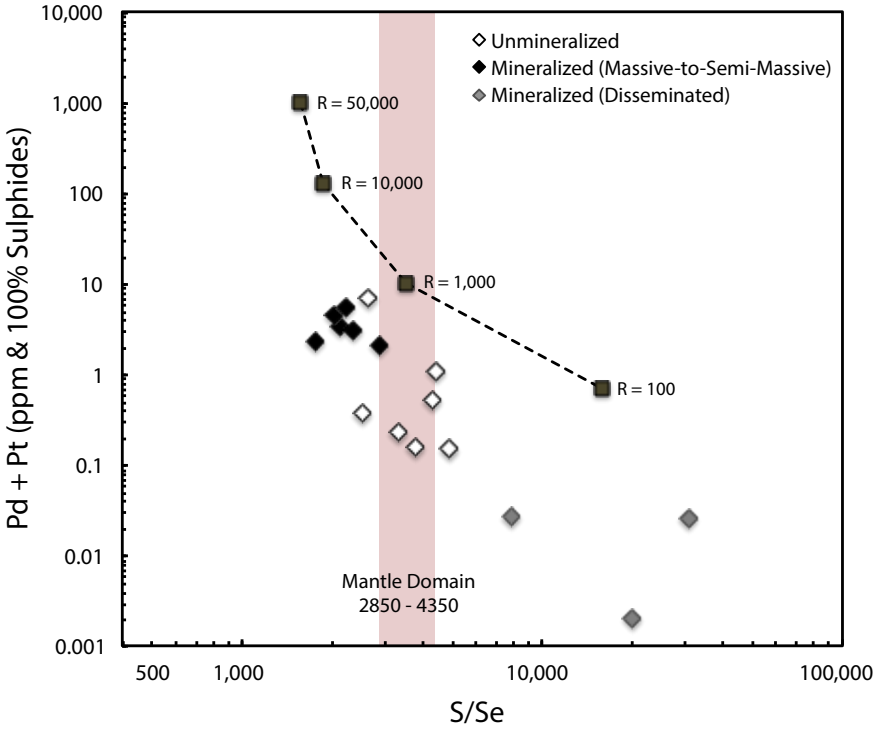

The majority of the unmineralized intrusions plot within the typical mantle S/Se ratio range between 2850 and 4350 (Eckstrand & Hulbert 1987) and are associated with low (Pt + Pd)$_{100\%\ Sulphides}$ from 0.1 to 1 ppm and low R-factors ($100 < R < 500$). This strongly suggests that the S associated with the minimal magmatic sulphides that occur in the unmineralized intrusions have an entirely mantle origin. On the other hand, most of the mineralized intrusions associated with massive-to-semi-massive sulphides are characterized by narrow S/Se ratios close to mantle values ranging between 1749 and 2873; they also have higher (Pt + Pd)$_{100\%\ Sulphides}$ from 1 to 10 ppm and moderate R-factors ($500 < R < 1000$). Whilst the mineralized intrusions associated with disseminated sulphides are characterized by S/Se ratios with crustal signature typically more than 7800 (Queffurus & Barnes 2015), extremely low (Pt + Pd)$_{100\%\ Sulphides}$ from 0.001 to 0.01 ppm and very low R-factors ($R < 100$).

Consequently, it is suggested that the sub-mantle S/Se ratios of the massive-semi-massive sulphides are due to partial resorption of the sulphides into a S-undersaturated magma during transport, a process proposed by Kerr & Leitch (2005) to explain the high tenors of the Voisey's Bay magmatic sulphides. Partial resorption would result in metals with low sulphide melt/silicate melt partition coefficients such as Fe being resorbed along with S into the magma, but those with high partition coefficients such as Cu, PGE, Au and Se being retained in the residual sulphide. As a result, the S/Se ratios of the sulphides would decrease and their PGE tenors increase. On the contrary, the S component of the magmatic disseminated sulphides in the mineralized intrusions is argued to be entirely of crustal origin. This is likely a consequence of the culmination of two factors: 1) a crustal S contribution from the country rock, which primarily caused the elevated S/Se ratios and 2) the lack of sulphide melt and silicate magma interaction (low R-factor < 100) to efficiently capture PGE and Se, which would have resulted in the depleted PGE abundances and high S/Se ratio of the disseminated magmatic sulphides.

6.2 Sulphur Isotope Geochemistry

Stable isotope ratio mass spectrometry was conducted to determine the S isotopic composition of 12 sulphide-rich samples from the mineralized mafic intrusions at Melba Flats, as well as 2 samples of the Crimson Creek Formation at Avebury. δ^{34}S values were calculated by normalizing the $^{34}S/^{32}S$ ratios of the sample relative to the Vienna Cañon Diablo Troilite (VCDT) international reference standard. Representative S isotope values of the sulphide-rich samples and the Crimson Creek Formation samples are summarized in Table. 6.3.

6.2.1 Results: Sulphur Isotope Geochemistry

Of the 12 S-rich samples analyzed, 10 are massive-to-semi-massive sulphide-rich whilst the remaining 2 are disseminated sulphide-rich. The massive-to-semi-massive sulphide-rich samples were characterized by δ^{34}S values between -0.2 and +2.6, with an average δ^{34}S value of +1.4 and a standard deviation of $\sim$ 0.7. On the other hand, the disseminated sulphide-rich samples were characterized by δ^{34}S values ranging between +4.0 and +4.6, with an average δ^{34}S value of +4.3 and a standard deviation of $\sim$ 0.4. Both samples of the Crimson Creek Formation sediments produced δ^{34}S values of +1.8.

TABLE 6.3: *Summary of S isotope values for the sulphide-rich samples from the mineralized Melba Flats mafic intrusions, along with their associated S/Se ratio.*

Massive-to-semi-massive Sulphides			
		δ^{34}S (%VCDT)	**S/Se**
MF19 Sill 1	MF19-41.32	1.2	2092
MF23 Sill 2	MF23-65.3	1.8	2041
	MF23-65.5	1.7	2072
	MF23-74.5	-0.2	4127
	MF23-74.6	1.2	1940
	MF23-75.0	1.2	2410
	MF81A-171.5	2.6	2391
	MF81A-174.44	1.4	2018
	MF81A-174.52	1.2	1958
MF83 Sill 1	MF83-139.55	1.8	2389
Disseminated Sulphides			
		δ^{34}S (%VCDT)	**S/Se**
MF93 Sill 4	MF93-335.2	4.6	7872
	MF93-356.3	4.0	7200

6.2.2 Significance of Sulphur Isotope Values in relation to S/Se Ratios

δ^{34}S data values are often used in conjunction with S/Se ratios to determine if the S of magmatic sulphides were crustally-derived or not (Eckstrand *et al.* 1989). Commonly for many magmatic Ni-Cu-PGE deposits, S/Se ratios higher than the upper limit of the mantle values (>4350), along with δ^{34}S values showing deviation from the mantle values ($\delta^{34}S = 0 \pm 2\%$) would indicate that some S component from the magmatic sulphides of these deposits is from the crust. Following this logic, δ^{34}S values are plotted against S/Se ratios in Fig. 6.7 in order to determine if the conclusions drawn from the S/Se ratios previously corroborates with the insight provided by the δ^{34}S values regarding the origin of S for the magmatic sulphides associated with the Melba Flats mineralized intrusions.

FIGURE 6.7: *Plot of $\delta^{34}S$ % vs. VCDT vs. S/Se comparing massive-to-semi-massive to disseminated sulphide-rich mineralized Melba Flats mafic intrusions. Mantle domain values from Eckstrand & Hulbert (1987). Mantle range (VCDT) from Ripley (1999).*

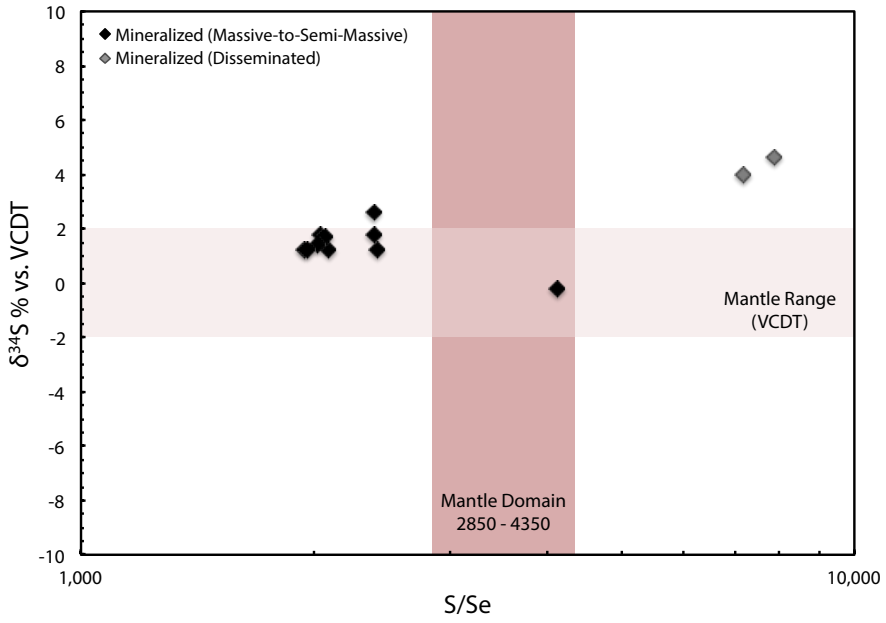

The $\delta^{34}S$ values of the massive-to-semi-massive sulphides ($\delta^{34}S = +1.4 \pm 0.7$) suggest strongly that the S component of these magmatic sulphides is of mantle origin. These mantle $\delta^{34}S$ values are associated with S/Se ratios that fall just below the mantle domain of 2850 - 4350 (Eckstrand & Hulbert 1987). Consequently, this corresponds with the initial hypothesis that the S component of these magmatic sulphides is mantle in origin, but became enriched in PGE and Se due to the magmatic sulphides being partially resorbed during transport to derive their current S/Se ratios. On the other hand, the $\delta^{34}S$ values of the disseminated sulphides implies that at least some component of these magmatic sulphides is of crustal origin. These crustal $\delta^{34}S$ values corroborates with the crustal S/Se ratios (S/Se $>$ 7800) of the magmatic disseminated sulphides.

Although, the $\delta^{34}S$ values of the local host sedimentary rock were not obtained as a consequence of low S abundances that were below detection limits, there was reasonable success in the attempts to determine $\delta^{34}S$ values for their correlates in the form of the Crimson Creek Formation sediments at Avebury. $\delta^{34}S$ values of the Crimson Creek Formation sediments indicate a mantle $\delta^{34}S$ signature ($\delta^{34}S = 1.8 \pm 0.04$ %). This suggests that the crustal contaminant responsible for the S component of the disseminated sulphides may not have been sourced locally, but were from a different crustal S source at depth. However, this will remain purely a speculation, unless the $\delta^{34}S$ values, along with S/Se ratios for the Melba Flats sediments are established. Until then, there is no clear way of verifying the source of S component for the disseminated sulphides at Melba Flats.

Chapter 7

Synthesis & Future Work

7.1 Correlation & Age of the Melba Flats Sediments

The sediment affiliation and depositional age of the Melba Flats sediments have remained unresolved in spite of the multitude of studies that have been conducted in the past to assign the Melba Flats sediments to a specific sedimentary formation/group and constrain the depositional age of the sedimentary unit (Adabi 1997; Blissett 1962; Brown 1986). The primary controversy surrounding the sediment affiliation of the Melba Flats sediments is the ambiguous correlation of this sedimentary unit to other possible correlates in the region. In particular, the Crimson Creek Formation has been brought up repeatedly as the most likely correlate to the Melba Flats sediments (Calver *et al.* 2014; Crawford & Keays 2010). To this end, a study combining U-Pb detrital zircon geochronology, $^{40}Ar^*/^{39}Ar$ detrital muscovite geochronology and trace element geochemistry was designed to rectify this ambiguity and to establish the depositional age of the sedimentary unit at the same time.

The U-Pb detrital zircon age spectra and trace element composition of the Melba Flats sediments was compared to the hanging-wall sediments at the Avebury Ni mine that has been assigned to the Crimson Creek Formation in order to establish its sediment affiliation. Through this comparison, it was determined that the two sedimentary rock units share strong detrital zircon age spectral similarities and very similar lithophile element and REE patterns. Based on these uncanny similarities, it is proposed that the Melba Flats sediments is more likely than not, a correlate to the Crimson Creek Formation sediments at Avebury and consequently, it should be assigned to the Crimson Creek Formation. This supports the petrographic interpretation of Crawford & Keays (2010) who argued that absence of unique detritus material such as felsic lava clasts and ophiolitic chromites in the Melba Flats sediments precludes it from being assigned to a Cambrian unit; whilst the presence of devitrified mafic glass and lavas, on the other hand, establishes a strong correlation to the Crimson Creek Formation.

The U-Pb detrital zircon age data, along with the $^{40}Ar^*/^{39}Ar$ detrital muscovite age data also established a maximum depositional age of *c.* 582 Ma for the Melba Flats sediments. This age corresponds with the depositional age range of *c.* 650 Ma to *c.* 580 for the Crimson Creek Formation inferred by Adabi (1997) based on carbon isotope chemostratigraphy, lending further weight to the argument that the Melba Flats sediments is equivalent to the Crimson Creek Formation. In addition, Calver *et al.* (2014) and Moore *et al.* (2015) argued that the Crimson Creek Formation was probably deposited between *c.* 582 Ma and *c.* 575 Ma or shortly before this time. Consequently, the incontrovertible evidence provided by the corroborated petrographic, geochemical and isotopic results, strongly implies that the Melba Flats sediments is equivalent to Crimson Creek Formation stratigraphically and was most likely deposited at *c.* 582 Ma in the late Ediacaran.

7.1.1 Future Work

Little work has been down to constrain the provenance of the Melba Flats sediments in this study as the primary focus was to determine its depositional age and to correlate it to other sedimentary units. The U-Pb detrital zircon and $^{40}Ar^*/^{39}Ar$ detrical muscovite age spectra of the Melba Flats sediments have provided some clues to possible source terranes in the wider region. Specifically, the major age mode of *c.* 660 Ma that is consistent throughout all the U-Pb detrital age spectra suggests a common and dominant source terrane in which the sediments were derived; however, further in-depth analysis of the data is required to identify the provenance of this dominant source. In addition, it is suggested that future Nd isotopic work to derive Nd model ages that can be useful in the discrimination between potential source regions (O'Nions *et al.* 1983), should be considered to complement the detrital zircon and muscovite dataset in a multi-pronged sedimentary provenance analytical approach as proposed by Vermeesch & Garzanti (2015). This approach would help provide further constraints on the provenance of the Melba Flats sediments. Furthermore, potential source terranes beyond Western Tasmania should be considered. In particular, within the context of SWEAT-like reconstruction of Rodinia for Australia, Antarctica and Laurentia similar to that suggested by Cawood *et al.* (2013), Moore *et al.* (2015) and Mulder *et al.* (2015).

7.2 Petrogenesis, Age & Tectonic Setting of the Melba Flats Mafic Intrusions

Geological interest in the Melba Flats mafic intrusions largely stems from the Ni-Cu-PGE-rich sulphides that they host, their close spatial proximity to the Avebury Ni mine and their unique position within the one of the most well-endowed poly-metallic provinces in the world. Despite the growing interest, the Melba Flats mafic intrusions are considered by Corbett *et al.* (2014a) and various authors (Brown 1986; Crawford & Keays 2010; Greenhill 1995) to be mafic rocks of uncertain affinity and age. Consequently, many questions have been raised about the petrogenesis of these mafic intrusions. In particular, the magmatic affiliation, age and tectonic setting of emplacement for these mafic intrusions are of interest. To address these pertinent questions, a combination of geochemical and geochronological studies that include major and trace element geochemistry and $^{40}Ar^*/^{39}Ar$ hornblende geochronology were launched as part of the research project.

The major and trace element geochemical data utilized by the various rock classification discrimination diagrams showed that mafic rocks of the Melba Flats intrusions are sub-alkaline gabbroic rocks, whilst the various magmatic affiliation discrimination plots have determined that the magma responsible for the formation of the Melba Flats mafic intrusions are of tholeiitic affinity, with MgO content between 13 and 16 wt%. These interpretations are consistent with the only previous geochemical study on the Melba Flats mafic intrusions by Crawford & Keays (2010) who suggested that the Melba Flats mafic intrusions were formed by a sub-alkaline tholeiitic magma, with 12 to 13 wt% MgO content.

In a review of the Proterozoic geological history of Tasmania, Calver *et al.* (2014) suggested some possible stratigraphic equivalents to the Melba Flats mafic intrusions. Subsequently, when the Melba Flats mafic intrusions were compared to these possible stratigraphic equivalents, it was found that the intrusions were geochemically most similar to the Spinks Creek Volcanics and most dissimilar to mafic intrusions at Avebury. Significantly, the geochemical signature of the Avebury mafic intrusions is that of a boninitic magma, which is vastly different from the primitive magma that formed the Melba Flats mafic intrusions. This strongly suggests that the Avebury mafic intrusions are most likely a part of the suite of mafic-ultramafics that host the Avebury Ni deposit, which are similarly formed from boninitic magmas as proposed by Keays & Jowitt (2013). On the other hand, the likely stratigraphic correlation between the Melba Flats mafic intrusions and the Spinks Creek volcanic is supported by Brown (1986) and Varne & Foden (1987) who reported weakly enriched LREE and relatively flat lithophile element patterns similar to the petrogenetic indicator element patterns of the Melba Flats mafic intrusions.

The Melba Flats intrusions has not been dated previously. However, inferred emplacement ages ranging from the Cambrian to the Devonian, based on stratigraphic correlations have been suggested by numerous authors (Nye & Blake 1938; Reid 1925; Blissett 1962). More recently, Calver *et al.* (2004), Meffre *et al.* (2004) and Moore *et al.* (2015) suggested an inferred emplacement age between *c.* 575 ± 3 Ma and 582 ± 4 ma for the Melba Flats mafic intrusions based on their stratigraphic equivalents. This study has established an emplacement age of 568 ± 5 Ma through $^{40}Ar^*/^{39}Ar$ hornblende geochronology for the Melba Flats mafic intrusions, which is largely coincident to the ages suggested by the more recent studies.

Furthermore, through trace element tectonic discrimination plots, it was suggested in this study that the Melba Flats intrusions were likely to have emplaced in a tectonic setting associated with an attenuated continental margin characterized by a high degree of attenuation and some magma-crust interaction. Significantly, the newly established emplacement age and tectonic setting corroborates strongly with Direen & Crawford (2003) and Crawford & Keays (2010) who proposed that the emplacement of the Melba Flats mafic intrusions had occurred along a *c.* 600 to *c.* 570 M passive continental margin characterized by a transitional rift setting, immediately prior to the rifting of the Tasmanian Craton. Additionally, the complex geochamical signature of the Melba Flats intrusions typified by a weak enrichment in LREE and an enrichment in crustal-associated lithophile elements (Cs, Ba and Th) ties in neatly with the proposed transitional rift setting where magma-crustal interaction is prevalent (Pearce 1996). A modern analogue for the proposed emplacement tectonic setting for the Melba Flats mafic intrusions can be found in the early Paleogene break-up margin of East Greenland (Crawford & Keays 2010; Meffre *et al.* 2004).

7.2.1 Future Work

Despite establishing a probable correlation between the Melba Flats mafic intrusions and the Spinks Creek Volcanics, it is suggested that further Sm-Nd isotopic work be completed for all the possible stratigraphic equivalents of the Melba Flats intrusions in order to place further constraints on the potential genetic relationships between these rocks. Consequently, a trio of petrographic, geochemical and isotopic indicators will hopefully provide irrefutable evidence that will establish the correlation between the Melba Flats mafic intrusions and the Spinks Creek Volcanics. Furthermore, Crawford & Keays (2010) and Direen & Crawford (2003) argued that the Melba Flats mafic intrusions forms part of a fossil seaward dipping reflector sequence along a passive margin that are characterized by a gradual evolution in the magmatic affinities of Neoproterozoic mafic intrusions between Western New South Wales and Western Tasmania. It is suggested that a detailed geochemical study of the entire suite of mafic intrusives along the passive margin is carried out in order to document the gradual

changes in magmatic affinities from the furthest, or most 'landward' from the eventual break-up site to the nearest, or most 'oceanward' from the break-up margin. Consequently, it might be possible to determine at which transitional point during the rifting process did the Melba Flats mafic intrusions occur.

7.3 Origin of the Melba Flats Ni-Cu-PGE Sulphides

The strong interest in the origin of the Melba Flats Ni-Cu-PGE sulphides stems from the close proximity of the Melba Flats Ni-Cu-PGE deposit to the Avebury Ni deposit nearby. The notion of a possibility that the Ni at Avebury Ni mine was derived from a suite of mafic intrusions argued to be similar to that of the Melba Flats mafic intrusions has driven exploration and mining companies to consider the prospect that the two deposits may be co-genetic and consequently, a Ni-rich mineralized province may potentially exist in Western Tasmania. For this reason, it was suggested by Crawford & Keays (2010) that if the Melba Flats Ni-Cu-PGE sulphides were formed at depth before being transported to their current sites within the mafic intrusions, a potentially significant amount of magmatic Ni-Cu-PGE sulphides may be concealed at depth. To this end, a geochemical study that employed trace element and PGE geochemistry, along with S isotope geochemistry was initiated to investigate this hypothesis.

The geochemical study of the Melba Flats Ni-Cu-PGE sulphides revealed two primary types of magmatic Ni-Cu-PGE sulphides at Melba Flats that are co-magmatic: 1) massive-to-semi-massive sulphides that are enriched in Ni, Cu and PGE and 2) disseminated sulphides that have low Ni, Cu and PGE contents. Some of these Ni-Cu-PGE-rich sulphides can contain up to 20.0% Ni, 6.7% Cu, 3320 ppb Pd and 1970 ppb Pt. In particular, characteristic geochemical features that were identified for the massive-to-semi-massive sulphides include their formation from a S-undersaturated magma, mantle-like δ^{34}S values and S/Se ratios (δ^{34}S = +1.4 ± 0.7; S/Se = 1749 to 2873), as well as the enriched Ni-Cu content and PGE tenors, which indicate that these magmatic sulphides is most likely mantle in origin and was formed at moderate R-factors (R-factors = 500 to 1000) during sulphide segregation. On the other hand, distinctive geochemical characteristics that were identified for the disseminated sulphides include their formation from a S-saturated magma, crustal-like δ^{34}S values and S/Se ratios (δ^{34}S = +4.3 ± 0.7; S/Se > 7800), as well as the depleted Ni-Cu content and PGE tenors, which indicate that these magmatic sulphides is most likely formed at low R-factors during the interaction with S-bearing crustal rocks. Significantly, these findings are more or less consistent with the initial assessment of the Melba Flats magmatic Ni-Cu-PGE sulphides by Crawford & Keays (2010) who proposed that two forms of magmatic sulphides characterizes the Melba Flats Ni-Cu-PGE deposit.

Consequently, the bulk of the geochemical data indicate that the Ni-Cu-PGE-rich massive-to-semi-massive magmatic sulphides at Melba Flats were formed at depth before being transported to their current sites by primitive magmas of high-MgO content (13-16 wt%), with a sub-alkaline affinity. During transport, these magmatic sulphides were most likely partially resorbed by the S-undersaturated carrier magma and as a result, their Ni, Cu and PGE tenors increased and their S/Se ratios decreased. Significantly, during this transportation process, it is likely that the primitive magmas underwent further interaction with S-bearing crustal rocks, leading to the S-saturation of the host magma and eventually, the formation of the Ni-Cu-PGE-poor disseminated magmatic sulphides. The proposed potential genetic model of the Melba Flats Ni-Cu-PGE sulphides is consistent with the genetic process suggested by Crawford & Keays (2010), and therefore, it is argued that it is highly plausible that significant amounts of magmatic Ni-Cu-PGE sulphides may remain concealed at depth within the Melba Flats Ni-Cu-PGE deposit.

However, when the Melba Flats mafic intrusions were compared to the suite of mafic intrusions at Avebury, it was shown that the source magma for the Melba Flats mafic intrusions was significantly different geochemically to that of the mafic intrusions at Avebury, which are characterized by a boninitic signature typified by significantly depleted LREE and 'U'-shaped lithophile element patterns. Although the Avebury mafic intrusions were clearly not the source of Ni at Avebury, there may be mafic intrusions similar to the Melba Flats mafic intrusions at depth below the Avebury Ni deposit. If these mafic intrusions contained significant amounts of magmatic Ni sulphides comparable to the Melba Flats mafic intrusions, they may have been the source of Ni for the Avebury Ni deposit. Consequently, the potential for a Ni-rich mineralized province within Western Tasmania may yet be fulfilled.

7.3.1 Future Work

Although, there were plans during the study to establish the emplacement ages for both the Melba Flats and Avebury mafic intrusions, a geological age was only derived for the Melba Flats mafic intrusions largely due to the lack of suitable age dating minerals in the Avebury mafic intrusions. It is suggested that in the future, larger amounts of Avebury mafic intrusions are sampled, in order to establish an emplacement age for the mafic intrusions, which would completely dispel the notion that the Melba Flats and Avebury mafic intrusions share a common magma source if their emplacement age are distinctively dissimilar. Furthermore, it is proposed that there is a renewed attempt to determine the S isotope values and S/Se ratios of the Melba Flats sediments using a more sensitive and precise analytical approach as reported by Queffurus & Barnes (2015), in order to constrain the S source for the crustal contaminant that is largely responsible for the formation of the magmatic disseminated sulphides at the Melba Flats Ni-Cu-PGE deposit. Last but not least, a 3-D structural study of the Melba Flats

mafic intrusions could be established in order to map the conduit-intrusion system similar to that of Voisey's Bay described by Evans-Lamswood *et al.* (2000), which is speculated to be responsible for the distribution of magmatic sulphides observed at the Melba Flats Ni-Cu-PGE deposit. Consequently, the source magma chamber could possibly be located through this 3-D structural study and therefore, providing access to the untapped magmatic Ni-Cu-PGE sulphides resource that may remain concealed at depth.

Chapter 8

Conclusion

Through a comprehensive geochemical and geochronological investigation, this study has addressed all the research aims set out initially and provided important constraints on the petrogenesis of the Melba Flats Ni-Cu-PGE deposit.

Together, the U-Pb detrital zircon, $^{40}Ar^*/^{39}Ar$ detrital muscovite ages and trace elements geochemical evidence have shed light on the sediment affiliation of the Melba Flats sediments. Based on the newly acquired data, it is determined that the Melba Flats sediments is more likely than not, a part of the Crimson Creek Formation. In addition, the maximum depositional age of the Melba Flats sediments and, by extension, the Crimson Creek Formation, is established to be *c.* 582 Ma. The newly established depositional age provides the first direct age determined for the Crimson Creek Formation.

$^{40}Ar^*/^{39}Ar$ hornblende ages, along with major and trace elements geochemical evidences have provided important constraints for the petrogenesis of the Melba Flats mafic intrusions. Based on major and trace elements geochemical evidence, it was determined that the Melba Flats mafic intrusions were formed from a primitive sub-alkaline magma source of tholeiitic affinity. Trace elements geochemical evidence, along with the $^{40}Ar^*/^{39}Ar$ hornblende ages established that the emplacement of the Melba Flats mafic intrusions had taken place along an attenuated continental margin characterized by a transitional rift setting at *c.* 568 Ma.

Platinum group elements geochemical evidence and S isotopic values have determined that two forms of magmatic Ni-Cu-PGE sulphides exist at the Melba Flats Ni-Cu-PGE deposit: 1) Ni-Cu-PGE-rich massive-to-semi-massive sulphides of mantle origin and 2) Ni-Cu-PGE-poor disseminated sulphides of crustal origin. Based on the acquired data, the magmatic Ni-Cu-PGE sulphides is suggested to have been derived from depth with a mantle origin, but later acquired a crustal signature due to the interaction between the primitive magma and the S-bearing crustal rocks during transport to its current sites.

In summary, this study has not only addressed some of the controversies that surround the host sedimentary rocks, the mafic intrusions and their associated magmatic Ni-Cu-PGE sulphides, but has also shown that there is considerable potential for significant Ni-Cu-PGE mineralization at depth within the Melba Flats Ni-Cu-PGE deposit, and quite possibly the wider Dundas region.

Appendix A

Petrographic Descriptions

A.1 Representative Melba Flats Sediments

General Description - MF40 - 56.3 m

Melba Flats sediment sample from drill hole MF40 at a depth of 56.3 m is described as a fine-to-medium grain volcaniclastic lithic greywacke, with detrital clasts commonly dominated by sub-rounded to angular quartz grains that are often polycrystalline and strained metamorphic quartz, occasional plagioclase grains, detrital muscovite flakes and chloritised glass clasts. Common volcaniclastic clasts are dominated by devitrified basaltic glass, and less commonly crystalline basaltic lava. Occasionally, there is occurrence of interstitial diagenetic pyrite and some pyrite lining chlorite veins. Common interstitial chlorite occurs as pervasive chloritic alteration within the rock.

FIGURE A.1: *Photomicrographs of representative Melba Flats sediments sample - MF40 - 56.3 m. (**a**) greywacke under plane polarized light (PPL) and (**b**) greywacke under cross polarized light. Note that: Ms - Muscovite, Pl - Plagioclase, Py - Pyrite and Qtz - Quartz.*

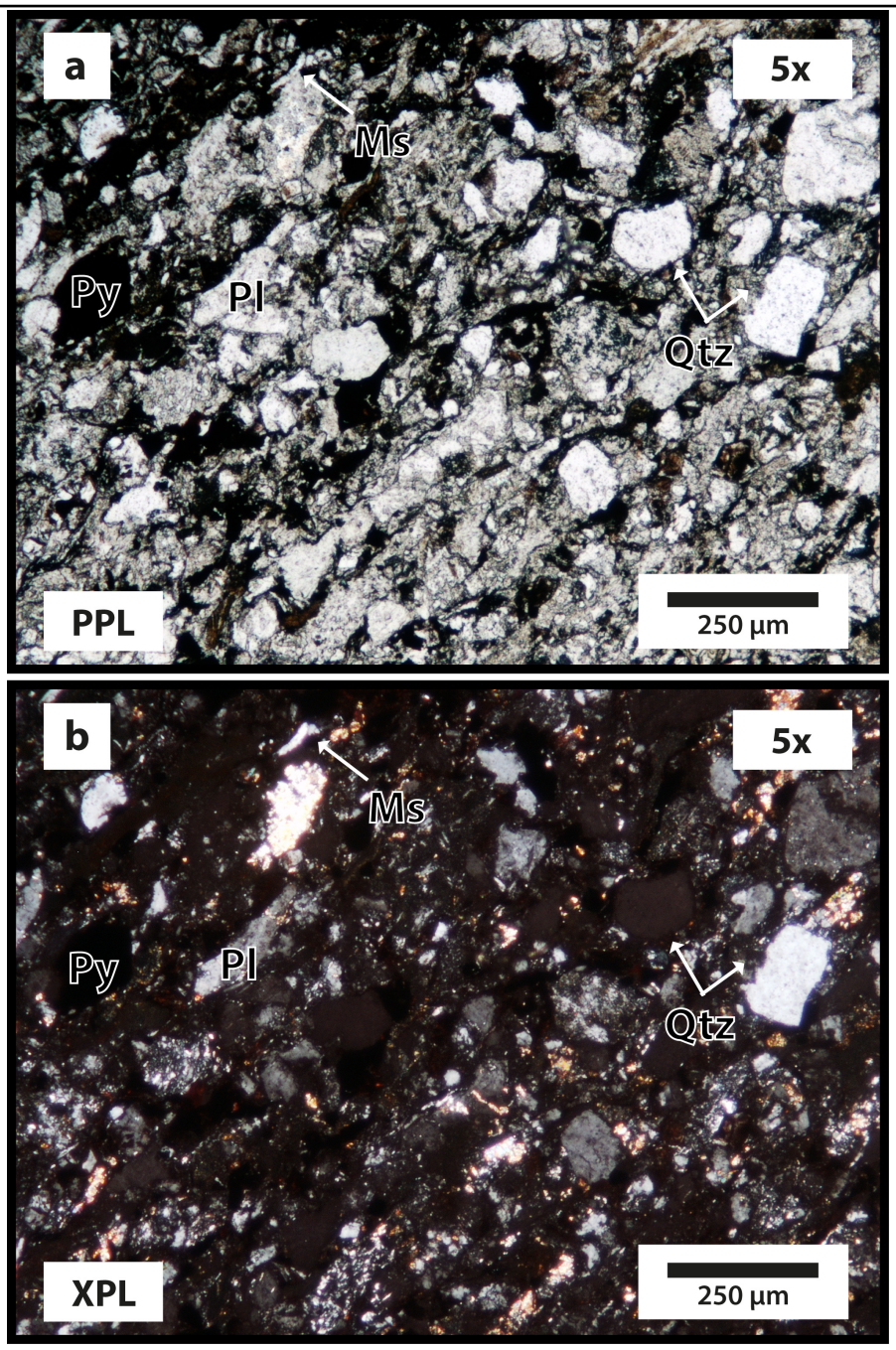

A.2 Representative Melba Flats Mafic Intrusions

General Description - MF93 - 332.0 m

Melba Flats mafic intrusion sample from drill hole MF93 at a depth of 332.0 m is described as a medium-to-coarse grain ophitic gabbro, with commonly large clinopyroxene grains throughout. Late-stage magmatic brown/khaki hornblende commonly rims clinopyroxenes and occurs within interstitial area. Occasionally, there is occurrence of sulphides along grain boundaries and late-stage calcite veinlets. Common interstitial chlorite occurs as pervasive chloritic alteration within the rock.

General Description - MF93 - 365.4 m

Melba Flats mafic intrusion sample from drill hole MF93 at the depth of 365.4 m is described as medium-to-coarse gabbro, with commonly large and fresh clinopyroxene grains throughout. Some late-stage magmatic brown hornblende commonly rims or replaces clinopyroxenes. Occasionally, there is occurrence of sulphides along grain boundaries. Common interstitial chlorite and actinolite occur as pervasive chloritic-actinolite alteration within the rock.

General Description - MF103 - 101.4 m

Melba Flats mafic intrusion sample from drill hole MF103 - 101.4 at a depth of 101.4 m is described as a medium grain gabbro, with commonly small-to-medium clinopyroxene grains throughout. Late-stage magmatic brown/khaki hornblende commonly rims or completely replaces clinopyroxenes. Laths of actinolite grains also commonly occur throughout the rock. Occasionally, there is occurrence of sulphides along grain boundaries. Common interstitial chlorite occur as pervasive chloritic alteration within the rock.

FIGURE A.2: *Photomicrographs of representative Melba Flats mafic intrusion sample - MF93 - 332.0 m. (**a**) gabbro under plane polarized light (PPL) and (**b**) gabbro under cross polarized light. Note that: Cal - Calcite, Chl - Chlorite, Cpx - Clinopyroxene and Hbl - Hornblende.*

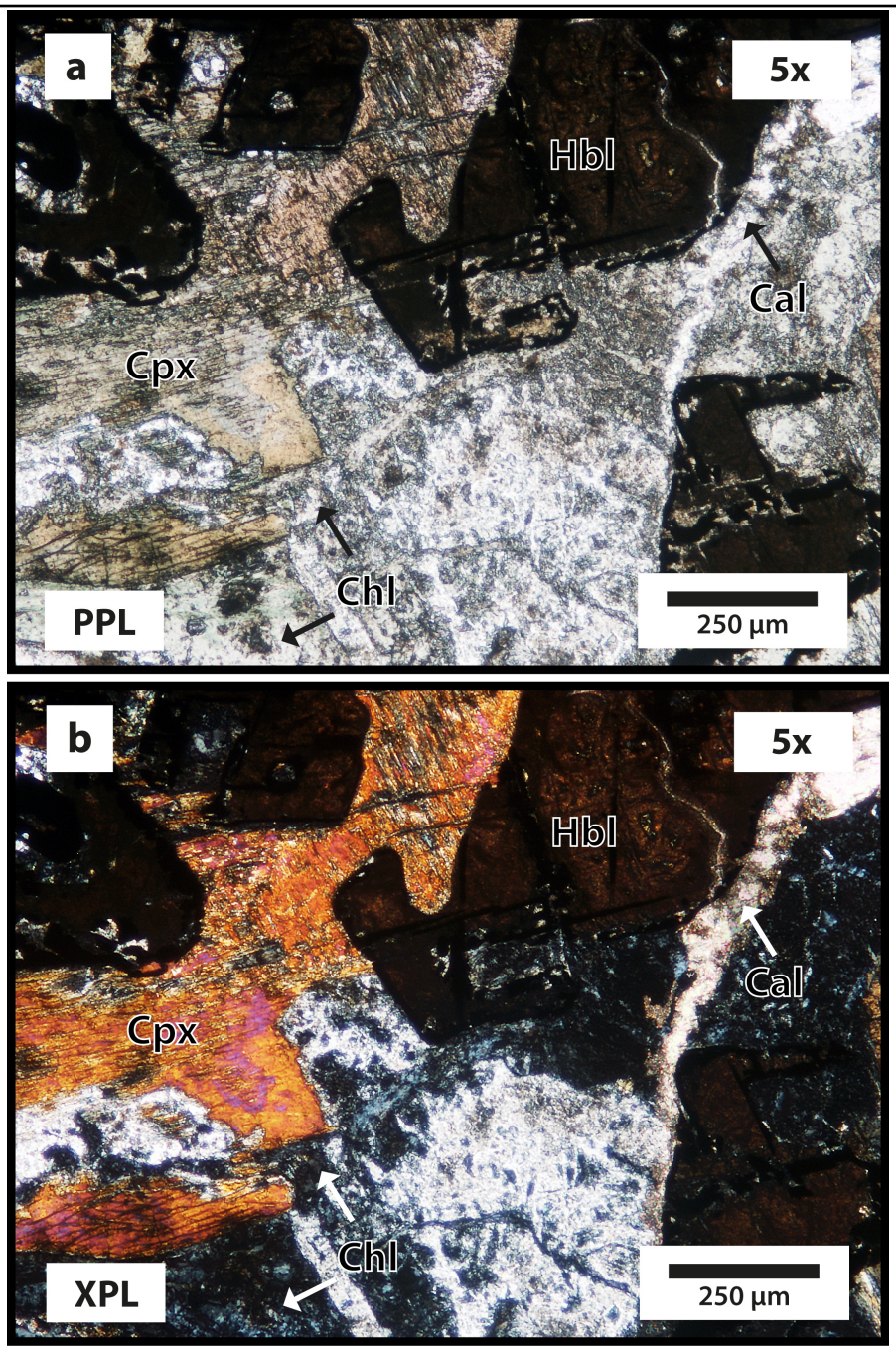

FIGURE A.3: *Photomicrographs of representative Melba Flats mafic intrusion sample - MF93 - 365.4 m. (**a**) gabbro under plane polarized light (PPL) and (**b**) gabbro under cross polarized light. Note that: Act - Actinolite, Cpx - Clinopyroxene and Hbl - Hornblende.*

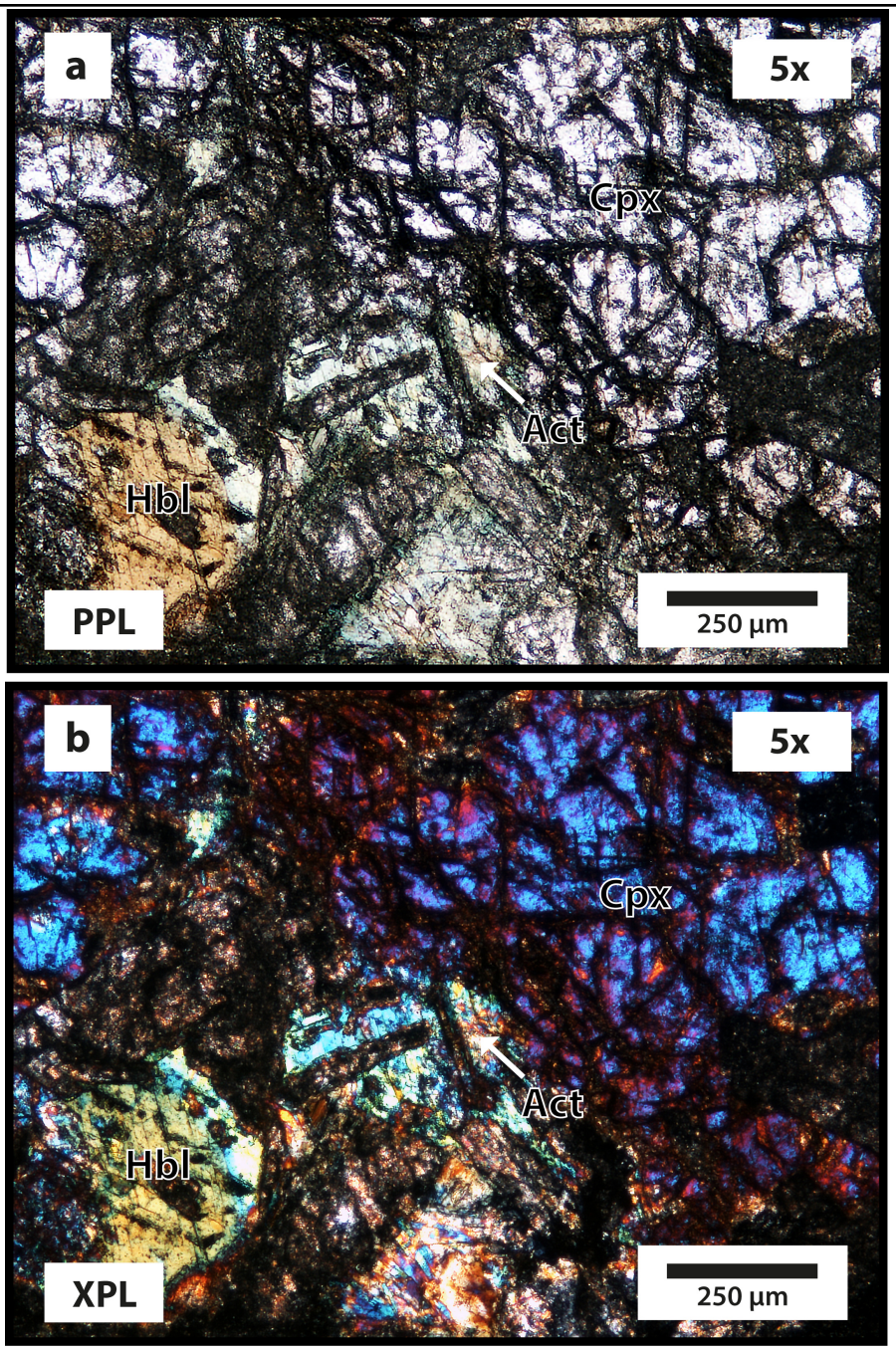

FIGURE A.4: *Photomicrographs of representative Melba Flats mafic intrusion sample - MF103 - 101.4 m. (**a**) gabbro under plane polarized light (PPL) and (**b**) gabbro under cross polarized light. Note that: Act - Actinolite, Chl - Chlorite, Cpx - Clinopyroxene and Hbl - Hornblende.*

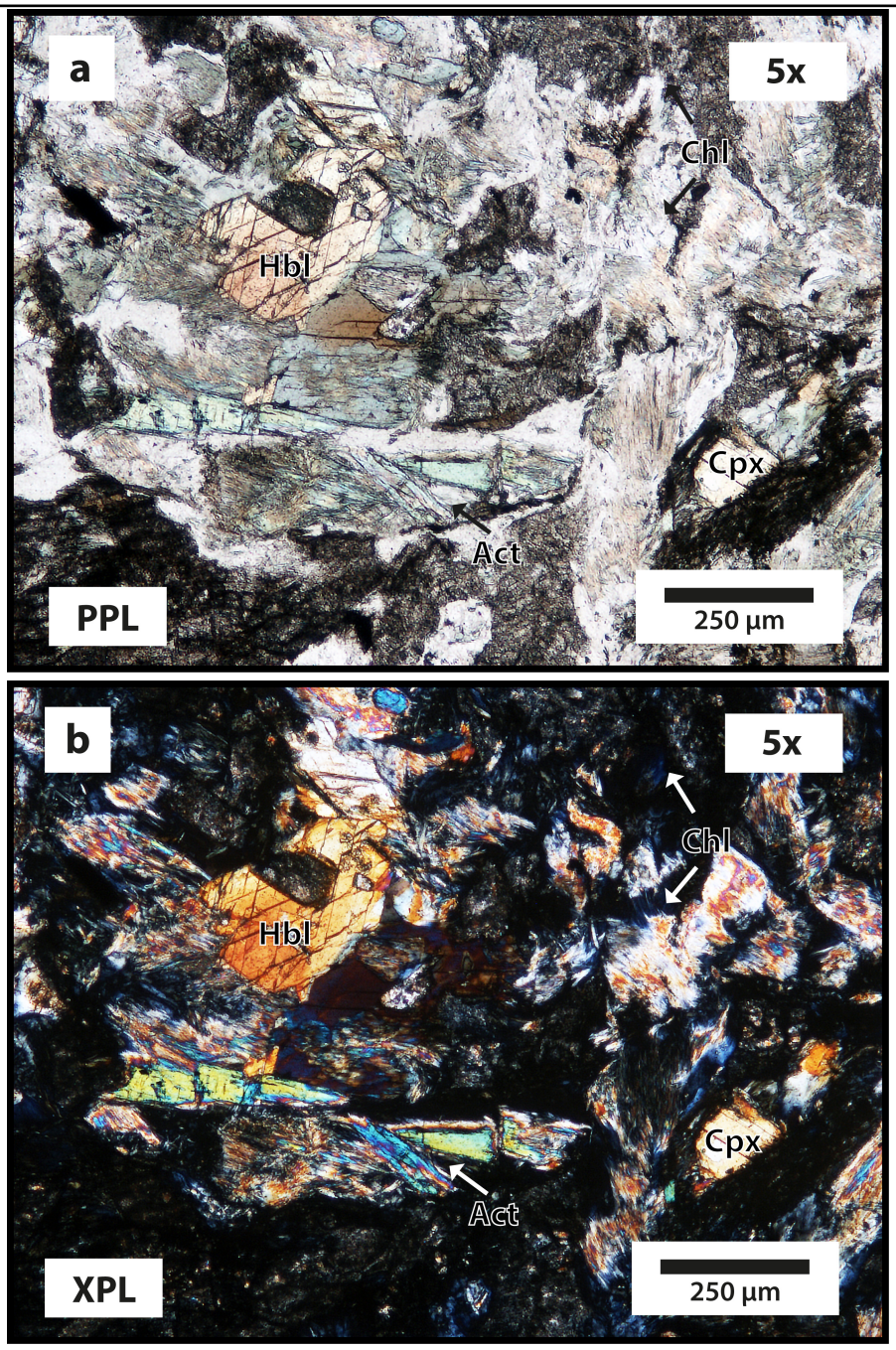

Appendix B

Dating Methods

B.1 The U-Pb Dating Method

U-Pb dating method is one of the oldest and most important isotopic dating methods, capable of highly precise and accurate measurements across geological timescales from the Hadean (~4.6 Ga) into the Quaternary. Remarkably prevalent in current geochronology research, the popularity and prolificacy of the U-Pb dating method is attributed to the abundance of suitable U-rich minerals in most terrestrial and extraterrestrial rocks, along with the well-established and continually refined analytical procedures and instrumentation since the first application of the method in the early twentieth century (Faure & Mensing 2005c; Schoene 2014).

The capability of U-Pb geochronology is drawn from the decay of multiple U and Th isotopes to different stable Pb isotopes. U has two dominant radioactive isotopes, ^{238}U (99.27%) and ^{235}U (0.72%), whilst Th exists primarily as ^{232}Th (100%). These principle isotopes each follow a separate sequence of alpha (α^-) and beta (β^-) decays involving numerous short-lived intermediate daughters, which leads to the formation of a series of radiogenic stable Pb isotopes that includes ^{206}Pb, ^{207}Pb and ^{208}Pb (Fig. B.1; Faure & Mensing (2005c); Schoene (2014)). The decay of ^{238}U → ^{206}Pb, ^{235}U → ^{207}Pb and ^{232}Th → ^{208}Pb by emission of α^- and β^- particles can be summarized by the following equations:

$$^{238}_{92}\mathrm{U} \rightarrow {}^{206}_{82}\mathrm{Pb} + 8\,^{4}_{2}\mathrm{He} + 6\beta^- + Q_1 \tag{B.1}$$

$$^{235}_{92}\mathrm{U} \rightarrow {}^{207}_{82}\mathrm{Pb} + 7\,^{4}_{2}\mathrm{He} + 4\beta^- + Q_2 \tag{B.2}$$

$$^{232}_{90}\mathrm{Th} \rightarrow {}^{208}_{82}\mathrm{Pb} + 6\,^{4}_{2}\mathrm{He} + 4\beta^- + Q_3 \tag{B.3}$$

where Q_1, Q_2 and Q_3 represents the total decay energies for each decay chain (Faure & Mensing 2005c). Significantly, since the decay chains are independent of each other, three

unique U-Pb ages can be calculated through the derivation of three separate isochron equations. These isochron equations are normalized to ^{204}Pb, the only non-radiogenic isotope of Pb, and written in terms of the atomic ^{206}Pb/^{204}Pb, ^{207}Pb/^{204}Pb and ^{208}Pb/^{204}Pb:

$$\frac{^{206}Pb}{^{204}Pb} = \left(\frac{^{206}Pb}{^{204}Pb}\right)_i + \frac{^{238}U}{^{204}Pb}(e^{\lambda_1 t} - 1) \tag{B.4}$$

$$\frac{^{207}Pb}{^{204}Pb} = \left(\frac{^{207}Pb}{^{204}Pb}\right)_i + \frac{^{235}U}{^{204}Pb}(e^{\lambda_2 t} - 1) \tag{B.5}$$

$$\frac{^{208}Pb}{^{204}Pb} = \left(\frac{^{208}Pb}{^{204}Pb}\right)_i + \frac{^{232}Th}{^{204}Pb}(e^{\lambda_3 t} - 1) \tag{B.6}$$

where the subscript i represents the initial isotopic ratio of Pb when the system closed, t refers to the time since the system closed and λ_1, λ_2 and λ_3 are decay constants of ^{238}U, ^{235}U and ^{232}Th respectively. Importantly, in mineral systems such as zircon and monazite where the initial Pb component is negligible compared to its radiogenic component, equations B.4-B.6 can be simplified to:

$$\left(\frac{^{206}Pb}{^{238}U}\right)^* = (e^{\lambda_1 t} - 1) \tag{B.7}$$

$$\left(\frac{^{207}Pb}{^{235}U}\right)^* = (e^{\lambda_2 t} - 1) \tag{B.8}$$

$$\left(\frac{^{208}Pb}{^{232}U}\right)^* = (e^{\lambda_3 t} - 1) \tag{B.9}$$

where * refers to the ratio of radiogenic ^{206}Pb/^{238}U, ^{207}Pb/^{235}U, and ^{208}Pb/^{232}Th and λ_1, λ_2 and λ_3 are decay constants of ^{238}U, ^{235}U and ^{232}Th respectively. Additionally, a fourth isochron equation can be constructed by dividing equation B.5 by equation B.4:

$$\frac{\left(\frac{^{207}Pb}{^{204}Pb}\right) - \left(\frac{^{207}Pb}{^{204}Pb}\right)_i}{\left(\frac{^{206}Pb}{^{204}Pb}\right) - \left(\frac{^{206}Pb}{^{204}Pb}\right)_i} = \left(\frac{^{235}U}{^{238}U}\right) \frac{(e^{\lambda_2 t} - 1)}{(e^{\lambda_1 t} - 1)} = \left(\frac{^{207}Pb}{^{206}Pb}\right)^* \tag{B.10}$$

where * refers to the ratio of radiogenic ^{207}Pb/^{206}Pb. This equation is especially useful as the present-day ^{235}U/^{238}U is assumed to be a known constant in terrestrial and meteoritic systems eliminating the need to measure U. The concentration of Pb can also be ignored. Equation B.10 can be used to calculate an age by linear fitting in ^{206}Pb/^{204}Pb-^{207}Pb/^{204}Pb space, or if initial Pb is negligible, then the measured (^{207}Pb/^{206}Pb)* can be used to directly calculate a date.

FIGURE B.1: *U-Th-Pb decay chains.*

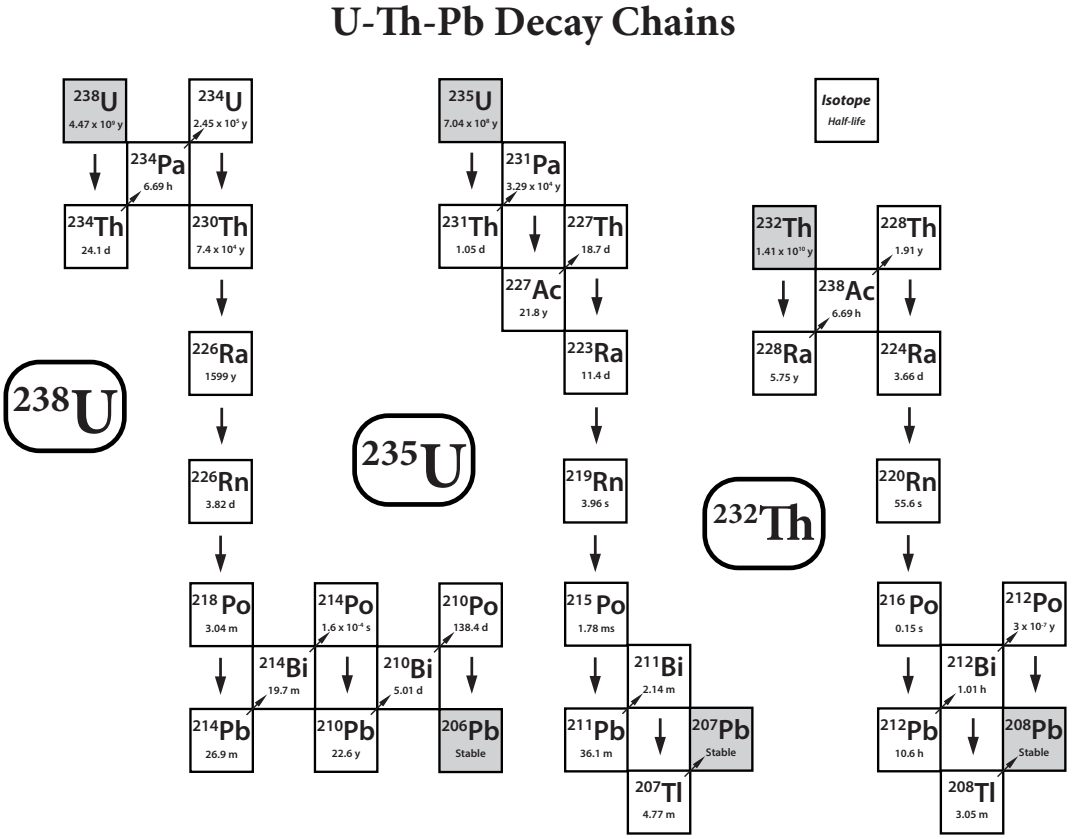

B.2 The $^{40}Ar^*/^{39}Ar$ Dating Method

The $^{40}Ar^*/^{39}Ar$ dating method, first described by Merrihue & Turner (1966), has its foundation in the K/Ar isotopic dating method that was developed based on the decay of the radioactive parent isotope ^{40}K to its daughter product $^{40}Ar^*$ more than half a century ago (Faure & Mensing 2005b; McDougall & Harrison 1999). Unlike the K/Ar method, geochronology by the $^{40}Ar^*/^{39}Ar$ method involves the neutron irradiation of samples in a nuclear reactor to produce ^{39}Ar through the following reaction with ^{39}K (Faure & Mensing 2005a):

$$^{39}_{19}\mathrm{K} \quad (\mathrm{n,p}) \quad ^{39}_{18}\mathrm{Ar} \tag{B.11}$$

where (n,p) is a nuclear reaction that occurs when a proton in the nucleus of an atom is replaced by a neutron (McDougall & Harrison 1999). This reaction allows the ^{39}Ar produced from the neutron bombardment to serve as a direct proxy to the original parent isotope ^{40}K as $^{39}Ar_K$ is dependent on the amount of ^{39}K in the sample and the $^{40}K/^{39}K$ ratio is invariant in nature. Significantly, this allows for the determination of the isotopic ratio of daughter ($^{40}Ar^*$) to parent (^{40}K) to be measured in a single $^{40}Ar/^{39}Ar$ analysis, in stark contrast to the K-Ar method. Consequently, the $^{40}Ar^*/^{39}Ar_K$ ratio is proportional to the $^{40}Ar^*/^{39}K$ in the sample, and therefore is proportional to the age (Faure & Mensing 2005a; McDougall & Harrison 1999). The amount of $^{39}Ar_K$ produced during neutron irradiation is dependant on the length of irradiation and other neutron flux parameters such as neutron flux density and neutron capture cross section. Rather than having to account for all neutron flux parameters, a standard sample of known age is irradiated together with an unknown, and the age of the unknown is derived by comparison with the $^{40}Ar^*/^{39}Ar_K$ of the fluence monitor standard (Faure & Mensing 2005a; McDougall & Harrison 1999). These neutron flux parameters can be represented with the neutron flux constant J as defined by the following equation:

$$J = \frac{e^{\lambda t}}{^{40}Ar*/^{39}Ar_K} \tag{B.12}$$

where t is the known age of the fluence monitor standard, λ is the known decay constant of ^{40}K and the $^{40}Ar^*/^{39}Ar_K$ is the measured value of this ratio in the monitor. Upon correction for mass discrimination, isotopes interference reactions, system blanks and atmospheric argon, the neutron flux constant J can be calculated in order to determine the $^{40}Ar^*/^{39}Ar$ age of the unknown sample through the following equation:

$$t = \frac{1}{\lambda} \ln\left(\frac{^{40}Ar*}{^{39}Ar_K} J + 1\right) \tag{B.13}$$

where t is the age of the unknown sample, λ is the known decay constant of ^{40}K, J is the neutron flux constant, ^{40}Ar* is the ^{40}Ar produced by *in situ* decay of ^{40}K and ^{39}Ar is the ^{39}Ar produced by neutron activation of ^{39}K.

B.2.1 Minerals used for ^{40}Ar*/^{39}Ar Dating

Some of the commonly used minerals for ^{40}Ar*/^{39}Ar dating include k-feldspar, biotite, muscovite and hornblende (Dalrymple & Lanphere 1969) as they generally exhibit good retention properties for radiogenic ^{40}Ar* that is fundamental to the application of the ^{40}Ar*/^{39}Ar technique (McDougall & Harrison 1999). Consequently, ^{40}Ar*/^{39}Ar dating of these minerals have been employed in a wide range of geological applications that include the dating of igneous and metamorphic rocks, as well as detrital studies in relation to the provenance, depositional age and cooling history of sedimentary sequences (Hodges *et al.* 2005; Kelley 2002).

White mica (or muscovite), $K_2Al_4Si_6Al_2O_{20}(OH,F)_4$, is a detrital mineral commonly associated with low grade, regionally metamorphosed sediments. It is widely utilized for detrital ^{40}Ar*/^{39}Ar studies due its low tendency to incorporate excess radiogenic ^{40}Ar* and its relatively high closure temperature (T_c; Dodson (1973)) of ~425°C at cooling rates of 10°C/Ma (Harrison *et al.* 2009; McDougall & Harrison 1999). Therefore, muscovite appears to be the most suitable mineral for the application of ^{40}Ar*/^{39}Ar geochronology in order to help establish the cooling history and constrain the minimum depositional age of the sedimentary sequence of interest in the study.

Hornblende is a commonly occurring mineral in a wide range of igneous and metamorphic rocks and it has a general formula of $(Ca,Na,K)_{2\text{-}3}(Mg,Fe,Al)_5(Si_7AlO_{22})(OH)_2$. It is extensively used for ^{40}Ar*/^{39}Ar dating of magmatic and metamorphic rocks due to its excellent radiogenic ^{40}Ar* retention properties; its minimal atmospheric argon content; and its relatively high closure temperature (T_c) of ~500°C at cooling rates of 10°C/Ma (Harrison 1981; Villa *et al.* 1996). Therefore, hornblende appears to be the most suitable mineral for the application of ^{40}Ar*/^{39}Ar geochronology in order to help establish the magmatic history and constrain the intrusive age of the gabbroic intrusions of interest in the study.

Appendix C

Whole Rock Geochemical Data

C.1 Major Elements Geochemical Data

C.1.1 Melba Flats Mafic Intrusions

TABLE C.1: *Major elements geochemical data for the Melba Flats Mafic Intrusions.*

		Unmineralized Major Elements (wt %)											
		Lab	**Al_2O_3**	**CaO**	**Cr_2O_3**	**FeO_T**	**K_2O**	**MgO**	**MnO**	**Na_2O**	**P_2O_5**	**SiO_2**	**TiO_2**
MF17 Sill 1	**MF17-69.6**	*BV*	16.01	6.46	0.09	11.97	0.18	14.32	0.19	2.39	0.08	47.45	0.83
	MF17-70.8	*BV*	15.87	4.47	0.10	12.47	0.15	15.43	0.18	2.01	0.08	48.38	0.85
	MF17-71.7	*BV*	16.30	4.25	0.09	12.56	0.23	15.19	0.18	2.10	0.09	48.13	0.88
	MF17-72.9	*BV*	16.81	4.83	0.09	12.40	0.35	15.35	0.18	2.15	0.09	46.81	0.95
		Mean	*16.25*	*5.00*	*0.09*	*12.35*	*0.23*	*15.07*	*0.18*	*2.16*	*0.08*	*47.69*	*0.88*
		S.D.	*0.41*	*1.00*	*0.01*	*0.26*	*0.09*	*0.51*	*0.01*	*0.16*	*0.00*	*0.71*	*0.05*
MF23 Sill 1	**MF23-48.35**	*ACME*	16.87	4.51	0.06	12.21	1.23	13.41	0.26	1.65	0.04	48.83	0.93
	MF23-49.52	*ACME*	17.60	6.02	0.04	10.28	1.61	10.69	0.22	2.52	0.07	49.92	1.04
		Mean	*17.23*	*5.26*	*0.05*	*11.24*	*1.42*	*12.05*	*0.24*	*2.09*	*0.06*	*49.37*	*0.98*
		S.D.	*0.51*	*1.07*	*0.01*	*1.37*	*0.27*	*1.93*	*0.02*	*0.61*	*0.02*	*0.77*	*0.08*
MF81A Sill 1	**MF81A-163.5**	*GEO*	15.73	7.57	0.08	10.96	0.74	12.12	0.26	2.85	0.07	48.75	0.86
	MF81A-164.2	*GEO*	16.22	5.69	0.09	11.92	0.52	12.61	0.24	3.29	0.08	48.38	0.96
	MF81A-167.45	*GEO*	15.86	6.74	0.05	10.71	0.67	10.11	0.21	3.45	0.12	50.83	1.24
	MF81A-169.2	*ACME*	17.30	5.15	0.08	10.93	0.69	13.15	0.19	3.13	0.07	48.35	0.96
	MF81A-170.9	*GEO*	15.36	8.77	0.16	11.64	0.19	15.53	0.26	1.75	0.07	45.48	0.79
		Mean	*16.09*	*6.79*	*0.09*	*11.23*	*0.56*	*12.70*	*0.23*	*2.90*	*0.08*	*48.36*	*0.96*
		S.D.	*0.74*	*1.45*	*0.04*	*0.52*	*0.22*	*1.95*	*0.03*	*0.68*	*0.02*	*1.91*	*0.17*
MF83 Sill 1	**MF83-143.2**	*BV*	15.69	5.24	0.09	13.01	0.64	14.57	0.18	2.24	0.08	47.42	0.84
	MF83-143.7	*ACME*	15.57	5.83	0.08	12.07	0.70	14.33	0.19	2.40	0.07	47.89	0.87
	MF83-145.2	*ACME*	16.46	3.98	0.08	12.00	1.17	13.61	0.17	1.79	0.06	49.76	0.93
		Mean	*15.91*	*5.02*	*0.08*	*12.36*	*0.84*	*14.17*	*0.18*	*2.14*	*0.07*	*48.36*	*0.88*
		S.D.	*0.48*	*0.95*	*0.01*	*0.56*	*0.29*	*0.50*	*0.01*	*0.32*	*0.01*	*1.24*	*0.04*
MF93 Sill 1	**MF93-128.55**	*GEO*	16.88	5.44	0.08	11.56	1.18	13.03	0.25	2.77	0.07	47.82	0.92
MF93 Sill 2	**MF93-159.0**	*GEO*	15.94	4.47	0.10	12.34	1.04	13.70	0.28	2.21	0.08	48.97	0.88
MF93 Sill 3	**MF93-306.1**	*GEO*	14.34	7.65	0.16	11.54	0.83	17.64	0.22	1.24	0.04	45.71	0.62
	MF93-310.55	*GEO*	15.68	7.40	0.10	12.14	2.42	12.75	0.23	1.80	0.08	46.51	0.89
	MF93-311.85	*BV*	15.94	5.97	0.09	12.68	3.07	13.12	0.22	1.06	0.08	46.87	0.90
		Mean	*15.32*	*7.01*	*0.12*	*12.12*	*2.11*	*14.50*	*0.22*	*1.37*	*0.07*	*46.37*	*0.80*
		S.D.	*0.86*	*0.90*	*0.04*	*0.57*	*1.15*	*2.73*	*0.01*	*0.39*	*0.02*	*0.59*	*0.16*
MF93 Sill 4	**MF93-323.3**	*GEO*	15.43	7.66	0.05	15.32	0.61	7.86	0.25	3.30	0.07	48.42	1.02
	MF93-330.55	*GEO*	13.04	8.35	0.00	18.61	1.37	6.95	0.30	2.10	0.09	47.81	1.36
	MF93-345.4	*GEO*	14.67	12.55	0.03	9.50	0.45	9.10	0.21	2.72	0.05	50.03	0.70
	MF93-356.0	*GEO*	12.69	12.69	0.07	9.97	1.03	11.59	0.25	1.69	0.05	49.25	0.73
	MF93-356.3	*ACME*	14.33	11.30	0.01	9.34	1.82	10.57	0.21	1.82	0.01	50.01	0.59
	MF93-365.2	*GEO*	17.45	9.58	0.08	9.02	1.38	13.15	0.21	1.55	0.03	47.08	0.46
	MF93-368.86	*GEO*	17.35	4.89	0.08	11.88	0.04	26.53	0.29	0.16	0.03	38.31	0.44
	MF93-376.5	*ACME*	9.86	3.40	0.28	13.47	0.05	27.25	0.22	0.11	0.02	44.90	0.44
	MF93-380.1	*ACME*	9.72	4.01	0.35	13.06	0.04	24.90	0.17	0.11	0.02	47.19	0.41
	MF93-381.3	*GEO*	10.39	5.73	0.65	11.95	0.02	26.15	0.18	0.13	0.03	44.38	0.40
		Mean	*13.49*	*8.02*	*0.16*	*12.21*	*0.68*	*16.40*	*0.23*	*1.37*	*0.04*	*46.74*	*0.65*
		S.D.	*2.87*	*3.47*	*0.21*	*3.05*	*0.67*	*8.63*	*0.04*	*1.18*	*0.03*	*3.53*	*0.32*

TABLE C.1 (continued): Major elements geochemical data for the Melba Flats Mafic Intrusions.

		Unmineralized Major Elements (wt %)											
		Lab	**Al_2O_3**	**CaO**	**Cr_2O_3**	**FeO_T**	**K_2O**	**MgO**	**MnO**	**Na_2O**	**P_2O_5**	**SiO_2**	**TiO_2**
MF95 Sill 1	**MF95-121.8**	*GEO*	18.07	3.99	0.09	13.56	3.45	13.93	0.48	0.28	0.09	44.99	1.06
	MF95-126.4	*GEO*	15.22	5.16	0.13	13.72	1.30	15.72	0.37	1.01	0.08	46.44	0.86
	MF95-127.7	*GEO*	15.90	6.43	0.11	12.13	1.65	13.78	0.36	1.28	0.08	47.36	0.92
		Mean	*16.40*	*5.19*	*0.11*	*13.14*	*2.13*	*14.48*	*0.40*	*0.86*	*0.08*	*46.27*	*0.94*
		S.D.	*1.49*	*1.22*	*0.02*	*0.87*	*1.16*	*1.08*	*0.06*	*0.51*	*0.01*	*1.20*	*0.10*
MF95 Sill 2	**MF95-212.15**	*BV*	16.17	7.20	0.08	12.11	1.09	12.33	0.35	2.25	0.08	47.42	0.92
	MF95-216.3	*BV*	18.75	4.60	0.05	10.02	2.12	10.95	0.31	3.08	0.10	49.17	0.84
	MF95-218.5	*BV*	17.41	3.61	0.08	12.22	1.63	13.80	0.23	2.24	0.09	47.74	0.94
	MF95-222.45	*BV*	12.52	6.83	0.23	12.65	0.13	22.84	0.22	0.38	0.06	43.58	0.56
	MF95-234.8	*BV*	15.36	7.03	0.09	11.69	0.84	13.75	0.19	2.65	0.08	47.43	0.87
		Mean	*16.04*	*5.86*	*0.11*	*11.74*	*1.16*	*14.73*	*0.26*	*2.12*	*0.08*	*47.07*	*0.83*
		S.D.	*2.35*	*1.64*	*0.07*	*1.02*	*0.76*	*4.68*	*0.07*	*1.03*	*0.02*	*2.08*	*0.15*
MF97 Sill 1	**MF97-209.2**	*BV*	10.68	7.04	0.21	15.23	0.03	21.68	0.22	0.13	0.07	43.93	0.78
	MF97-215.9	*BV*	16.29	5.10	0.11	12.22	0.93	14.60	0.25	2.59	0.08	46.94	0.89
		Mean	*13.49*	*6.07*	*0.16*	*13.73*	*0.48*	*18.14*	*0.23*	*1.36*	*0.08*	*45.43*	*0.84*
		S.D.	*3.97*	*1.37*	*0.07*	*2.13*	*0.63*	*5.01*	*0.02*	*1.74*	*0.01*	*2.12*	*0.08*
MF103 Sill 1	**MF103-101.4**	*BV*	15.31	6.52	0.14	11.25	0.91	17.89	0.22	1.57	0.07	45.51	0.61
	MF103-105.35	*BV*	14.22	8.91	0.15	12.12	0.08	17.88	0.22	0.95	0.06	44.73	0.69
	MF103-111.2	*BV*	14.66	8.18	0.12	11.84	0.22	16.37	0.19	1.73	0.07	45.86	0.75
	MF103-115.3	*BV*	15.11	9.36	0.09	11.20	0.30	14.05	0.20	2.29	0.08	46.47	0.84
	MF103-119.9	*BV*	15.13	8.40	0.09	11.60	0.26	14.17	0.21	2.30	0.08	46.87	0.86
	MF103-124	*BV*	15.22	8.96	0.09	11.69	0.49	13.95	0.21	2.25	0.08	46.16	0.89
	MF103-129.05	*BV*	14.92	9.20	0.10	11.68	0.50	14.49	0.23	2.07	0.08	45.90	0.84
	MF103-133.3	*BV*	14.93	7.66	0.12	11.88	0.44	15.47	0.24	2.04	0.08	46.34	0.79
	MF103-137.5	*BV*	14.55	7.45	0.14	12.01	0.75	17.17	0.20	1.50	0.06	45.46	0.72
	MF103-141.7	*BV*	14.62	7.79	0.11	12.04	0.91	16.41	0.22	1.25	0.07	45.81	0.75
	MF103-143.65	*BV*	16.56	6.19	0.12	10.54	0.89	17.69	0.20	1.71	0.05	45.45	0.59
		Mean	*15.02*	*8.06*	*0.12*	*11.62*	*0.52*	*15.96*	*0.21*	*1.79*	*0.07*	*45.87*	*0.76*
		S.D.	*0.61*	*1.06*	*0.02*	*0.47*	*0.30*	*1.60*	*0.01*	*0.45*	*0.01*	*0.59*	*0.10*

TABLE C.1 (continued): Major elements geochemical data for the Melba Flats Mafic Intrusions.

		Mineralized Major Elements (wt %)											
		Lab	Al_2O_3	CaO	Cr_2O_3	FeO_T	K_2O	MgO	MnO	Na_2O	P_2O_5	SiO_2	TiO_2
MF19 Sill 1	MF19-34.25	*BV*	17.78	16.60	0.11	9.13	4.86	8.20	0.43	1.11	0.09	40.73	0.95
	MF19-39.5	*ACME*	0.16	7.02	0.01	89.33	0.02	1.52	0.50	0.02	0.04	1.32	0.06
	MF19-41.32	*ACME*	0.09	6.06	0.01	91.71	0.01	1.21	0.32	0.01	0.04	0.53	0.01
		Mean	*6.01*	*9.89*	*0.04*	*63.39*	*1.63*	*3.64*	*0.42*	*0.38*	*0.06*	*14.19*	*0.34*
		S.D.	*10.20*	*5.83*	*0.06*	*47.01*	*2.80*	*3.95*	*0.09*	*0.63*	*0.03*	*22.98*	*0.53*
MF23 Sill 2	MF23-64.8	*ACME*	16.50	3.17	0.09	32.07	0.01	12.33	0.25	0.02	0.04	34.62	0.92
	MF23-65.3	*ACME*	0.20	4.39	0.00	86.54	0.01	2.62	0.51	0.01	0.04	5.68	0.01
	MF23-65.5	*ACME*	1.44	6.78	0.01	62.78	0.01	3.41	0.53	0.01	0.05	24.94	0.05
	MF23-65.6	*ACME*	15.87	7.82	0.09	25.00	0.01	12.46	0.30	0.03	0.06	37.48	0.89
	MF23-74.5	*ACME*	15.17	0.70	0.08	32.61	0.05	8.61	0.19	0.02	0.03	41.70	0.85
	MF23-74.6	*ACME*	0.41	9.65	0.01	86.94	0.01	0.52	0.50	0.01	0.05	1.88	0.02
	MF23-75	*ACME*	16.43	3.70	0.12	30.09	0.02	10.61	0.27	0.02	0.05	37.80	0.88
		Mean	*9.43*	*5.17*	*0.06*	*50.86*	*0.02*	*7.22*	*0.36*	*0.02*	*0.04*	*26.30*	*0.52*
		S.D.	*8.21*	*3.07*	*0.05*	*27.39*	*0.01*	*4.96*	*0.15*	*0.01*	*0.01*	*16.26*	*0.46*
MF81A Sill 1	MF81A-171.5	*ACME*	14.68	7.00	0.13	13.67	0.08	14.74	0.23	1.61	0.05	46.97	0.86
	MF81A-174.44	*ACME*	0.12	0.06	0.01	95.26	0.01	0.12	0.14	0.01	0.01	4.23	0.04
	MF81A-174.52	*ACME*	0.18	0.22	0.01	95.34	0.02	0.26	0.44	0.02	0.04	3.46	0.02
		Mean	*4.99*	*2.43*	*0.05*	*68.09*	*0.04*	*5.04*	*0.27*	*0.55*	*0.03*	*18.22*	*0.31*
		S.D.	*8.39*	*3.96*	*0.07*	*47.13*	*0.04*	*8.40*	*0.16*	*0.92*	*0.02*	*24.90*	*0.48*
MF83 Sill 1	MF83-139.0	*BV*	13.93	2.82	0.18	19.69	0.02	18.96	0.14	0.04	0.07	43.48	0.69
	MF83-139.55	*ACME*	11.47	6.54	0.11	27.01	0.01	15.65	0.23	0.02	0.02	38.34	0.59
		Mean	*12.70*	*4.68*	*0.14*	*23.35*	*0.01*	*17.30*	*0.19*	*0.03*	*0.05*	*40.91*	*0.64*
		S.D.	*1.73*	*2.63*	*0.05*	*5.18*	*0.01*	*2.34*	*0.07*	*0.01*	*0.03*	*3.63*	*0.07*
MF93 Sill 2	MF93-151.55	*GEO*	12.20	7.36	0.25	16.29	0.02	19.56	0.34	0.06	0.07	43.14	0.71
	MF93-155.21	*GEO*	13.41	2.45	0.14	27.18	0.05	16.85	0.24	0.09	0.08	38.84	0.67
		Mean	*12.80*	*4.90*	*0.20*	*21.74*	*0.04*	*18.21*	*0.29*	*0.07*	*0.07*	*40.99*	*0.69*
		S.D.	*0.85*	*3.47*	*0.07*	*7.70*	*0.02*	*1.91*	*0.07*	*0.02*	*0.00*	*3.04*	*0.03*
MF93 Sill 3	MF93-304.0	*GEO*	17.00	3.15	0.00	11.52	0.91	4.91	0.19	5.52	0.39	54.66	1.75
MF93 Sill 4	MF93-335.2	*ACME*	15.91	4.29	0.00	28.55	0.15	10.44	0.27	0.80	0.08	37.29	2.21
MF95 Sill 1	MF95-123.35	*GEO*	12.18	4.31	0.15	25.64	0.18	15.21	0.38	0.06	0.06	41.18	0.63
MF97 Sill 1	MF97-207.7	*BV*	17.74	2.88	0.03	14.40	0.67	10.86	0.16	3.69	0.10	48.24	1.23
	MF97-212.0	*BV*	11.95	8.35	0.16	17.30	0.11	17.39	0.38	0.11	0.06	43.47	0.71
		Mean	*14.85*	*5.62*	*0.09*	*15.85*	*0.39*	*14.13*	*0.27*	*1.90*	*0.08*	*45.85*	*0.97*
		S.D.	*4.09*	*3.87*	*0.09*	*2.05*	*0.39*	*4.62*	*0.15*	*2.53*	*0.02*	*3.37*	*0.37*
MF103 Sill 1	MF103-146.0	*BV*	16.72	4.66	0.11	13.43	0.89	14.03	0.18	2.54	0.08	46.52	0.84

C.2 Trace Elements Geochemical Data

C.2.1 Melba Flats Sediments

TABLE C.2: *Trace elements geochemical data for the Avebury and Melba Flats Sediments.*

Trace Elements (ppm)															
Sample	**Easting (m)**	**Northing (m)**	**Lab**	**La**	**Ce**	**Pr**	**Nd**	**Sm**	**Eu**	**Gd**	**Tb**	**Dy**	**Ho**	**Er**	**Tm**
A150-144.7	354729	5357595	UOM	27.85	61.86	7.87	32.36	7.23	2.05	7.02	1.06	6.10	1.21	3.23	0.47
A150-156.4	354729	5357595	UOM	31.53	72.32	9.27	37.77	8.37	2.33	7.99	1.22	7.05	1.39	3.76	0.54
A207-40.4	354828	5357861	UOM	29.77	65.31	8.05	32.36	7.06	1.85	6.92	1.12	6.65	1.38	3.80	0.56
A231-279.6	355567	5357932	UOM	40.25	91.21	11.41	45.81	9.88	2.32	8.94	1.34	7.62	1.52	4.09	0.60
MF23-44.6	366427	5365956	UOM	44.53	99.27	12.40	49.47	10.65	2.57	10.18	1.56	9.04	1.77	4.70	0.67
MF40-56.3	366480	5367950	UOM	50.40	112.57	13.70	54.18	11.50	2.86	10.99	1.68	9.64	1.88	4.95	0.71
MF83-152.0	365586	5365567	UOM	46.93	100.32	12.38	48.18	10.07	2.38	9.36	1.42	8.20	1.61	4.27	0.61
MF93-123.55	366668	5367827	GEO	54.75	121.41	15.18	60.18	13.15	2.95	12.33	1.86	10.99	2.09	5.54	0.76
MF103-149.8	366477	5367634	UOM	57.84	122.07	15.14	59.87	13.02	2.33	13.63	2.15	12.34	2.38	6.20	0.87

TABLE C.2 (continued): Trace elements geochemical data for the Avebury and Melba Flats Sediments

Trace Elements (ppm)														
Sample	**Easting (m)**	**Northing (m)**	**Lab**	**Yb**	**Lu**	**Ba**	**Be**	**Bi**	**C**	**Cd**	**Co**	**Cr**	**Cs**	**Cu**
A150-144.7	354729	5357595	UOM	2.95	0.43	99.25	1.51	0.12	300	0.06	36.90	207.03	8.94	17.23
A150-156.4	354729	5357595	UOM	3.38	0.50	149.02	1.42	0.13	300	0.02	45.62	366.75	11.17	11.92
A207-40.4	354828	5357861	UOM	3.56	0.53	236.64	1.22	0.04	300	0.05	49.27	548.18	18.83	31.74
A231-279.6	355567	5357932	UOM	3.79	0.57	1888.32	2.06	0.08	900	0.05	39.03	196.30	31.60	46.68
MF23-44.6	366427	5365956	UOM	4.08	0.57	267.92	2.23	0.12	3600	0.03	34.61	258.00	13.91	8.98
MF40-56.3	366480	5367950	UOM	4.40	0.62	337.38	2.41	0.14	4100	0.04	42.43	423.45	30.54	37.06
MF83-152.0	365586	5365567	UOM	3.73	0.52	524.96	1.36	0.11	9600	0.03	37.30	289.60	3.77	0.13
MF93-123.55	366668	5367827	GEO	4.58	0.65	207.40	3.07	0.08	3002	0.01	49.38	224.00	23.76	9.80
MF103-149.8	366477	5367634	UOM	5.32	0.74	472.62	3.85	0.14	300	0.01	36.47	196.62	38.13	38.28

TABLE C.2 (continued): Trace elements geochemical data for the Avebury and Melba Flats Sediments

Trace Elements (ppm)														
Sample	**Easting (m)**	**Northing (m)**	**Lab**	**Ga**	**Hf**	**In**	**Li**	**Nb**	**Ni**	**Pb**	**Rb**	**S**	**Sb**	**Sc**
A150-144.7	354729	5357595	UOM	17.04	5.73	0.05	32.24	22.77	99.61	7.07	22.22	200	0.57	28.60
A150-156.4	354729	5357595	UOM	21.69	7.36	0.07	30.26	31.28	127.80	3.02	30.14	200	1.31	32.55
A207-40.4	354828	5357861	UOM	20.68	8.50	0.09	30.67	31.11	142.21	5.40	40.90	100	0.53	44.76
A231-279.6	355567	5357932	UOM	24.31	6.87	0.12	74.46	29.14	111.05	7.07	213.08	100	0.34	33.98
MF23-44.6	366427	5365956	UOM	20.26	8.70	0.10	30.52	39.92	96.70	14.39	71.21	50	1.27	23.57
MF40-56.3	366480	5367950	UOM	21.21	11.35	0.11	36.01	45.38	113.48	10.08	98.84	50	1.20	27.43
MF83-152.0	365586	5365567	UOM	17.46	7.91	0.10	28.72	38.50	92.83	13.98	13.97	50	2.31	21.67
MF93-123.55	366668	5367827	GEO	24.69	8.81	0.04	54.75	41.01	106.40	8.60	108.75	2200	3.06	28.30
MF103-149.8	366477	5367634	UOM	30.57	8.37	0.16	34.97	40.95	115.64	5.84	217.45	50	0.78	31.20

TABLE C.2 (continued): Trace elements geochemical data for the Avebury and Melba Flats Sediments

Trace Elements (ppm)													
Sample	**Easting (m)**	**Northing (m)**	**Lab**	**Sn**	**Sr**	**Ta**	**Th**	**Tl**	**U**	**V**	**W**	**Y**	**Zn**	**Zr**
A150-144.7	354729	5357595	UOM	0.20	89.71	1.42	4.77	0.38	1.14	180.46	0.73	29.00	122.06	227.41
A150-156.4	354729	5357595	UOM	0.21	118.96	1.96	6.27	0.67	1.49	280.72	0.87	34.56	99.29	288.77
A207-40.4	354828	5357861	UOM	2.66	83.76	1.79	7.03	0.53	1.51	369.99	0.79	34.82	276.58	334.30
A231-279.6	355567	5357932	UOM	1.08	100.58	1.85	6.35	1.74	1.83	230.99	2.30	37.15	127.80	268.52
MF23-44.6	366427	5365956	UOM	0.44	75.59	2.19	8.83	0.39	2.40	179.03	1.39	44.90	124.05	335.71
MF40-56.3	366480	5367950	UOM	5.42	111.49	2.81	9.15	0.60	2.78	232.63	1.44	47.20	166.04	446.16
MF83-152.0	365586	5365567	UOM	4.92	108.53	2.42	8.61	0.07	2.32	173.91	1.21	40.06	126.37	304.16
MF93-123.55	366668	5367827	GEO	4.82	50.40	2.77	10.02	0.86	2.65	192.80	82.02	54.72	146.00	339.00
MF103-149.8	366477	5367634	UOM	0.40	46.51	2.69	12.09	1.08	3.03	218.71	2.33	61.03	119.79	322.22

C.2.2 Melba Flats Mafic Intrusions

TABLE C.3: *Lithophile elements geochemical data for the Melba Flats mafic intrusions.*

		Unmineralized Lithophile Elements (ppm)											
		Lab	**Cs**	**Rb**	**Ba**	**Th**	**U**	**Nb**	**Ta**	**K**	**La**	**Ce**	**Pb**
MF17 Sill 1	**MF17-69.6**	*BV*	9.33	11.00	80.00	1.04	0.24	2.89	0.17	1534.21	4.29	9.66	24.00
	MF17-70.8	*BV*	10.70	9.35	313.00	1.05	0.26	2.86	0.18	1261.13	4.45	9.80	14.00
	MF17-71.7	*BV*	11.10	13.30	603.00	1.13	0.28	3.01	0.19	1926.68	4.69	10.50	16.00
	MF17-72.9	*BV*	11.00	15.40	387.00	1.19	0.32	3.33	0.20	2881.18	4.92	11.10	9.00
		Mean	*10.53*	*12.26*	*345.75*	*1.10*	*0.28*	*3.02*	*0.19*	*1900.80*	*4.59*	*10.27*	*15.75*
		S.D.	*0.82*	*2.65*	*215.70*	*0.07*	*0.03*	*0.22*	*0.01*	*708.37*	*0.28*	*0.67*	*6.24*
MF23 Sill 1	**MF23-48.35**	*ACME*	8.70	44.20	295.00	0.40	0.40	3.10	0.10	10200.55	4.50	11.10	3.30
	MF23-49.52	*ACME*	9.40	57.70	154.00	0.30	0.40	3.10	0.20	13337.60	5.20	11.00	2.00
		Mean	*9.05*	*50.95*	*224.50*	*0.35*	*0.40*	*3.10*	*0.15*	*11769.08*	*4.85*	*11.05*	*2.65*
		S.D.	*0.49*	*9.55*	*99.70*	*0.07*	*0.00*	*0.00*	*0.07*	*2218.23*	*0.49*	*0.07*	*0.92*
MF81A Sill 1	**MF81A-163.5**	*GEO*	8.57	24.76	394.80	0.81	0.23	2.78	0.23	6165.66	3.82	8.90	2.70
	MF81A-164.2	*GEO*	9.89	16.68	353.90	0.93	0.27	3.09	0.22	4293.09	4.60	10.33	4.10
	MF81A-167.45	*GEO*	10.50	23.80	519.50	1.34	0.38	4.28	0.29	5527.61	6.67	14.96	8.20
	MF81A-169.2	*ACME*	10.50	22.00	70.00	0.50	0.20	2.60	0.20	5696.77	4.90	10.40	0.50
	MF81A-170.9	*GEO*	9.41	6.29	65.30	0.53	0.18	2.36	0.16	1562.53	3.04	7.06	2.60
		Mean	*9.77*	*18.71*	*280.70*	*0.82*	*0.25*	*3.02*	*0.22*	*4649.13*	*4.61*	*10.33*	*3.62*
		S.D.	*0.82*	*7.61*	*203.83*	*0.34*	*0.08*	*0.75*	*0.05*	*1858.97*	*1.36*	*2.92*	*2.86*
MF83 Sill 1	**MF83-143.2**	*BV*	12.30	27.30	333.00	1.02	0.26	2.79	0.17	5289.02	4.26	9.68	6.00
	MF83-143.7	*ACME*	11.50	31.30	216.00	0.70	0.30	2.50	0.30	5807.49	3.80	10.20	0.90
	MF83-145.2	*ACME*	7.00	34.50	823.00	0.40	0.20	2.50	0.10	9719.83	4.80	9.80	1.30
		Mean	*10.27*	*31.03*	*457.33*	*0.71*	*0.25*	*2.60*	*0.19*	*6938.78*	*4.29*	*9.89*	*2.73*
		S.D.	*2.86*	*3.61*	*322.03*	*0.31*	*0.05*	*0.17*	*0.10*	*2422.37*	*0.50*	*0.27*	*2.84*
MF93 Sill 1	**MF93-128.55**	*GEO*	23.12	34.69	437.90	0.90	0.27	2.95	0.21	9809.12	4.90	10.63	12.50
MF93 Sill 2	**MF93-159.0**	*GEO*	19.62	25.59	416.60	0.96	0.28	3.05	0.22	8615.08	4.31	9.84	14.10
MF93 Sill 3	**MF93-306.1**	*GEO*	19.88	30.08	156.90	0.59	0.18	1.93	0.14	6869.48	2.99	6.75	1.70
	MF93-310.55	*GEO*	12.32	75.58	541.50	1.05	0.30	3.23	0.23	20089.93	6.28	12.74	3.30
	MF93-311.85	*BV*	14.60	89.00	1050.00	1.20	0.32	3.05	0.17	25453.19	5.26	11.30	2.00
		Mean	*15.60*	*64.89*	*582.80*	*0.95*	*0.26*	*2.74*	*0.18*	*17470.86*	*4.84*	*10.26*	*2.33*
		S.D.	*3.88*	*30.88*	*447.98*	*0.32*	*0.08*	*0.70*	*0.05*	*9564.69*	*1.68*	*3.13*	*0.85*
MF93 Sill 4	**MF93-323.3**	*GEO*	15.95	30.73	145.10	0.88	0.21	3.23	0.28	5094.72	3.18	7.78	0.60
	MF93-330.55	*GEO*	87.67	87.56	289.60	0.87	0.24	3.82	0.31	11402.22	4.67	10.65	0.80
	MF93-345.4	*GEO*	5.83	15.19	250.00	0.50	0.13	2.25	0.23	3734.15	2.71	6.11	0.60
	MF93-356.0	*GEO*	8.93	38.19	401.80	0.43	0.12	2.10	0.19	8518.99	2.47	5.67	1.40
	MF93-356.3	*ACME*	8.70	57.50	142.00	0.20	0.10	1.50	0.10	15129.30	2.40	4.00	0.50
	MF93-365.2	*GEO*	15.02	44.72	1996.00	0.35	0.10	1.76	0.15	11416.34	1.88	4.30	0.70
	MF93-368.86	*GEO*	13.11	5.34	2.70	0.21	0.09	1.26	0.09	370.30	1.38	3.22	6.40
	MF93-376.5	*ACME*	49.60	11.20	6.00	0.20	0.05	0.40	0.05	378.07	1.30	2.30	0.80
	MF93-380.1	*ACME*	23.00	12.10	4.00	0.10	0.05	0.40	0.05	372.13	0.90	1.60	1.70
	MF93-381.3	*GEO*	13.45	3.48	3.10	0.13	0.04	0.60	0.05	182.52	0.60	1.53	1.20
		Mean	*24.13*	*30.60*	*324.03*	*0.39*	*0.11*	*1.73*	*0.15*	*5659.87*	*2.15*	*4.72*	*1.47*
		S.D.	*25.55*	*26.99*	*603.98*	*0.29*	*0.07*	*1.16*	*0.10*	*5595.86*	*1.21*	*2.91*	*1.78*

TABLE C.3 (continued): Lithophile elements geochemical data for the Melba Flats mafic intrusions.

		Unmineralized Lithophile Elements (ppm)												
		Lab	**Pr**	**Sr**	**P**	**Nd**	**Zr**	**Sm**	**Eu**	**Ti**	**Dy**	**Y**	**Yb**	**Lu**
MF17 Sill 1	**MF17-69.6**	*BV*	1.45	172.00	359.28	6.93	45.50	1.97	0.74	5002.88	3.26	20.10	1.93	0.27
	MF17-70.8	*BV*	1.38	183.00	351.25	6.62	48.00	2.13	0.71	5093.13	3.33	20.30	2.25	0.29
	MF17-71.7	*BV*	1.62	196.00	375.24	7.39	48.50	2.18	0.81	5288.38	3.64	20.90	2.12	0.31
	MF17-72.9	*BV*	1.55	182.00	391.17	7.20	51.50	2.16	0.83	5709.21	3.70	21.30	2.14	0.33
		Mean	*1.50*	*183.25*	*369.23*	*7.04*	*48.38*	*2.11*	*0.77*	*5273.40*	*3.48*	*20.65*	*2.11*	*0.30*
		S.D.	*0.11*	*9.84*	*17.70*	*0.33*	*2.46*	*0.10*	*0.06*	*314.03*	*0.22*	*0.55*	*0.13*	*0.03*
MF23 Sill 1	**MF23-48.35**	*ACME*	1.36	142.30	195.15	6.50	50.10	1.78	0.68	5562.34	3.67	19.40	2.06	0.31
	MF23-49.52	*ACME*	1.52	183.40	292.37	7.60	55.40	2.41	0.82	6225.10	3.15	19.90	2.50	0.32
		Mean	*1.44*	*162.85*	*243.76*	*7.05*	*52.75*	*2.10*	*0.75*	*5893.72*	*3.41*	*19.65*	*2.28*	*0.32*
		S.D.	*0.11*	*29.06*	*68.75*	*0.78*	*3.75*	*0.45*	*0.10*	*468.64*	*0.37*	*0.35*	*0.31*	*0.01*
MF81A Sill 1	**MF81A-163.5**	*GEO*	1.24	305.10	286.21	6.00	46.00	2.07	0.69	5176.62	3.72	20.65	2.21	0.33
	MF81A-164.2	*GEO*	1.42	313.80	336.39	6.79	55.00	2.26	0.92	5743.01	3.86	21.46	2.25	0.34
	MF81A-167.45	*GEO*	2.07	264.80	533.15	9.77	78.00	3.23	1.19	7456.80	5.43	29.93	3.22	0.48
	MF81A-169.2	*ACME*	1.39	169.70	290.04	6.40	48.50	2.24	0.85	5777.03	3.30	21.00	2.17	0.27
	MF81A-170.9	*GEO*	0.98	130.10	308.27	4.73	42.00	1.66	0.65	4728.59	2.84	16.35	1.81	0.26
		Mean	*1.42*	*236.70*	*350.81*	*6.74*	*53.90*	*2.29*	*0.86*	*5776.41*	*3.83*	*21.88*	*2.33*	*0.34*
		S.D.	*0.40*	*82.56*	*103.84*	*1.86*	*14.28*	*0.58*	*0.21*	*1034.71*	*0.98*	*4.95*	*0.52*	*0.09*
MF83 Sill 1	**MF83-143.2**	*BV*	1.43	136.00	356.99	6.21	44.00	2.04	0.73	5038.17	3.43	20.10	1.98	0.29
	MF83-143.7	*ACME*	1.50	147.90	290.98	5.70	49.70	1.94	0.81	5196.26	3.56	20.50	2.07	0.31
	MF83-145.2	*ACME*	1.24	204.30	243.50	6.00	46.90	1.66	0.63	5552.59	3.10	17.00	1.65	0.32
		Mean	*1.39*	*162.73*	*297.16*	*5.97*	*46.87*	*1.88*	*0.72*	*5262.34*	*3.36*	*19.20*	*1.90*	*0.31*
		S.D.	*0.13*	*36.49*	*56.99*	*0.26*	*2.85*	*0.20*	*0.09*	*263.50*	*0.24*	*1.92*	*0.22*	*0.02*
MF93 Sill 1	**MF93-128.55**	*GEO*	1.47	225.70	294.89	6.83	50.00	2.20	0.89	5536.09	3.51	19.22	2.04	0.31
MF93 Sill 2	**MF93-159.0**	*GEO*	1.39	162.40	341.15	6.62	53.00	2.21	0.82	5288.74	3.71	20.53	2.18	0.33
MF93 Sill 3	**MF93-306.1**	*GEO*	0.95	102.50	192.75	4.41	34.00	1.49	0.54	3706.80	2.47	14.07	1.47	0.22
	MF93-310.55	*GEO*	1.72	138.10	331.77	8.18	56.00	2.51	0.81	5338.70	3.97	22.46	2.32	0.35
	MF93-311.85	*BV*	1.51	97.50	354.88	7.52	52.50	2.46	0.86	5394.88	3.52	21.70	2.07	0.29
		Mean	*1.39*	*112.70*	*293.13*	*6.70*	*47.50*	*2.15*	*0.74*	*4813.46*	*3.32*	*19.41*	*1.95*	*0.29*
		S.D.	*0.40*	*22.14*	*87.70*	*2.01*	*11.82*	*0.58*	*0.17*	*958.81*	*0.77*	*4.64*	*0.43*	*0.06*
MF93 Sill 4	**MF93-323.3**	*GEO*	1.10	180.80	323.49	5.47	46.00	2.08	0.78	6094.13	5.03	30.41	3.33	0.50
	MF93-330.55	*GEO*	1.47	153.00	412.12	7.15	61.00	2.77	1.11	8177.30	6.21	36.56	3.90	0.60
	MF93-345.4	*GEO*	0.85	234.70	228.43	4.23	37.00	1.71	0.72	4204.81	4.00	23.52	2.56	0.38
	MF93-356.0	*GEO*	0.83	194.60	226.35	4.09	33.00	1.64	0.65	4353.11	4.03	23.78	2.49	0.37
	MF93-356.3	*ACME*	0.70	289.00	45.74	3.60	26.90	1.17	0.55	3518.89	3.53	19.90	1.98	0.30
	MF93-365.2	*GEO*	0.61	362.00	139.68	2.83	24.00	1.12	0.50	2750.13	2.61	15.06	1.66	0.25
	MF93-368.86	*GEO*	0.45	12.40	146.11	2.28	22.00	0.94	0.30	2609.17	2.10	11.40	1.25	0.19
	MF93-376.5	*ACME*	0.32	25.80	99.45	1.00	19.00	0.89	0.28	2663.95	2.33	12.80	1.38	0.18
	MF93-380.1	*ACME*	0.25	16.50	97.89	1.40	17.80	0.73	0.35	2487.63	1.81	12.30	1.43	0.17
	MF93-381.3	*GEO*	0.25	17.70	144.03	1.46	17.00	0.77	0.31	2374.27	2.25	12.64	1.35	0.21
		Mean	*0.68*	*148.65*	*186.33*	*3.35*	*30.37*	*1.38*	*0.55*	*3923.34*	*3.39*	*19.84*	*2.13*	*0.31*
		S.D.	*0.40*	*126.51*	*112.49*	*1.96*	*14.23*	*0.66*	*0.27*	*1896.97*	*1.44*	*8.65*	*0.92*	*0.15*

TABLE C.3 (continued): Lithophile elements geochemical data for the Melba Flats mafic intrusions.

		Unmineralized Lithophile Elements (ppm)											
		Lab	**Cs**	**Rb**	**Ba**	**Th**	**U**	**Nb**	**Ta**	**K**	**La**	**Ce**	**Pb**
MF95 Sill 1	**MF95-121.8**	*GEO*	26.08	192.13	1021.90	1.09	0.31	3.46	0.23	28659.08	5.43	11.58	24.90
	MF95-126.4	*GEO*	30.88	96.96	396.20	0.89	0.26	2.87	0.20	10754.63	4.15	9.45	18.80
	MF95-127.7	*GEO*	26.92	76.42	605.20	0.91	0.27	2.92	0.21	13700.56	4.28	9.52	12.40
		Mean	*27.96*	*121.84*	*674.43*	*0.96*	*0.28*	*3.08*	*0.21*	*17704.75*	*4.62*	*10.18*	*18.70*
		S.D.	*2.56*	*61.74*	*318.54*	*0.11*	*0.03*	*0.33*	*0.02*	*9600.39*	*0.70*	*1.21*	*6.25*
MF95 Sill 2	**MF95-212.15**	*BV*	19.80	47.00	324.00	1.20	0.31	2.88	0.16	9061.99	4.86	10.20	16.00
	MF95-216.3	*BV*	29.80	92.90	685.00	1.39	0.40	3.56	0.20	17568.50	5.85	12.40	7.00
	MF95-218.5	*BV*	19.00	44.20	568.00	1.17	0.29	3.24	0.18	13534.37	4.86	10.70	4.00
	MF95-222.45	*BV*	18.80	5.30	46.50	0.58	0.15	1.97	0.10	1074.90	2.49	6.06	0.50
	MF95-234.8	*BV*	18.40	70.20	297.00	1.06	0.29	2.93	0.16	6976.23	4.71	10.10	2.00
		Mean	*21.16*	*51.92*	*384.10*	*1.08*	*0.29*	*2.92*	*0.16*	*9643.20*	*4.55*	*9.89*	*5.90*
		S.D.	*4.86*	*32.68*	*249.77*	*0.30*	*0.09*	*0.60*	*0.04*	*6301.15*	*1.24*	*2.33*	*6.15*
MF97 Sill 1	**MF97-209.2**	*BV*	21.80	3.60	25.50	0.51	0.11	2.13	0.14	230.84	1.97	4.94	1.00
	MF97-215.9	*BV*	23.20	47.00	425.00	1.03	0.30	3.07	0.16	7678.39	4.55	10.20	12.00
		Mean	*22.50*	*25.30*	*225.25*	*0.77*	*0.21*	*2.60*	*0.15*	*3954.62*	*3.26*	*7.57*	*6.50*
		S.D.	*0.99*	*30.69*	*282.49*	*0.37*	*0.13*	*0.66*	*0.01*	*5266.21*	*1.82*	*3.72*	*7.78*
MF103 Sill 1	**MF103-101.4**	*BV*	12.50	26.70	348.00	1.00	0.25	2.36	0.15	7519.95	4.07	8.90	2.00
	MF103-105.35	*BV*	12.70	3.45	37.50	0.88	0.24	2.38	0.14	696.99	3.68	8.22	0.50
	MF103-111.2	*BV*	15.70	9.85	78.50	0.96	0.27	2.66	0.15	1784.24	3.94	9.36	0.50
	MF103-115.3	*BV*	12.10	13.90	89.50	1.11	0.29	2.92	0.19	2471.81	4.59	9.92	0.50
	MF103-119.9	*BV*	11.00	10.20	107.00	1.18	0.31	3.03	0.18	2183.74	5.05	10.50	0.50
	MF103-124	*BV*	9.84	17.00	159.00	1.19	0.29	3.03	0.18	4079.96	5.03	10.80	9.00
	MF103-129.05	*BV*	10.00	21.20	197.00	1.12	0.33	3.00	0.19	4165.81	4.60	10.30	0.50
	MF103-133.3	*BV*	18.60	34.50	124.00	1.06	0.29	2.56	0.16	3688.99	4.59	9.74	0.50
	MF103-137.5	*BV*	16.60	35.70	302.00	0.88	0.23	2.44	0.13	6233.18	3.57	8.22	0.50
	MF103-141.7	*BV*	18.80	41.80	368.00	0.97	0.26	2.44	0.15	7582.29	4.11	8.82	1.00
	MF103-143.65	*BV*	21.60	26.30	498.00	0.62	0.20	1.73	0.11	7393.38	2.91	6.32	12.00
		Mean	*14.49*	*21.87*	*209.86*	*1.00*	*0.27*	*2.60*	*0.16*	*4345.49*	*4.19*	*9.19*	*2.50*
		S.D.	*3.98*	*12.24*	*147.57*	*0.17*	*0.04*	*0.39*	*0.03*	*2489.90*	*0.66*	*1.29*	*4.04*

TABLE C.3 (continued): Lithophile elements geochemical data for the Melba Flats mafic intrusions.

		Unmineralized Lithophile Elements (ppm)											
		Lab	**Cs**	**Rb**	**Ba**	**Th**	**U**	**Nb**	**Ta**	**K**	**La**	**Ce**	**Pb**
MF95 Sill 1	**MF95-121.8**	*GEO*	26.08	192.13	1021.90	1.09	0.31	3.46	0.23	28659.08	5.43	11.58	24.90
	MF95-126.4	*GEO*	30.88	96.96	396.20	0.89	0.26	2.87	0.20	10754.63	4.15	9.45	18.80
	MF95-127.7	*GEO*	26.92	76.42	605.20	0.91	0.27	2.92	0.21	13700.56	4.28	9.52	12.40
		Mean	*27.96*	*121.84*	*674.43*	*0.96*	*0.28*	*3.08*	*0.21*	*17704.75*	*4.62*	*10.18*	*18.70*
		S.D.	*2.56*	*61.74*	*318.54*	*0.11*	*0.03*	*0.33*	*0.02*	*9600.39*	*0.70*	*1.21*	*6.25*
MF95 Sill 2	**MF95-212.15**	*BV*	19.80	47.00	324.00	1.20	0.31	2.88	0.16	9061.99	4.86	10.20	16.00
	MF95-216.3	*BV*	29.80	92.90	685.00	1.39	0.40	3.56	0.20	17568.50	5.85	12.40	7.00
	MF95-218.5	*BV*	19.00	44.20	568.00	1.17	0.29	3.24	0.18	13534.37	4.86	10.70	4.00
	MF95-222.45	*BV*	18.80	5.30	46.50	0.58	0.15	1.97	0.10	1074.90	2.49	6.06	0.50
	MF95-234.8	*BV*	18.40	70.20	297.00	1.06	0.29	2.93	0.16	6976.23	4.71	10.10	2.00
		Mean	*21.16*	*51.92*	*384.10*	*1.08*	*0.29*	*2.92*	*0.16*	*9643.20*	*4.55*	*9.89*	*5.90*
		S.D.	*4.86*	*32.68*	*249.77*	*0.30*	*0.09*	*0.60*	*0.04*	*6301.15*	*1.24*	*2.33*	*6.15*
MF97 Sill 1	**MF97-209.2**	*BV*	21.80	3.60	25.50	0.51	0.11	2.13	0.14	230.84	1.97	4.94	1.00
	MF97-215.9	*BV*	23.20	47.00	425.00	1.03	0.30	3.07	0.16	7678.39	4.55	10.20	12.00
		Mean	*22.50*	*25.30*	*225.25*	*0.77*	*0.21*	*2.60*	*0.15*	*3954.62*	*3.26*	*7.57*	*6.50*
		S.D.	*0.99*	*30.69*	*282.49*	*0.37*	*0.13*	*0.66*	*0.01*	*5266.21*	*1.82*	*3.72*	*7.78*
MF103 Sill 1	**MF103-101.4**	*BV*	12.50	26.70	348.00	1.00	0.25	2.36	0.15	7519.95	4.07	8.90	2.00
	MF103-105.35	*BV*	12.70	3.45	37.50	0.88	0.24	2.38	0.14	696.99	3.68	8.22	0.50
	MF103-111.2	*BV*	15.70	9.85	78.50	0.96	0.27	2.66	0.15	1784.24	3.94	9.36	0.50
	MF103-115.3	*BV*	12.10	13.90	89.50	1.11	0.29	2.92	0.19	2471.81	4.59	9.92	0.50
	MF103-119.9	*BV*	11.00	10.20	107.00	1.18	0.31	3.03	0.18	2183.74	5.05	10.50	0.50
	MF103-124	*BV*	9.84	17.00	159.00	1.19	0.29	3.03	0.18	4079.96	5.03	10.80	9.00
	MF103-129.05	*BV*	10.00	21.20	197.00	1.12	0.33	3.00	0.19	4165.81	4.60	10.30	0.50
	MF103-133.3	*BV*	18.60	34.50	124.00	1.06	0.29	2.56	0.16	3688.99	4.59	9.74	0.50
	MF103-137.5	*BV*	16.60	35.70	302.00	0.88	0.23	2.44	0.13	6233.18	3.57	8.22	0.50
	MF103-141.7	*BV*	18.80	41.80	368.00	0.97	0.26	2.44	0.15	7582.29	4.11	8.82	1.00
	MF103-143.65	*BV*	21.60	26.30	498.00	0.62	0.20	1.73	0.11	7393.38	2.91	6.32	12.00
		Mean	*14.49*	*21.87*	*209.86*	*1.00*	*0.27*	*2.60*	*0.16*	*4345.49*	*4.19*	*9.19*	*2.50*
		S.D.	*3.98*	*12.24*	*147.57*	*0.17*	*0.04*	*0.39*	*0.03*	*2489.90*	*0.66*	*1.29*	*4.04*

TABLE C.3 (continued): Lithophile elements geochemical data for the Melba Flats mafic intrusions.

		Unmineralized Lithophile Elements (ppm)												
		Lab	**Pr**	**Sr**	**P**	**Nd**	**Zr**	**Sm**	**Eu**	**Ti**	**Dy**	**Y**	**Yb**	**Lu**
MF95 Sill 1	**MF95-121.8**	*GEO*	1.58	52.00	396.78	7.38	59.00	2.41	0.54	6336.07	4.02	21.78	2.31	0.35
	MF95-126.4	*GEO*	1.34	94.20	353.62	6.33	49.00	2.10	0.78	5135.20	3.52	19.70	2.05	0.31
	MF95-127.7	*GEO*	1.30	148.00	345.58	6.45	51.00	2.15	0.71	5493.12	3.60	19.78	2.11	0.33
		Mean	*1.41*	*98.07*	*365.33*	*6.72*	*53.00*	*2.22*	*0.68*	*5654.80*	*3.71*	*20.42*	*2.16*	*0.33*
		S.D.	*0.15*	*48.12*	*27.53*	*0.57*	*5.29*	*0.17*	*0.12*	*616.54*	*0.27*	*1.18*	*0.14*	*0.02*
MF95 Sill 2	**MF95-212.15**	*BV*	1.50	181.00	370.15	7.06	48.00	2.37	0.71	5491.36	3.39	21.20	2.05	0.30
	MF95-216.3	*BV*	1.73	263.00	442.88	8.24	60.00	2.66	0.95	5025.69	4.38	23.70	2.42	0.36
	MF95-218.5	*BV*	1.50	180.00	401.42	7.28	52.00	2.30	0.80	5645.45	3.73	22.30	2.05	0.30
	MF95-222.45	*BV*	0.86	35.00	254.00	4.38	29.50	1.31	0.52	3357.41	2.08	12.40	1.31	0.16
	MF95-234.8	*BV*	1.54	106.00	370.30	7.30	45.00	2.35	0.77	5215.46	3.63	21.10	2.11	0.28
		Mean	*1.43*	*153.00*	*367.75*	*6.85*	*46.90*	*2.20*	*0.75*	*4947.07*	*3.44*	*20.14*	*1.99*	*0.28*
		S.D.	*0.33*	*86.24*	*70.23*	*1.45*	*11.24*	*0.52*	*0.16*	*920.49*	*0.84*	*4.45*	*0.41*	*0.07*
MF97 Sill 1	**MF97-209.2**	*BV*	0.78	52.70	318.80	3.78	34.00	1.55	0.58	4657.23	2.59	14.10	1.12	0.14
	MF97-215.9	*BV*	1.41	168.00	370.38	6.86	47.50	2.23	0.72	5359.10	3.50	20.10	1.91	0.27
		Mean	*1.10*	*110.35*	*344.59*	*5.32*	*40.75*	*1.89*	*0.65*	*5008.17*	*3.05*	*17.10*	*1.52*	*0.21*
		S.D.	*0.45*	*81.53*	*36.47*	*2.18*	*9.55*	*0.48*	*0.10*	*496.30*	*0.64*	*4.24*	*0.56*	*0.09*
MF103 Sill 1	**MF103-101.4**	*BV*	1.32	81.80	310.48	5.66	39.00	1.86	0.67	3683.35	3.03	17.70	1.84	0.26
	MF103-105.35	*BV*	1.24	35.80	282.07	5.73	37.50	1.84	0.69	4132.98	2.86	16.40	1.81	0.25
	MF103-111.2	*BV*	1.32	94.20	322.24	6.41	43.00	2.04	0.74	4490.59	3.31	19.90	1.89	0.27
	MF103-115.3	*BV*	1.43	108.00	334.39	6.83	47.00	2.19	0.80	5040.01	3.69	21.40	2.28	0.29
	MF103-119.9	*BV*	1.52	145.00	353.50	7.22	49.00	2.52	0.78	5175.32	3.61	21.60	2.15	0.31
	MF103-124	*BV*	1.57	149.00	367.04	7.21	50.00	2.37	0.78	5360.95	3.48	21.60	2.25	0.31
	MF103-129.05	*BV*	1.45	147.00	355.90	7.13	48.00	2.13	0.77	5017.60	3.69	21.60	2.05	0.31
	MF103-133.3	*BV*	1.39	139.00	330.55	7.20	45.50	2.19	0.72	4735.19	3.46	20.20	1.96	0.29
	MF103-137.5	*BV*	1.22	110.00	276.85	5.68	39.50	1.69	0.67	4327.58	2.98	17.80	1.87	0.26
	MF103-141.7	*BV*	1.22	127.00	314.02	5.89	42.00	1.92	0.75	4515.78	3.16	18.30	1.85	0.27
	MF103-143.65	*BV*	0.89	148.00	236.03	4.04	28.50	1.47	0.48	3512.52	2.33	13.40	1.35	0.17
		Mean	*1.32*	*116.80*	*316.64*	*6.27*	*42.64*	*2.02*	*0.71*	*4544.72*	*3.24*	*19.08*	*1.94*	*0.27*
		S.D.	*0.19*	*35.69*	*39.12*	*0.99*	*6.33*	*0.30*	*0.09*	*599.75*	*0.42*	*2.64*	*0.26*	*0.04*

TABLE C.3 (continued): Lithophile elements geochemical data for the Melba Flats mafic intrusions.

		Mineralized Lithophile Elements (ppm)											
		Lab	**Cs**	**Rb**	**Ba**	**Th**	**U**	**Nb**	**Ta**	**K**	**La**	**Ce**	**Pb**
MF19 Sill 1	**MF19-34.25**	*BV*	19.80	145.00	222.00	0.87	0.37	2.48	0.14	40346.29	3.91	8.60	293.00
	MF19-39.5	*ACME*	0.05	0.90	8.00	0.30	0.05	2.60	0.05	166.30	6.00	11.10	274.40
	MF19-41.32	*ACME*	0.05	0.20	4.00	0.05	0.05	0.50	0.05	88.15	6.30	6.60	189.70
		Mean	*6.63*	*48.70*	*78.00*	*0.41*	*0.16*	*1.86*	*0.08*	*13533.58*	*5.40*	*8.77*	*252.37*
		S.D.	*11.40*	*83.40*	*124.72*	*0.42*	*0.18*	*1.18*	*0.05*	*23220.52*	*1.30*	*2.25*	*55.06*
MF23 Sill 2	**MF23-64.8**	*ACME*	13.70	1.00	14.00	0.30	0.20	2.60	0.20	48.46	5.80	12.40	7.80
	MF23-65.3	*ACME*	0.10	0.40	4.00	0.05	0.05	0.05	0.05	81.22	1.70	3.10	99.60
	MF23-65.5	*ACME*	0.20	0.20	5.00	0.05	0.05	0.30	0.05	96.30	3.00	4.90	72.70
	MF23-65.6	*ACME*	3.80	0.70	7.00	0.20	0.20	2.20	0.20	47.70	9.70	17.80	14.50
	MF23-74.5	*ACME*	12.00	2.20	18.00	0.30	0.50	2.90	0.30	385.12	12.00	20.90	6.50
	MF23-74.6	*ACME*	0.20	0.10	3.00	0.05	0.05	0.05	0.05	93.98	4.50	8.80	43.50
	MF23-75	*ACME*	7.20	1.60	11.00	0.30	0.20	2.60	0.10	196.84	9.90	19.10	964.40
		Mean	*5.31*	*0.89*	*8.86*	*0.18*	*0.18*	*1.53*	*0.14*	*135.66*	*6.66*	*12.43*	*172.71*
		S.D.	*5.78*	*0.78*	*5.64*	*0.13*	*0.16*	*1.32*	*0.10*	*120.81*	*3.91*	*7.09*	*350.87*
MF81A Sill 1	**MF81A-171.5**	*ACME*	9.80	3.70	5.00	0.50	0.30	2.50	0.20	657.34	4.30	9.90	12.40
	MF81A-174.44	*ACME*	4.40	0.80	2.00	0.05	0.05	0.05	0.50	80.87	0.80	1.00	30.20
	MF81A-174.52	*ACME*	4.90	1.00	2.00	0.05	0.05	0.30	0.50	152.70	1.90	3.30	45.80
		Mean	*6.37*	*1.83*	*3.00*	*0.20*	*0.13*	*0.95*	*0.40*	*296.97*	*2.33*	*4.73*	*29.47*
		S.D.	*2.98*	*1.62*	*1.73*	*0.26*	*0.14*	*1.35*	*0.17*	*314.15*	*1.79*	*4.62*	*16.71*
MF83 Sill 1	**MF83-139.0**	*BV*	8.31	1.30	52.00	0.85	0.22	2.24	0.13	135.91	3.12	7.14	9.00
	MF83-139.55	*ACME*	5.10	0.80	37.00	0.30	0.05	1.70	0.50	50.95	3.30	7.20	27.00
		Mean	*6.71*	*1.05*	*44.50*	*0.58*	*0.14*	*1.97*	*0.32*	*93.43*	*3.21*	*7.17*	*18.00*
		S.D.	*2.27*	*0.35*	*10.61*	*0.39*	*0.12*	*0.38*	*0.26*	*60.08*	*0.13*	*0.04*	*12.73*
MF93 Sill 2	**MF93-151.55**	*GEO*	10.80	1.84	13.50	0.60	0.17	2.27	0.16	199.46	3.37	7.80	3.60
	MF93-155.21	*GEO*	15.59	3.97	18.40	0.64	0.18	2.18	0.15	420.47	3.15	7.31	11.20
		Mean	*13.19*	*2.91*	*15.95*	*0.62*	*0.18*	*2.23*	*0.15*	*309.97*	*3.26*	*7.56*	*7.40*
		S.D.	*3.39*	*1.51*	*3.46*	*0.02*	*0.01*	*0.07*	*0.01*	*156.28*	*0.16*	*0.35*	*5.37*
MF93 Sill 3	**MF93-304.0**	*GEO*	21.05	46.68	193.60	2.86	0.79	9.14	0.63	7580.45	15.24	34.16	13.90
MF93 Sill 4	**MF93-335.2**	*ACME*	6.50	4.80	4.00	0.30	0.10	4.70	0.20	1217.64	3.30	8.80	62.10
MF95 Sill 1	**MF95-123.35**	*GEO*	6.94	19.18	8.70	0.57	0.16	2.02	0.15	1469.44	2.79	6.37	140.70
MF97 Sill 1	**MF97-207.7**	*BV*	17.60	23.50	326.00	0.80	0.21	2.54	0.18	5561.59	3.88	8.82	4.00
	MF97-212.0	*BV*	24.40	23.60	21.50	0.71	0.19	2.13	0.13	934.71	3.09	6.48	16.00
		Mean	*21.00*	*23.55*	*173.75*	*0.76*	*0.20*	*2.34*	*0.16*	*3248.15*	*3.49*	*7.65*	*10.00*
		S.D.	*4.81*	*0.07*	*215.31*	*0.06*	*0.01*	*0.29*	*0.04*	*3271.70*	*0.56*	*1.65*	*8.49*
MF103 Sill 1	**MF103-146.0**	*BV*	14.20	23.60	662.00	0.99	0.26	2.59	0.13	7391.15	5.00	10.20	4.00

TABLE C.3 (continued): Lithophile elements geochemical data for the Melba Flats mafic intrusions.

		Mineralized Lithophile Elements (ppm)												
		Lab	**Pr**	**Sr**	**P**	**Nd**	**Zr**	**Sm**	**Eu**	**Ti**	**Dy**	**Y**	**Yb**	**Lu**
MF19 Sill 1	**MF19-34.25**	*BV*	1.21	48.50	382.30	5.27	39.00	1.72	0.49	5721.79	2.46	15.20	1.38	0.20
	MF19-39.5	*ACME*	1.27	41.40	174.98	4.30	3.20	0.79	0.31	360.54	0.60	3.10	0.19	0.03
	MF19-41.32	*ACME*	0.78	36.60	185.50	2.80	1.10	0.53	0.17	63.70	0.54	3.10	0.18	0.01
		Mean	*1.09*	*42.17*	*247.59*	*4.12*	*14.43*	*1.01*	*0.32*	*2048.68*	*1.20*	*7.13*	*0.58*	*0.08*
		S.D.	*0.27*	*5.99*	*116.78*	*1.24*	*21.30*	*0.63*	*0.16*	*3184.47*	*1.09*	*6.99*	*0.69*	*0.10*
MF23 Sill 2	**MF23-64.8**	*ACME*	1.48	14.80	152.98	7.50	46.60	2.02	0.47	5533.69	2.31	12.40	1.28	0.19
	MF23-65.3	*ACME*	0.38	52.80	170.93	1.70	0.60	0.51	0.23	58.70	0.72	5.50	0.30	0.04
	MF23-65.5	*ACME*	0.54	17.60	202.65	2.50	1.40	0.79	0.31	278.37	1.29	6.90	0.54	0.09
	MF23-65.6	*ACME*	2.00	77.40	250.96	10.10	44.10	1.94	0.62	5308.99	2.57	15.80	1.42	0.28
	MF23-74.5	*ACME*	2.63	10.70	151.96	11.60	46.40	2.16	0.50	5079.40	1.93	12.00	0.75	0.11
	MF23-74.6	*ACME*	0.95	36.50	197.78	3.80	0.70	1.04	0.25	135.84	0.80	4.60	0.34	0.05
	MF23-75	*ACME*	2.46	38.10	207.12	10.20	47.30	2.79	0.77	5263.41	3.13	15.40	1.04	0.17
		Mean	*1.49*	*35.41*	*190.62*	*6.77*	*26.73*	*1.61*	*0.45*	*3094.06*	*1.82*	*10.37*	*0.81*	*0.13*
		S.D.	*0.91*	*23.90*	*35.14*	*4.07*	*24.18*	*0.83*	*0.20*	*2750.69*	*0.92*	*4.67*	*0.45*	*0.09*
MF81A Sill 1	**MF81A-171.5**	*ACME*	1.30	104.10	197.61	6.60	46.70	1.94	0.68	5157.67	3.16	19.20	1.88	0.29
	MF81A-174.44	*ACME*	0.08	0.60	42.55	0.40	0.50	0.08	0.04	233.77	0.10	1.10	0.03	0.01
	MF81A-174.52	*ACME*	0.32	1.10	160.67	1.40	1.10	0.33	0.16	110.35	0.43	2.80	0.11	0.01
		Mean	*0.57*	*35.27*	*133.61*	*2.80*	*16.10*	*0.78*	*0.29*	*1833.93*	*1.23*	*7.70*	*0.67*	*0.10*
		S.D.	*0.65*	*59.61*	*81.00*	*3.33*	*26.50*	*1.01*	*0.34*	*2879.10*	*1.68*	*10.00*	*1.05*	*0.16*
MF83 Sill 1	**MF83-139.0**	*BV*	1.01	63.10	291.12	4.53	38.50	1.65	0.38	4139.39	2.75	16.10	1.65	0.27
	MF83-139.55	*ACME*	0.98	89.80	107.22	4.50	33.60	1.33	0.58	3534.83	2.10	14.00	1.28	0.19
		Mean	*1.00*	*76.45*	*199.17*	*4.52*	*36.05*	*1.49*	*0.48*	*3837.11*	*2.43*	*15.05*	*1.47*	*0.23*
		S.D.	*0.02*	*18.88*	*130.04*	*0.02*	*3.46*	*0.23*	*0.14*	*427.49*	*0.46*	*1.48*	*0.26*	*0.06*
MF93 Sill 2	**MF93-151.55**	*GEO*	1.07	55.30	314.81	5.14	39.00	1.66	0.64	4252.34	2.81	15.68	1.65	0.25
	MF93-155.21	*GEO*	1.01	22.80	331.82	4.69	39.00	1.52	0.53	4026.27	2.48	13.76	1.50	0.23
		Mean	*1.04*	*39.05*	*323.31*	*4.92*	*39.00*	*1.59*	*0.59*	*4139.31*	*2.65*	*14.72*	*1.57*	*0.24*
		S.D.	*0.04*	*22.98*	*12.03*	*0.32*	*0.00*	*0.10*	*0.07*	*159.85*	*0.24*	*1.36*	*0.11*	*0.02*
MF93 Sill 3	**MF93-304.0**	*GEO*	4.76	208.60	1689.06	22.17	139.00	6.84	2.11	10505.39	10.49	57.62	5.87	0.87
MF93 Sill 4	**MF93-335.2**	*ACME*	1.27	34.60	344.94	5.30	53.90	1.90	0.86	13267.27	6.30	34.90	2.83	0.43
MF95 Sill 1	**MF95-123.35**	*GEO*	0.91	13.10	276.10	4.45	33.00	1.40	0.43	3792.65	2.35	13.17	1.38	0.21
MF97 Sill 1	**MF97-207.7**	*BV*	1.14	235.00	417.99	5.94	53.50	3.10	1.07	7373.01	5.44	29.20	2.41	0.33
	MF97-212.0	*BV*	0.95	61.10	283.29	4.24	33.00	1.54	0.56	4258.58	2.50	15.30	1.62	0.22
		Mean	*1.05*	*148.05*	*350.64*	*5.09*	*43.25*	*2.32*	*0.82*	*5815.80*	*3.97*	*22.25*	*2.02*	*0.28*
		S.D.	*0.13*	*122.97*	*95.25*	*1.20*	*14.50*	*1.10*	*0.36*	*2202.23*	*2.08*	*9.83*	*0.56*	*0.08*
MF103 Sill 1	**MF103-146.0**	*BV*	1.40	196.00	357.50	7.11	43.00	2.02	0.65	5045.47	3.41	18.10	2.04	0.28

TABLE C.4: *REE geochemical data for the Melba Flats mafic intrusions.*

		Unmineralized Rare Earth Elements (ppm)															
		Lab	**La**	**Ce**	**Pr**	**Nd**	**Sm**	**Eu**	**Gd**	**Tb**	**Dy**	**Ho**	**Er**	**Tm**	**Yb**	**Lu**
MF17 Sill 1	**MF17-69.6**	*BV*	4.29	9.66	1.45	6.93	1.97	0.74	2.87	0.50	3.26	0.74	2.26	0.32	1.93	0.27
	MF17-70.8	*BV*	4.45	9.80	1.38	6.62	2.13	0.71	2.91	0.52	3.33	0.79	2.45	0.30	2.25	0.29
	MF17-71.7	*BV*	4.69	10.50	1.62	7.39	2.18	0.81	3.26	0.54	3.64	0.85	2.27	0.33	2.12	0.31
	MF17-72.9	*BV*	4.92	11.10	1.55	7.20	2.16	0.83	3.11	0.54	3.70	0.74	2.40	0.35	2.14	0.33
		Mean	*4.59*	*10.27*	*1.50*	*7.04*	*2.11*	*0.77*	*3.04*	*0.53*	*3.48*	*0.78*	*2.35*	*0.33*	*2.11*	*0.30*
		S.D.	*0.28*	*0.67*	*0.11*	*0.33*	*0.10*	*0.06*	*0.18*	*0.02*	*0.22*	*0.05*	*0.09*	*0.02*	*0.13*	*0.03*
MF23 Sill 1	**MF23-48.35**	*ACME*	4.50	11.10	1.36	6.50	1.78	0.68	2.69	0.50	3.67	0.74	2.24	0.34	2.06	0.31
	MF23-49.52	*ACME*	5.20	11.00	1.52	7.60	2.41	0.82	2.83	0.58	3.15	0.75	2.36	0.27	2.50	0.32
		Mean	*4.85*	*11.05*	*1.44*	*7.05*	*2.10*	*0.75*	*2.76*	*0.54*	*3.41*	*0.75*	*2.30*	*0.31*	*2.28*	*0.32*
		S.D.	*0.49*	*0.07*	*0.11*	*0.78*	*0.45*	*0.10*	*0.10*	*0.06*	*0.37*	*0.01*	*0.08*	*0.05*	*0.31*	*0.01*
MF81A Sill 1	**MF81A-163.5**	*GEO*	3.82	8.90	1.24	6.00	2.07	0.69	2.94	0.54	3.72	0.79	2.34	0.34	2.21	0.33
	MF81A-164.2	*GEO*	4.60	10.33	1.42	6.79	2.26	0.92	3.19	0.56	3.86	0.81	2.37	0.35	2.25	0.34
	MF81A-167.45	*GEO*	6.67	14.96	2.07	9.77	3.23	1.19	4.46	0.79	5.43	1.14	3.42	0.50	3.22	0.48
	MF81A-169.2	*ACME*	4.90	10.40	1.39	6.40	2.24	0.85	3.18	0.57	3.30	0.75	2.03	0.32	2.17	0.27
	MF81A-170.9	*GEO*	3.04	7.06	0.98	4.73	1.66	0.65	2.21	0.41	2.84	0.61	1.80	0.27	1.81	0.26
		Mean	*4.61*	*10.33*	*1.42*	*6.74*	*2.29*	*0.86*	*3.20*	*0.58*	*3.83*	*0.82*	*2.39*	*0.36*	*2.33*	*0.34*
		S.D.	*1.36*	*2.92*	*0.40*	*1.86*	*0.58*	*0.21*	*0.81*	*0.14*	*0.98*	*0.20*	*0.62*	*0.09*	*0.52*	*0.09*
MF83 Sill 1	**MF83-143.2**	*BV*	4.26	9.68	1.43	6.21	2.04	0.73	2.81	0.53	3.43	0.76	2.21	0.32	1.98	0.29
	MF83-143.7	*ACME*	3.80	10.20	1.50	5.70	1.94	0.81	2.77	0.50	3.56	0.64	1.82	0.27	2.07	0.31
	MF83-145.2	*ACME*	4.80	9.80	1.24	6.00	1.66	0.63	2.68	0.49	3.10	0.64	2.11	0.31	1.65	0.32
		Mean	*4.29*	*9.89*	*1.39*	*5.97*	*1.88*	*0.72*	*2.75*	*0.51*	*3.36*	*0.68*	*2.05*	*0.30*	*1.90*	*0.31*
		S.D.	*0.50*	*0.27*	*0.13*	*0.26*	*0.20*	*0.09*	*0.07*	*0.02*	*0.24*	*0.07*	*0.20*	*0.03*	*0.22*	*0.02*
MF93 Sill 1	**MF93-128.55**	*GEO*	4.90	10.63	1.47	6.83	2.20	0.89	2.95	0.54	3.51	0.75	2.22	0.32	2.04	0.31
MF93 Sill 2	**MF93-159.0**	*GEO*	4.31	9.84	1.39	6.62	2.21	0.82	3.04	0.55	3.71	0.80	2.31	0.34	2.18	0.33
MF93 Sill 3	**MF93-306.1**	*GEO*	2.99	6.75	0.95	4.41	1.49	0.54	2.03	0.37	2.47	0.53	1.55	0.23	1.47	0.22
	MF93-310.55	*GEO*	6.28	12.74	1.72	8.18	2.51	0.81	3.34	0.59	3.97	0.85	2.45	0.36	2.32	0.35
	MF93-311.85	*BV*	5.26	11.30	1.51	7.52	2.46	0.86	3.14	0.57	3.52	0.84	2.33	0.34	2.07	0.29
		Mean	*4.84*	*10.26*	*1.39*	*6.70*	*2.15*	*0.74*	*2.84*	*0.51*	*3.32*	*0.74*	*2.11*	*0.31*	*1.95*	*0.29*
		S.D.	*1.68*	*3.13*	*0.40*	*2.01*	*0.58*	*0.17*	*0.70*	*0.12*	*0.77*	*0.18*	*0.49*	*0.07*	*0.43*	*0.06*
MF93 Sill 4	**MF93-323.3**	*GEO*	3.18	7.78	1.10	5.47	2.08	0.78	3.52	0.71	5.03	1.14	3.47	0.51	3.33	0.50
	MF93-330.55	*GEO*	4.67	10.65	1.47	7.15	2.77	1.11	4.46	0.87	6.21	1.38	4.16	0.61	3.90	0.60
	MF93-345.4	*GEO*	2.71	6.11	0.85	4.23	1.71	0.72	2.87	0.56	4.00	0.89	2.67	0.39	2.56	0.38
	MF93-356.0	*GEO*	2.47	5.67	0.83	4.09	1.64	0.65	2.81	0.56	4.03	0.90	2.68	0.39	2.49	0.37
	MF93-356.3	*ACME*	2.40	4.00	0.70	3.60	1.17	0.55	2.27	0.46	3.53	0.72	1.92	0.28	1.98	0.30
	MF93-365.2	*GEO*	1.88	4.30	0.61	2.83	1.12	0.50	1.80	0.35	2.61	0.57	1.69	0.25	1.66	0.25
	MF93-368.86	*GEO*	1.38	3.22	0.45	2.28	0.94	0.30	1.50	0.30	2.10	0.46	1.37	0.20	1.25	0.19
	MF93-376.5	*ACME*	1.30	2.30	0.32	1.00	0.89	0.28	1.64	0.32	2.33	0.46	1.41	0.18	1.38	0.18
	MF93-380.1	*ACME*	0.90	1.60	0.25	1.40	0.73	0.35	1.34	0.31	1.81	0.42	1.21	0.19	1.43	0.17
	MF93-381.3	*GEO*	0.60	1.53	0.25	1.46	0.77	0.31	1.55	0.31	2.25	0.50	1.48	0.21	1.35	0.21
		Mean	*2.15*	*4.72*	*0.68*	*3.35*	*1.38*	*0.55*	*2.38*	*0.47*	*3.39*	*0.74*	*2.21*	*0.32*	*2.13*	*0.31*
		S.D.	*1.21*	*2.91*	*0.40*	*1.96*	*0.66*	*0.27*	*1.03*	*0.20*	*1.44*	*0.33*	*1.00*	*0.15*	*0.92*	*0.15*

TABLE C.4 (continued): REE geochemical data for the Melba Flats mafic intrusions.

		Unmineralized Rare Earth Elements (ppm)														
		Lab	**La**	**Ce**	**Pr**	**Nd**	**Sm**	**Eu**	**Gd**	**Tb**	**Dy**	**Ho**	**Er**	**Tm**	**Yb**	**Lu**
MF95 Sill 1	**MF95-121.8**	*GEO*	5.43	11.58	1.58	7.38	2.41	0.54	3.30	0.59	4.02	0.84	2.48	0.36	2.31	0.35
	MF95-126.4	*GEO*	4.15	9.45	1.34	6.33	2.10	0.78	2.87	0.51	3.52	0.75	2.23	0.32	2.05	0.31
	MF95-127.7	*GEO*	4.28	9.52	1.30	6.45	2.15	0.71	2.87	0.53	3.60	0.76	2.26	0.33	2.11	0.33
		Mean	*4.62*	*10.18*	*1.41*	*6.72*	*2.22*	*0.68*	*3.01*	*0.54*	*3.71*	*0.78*	*2.33*	*0.34*	*2.16*	*0.33*
		S.D.	*0.70*	*1.21*	*0.15*	*0.57*	*0.17*	*0.12*	*0.25*	*0.04*	*0.27*	*0.05*	*0.14*	*0.02*	*0.14*	*0.02*
MF95 Sill 2	**MF95-212.15**	*BV*	4.86	10.20	1.50	7.06	2.37	0.71	2.75	0.53	3.39	0.79	2.20	0.33	2.05	0.30
	MF95-216.3	*BV*	5.85	12.40	1.73	8.24	2.66	0.95	3.12	0.64	4.38	0.86	2.51	0.36	2.42	0.36
	MF95-218.5	*BV*	4.86	10.70	1.50	7.28	2.30	0.80	3.00	0.62	3.73	0.83	2.35	0.32	2.05	0.30
	MF95-222.45	*BV*	2.49	6.06	0.86	4.38	1.31	0.52	1.81	0.33	2.08	0.45	1.36	0.20	1.31	0.16
	MF95-234.8	*BV*	4.71	10.10	1.54	7.30	2.35	0.77	3.04	0.54	3.63	0.76	2.52	0.32	2.11	0.28
		Mean	*4.55*	*9.89*	*1.43*	*6.85*	*2.20*	*0.75*	*2.74*	*0.53*	*3.44*	*0.74*	*2.19*	*0.31*	*1.99*	*0.28*
		S.D.	*1.24*	*2.33*	*0.33*	*1.45*	*0.52*	*0.16*	*0.54*	*0.12*	*0.84*	*0.17*	*0.48*	*0.06*	*0.41*	*0.07*
MF97 Sill 1	**MF97-209.2**	*BV*	1.97	4.94	0.78	3.78	1.55	0.58	2.16	0.42	2.59	0.56	1.36	0.18	1.12	0.14
	MF97-215.9	*BV*	4.55	10.20	1.41	6.86	2.23	0.72	3.04	0.53	3.50	0.78	2.26	0.29	1.91	0.27
		Mean	*3.26*	*7.57*	*1.10*	*5.32*	*1.89*	*0.65*	*2.60*	*0.48*	*3.05*	*0.67*	*1.81*	*0.24*	*1.52*	*0.21*
		S.D.	*1.82*	*3.72*	*0.45*	*2.18*	*0.48*	*0.10*	*0.62*	*0.08*	*0.64*	*0.16*	*0.64*	*0.08*	*0.56*	*0.09*
MF103 Sill 1	**MF103-101.4**	*BV*	4.07	8.90	1.32	5.66	1.86	0.67	2.50	0.40	3.03	0.69	1.98	0.26	1.84	0.26
	MF103-105.35	*BV*	3.68	8.22	1.24	5.73	1.84	0.69	2.57	0.44	2.86	0.63	1.85	0.23	1.81	0.25
	MF103-111.2	*BV*	3.94	9.36	1.32	6.41	2.04	0.74	2.86	0.49	3.31	0.77	2.17	0.27	1.89	0.27
	MF103-115.3	*BV*	4.59	9.92	1.43	6.83	2.19	0.80	3.02	0.50	3.69	0.77	2.44	0.29	2.28	0.29
	MF103-119.9	*BV*	5.05	10.50	1.52	7.22	2.52	0.78	3.06	0.53	3.61	0.81	2.39	0.34	2.15	0.31
	MF103-124	*BV*	5.03	10.80	1.57	7.21	2.37	0.78	3.09	0.53	3.48	0.86	2.37	0.31	2.25	0.31
	MF103-129.05	*BV*	4.60	10.30	1.45	7.13	2.13	0.77	2.94	0.55	3.69	0.77	2.25	0.32	2.05	0.31
	MF103-133.3	*BV*	4.59	9.74	1.39	7.20	2.19	0.72	2.78	0.50	3.46	0.77	2.18	0.30	1.96	0.29
	MF103-137.5	*BV*	3.57	8.22	1.22	5.68	1.69	0.67	2.50	0.44	2.98	0.67	1.99	0.28	1.87	0.26
	MF103-141.7	*BV*	4.11	8.82	1.22	5.89	1.92	0.75	2.39	0.45	3.16	0.75	2.01	0.27	1.85	0.27
	MF103-143.65	*BV*	2.91	6.32	0.89	4.04	1.47	0.48	1.90	0.32	2.33	0.47	1.49	0.22	1.35	0.17
		Mean	*4.19*	*9.19*	*1.32*	*6.27*	*2.02*	*0.71*	*2.69*	*0.47*	*3.24*	*0.72*	*2.10*	*0.28*	*1.94*	*0.27*
		S.D.	*0.66*	*1.29*	*0.19*	*0.99*	*0.30*	*0.09*	*0.36*	*0.07*	*0.42*	*0.11*	*0.28*	*0.04*	*0.26*	*0.04*

TABLE C.4 (continued): REE geochemical data for the Melba Flats mafic intrusions.

		Mineralized Rare Earth Elements (ppm)														
		Lab	**La**	**Ce**	**Pr**	**Nd**	**Sm**	**Eu**	**Gd**	**Tb**	**Dy**	**Ho**	**Er**	**Tm**	**Yb**	**Lu**
MF19 Sill 1	**MF19-34.25**	*BV*	3.91	8.60	1.21	5.27	1.72	0.49	2.75	0.41	2.46	0.58	1.67	0.21	1.38	0.20
	MF19-39.5	*ACME*	6.00	11.10	1.27	4.30	0.79	0.31	0.75	0.11	0.60	0.10	0.20	0.03	0.19	0.03
	MF19-41.32	*ACME*	6.30	6.60	0.78	2.80	0.53	0.17	0.59	0.10	0.54	0.09	0.28	0.03	0.18	0.01
		Mean	*5.40*	*8.77*	*1.09*	*4.12*	*1.01*	*0.32*	*1.36*	*0.21*	*1.20*	*0.26*	*0.72*	*0.09*	*0.58*	*0.08*
		S.D.	*1.30*	*2.25*	*0.27*	*1.24*	*0.63*	*0.16*	*1.20*	*0.18*	*1.09*	*0.28*	*0.83*	*0.10*	*0.69*	*0.10*
MF23 Sill 2	**MF23-64.8**	*ACME*	5.80	12.40	1.48	7.50	2.02	0.47	2.15	0.40	2.31	0.38	1.30	0.19	1.28	0.19
	MF23-65.3	*ACME*	1.70	3.10	0.38	1.70	0.51	0.23	0.73	0.11	0.72	0.13	0.35	0.05	0.30	0.04
	MF23-65.5	*ACME*	3.00	4.90	0.54	2.50	0.79	0.31	1.10	0.21	1.29	0.22	0.57	0.08	0.54	0.09
	MF23-65.6	*ACME*	9.70	17.80	2.00	10.10	1.94	0.62	3.17	0.53	2.57	0.50	1.70	0.26	1.42	0.28
	MF23-74.5	*ACME*	12.00	20.90	2.63	11.60	2.16	0.50	2.58	0.40	1.93	0.34	1.04	0.14	0.75	0.11
	MF23-74.6	*ACME*	4.50	8.80	0.95	3.80	1.04	0.25	0.98	0.14	0.80	0.13	0.33	0.04	0.34	0.05
	MF23-75	*ACME*	9.90	19.10	2.46	10.20	2.79	0.77	3.08	0.51	3.13	0.54	1.65	0.19	1.04	0.17
		Mean	*6.66*	*12.43*	*1.49*	*6.77*	*1.61*	*0.45*	*1.97*	*0.33*	*1.82*	*0.32*	*0.99*	*0.14*	*0.81*	*0.13*
		S.D.	*3.91*	*7.09*	*0.91*	*4.07*	*0.83*	*0.20*	*1.03*	*0.17*	*0.92*	*0.17*	*0.59*	*0.08*	*0.45*	*0.09*
MF81A Sill 1	**MF81A-171.5**	*ACME*	4.30	9.90	1.30	6.60	1.94	0.68	2.60	0.51	3.16	0.59	1.83	0.29	1.88	0.29
	MF81A-174.44	*ACME*	0.80	1.00	0.08	0.40	0.08	0.04	0.14	0.02	0.10	0.02	0.07	0.01	0.03	0.01
	MF81A-174.52	*ACME*	1.90	3.30	0.32	1.40	0.33	0.16	0.37	0.05	0.43	0.07	0.15	0.03	0.11	0.01
		Mean	*2.33*	*4.73*	*0.57*	*2.80*	*0.78*	*0.29*	*1.04*	*0.19*	*1.23*	*0.23*	*0.68*	*0.11*	*0.67*	*0.10*
		S.D.	*1.79*	*4.62*	*0.65*	*3.33*	*1.01*	*0.34*	*1.36*	*0.27*	*1.68*	*0.32*	*0.99*	*0.16*	*1.05*	*0.16*
MF83 Sill 1	**MF83-139.0**	*BV*	3.12	7.14	1.01	4.53	1.65	0.38	2.25	0.39	2.75	0.61	1.78	0.27	1.65	0.27
	MF83-139.55	*ACME*	3.30	7.20	0.98	4.50	1.33	0.58	1.89	0.35	2.10	0.49	1.37	0.20	1.28	0.19
		Mean	*3.21*	*7.17*	*1.00*	*4.52*	*1.49*	*0.48*	*2.07*	*0.37*	*2.43*	*0.55*	*1.58*	*0.24*	*1.47*	*0.23*
		S.D.	*0.13*	*0.04*	*0.02*	*0.02*	*0.23*	*0.14*	*0.25*	*0.03*	*0.46*	*0.08*	*0.29*	*0.05*	*0.26*	*0.06*
MF93 Sill 2	**MF93-151.55**	*GEO*	4.07	8.90	1.32	5.66	1.86	0.67	2.50	0.40	3.03	0.69	1.98	0.26	1.84	0.26
	MF93-155.21	*GEO*	3.68	8.22	1.24	5.73	1.84	0.69	2.57	0.44	2.86	0.63	1.85	0.23	1.81	0.25
		Mean	*3.88*	*8.56*	*1.28*	*5.70*	*1.85*	*0.68*	*2.54*	*0.42*	*2.95*	*0.66*	*1.92*	*0.25*	*1.83*	*0.26*
		S.D.	*0.28*	*0.48*	*0.06*	*0.05*	*0.01*	*0.01*	*0.05*	*0.03*	*0.12*	*0.04*	*0.09*	*0.02*	*0.02*	*0.01*
MF93 Sill 3	**MF93-304.0**	*GEO*	3.94	9.36	1.32	6.41	2.04	0.74	2.86	0.49	3.31	0.77	2.17	0.27	1.89	0.27
MF93 Sill 4	**MF93-335.2**	*ACME*	4.59	9.92	1.43	6.83	2.19	0.80	3.02	0.50	3.69	0.77	2.44	0.29	2.28	0.29
MF95 Sill 1	**MF95-123.35**	*GEO*	5.05	10.50	1.52	7.22	2.52	0.78	3.06	0.53	3.61	0.81	2.39	0.34	2.15	0.31
MF97 Sill 1	**MF97-207.7**	*BV*	5.03	10.80	1.57	7.21	2.37	0.78	3.09	0.53	3.48	0.86	2.37	0.31	2.25	0.31
	MF97-212.0	*BV*	4.60	10.30	1.45	7.13	2.13	0.77	2.94	0.55	3.69	0.77	2.25	0.32	2.05	0.31
		Mean	*4.82*	*10.55*	*1.51*	*7.17*	*2.25*	*0.78*	*3.02*	*0.54*	*3.59*	*0.82*	*2.31*	*0.32*	*2.15*	*0.31*
		S.D.	*0.30*	*0.35*	*0.08*	*0.06*	*0.17*	*0.01*	*0.11*	*0.01*	*0.15*	*0.06*	*0.08*	*0.01*	*0.14*	*0.00*
MF103 Sill 1	**MF103-146.0**	*BV*	4.59	9.74	1.39	7.20	2.19	0.72	2.78	0.50	3.46	0.77	2.18	0.30	1.96	0.29

C.3 Platinum Group Elements Geochemical Data

C.3.1 Melba Flats Mafic Intrusions

TABLE C.5: *PGE geochemical data for the Melba Flats mafic intrusions.*

			Unmineralized Platinum Group Elements				
			(ppm)	(ppb)			(ppm)
		Lab	Ni	Pt	Pd	Au	Cu
MF17 Sill 1	**MF17-69.6**	*BV*	361.48	0.05	0.05	0.90	103.85
	MF17-70.8	*BV*	565.80	3.30	1.70	3.00	207.70
	MF17-71.7	*BV*	385.06	0.70	0.05	0.90	87.87
	MF17-72.9	*BV*	345.77	0.05	0.05	1.40	71.90
		Mean	*414.53*	*1.03*	*0.46*	*1.55*	*117.83*
		S.D.	*102.13*	*1.55*	*0.83*	*0.99*	*61.32*
MF93 Sill 1	**MF93-128.55**	*GEO*	267.20	0.26	0.27	0.49	65.40
MF93 Sill 3	**MF93-306.1**	*GEO*	576.60	0.92	0.99	0.61	132.70
	MF93-310.55	*GEO*	370.30	0.62	0.73	1.14	106.30
	MF93-311.85	*BV*	361.48	0.05	0.05	0.70	119.83
		Mean	*436.13*	*0.53*	*0.59*	*0.82*	*119.61*
		S.D.	*121.73*	*0.44*	*0.49*	*0.28*	*13.20*
MF93 Sill 4	**MF93-323.3**	*GEO*	71.60	0.39	4.79	0.56	5.40
	MF93-330.55	*GEO*	24.80	0.09	0.06	0.90	40.20
	MF93-345.4	*GEO*	77.10	0.09	0.06	0.59	53.20
	MF93-356.0	*GEO*	126.80	0.09	0.06	0.47	66.60
	MF93-356.3	*ACME*	137.00	0.50	1.00	3.00	85.20
	MF93-365.2	*GEO*	312.80	0.33	0.45	0.46	47.80
	MF93-368.86	*GEO*	537.40	0.19	0.23	0.41	2.80
	MF93-376.5	*ACME*	2004.00	56.20	60.80	5.40	247.20
	MF93-380.1	*ACME*	2877.00	42.40	120.70	1.50	829.80
	MF93-381.3	*GEO*	2059.80	23.90	74.20	1.73	507.20
		Mean	*822.83*	*12.42*	*26.24*	*1.50*	*188.54*
		S.D.	*1064.51*	*21.04*	*43.35*	*1.60*	*272.83*
MF95 Sill 2	**MF95-212.15**	*BV*	337.91	0.05	0.05	1.90	119.83
	MF95-216.3	*BV*	306.47	0.10	0.05	0.40	87.87
	MF95-218.5	*BV*	345.77	0.05	0.05	0.70	119.83
	MF95-222.45	*BV*	848.70	0.70	0.20	1.00	175.75
	MF95-234.8	*BV*	392.91	0.05	0.05	0.60	111.84
		Mean	*446.35*	*0.19*	*0.08*	*0.92*	*123.02*
		S.D.	*227.04*	*0.29*	*0.07*	*0.59*	*32.25*
MF97 Sill 1	**MF97-209.2**	*BV*	1005.86	0.20	0.05	34.40	175.75
	MF97-215.9	*BV*	762.26	6.90	5.50	3.90	431.38
		Mean	*884.06*	*3.55*	*2.78*	*19.15*	*303.56*
		S.D.	*172.26*	*4.74*	*3.85*	*21.57*	*180.76*
MF103 Sill 1	**MF103-101.4**	*BV*	557.94	0.05	0.05	0.40	79.88
	MF103-105.35	*BV*	667.96	0.20	0.20	0.70	159.77
	MF103-111.2	*BV*	534.36	1.20	0.05	0.90	127.81
	MF103-115.3	*BV*	392.91	0.05	0.05	0.60	103.85
	MF103-119.9	*BV*	385.06	0.05	0.05	0.70	103.85
	MF103-124	*BV*	385.06	0.05	0.05	1.70	103.85
	MF103-129.05	*BV*	432.21	0.40	0.05	0.50	119.83
	MF103-133.3	*BV*	510.79	0.10	0.50	0.90	127.81
	MF103-137.5	*BV*	581.51	0.70	0.05	0.90	119.83
	MF103-141.7	*BV*	534.36	0.05	0.05	1.00	159.77
	MF103-143.65	*BV*	495.07	1.10	0.05	0.50	111.84
		Mean	*497.93*	*0.36*	*0.10*	*0.80*	*119.83*
		S.D.	*91.19*	*0.44*	*0.14*	*0.36*	*23.97*

TABLE C.5 (continued): PGE geochemical data for the Melba Flats mafic intrusions.

			Mineralized Platinum Group Elements				
			(ppm)	(ppb)			(ppm)
		Lab	Ni	Pt	Pd	Au	Cu
MF19 Sill 1	**MF19-34.25**	*BV*	6090.18	226.00	268.00	27.80	1310.10
	MF19-39.5	*ACME*	59800.00	794.00	1971.00	607.00	59800.00
	MF19-41.32	*ACME*	81200.00	576.60	861.20	516.00	66900.00
		Mean	*49030.06*	*532.20*	*1033.40*	*383.60*	*42670.03*
		S.D.	*38695.80*	*286.59*	*864.46*	*311.47*	*35994.24*
MF23 Sill 2	**MF23-64.8**	*ACME*	5031.60	35.20	131.10	112.40	9531.60
	MF23-65.3	*ACME*	70200.00	1057.00	665.00	794.90	32900.00
	MF23-65.5	*ACME*	200160.00	885.00	1361.00	961.00	6422.40
	MF23-65.6	*ACME*	6724.80	257.60	310.20	106.30	7860.70
	MF23-74.5	*ACME*	16700.00	103.10	188.50	35.90	4807.40
	MF23-74.6	*ACME*	141100.00	556.20	482.90	241.90	58700.00
	MF23-75	*ACME*	22800.00	167.10	230.40	32.40	6096.90
		Mean	*66102.34*	*437.31*	*481.30*	*326.40*	*18045.57*
		S.D.	*76576.66*	*403.58*	*429.77*	*386.09*	*20423.74*
MF81A Sill 1	**MF81A-171.5**	*ACME*	3308.00	100.60	140.90	93.00	3268.90
	MF81A-174.44	*ACME*	144700.00	3323.00	1022.00	513.00	24400.00
	MF81A-174.52	*ACME*	97900.00	881.40	710.10	361.60	37300.00
		Mean	*81969.33*	*1435.00*	*624.33*	*322.53*	*21656.30*
		S.D.	*72029.61*	*1681.02*	*446.77*	*212.71*	*17180.65*
MF83 Sill 1	**MF83-139.0**	*BV*	9822.87	164.00	229.00	113.00	6127.13
	MF83-139.55	*ACME*	23200.00	343.60	541.20	401.90	15200.00
		Mean	*16511.44*	*253.80*	*385.10*	*257.45*	*10663.56*
		S.D.	*9459.06*	*127.00*	*220.76*	*204.28*	*6415.49*
MF93 Sill 2	**MF93-151.55**	*GEO*	5808.22	96.10	131.00	57.50	3895.05
	MF93-155.21	*GEO*	20241.68	308.00	625.00	122.00	13230.04
		Mean	*13024.95*	*202.05*	*378.00*	*89.75*	*8562.54*
		S.D.	*10206.00*	*149.84*	*349.31*	*45.61*	*6600.84*
MF93 Sill 3	**MF93-304.0**	*GEO*	16.30	0.48	0.49	2.44	139.00
MF93 Sill 4	**MF93-335.2**	*ACME*	35.00	0.70	1.40	3.00	266.10
MF95 Sill 1	**MF95-123.35**	*GEO*	20320.46	238.00	322.00	156.00	12102.85
MF97 Sill 1	**MF97-207.7**	*BV*	141.45	0.05	0.05	9.90	119.83
	MF97-212.0	*BV*	8329.80	115.00	165.00	61.90	4745.13
		Mean	*4235.62*	*57.53*	*82.53*	*35.90*	*2432.48*
		S.D.	*5790.04*	*81.28*	*116.64*	*36.77*	*3270.58*
MF103 Sill 1	**MF103-146.0**	*BV*	416.49	0.05	0.05	2.60	71.90

Appendix D

$^{40}Ar^*/^{39}Ar$ Analytical Data

D.1 ARGUS-VI $^{40}Ar^*/^{39}Ar$ Detrital Muscovite Analytical Data

TABLE D.1: $^{40}Ar^*/^{39}Ar$ analytical data from ARGUS-VI laser step-heating analyses of single muscovite grains.[a]

Sample ID	Step No.	Laser Power (%)	Laser Power (W)	^{40}Ar (fA)	± 1σ	^{39}Ar (fA)[b]	± 1σ	^{38}Ar (fA)	± 1σ	^{37}Ar (fA)[b]	± 1σ	^{36}Ar (fA)	± 1σ	^{39}Ar (x10^{-14} moles)	Ca/K	± 1σ	$\%^{40}Ar^*$	$^{40}Ar^*/^{39}Ar$	± 1σ	Cum.% ^{39}Ar	Age (Ma)	± 1σ	Included in Weighted Mean Age Calculation?	Total Gas Age Calculation: $^{39}Ar/^{39}Ar_{Total}$	Total Gas Age Calculation: Calc $(^{40}Ar^*/^{39}Ar)_{Total}$	Total Gas Age Calculation: ± 1σ
Sample MF40 - 56.3 m			***J-Value =***	***0.020701***	***±***	***0.0000079493***	***(1σ)***	***0.038***	***%***[c]																	
Aliquot MF40-1			***Single Muscovite Grain***																							
MF40-1a	1	1	0.22	82.6221	0.0322	4.6916	0.0048	0.0015	0.0000	-0.0188	-0.5023	0.0078	0.0003	0.0167	-0.01	-0.19	97.2	17.113	0.025	3.73	547.087	0.692		0.0373	0.6381	0.0009
MF40-1b	2	3	0.75	1889.2594	0.5668	91.3774	0.0265	0.0014	0.0001	-0.6501	-0.4283	0.0076	0.0004	0.3244	-0.01	-0.01	99.9	20.651	0.009	76.36	642.112	0.228	Y	0.7263	14.9983	0.0063
MF40-1c	3	5	1.22	225.9145	0.0587	10.8936	0.0196	0.0001	0.0001	0.0887	0.4166	0.0006	0.0003	0.0387	0.01	0.07	99.9	20.721	0.039	85.02	643.955	1.013	Y	0.0866	1.7941	0.0034
MF40-1d	4	10	2.18	265.4506	0.0849	12.7920	0.0145	0.0003	0.0001	0.1007	0.6009	0.0017	0.0003	0.0454	0.01	0.08	99.8	20.712	0.025	95.18	643.707	0.664	Y	0.1017	2.1058	0.0026
MF40-1e	5	30	5.31	126.5048	0.0417	6.0596	0.0092	0.0031	0.0001	0.1946	0.3773	0.0165	0.0004	0.0215	0.06	0.11	96.1	20.066	0.037	100.00	626.747	0.977		0.0482	0.9664	0.0018
Total						125.8141												20.503	0.015		638.241	0.220		1.0000	20.5029	0.0150
Total Gas Age[d]***:***																								***638.2***	***±***	***0.2*** ***(1σ)***
Plateau Age[d]***:***								^{39}Ar %	-			*MSWD*	-				*Prob. of fit*	-						***No Plateau***		
Weighted Mean Age[d]***, Steps 2 to 4:***								^{39}Ar %	*91.5*			*MSWD*	*3.9*				*Prob. of fit*	*0.021*						***642.4***	***±***	***0.3*** ***(1σ)***

[a] Data was corrected for mass spectrometer backgrounds, discrimination, radioactive decay and interference corrections. All negative values were set to zero for the correction of the data.

[b] Interference corrections: $(^{36}Ar/^{37}Ar)_{Ca} = (2.5782 \pm 0.0018) \times 10^{-4}$; $(^{39}Ar/^{37}Ar)_{Ca} = (6.5620 \pm 0.0164) \times 10^{-4}$; $(^{40}Ar/^{39}Ar)_{K} = (0.0000 \pm 0.0000) \times 10^{-4}$; $(^{38}Ar/^{39}Ar)_{K} = (1.2246 \pm 0.0028) \times 10^{-2}$.

[c] J-value was calculated relative to an assumed age of 28.02 ± 0.14 Ma (1σ) for the Fish Canyon Tuff sanidine (Renne et al. 1998).

[d] All errors associated with the total gas, plateau and weighted mean ages are reported at the 1σ level and include the uncertainties in the J-value.

TABLE D.1 (continued): $^{40}Ar^*/^{39}Ar$ analytical data from ARGUS-VI laser step-heating analyses of single muscovite grains.[a]

Sample ID	Step No.	Laser Power (%)	Laser Power (W)	^{40}Ar (fA)	± 1σ	^{39}Ar (fA)[b]	± 1σ	^{38}Ar (fA)	± 1σ	^{37}Ar (fA)[b]	± 1σ	^{36}Ar (fA)	± 1σ	^{39}Ar (x10^{-14} moles)	Ca/K	± 1σ	%$^{40}Ar^*$	$^{40}Ar^*/^{39}Ar$	± 1σ	Cum.% ^{39}Ar	Age (Ma)	± 1σ	Included in Weighted Mean Age Calculation?	Total Gas Age Calculation: $^{39}Ar/^{39}Ar_{Total}$	Total Gas Age Calculation: Calc $(^{40}Ar^*/^{39}Ar)_{Total}$	Total Gas Age Calculation: ± 1σ
Sample MF40 - 56.3 m			***J-Value =***	***0.020701***	***±***	***0.0000079493***	***(1σ)***	***0.038***	***%***[c]																	
Aliquot MF40-2			***Single Muscovite Grain***																							
MF40-2a	1	1	0.22	148.3443	0.0445	7.2023	0.0170	0.0045	0.0001	3.4119	0.7043	0.0238	0.0004	0.0256	0.83	0.17	95.2	19.609	0.050	2.47	614.654	1.322		0.0247	0.4838	0.0012
MF40-2b	2	3	0.75	4774.6989	1.4324	228.6646	0.0938	0.0235	0.0002	0.4645	0.7675	0.1246	0.0010	0.8118	0.00	0.01	99.2	20.718	0.011	80.79	643.877	0.278	Y	0.7832	16.2274	0.0083
MF40-2c	3	5	1.22	376.1020	0.0865	18.0596	0.0154	0.0008	0.0001	1.1066	0.8569	0.0041	0.0004	0.0641	0.11	0.08	99.7	20.758	0.019	86.98	644.915	0.503	Y	0.0619	1.2841	0.0012
MF40-2d	4	10	2.18	83.4267	0.0325	4.0151	0.0101	0.0002	0.0001	0.0020	0.7329	0.0011	0.0003	0.0143	0.00	0.32	99.6	20.694	0.058	88.35	643.258	1.510	Y	0.0138	0.2846	0.0008
MF40-2e	5	30	5.31	709.0687	0.2127	34.0043	0.0279	0.0008	0.0001	-0.0736	-0.5980	0.0043	0.0005	0.1207	0.00	-0.03	99.8	20.814	0.019	100.00	646.386	0.486		0.1165	2.4243	0.0022
Total						291.9458												20.704	0.014		643.510	0.219		1.0000	20.7041	0.0137
Total Gas Age[d]***:***																									***643.5 ± 0.2 (1σ)***	
Plateau Age[d]***:***								^{39}Ar %	*85.9*		*MSWD*	*1.8*					*Prob. of fit*	*0.17*							***644.1 ± 0.3 (1σ)***	
Weighted Mean Age[d]***, Steps 2 to 4:***								^{39}Ar %	*85.9*		*MSWD*	*1.8*					*Prob. of fit*	*0.17*							***644.1 ± 0.3 (1σ)***	

[a] Data was corrected for mass spectrometer backgrounds, discrimination, radioactive decay and interference corrections. All negative values were set to zero for the correction of the data.

[b] Interference corrections: $(^{36}Ar/^{37}Ar)_{Ca} = (2.5782 \pm 0.0018) \times 10^{-4}$; $(^{39}Ar/^{37}Ar)_{Ca} = (6.5620 \pm 0.0164) \times 10^{-4}$; $(^{40}Ar/^{39}Ar)_{K} = (0.0000 \pm 0.0000) \times 10^{-4}$; $(^{38}Ar/^{39}Ar)_{K} = (1.2246 \pm 0.0028) \times 10^{-2}$.

[c] J-value was calculated relative to an assumed age of 28.02 ± 0.14 Ma (1σ) for the Fish Canyon Tuff sanidine (Renne et al. 1998).

[d] All errors associated with the total gas, plateau and weighted mean ages are reported at the 1σ level and include the uncertainties in the J-value.

TABLE D.1 (continued): $^{40}Ar^*/^{39}Ar$ analytical data from ARGUS-VI laser step-heating analyses of single muscovite grains.[a]

Sample ID	Step No.	Laser Power (%)	Laser Power (W)	^{40}Ar (fA)	± 1σ	^{39}Ar (fA)[b]	± 1σ	^{38}Ar (fA)	± 1σ	^{37}Ar (fA)[b]	± 1σ	^{36}Ar (fA)	± 1σ	^{39}Ar (x10^{-14} moles)	Ca/K	± 1σ	%$^{40}Ar^*$	$^{40}Ar^*/^{39}Ar$	± 1σ	Cum.% ^{39}Ar	Age (Ma)	± 1σ	Included in Weighted Mean Age Calculation?	Total Gas Age Calculation: $^{39}Ar/^{39}Ar_{Total}$	Total Gas Age Calculation: Calc $(^{40}Ar^*/^{39}Ar)_{Total}$	Total Gas Age Calculation: ± 1σ
Sample MF40 - 56.3 m			***J-Value =***	***0.020701***	***±***	***0.0000079493***	***(1σ)***	***0.038***	***%[c]***																	
Aliquot MF40-3			***Single Muscovite Grain***																							
MF40-3a	1	1	0.22	239.9571	0.1080	10.3235	0.0181	0.0050	0.0001	-0.1035	-0.7312	0.0263	0.0007	0.0366	-0.02	-0.12	96.7	22.482	0.045	4.19	689.406	1.157		0.0419	0.9415	0.0019
MF40-3b	2	3	0.75	4854.0386	1.3591	194.2668	0.0816	0.0196	0.0001	0.0907	0.7682	0.1039	0.0005	0.6896	0.00	0.01	99.4	24.827	0.013	82.99	748.190	0.310	Y	0.7881	19.5650	0.0099
MF40-3c	3	5	1.22	172.4278	0.0466	6.9072	0.0041	0.0002	0.0001	0.3971	1.1517	0.0013	0.0004	0.0245	0.10	0.29	99.8	24.908	0.024	85.80	750.203	0.598	Y	0.0280	0.6979	0.0007
MF40-3d	4	10	2.18	260.9547	0.0626	10.4630	0.0131	0.0004	0.0001	-0.6706	-0.4584	0.0020	0.0003	0.0371	-0.11	-0.08	99.8	24.883	0.033	90.04	749.568	0.804	Y	0.0424	1.0561	0.0014
MF40-3e	5	30	5.31	597.2746	0.1254	24.5529	0.0165	0.0042	0.0001	-0.5629	-0.5939	0.0225	0.0004	0.0872	-0.04	-0.04	98.9	24.052	0.018	100.00	728.979	0.440		0.0996	2.3956	0.0018
Total						246.5133												24.656	0.016		743.974	0.251		1.0000	24.6561	0.0156

Total Gas Age[d]:							***744.0 ± 0.3 (1σ)***
Plateau Age[d]:	^{39}Ar %	-	MSWD	-	Prob. of fit	-	***No Plateau***
Weighted Mean Age[d], Steps 2 to 4:	^{39}Ar %	*85.9*	MSWD	*5.1*	Prob. of fit	*0.006*	***748.8 ± 0.4 (1σ)***

[a] Data was corrected for mass spectrometer backgrounds, discrimination, radioactive decay and interference corrections. All negative values were set to zero for the correction of the data.

[b] Interference corrections: $(^{36}Ar/^{37}Ar)_{Ca} = (2.5782 \pm 0.0018) \times 10^{-4}$; $(^{39}Ar/^{37}Ar)_{Ca} = (6.5620 \pm 0.0164) \times 10^{-4}$; $(^{40}Ar/^{39}Ar)_{K} = (0.0000 \pm 0.0000) \times 10^{-4}$; $(^{38}Ar/^{39}Ar)_{K} = (1.2246 \pm 0.0028) \times 10^{-2}$.

[c] J-value was calculated relative to an assumed age of 28.02 ± 0.14 Ma (1σ) for the Fish Canyon Tuff sanidine (Renne et al. 1998).

[d] All errors associated with the total gas, plateau and weighted mean ages are reported at the 1σ level and include the uncertainties in the J-value.

TABLE D.1 (continued): $^{40}Ar^*/^{39}Ar$ analytical data from ARGUS-VI laser step-heating analyses of single muscovite grains.[a]

Sample ID	Step No.	Laser Power (%)	Laser Power (W)	^{40}Ar (fA)	± 1σ	^{39}Ar (fA)[b]	± 1σ	^{38}Ar (fA)	± 1σ	^{37}Ar (fA)[b]	± 1σ	^{36}Ar (fA)	± 1σ	^{39}Ar (x10^{-14} moles)	Ca/K	± 1σ	%$^{40}Ar^*$	$^{40}Ar^*/^{39}Ar$	± 1σ	Cum.% ^{39}Ar	Age (Ma)	± 1σ	Included in Weighted Mean Age Calculation?	Total Gas Age Calculation: $^{39}Ar/^{39}Ar_{total}$	Total Gas Age Calculation: Calc $(^{40}Ar^*/^{39}Ar)_{Total}$	Total Gas Age Calculation: ± 1σ
Sample MF40 - 56.3 m			***J-Value =***	***0.020701***	±	***0.0000079493***	***(1σ)***	***0.038***	***%***[c]																	
Aliquot MF40-4			***Single Muscovite Grain***																							
MF40-4a	1	1	0.22	144.3297	0.0361	8.2809	0.0076	0.0024	0.0001	2.3558	0.6584	0.0129	0.0005	0.0294	0.50	0.14	97.3	16.962	0.023	2.32	542.943	0.649		0.0232	0.3938	0.0005
MF40-4b	2	3	0.75	3240.4658	1.2962	156.8349	0.0831	0.0083	0.0000	1.4755	0.5079	0.0443	0.0002	0.5568	0.02	0.01	99.6	20.577	0.014	46.29	640.193	0.359		0.4397	9.0469	0.0060
MF40-4c	3	5	1.22	2637.8009	0.8441	127.0827	0.0445	0.0022	0.0001	1.0324	0.7391	0.0119	0.0004	0.4511	0.01	0.01	99.9	20.729	0.010	81.91	644.151	0.259	Y	0.3562	7.3845	0.0035
MF40-4d	4	7	1.51	986.2150	0.2959	47.4403	0.0157	0.0004	0.0000	0.0495	0.4570	0.0024	0.0003	0.1684	0.00	0.02	99.9	20.774	0.009	95.21	645.325	0.246	Y	0.1330	2.7626	0.0013
MF40-4e	5	10	2.18	211.0217	0.0612	10.1248	0.0094	0.0001	0.0001	0.4704	0.6321	0.0003	0.0003	0.0359	0.08	0.11	100.0	20.834	0.022	98.05	646.903	0.586	Y	0.0284	0.5913	0.0006
MF40-4f	6	30	5.31	147.0006	0.0338	6.9617	0.0191	0.0006	0.0001	-0.1529	-0.7070	0.0033	0.0003	0.0247	-0.04	-0.18	99.3	20.975	0.059	100.00	650.572	1.537		0.0195	0.4093	0.0012
Total						356.7254												20.179	0.012		629.733	0.212		1.0000	20.1791	0.0120
Total Gas Age[d]:																								***629.7 ± 0.2 (1σ)***		
Plateau Age[d]:									^{39}Ar %	-		MSWD	-				Prob. of fit	-						***No Plateau***		
Weighted Mean Age[d], Steps 3 to 5:									^{39}Ar %	*51.8*		MSWD	*11.5*				Prob. of fit	*0.001*						***644.9 ± 0.3 (1σ)***		

[a] Data was corrected for mass spectrometer backgrounds, discrimination, radioactive decay and interference corrections. All negative values were set to zero for the correction of the data.

[b] Interference corrections: $(^{36}Ar/^{37}Ar)_{Ca} = (2.5782 \pm 0.0018) \times 10^{-4}$; $(^{39}Ar/^{37}Ar)_{Ca} = (6.5620 \pm 0.0164) \times 10^{-4}$; $(^{40}Ar/^{39}Ar)_{K} = (0.0000 \pm 0.0000) \times 10^{-4}$; $(^{38}Ar/^{39}Ar)_{K} = (1.2246 \pm 0.0028) \times 10^{-2}$.

[c] J-value was calculated relative to an assumed age of 28.02 ± 0.14 Ma (1σ) for the Fish Canyon Tuff sanidine (Renne et al. 1998).

[d] All errors associated with the total gas, plateau and weighted mean ages are reported at the 1σ level and include the uncertainties in the J-value.

TABLE D.1 (continued): $^{40}Ar^*/^{39}Ar$ analytical data from ARGUS-VI laser step-heating analyses of single muscovite grains.[a]

Sample ID	Step No.	Laser Power (%)	Laser Power (W)	^{40}Ar (fA)	± 1σ	^{39}Ar (fA)[b]	± 1σ	^{38}Ar (fA)	± 1σ	^{37}Ar (fA)[b]	± 1σ	^{36}Ar (fA)	± 1σ	^{39}Ar (x10^{-14} moles)	Ca/K	± 1σ	%$^{40}Ar^*$	$^{40}Ar^*/^{39}Ar$	± 1σ	Cum.% ^{39}Ar	Age (Ma)	± 1σ	Included in Weighted Mean Age Calculation?	Total Gas Age Calculation: $^{39}Ar/^{39}Ar_{Total}$	Total Gas Age Calculation: Calc $(^{40}Ar^*/^{39}Ar)_{Total}$	Total Gas Age Calculation: ± 1σ
Sample MF40 - 56.3 m			***J-Value =***	***0.020701***	***±***	***0.0000079493***	***(1σ)***	***0.038***	***%[c]***																	
Aliquot MF40-5			***Single Muscovite Grain***																							
MF40-5a	1	1	0.22	157.7349	0.0536	8.2476	0.0213	0.0068	0.0001	-0.5187	-0.7634	0.0362	0.0003	0.0293	-0.11	-0.16	93.1	17.814	0.048	1.55	566.340	1.308		0.0155	0.2768	0.0007
MF40-5b	2	3	0.75	3020.7795	0.8760	145.5222	0.0262	0.0115	0.0001	0.7454	0.9056	0.0608	0.0003	0.5166	0.01	0.01	99.4	20.633	0.007	28.97	641.661	0.186		0.2741	5.6565	0.0019
MF40-5c	3	5	1.22	2588.8936	0.8802	124.9448	0.0575	0.0024	0.0001	-0.7618	-0.8573	0.0127	0.0004	0.4436	-0.01	-0.01	99.9	20.690	0.012	52.51	643.140	0.311	Y	0.2354	4.8699	0.0028
MF40-5d	4	7	1.51	3410.1118	1.1253	164.3213	0.0493	0.0019	0.0001	0.3672	0.8771	0.0099	0.0005	0.5833	0.00	0.01	99.9	20.735	0.009	83.46	644.312	0.243	Y	0.3096	6.4186	0.0029
MF40-5e	5	10	2.18	603.9397	0.1631	29.0676	0.0253	0.0005	0.0001	0.1894	0.5698	0.0029	0.0003	0.1032	0.01	0.03	99.9	20.747	0.019	88.94	644.641	0.501	Y	0.0548	1.1361	0.0010
MF40-5f	6	30	5.31	1224.9182	0.3185	58.7247	0.0270	0.0009	0.0000	-0.3187	-0.5455	0.0048	0.0002	0.2085	-0.01	-0.02	99.9	20.834	0.011	100.00	646.907	0.289		0.1106	2.3049	0.0012
Total						530.8282												20.663	0.011		642.429	0.213		1.0000	20.6628	0.0106
Total Gas Age[d]:																									***642.4 ± 0.2 (1σ)***	
Plateau Age[d]:									^{39}Ar %	-		MSWD	-				Prob. of fit	-							***No Plateau***	
Weighted Mean Age[d], Steps 3 to 5:									^{39}Ar %	*60.0*		MSWD	*5.5*				Prob. of fit	*0.004*							***644.0 ± 0.3 (1σ)***	

[a] Data was corrected for mass spectrometer backgrounds, discrimination, radioactive decay and interference corrections. All negative values were set to zero for the correction of the data.

[b] Interference corrections: $(^{36}Ar/^{37}Ar)_{Ca} = (2.5782 \pm 0.0018) \times 10^{-4}$; $(^{39}Ar/^{37}Ar)_{Ca} = (6.5620 \pm 0.0164) \times 10^{-4}$; $(^{40}Ar/^{39}Ar)_{K} = (0.0000 \pm 0.0000) \times 10^{-4}$; $(^{38}Ar/^{39}Ar)_{K} = (1.2246 \pm 0.0028) \times 10^{-2}$.

[c] J-value was calculated relative to an assumed age of 28.02 ± 0.14 Ma (1σ) for the Fish Canyon Tuff sanidine (Renne et al. 1998).

[d] All errors associated with the total gas, plateau and weighted mean ages are reported at the 1σ level and include the uncertainties in the J-value.

TABLE D.1 (continued): $^{40}Ar^*/^{39}Ar$ analytical data from ARGUS-VI laser step-heating analyses of single muscovite grains.[a]

Sample ID	Step No.	Laser Power (%)	Laser Power (W)	^{40}Ar (fA)	± 1σ	^{39}Ar (fA)[b]	± 1σ	^{38}Ar (fA)	± 1σ	^{37}Ar (fA)[b]	± 1σ	^{36}Ar (fA)	± 1σ	^{39}Ar (x10^{-14} moles)	Ca/K	± 1σ	%$^{40}Ar^*$	$^{40}Ar^*/^{39}Ar$	± 1σ	Cum.% ^{39}Ar	Age (Ma)	± 1σ	Included in Weighted Mean Age Calculation?	Total Gas Age Calculation: $^{39}Ar/^{39}Ar_{Total}$	Total Gas Age Calculation: Calc ($^{40}Ar^*/^{39}Ar)_{Total}$	Total Gas Age Calculation: ± 1σ
Sample MF40 - 56.3 m			***J-Value =***	***0.020701***	***±***	***0.0000079493***	***(1σ)***	***0.038***	***%[c]***																	
Aliquot MF40-6			***Single Muscovite Grain***																							
MF40-6a	1	1	0.22	170.9515	0.0444	8.3753	0.0121	0.0024	0.0001	0.7354	0.4575	0.0125	0.0003	0.0297	0.15	0.10	97.8	19.965	0.032	1.40	624.085	0.837		0.0140	0.2805	0.0004
MF40-6b	2	2	0.51	8321.0923	4.5766	335.7002	0.2048	0.0200	0.0002	1.7215	0.5195	0.1059	0.0010	1.1917	0.01	0.00	99.6	24.693	0.020	57.72	744.887	0.503	Y	0.5631	13.9049	0.0115
MF40-6c	3	3	0.75	1260.3298	0.5041	50.7793	0.0218	0.0022	0.0001	0.2806	0.7991	0.0119	0.0003	0.1803	0.01	0.03	99.7	24.750	0.015	66.23	746.290	0.362	Y	0.0852	2.1081	0.0012
MF40-6d	4	5	1.22	1216.6792	0.3893	48.8917	0.0274	0.0018	0.0001	-0.5594	-0.6582	0.0093	0.0004	0.1736	-0.02	-0.02	99.8	24.828	0.016	74.44	748.226	0.400	Y	0.0820	2.0362	0.0013
MF40-6e	5	7	1.51	857.4700	0.1972	34.4260	0.0196	0.0004	0.0001	-0.3244	-0.6154	0.0021	0.0003	0.1222	-0.02	-0.03	99.9	24.890	0.016	80.21	749.737	0.383		0.0577	1.4373	0.0009
MF40-6f	6	10	2.18	288.5095	0.1067	11.5623	0.0153	0.0003	0.0001	0.0758	0.5686	0.0018	0.0004	0.0410	0.01	0.09	99.8	24.906	0.036	82.15	750.132	0.885		0.0194	0.4830	0.0007
MF40-6g	7	30	5.31	2656.2625	0.7703	106.4177	0.0245	0.0019	0.0001	-0.0769	-0.7689	0.0102	0.0005	0.3778	0.00	-0.01	99.9	24.932	0.009	100.00	750.785	0.230		0.1785	4.4506	0.0017
Total						596.1525												24.701	0.018		745.076	0.256		1.0000	24.7007	0.0177
Total Gas Age[d]:																									***745.1 ± 0.3 (1σ)***	
Plateau Age[d]:									^{39}Ar %	-		MSWD	-				Prob. of fit	-							***No Plateau***	
Weighted Mean Age[d], Steps 2 to 4:									^{39}Ar %	*73.0*		MSWD	*14.0*				Prob. of fit	*0.001*							***746.7 ± 0.3 (1σ)***	

[a] Data was corrected for mass spectrometer backgrounds, discrimination, radioactive decay and interference corrections. All negative values were set to zero for the correction of the data.

[b] Interference corrections: $(^{36}Ar/^{37}Ar)_{Ca} = (2.5782 \pm 0.0018) \times 10^{-4}$; $(^{39}Ar/^{37}Ar)_{Ca} = (6.5620 \pm 0.0164) \times 10^{-4}$; $(^{40}Ar/^{39}Ar)_{K} = (0.0000 \pm 0.0000) \times 10^{-4}$; $(^{38}Ar/^{39}Ar)_{K} = (1.2246 \pm 0.0028) \times 10^{-2}$.

[c] J-value was calculated relative to an assumed age of 28.02 ± 0.14 Ma (1σ) for the Fish Canyon Tuff sanidine (Renne et al. 1998).

[d] All errors associated with the total gas, plateau and weighted mean ages are reported at the 1σ level and include the uncertainties in the J-value.

TABLE D.2: *$^{40}Ar^*/^{39}Ar$ raw analytical data from ARGUS-VI laser step-heating analyses of single muscovite grains.*[a]

Sample ID	Step No.	Laser Power (%)	Laser Power (W)	^{40}Ar (fA)	± 1σ	^{39}Ar (fA)	± 1σ	^{38}Ar (fA)	± 1σ	^{37}Ar (fA)	± 1σ	^{36}Ar (fA)	± 1σ
Sample MF40 - 56.3 m			***J-Value =***	***0.020701***	±	***0.0000079493 (1σ)***		***0.038 %***[a]					
Aliquot MF40-1			***Single Muscovite Grain***										
MF40-1a	1	1	0.22	82.6221	0.0322	4.6916	0.0048	0.0725	0.0239	-0.0188	-0.5023	0.0078	0.0002
MF40-1b	2	3	0.75	1889.2594	0.5668	91.3769	0.0265	1.1059	0.0227	-0.6501	-0.4283	0.0074	0.0003
MF40-1c	3	5	1.22	225.9145	0.0587	10.8937	0.0196	0.1798	0.0569	0.0887	0.4166	0.0007	0.0003
MF40-1d	4	10	2.18	265.4506	0.0849	12.7921	0.0145	0.1799	0.0493	0.1007	0.6009	0.0017	0.0003
MF40-1e	5	30	5.31	126.5048	0.0417	6.0597	0.0092	0.0565	0.0426	0.1946	0.3773	0.0165	0.0004

[a] J-value was calculated relative to an assumed age of 28.02 ± 0.14 Ma (1σ) for the Fish Canyon Tuff sanidine (Renne et al. 1998).

TABLE D.2 (continued): $^{40}Ar^*/^{39}Ar$ raw analytical data from ARGUS-VI laser step-heating analyses of single muscovite grains.[a]

Sample ID	Step No.	Laser Power (%)	Laser Power (W)	^{40}Ar (fA)	± 1σ	^{39}Ar (fA)	± 1σ	^{38}Ar (fA)	± 1σ	^{37}Ar (fA)	± 1σ	^{36}Ar (fA)	± 1σ
Sample MF40 - 56.3 m			***J-Value =***	***0.020701***	±	***0.0000079493 (1σ)***		***0.038 %***[a]					
Aliquot MF40-2			***Single Muscovite Grain***										
MF40-2a	1	1	0.22	148.3443	0.0445	7.2045	0.0170	0.0665	0.0445	3.4119	0.7043	0.0247	0.0004
MF40-2b	2	3	0.75	4774.6989	1.4324	228.6649	0.0938	2.8149	0.0296	0.4645	0.7675	0.1247	0.0010
MF40-2c	3	5	1.22	376.1020	0.0865	18.0603	0.0154	0.2331	0.0408	1.1066	0.8569	0.0044	0.0003
MF40-2d	4	10	2.18	83.4267	0.0325	4.0151	0.0101	0.1376	0.0291	0.0020	0.7329	0.0011	0.0003
MF40-2e	5	30	5.31	709.0687	0.2127	34.0042	0.0279	0.4232	0.0280	-0.0736	-0.5980	0.0043	0.0004

[a] J-value was calculated relative to an assumed age of 28.02 ± 0.14 Ma (1σ) for the Fish Canyon Tuff sanidine (Renne et al. 1998).

TABLE D.2 (continued): $^{40}Ar^*/^{39}Ar$ raw analytical data from ARGUS-VI laser step-heating analyses of single muscovite grains.[a]

Sample ID	Step No.	Laser Power		^{40}Ar	± 1σ	^{39}Ar	± 1σ	^{38}Ar	± 1σ	^{37}Ar	± 1σ	^{36}Ar	± 1σ
		(%)	(W)	(fA)		(fA)		(fA)		(fA)		(fA)	
Sample MF40 - 56.3 m			***J-Value =***	***0.020701***	±	***0.0000079493 (1σ)***		***0.038 %***[a]					
Aliquot MF40-3			***Single Muscovite Grain***										
MF40-3a	1	1	0.22	239.9571	0.1080	10.3234	0.0181	0.0951	0.0368	-0.1035	-0.7312	0.0263	0.0007
MF40-3b	2	3	0.75	4854.0386	1.3591	194.2668	0.0816	2.3184	0.0426	0.0907	0.7682	0.1039	0.0005
MF40-3c	3	5	1.22	172.4278	0.0466	6.9074	0.0041	0.1025	0.0425	0.3971	1.1517	0.0014	0.0003
MF40-3d	4	10	2.18	260.9548	0.0626	10.4625	0.0131	0.1384	0.0322	-0.6706	-0.4584	0.0019	0.0002
MF40-3e	5	30	5.31	597.2746	0.1254	24.5526	0.0165	0.3378	0.0333	-0.5629	-0.5939	0.0224	0.0004

[a] J-value was calculated relative to an assumed age of 28.02 ± 0.14 Ma (1σ) for the Fish Canyon Tuff sanidine (Renne et al. 1998).

TABLE D.2 (continued): $^{40}Ar^*/^{39}Ar$ raw analytical data from ARGUS-VI laser step-heating analyses of single muscovite grains.[a]

Sample ID	Step No.	Laser Power (%)	Laser Power (W)	^{40}Ar (fA)	± 1σ	^{39}Ar (fA)	± 1σ	^{38}Ar (fA)	± 1σ	^{37}Ar (fA)	± 1σ	^{36}Ar (fA)	± 1σ
Sample MF40 - 56.3 m			***J-Value =***	***0.020701***	±	***0.0000079493 (1σ)***		***0.038 %***[a]					
Aliquot MF40-4			***Single Muscovite Grain***										
MF40-4a	1	1	0.22	144.3297	0.0361	8.2824	0.0076	0.1336	0.0284	2.3558	0.6584	0.0136	0.0004
MF40-4b	2	3	0.75	3240.4658	1.2962	156.8359	0.0831	1.9131	0.0205	1.4755	0.5079	0.0446	0.0002
MF40-4c	3	5	1.22	2637.8009	0.8441	127.0834	0.0445	1.5543	0.0289	1.0324	0.7391	0.0122	0.0004
MF40-4d	4	7	1.51	986.2150	0.2959	47.4404	0.0157	0.5980	0.0282	0.0495	0.4570	0.0024	0.0002
MF40-4e	5	10	2.18	211.0217	0.0612	10.1251	0.0094	0.1201	0.0324	0.4704	0.6321	0.0004	0.0003
MF40-4f	6	30	5.31	147.0006	0.0338	6.9616	0.0191	0.0959	0.0326	-0.1529	-0.7070	0.0032	0.0002

[a] J-value was calculated relative to an assumed age of 28.02 ± 0.14 Ma (1σ) for the Fish Canyon Tuff sanidine (Renne et al. 1998).

TABLE D.2 (continued): $^{40}Ar^*/^{39}Ar$ raw analytical data from ARGUS-VI laser step-heating analyses of single muscovite grains.[a]

Sample ID	Step No.	Laser Power (%)	Laser Power (W)	^{40}Ar (fA)	± 1σ	^{39}Ar (fA)	± 1σ	^{38}Ar (fA)	± 1σ	^{37}Ar (fA)	± 1σ	^{36}Ar (fA)	± 1σ
Sample MF40 - 56.3 m			***J-Value =***	***0.020701***	±	***0.0000079493 (1σ)***		***0.038 %***[a]					
Aliquot MF40-5			***Single Muscovite Grain***										
MF40-5a	1	1	0.22	157.7349	0.0536	8.2473	0.0213	0.1585	0.0257	-0.5187	-0.7634	0.0361	0.0003
MF40-5b	2	3	0.75	3020.7795	0.8760	145.5227	0.0262	1.8377	0.0300	0.7454	0.9056	0.0610	0.0002
MF40-5c	3	5	1.22	2588.8936	0.8802	124.9443	0.0575	1.5400	0.0433	-0.7618	-0.8573	0.0125	0.0003
MF40-5d	4	7	1.51	3410.1118	1.1253	164.3215	0.0493	2.0142	0.0264	0.3672	0.8771	0.0100	0.0005
MF40-5e	5	10	2.18	603.9397	0.1631	29.0677	0.0253	0.3508	0.0167	0.1894	0.5698	0.0029	0.0003
MF40-5f	6	30	5.31	1224.9182	0.3185	58.7245	0.0270	0.7509	0.0307	-0.3187	-0.5455	0.0047	0.0002

[a] J-value was calculated relative to an assumed age of 28.02 ± 0.14 Ma (1σ) for the Fish Canyon Tuff sanidine (Renne et al. 1998).

TABLE D.2 (continued): $^{40}Ar^*/^{39}Ar$ raw analytical data from ARGUS-VI laser step-heating analyses of single muscovite grains.[a]

Sample ID	Step No.	Laser Power (%)	Laser Power (W)	^{40}Ar (fA)	± 1σ	^{39}Ar (fA)	± 1σ	^{38}Ar (fA)	± 1σ	^{37}Ar (fA)	± 1σ	^{36}Ar (fA)	± 1σ
Sample MF40 - 56.3 m			***J-Value =***	***0.020701***	±	***0.0000079493 (1σ)***		***0.038 %***[a]					
Aliquot MF40-6			***Single Muscovite Grain***										
MF40-6a	1	1	0.22	170.9515	0.0444	8.3758	0.0121	0.1427	0.0365	0.7354	0.4575	0.0127	0.0003
MF40-6b	2	2	0.51	8321.0923	4.5766	335.7014	0.2048	4.0607	0.0254	1.7215	0.5195	0.1064	0.0010
MF40-6c	3	3	0.75	1260.3298	0.5041	50.7794	0.0218	0.5452	0.0396	0.2806	0.7991	0.0119	0.0002
MF40-6d	4	5	1.22	1216.6792	0.3893	48.8914	0.0274	0.5445	0.0278	-0.5594	-0.6582	0.0092	0.0004
MF40-6e	5	7	1.51	857.4700	0.1972	34.4258	0.0196	0.3977	0.0246	-0.3244	-0.6154	0.0020	0.0003
MF40-6f	6	10	2.18	288.5095	0.1067	11.5623	0.0153	0.0967	0.0263	0.0758	0.5686	0.0018	0.0004
MF40-6g	7	30	5.31	2656.2625	0.7703	106.4177	0.0245	1.1847	0.0203	-0.0769	-0.7689	0.0102	0.0004

[a] J-value was calculated relative to an assumed age of 28.02 ± 0.14 Ma (1σ) for the Fish Canyon Tuff sanidine (Renne et al. 1998).

TABLE D.3: *$^{40}Ar^*/^{39}Ar$ blank values from ARGUS-VI laser step-heating analyses of single muscovite grains.*[a]

Sample ID	Step No.	Laser Power (%)	Laser Power (W)	Blank No.	^{40}Ar (fA)	± 1σ	^{39}Ar (fA)	± 1σ	^{38}Ar (fA)	± 1σ	^{37}Ar (fA)	± 1σ	^{36}Ar (fA)	± 1σ
Sample MF40 - 56.3 m			***J-Value =***	***0.020701***	±	***0.0000079493 (1σ)***		***0.038 %***[a]						
Aliquot MF40-1			***Single Muscovite Grain***											
MF40-1a	1	1	0.22	EXB#2	0.6538	0.0177	-0.0155	0.0018	0.0066	0.0088	0.0050	0.0131	0.0072	0.0002
MF40-1b	2	3	0.75	EXB#2	0.6538	0.0177	-0.0155	0.0018	0.0066	0.0088	0.0050	0.0131	0.0072	0.0002
MF40-1c	3	5	1.22	EXB#3	0.7186	0.0384	-0.0199	0.0059	-0.0335	0.0414	-0.0379	0.0096	0.0075	0.0002
MF40-1d	4	10	2.18	EXB#3	0.7186	0.0384	-0.0199	0.0059	-0.0335	0.0414	-0.0379	0.0096	0.0075	0.0002
MF40-1e	5	30	5.31	EXB#3	0.7186	0.0384	-0.0199	0.0059	-0.0335	0.0414	-0.0379	0.0096	0.0075	0.0002

[a] J-value was calculated relative to an assumed age of 28.02 ± 0.14 Ma (1σ) for the Fish Canyon Tuff sanidine (Renne et al. 1998).

TABLE D.3 (continued): $^{40}Ar^*/^{39}Ar$ blank values from ARGUS-VI laser step-heating analyses of single muscovite grains.[a]

Sample ID	Step No.	Laser Power (%)	Laser Power (W)	Blank No.	^{40}Ar (fA)	± 1σ	^{39}Ar (fA)	± 1σ	^{38}Ar (fA)	± 1σ	^{37}Ar (fA)	± 1σ	^{36}Ar (fA)	± 1σ
Sample MF40 - 56.3 m			***J-Value =***	***0.020701***	±	***0.0000079493 (1σ)***		***0.038 %***[a]						
Aliquot MF40-2				***Single Muscovite Grain***										
MF40-2a	1	1	0.22	EXB#5	0.6608	0.0110	-0.0208	0.0096	-0.0088	0.0284	-0.0333	0.0250	0.0073	0.0002
MF40-2b	2	3	0.75	EXB#5	0.6608	0.0110	-0.0208	0.0096	-0.0088	0.0284	-0.0333	0.0250	0.0073	0.0002
MF40-2c	3	5	1.22	EXB#5	0.6608	0.0110	-0.0208	0.0096	-0.0088	0.0284	-0.0333	0.0250	0.0073	0.0002
MF40-2d	4	10	2.18	EXB#6	0.7296	0.0223	-0.0035	0.0091	-0.0161	0.0170	-0.0235	0.0229	0.0080	0.0002
MF40-2e	5	30	5.31	EXB#6	0.7296	0.0223	-0.0035	0.0091	-0.0161	0.0170	-0.0235	0.0229	0.0080	0.0002

[a] J-value was calculated relative to an assumed age of 28.02 ± 0.14 Ma (1σ) for the Fish Canyon Tuff sanidine (Renne et al. 1998).

TABLE D.3 (continued): $^{40}Ar^*/^{39}Ar$ blank values from ARGUS-VI laser step-heating analyses of single muscovite grains.[a]

Sample ID	Step No.	Laser Power (%)	Laser Power (W)	Blank No.	^{40}Ar (fA)	± 1σ	^{39}Ar (fA)	± 1σ	^{38}Ar (fA)	± 1σ	^{37}Ar (fA)	± 1σ	^{36}Ar (fA)	± 1σ
Sample MF40 - 56.3 m			***J-Value =***	***0.020701***	±	***0.0000079493 (1σ)***		***0.038 %***[a]						
Aliquot MF40-3				***Single Muscovite Grain***										
MF40-3a	1	1	0.22	EXB#7	0.8363	0.0178	0.0041	0.0024	-0.0100	0.0304	-0.0141	0.0277	0.0080	0.0002
MF40-3b	2	3	0.75	EXB#7	0.8363	0.0178	0.0041	0.0024	-0.0100	0.0304	-0.0141	0.0277	0.0080	0.0002
MF40-3c	3	5	1.22	EXB#7	0.8363	0.0178	0.0041	0.0024	-0.0100	0.0304	-0.0141	0.0277	0.0080	0.0002
MF40-3d	4	10	2.18	EXB#8	0.7203	0.0234	-0.0029	0.0070	-0.0367	0.0241	0.0020	0.0111	0.0076	0.0002
MF40-3e	5	30	5.31	EXB#8	0.7203	0.0234	-0.0029	0.0070	-0.0367	0.0241	0.0020	0.0111	0.0076	0.0002

[a] J-value was calculated relative to an assumed age of 28.02 ± 0.14 Ma (1σ) for the Fish Canyon Tuff sanidine (Renne et al. 1998).

TABLE D.3 (continued): $^{40}Ar^*/^{39}Ar$ blank values from ARGUS-VI laser step-heating analyses of single muscovite grains.[a]

Sample ID	Step No.	Laser Power (%)	Laser Power (W)	Blank No.	^{40}Ar (fA)	± 1σ	^{39}Ar (fA)	± 1σ	^{38}Ar (fA)	± 1σ	^{37}Ar (fA)	± 1σ	^{36}Ar (fA)	± 1σ
Sample MF40 - 56.3 m			***J-Value =***	***0.020701***	±	***0.0000079493 (1σ)***		***0.038 %***[a]						
Aliquot MF40-4				***Single Muscovite Grain***										
MF40-4a	1	1	0.22	EXB#8	0.7203	0.0234	-0.0029	0.0070	-0.0367	0.0241	0.0020	0.0111	0.0076	0.0002
MF40-4b	2	3	0.75	EXB#9	0.7365	0.0285	-0.0152	0.0098	0.0044	0.0200	-0.0472	0.0152	0.0080	0.0001
MF40-4c	3	5	1.22	EXB#9	0.7365	0.0285	-0.0152	0.0098	0.0044	0.0200	-0.0472	0.0152	0.0080	0.0001
MF40-4d	4	7	1.51	EXB#9	0.7365	0.0285	-0.0152	0.0098	0.0044	0.0200	-0.0472	0.0152	0.0080	0.0001
MF40-4e	5	10	2.18	EXB#10	0.7178	0.0247	-0.0058	0.0016	-0.0120	0.0287	-0.0133	0.0176	0.0086	0.0002
MF40-4f	6	30	5.31	EXB#10	0.7178	0.0247	-0.0058	0.0016	-0.0120	0.0287	-0.0133	0.0176	0.0086	0.0002

[a] J-value was calculated relative to an assumed age of 28.02 ± 0.14 Ma (1σ) for the Fish Canyon Tuff sanidine (Renne et al. 1998).

TABLE D.3 (continued): $^{40}Ar^*/^{39}Ar$ blank values from ARGUS-VI laser step-heating analyses of single muscovite grains.[a]

Sample ID	Step No.	Laser Power (%)	Laser Power (W)	Blank No.	^{40}Ar (fA)	± 1σ	^{39}Ar (fA)	± 1σ	^{38}Ar (fA)	± 1σ	^{37}Ar (fA)	± 1σ	^{36}Ar (fA)	± 1σ
Sample MF40 - 56.3 m			***J-Value =***	***0.020701***	±	***0.0000079493 (1σ)***		***0.038 %***[a]						
Aliquot MF40-5				***Single Muscovite Grain***										
MF40-5a	1	1	0.22	EXB#12	0.6283	0.0099	-0.0185	0.0155	-0.0294	0.0244	-0.0082	0.0260	0.0072	0.0001
MF40-5b	2	3	0.75	EXB#12	0.6283	0.0099	-0.0185	0.0155	-0.0294	0.0244	-0.0082	0.0260	0.0072	0.0001
MF40-5c	3	5	1.22	EXB#12	0.6283	0.0099	-0.0185	0.0155	-0.0294	0.0244	-0.0082	0.0260	0.0072	0.0001
MF40-5d	4	7	1.51	EXB#12	0.6283	0.0099	-0.0185	0.0155	-0.0294	0.0244	-0.0082	0.0260	0.0072	0.0001
MF40-5e	5	10	2.18	EXB#14	0.6739	0.0304	-0.0133	0.0096	-0.0355	0.0142	-0.0124	0.0162	0.0079	0.0002
MF40-5f	6	30	5.31	EXB#14	0.6739	0.0304	-0.0133	0.0096	-0.0355	0.0142	-0.0124	0.0162	0.0079	0.0002

[a] J-value was calculated relative to an assumed age of 28.02 ± 0.14 Ma (1σ) for the Fish Canyon Tuff sanidine (Renne et al. 1998).

TABLE D.3 (continued): $^{40}Ar^*/^{39}Ar$ blank values from ARGUS-VI laser step-heating analyses of single muscovite grains.[a]

Sample ID	Step No.	Laser Power (%)	Laser Power (W)	Blank No.	^{40}Ar (fA)	± 1σ	^{39}Ar (fA)	± 1σ	^{38}Ar (fA)	± 1σ	^{37}Ar (fA)	± 1σ	^{36}Ar (fA)	± 1σ
Sample MF40 - 56.3 m			***J-Value =***	***0.020701***	±	***0.0000079493 (1σ)***		***0.038 %***[a]						
Aliquot MF40-6				***Single Muscovite Grain***										
MF40-6a	1	1	0.22	EXB#14	0.6739	0.0304	-0.0133	0.0096	-0.0355	0.0142	-0.0124	0.0162	0.0079	0.0002
MF40-6b	2	2	0.51	EXB#14	0.6739	0.0304	-0.0133	0.0096	-0.0355	0.0142	-0.0124	0.0162	0.0079	0.0002
MF40-6c	3	3	0.75	EXB#16	0.8566	0.0660	0.0210	0.0122	0.0238	0.0195	0.0011	0.0056	0.0094	0.0001
MF40-6d	4	5	1.22	EXB#16	0.8566	0.0660	0.0210	0.0122	0.0238	0.0195	0.0011	0.0056	0.0094	0.0001
MF40-6e	5	7	1.51	EXB#16	0.8566	0.0660	0.0210	0.0122	0.0238	0.0195	0.0011	0.0056	0.0094	0.0001
MF40-6f	6	10	2.18	EXB#17	0.7501	0.0307	0.0076	0.0020	0.0361	0.0181	-0.0087	0.0184	0.0088	0.0002
MF40-6g	7	30	5.31	EXB#17	0.7501	0.0307	0.0076	0.0020	0.0361	0.0181	-0.0087	0.0184	0.0088	0.0002

[a] J-value was calculated relative to an assumed age of 28.02 ± 0.14 Ma (1σ) for the Fish Canyon Tuff sanidine (Renne et al. 1998).

D.2 VG3600 $^{40}Ar^*/^{39}Ar$ Hornblende Analytical Data

TABLE D.4: $^{40}Ar^*/^{39}Ar$ analytical data from VG3600 furnace step-heating analyses of multiple hornblende aliquots.[a]

Temp (°C)	^{40}Ar (x10^{-13} moles)	± 1σ	^{39}Ar (x10^{-14} moles)[b]	± 1σ	^{38}Ar (x10^{-16} moles)	± 1σ	^{37}Ar (x10^{-16} moles)[b]	± 1σ	^{36}Ar (x10^{-16} moles)	± 1σ	Ca/K	± 1σ	%$^{40}Ar^*$	$^{40}Ar^*/^{39}Ar$	± 1σ	Cum.% ^{39}Ar	Age (Ma)	± 1σ	Included in Weighted Mean Age Calculation?	Total Gas Age Calculation: $^{39}Ar/^{39}Ar_{Total}$	Calc ($^{40}Ar^*/^{39}Ar)_{Total}$	± 1σ
Sample MF103 - 112.4 m				***J-Value =***	***0.020239***	***±***	***0.000150 (1σ)***		***0.74***	***%***[c]												
Aliquot MF103-1		**184 mg**																				
800	0.0532	0.0001	0.0068	0.0006	0.0004	0.0303	10.3705	0.1403	0.0129	0.0185	26.67	2.33	92.7	72.521	10.235	0.40	1629.623	151.435		0.0040	0.2903	0.0410
900	0.0512	0.0003	0.0152	0.0004	0.2186	0.0403	27.4136	0.1498	0.1305	0.0390	31.66	0.78	23.9	8.075	7.610	1.29	273.082	238.843		0.0089	0.0720	0.0678
980	0.0903	0.0002	0.0242	0.0017	0.2059	0.0254	29.7776	1.4230	0.2437	0.0325	21.50	1.84	19.4	7.224	3.993	2.72	246.165	127.202		0.0143	0.1030	0.0569
1010	0.1029	0.0005	0.0209	0.0003	0.1370	0.0276	35.9658	0.8137	0.2121	0.0165	30.11	0.78	38.5	18.929	2.355	3.95	585.108	62.181		0.0123	0.2327	0.0290
1030	0.1309	0.0003	0.0223	0.0006	0.0159	0.0617	27.1422	0.4506	0.2729	0.0418	21.29	0.68	37.7	22.139	5.566	5.26	667.926	140.343		0.0131	0.2905	0.0730
1050	0.1695	0.0003	0.0301	0.0012	0.0004	0.0014	40.2441	0.2401	0.5666	0.0952	23.43	0.96	0.2	0.122	9.359	7.03	4.453	340.892		0.0177	0.0022	0.1655
1070	0.2517	0.0004	0.0656	0.0015	0.1730	0.2235	66.6234	1.7494	0.4689	0.0692	17.76	0.61	44.4	17.023	3.138	10.89	534.082	85.216		0.0386	0.6572	0.1211
1100	0.6115	0.0009	0.2458	0.0008	0.7110	0.0140	266.8235	1.8394	0.6718	0.0507	19.00	0.15	67.2	16.719	0.613	25.34	525.814	16.730		0.1446	2.4168	0.0886
1130	0.5005	0.0007	0.1769	0.0008	0.7510	0.0135	199.1510	1.1118	0.6709	0.1710	19.71	0.14	60.0	16.974	2.859	35.75	532.754	77.697	Y	0.1040	1.7657	0.2974
1170	0.6570	0.0011	0.2504	0.0013	0.6498	0.0438	278.3697	1.5364	0.6708	0.0211	19.45	0.15	69.5	18.241	0.270	50.47	566.849	7.207	Y	0.1473	2.6865	0.0398
1200	0.7343	0.0013	0.3061	0.0008	0.6701	0.0279	349.2334	1.4493	0.8178	0.0236	19.97	0.10	66.8	16.015	0.235	68.47	506.511	6.473		0.1800	2.8830	0.0423
1250	0.8564	0.0012	0.4088	0.0008	0.9492	0.0381	457.0786	3.9290	0.4161	0.0197	19.57	0.17	85.5	17.912	0.150	92.52	558.075	4.009	Y	0.2404	4.3068	0.0360
1350	0.3426	0.0005	0.1232	0.0008	0.2200	0.0577	129.6314	1.0969	0.3618	0.0348	18.42	0.20	68.5	19.051	0.845	99.76	588.327	22.255	Y	0.0724	1.3800	0.0612
1450	0.1585	0.0002	0.0040	0.0003	0.1683	0.0235	0.0444	0.1084	0.5087	0.0138	0.19	0.47	4.2	16.251	10.170	100.00	513.003	279.439		0.0024	0.0387	0.0242
Total			1.7002											17.125	1.144		536.857	6.326		1.0000	17.1253	1.1438

Total Gas Age[d]***:***							***536.9 ± 6.3 (1σ)***
Plateau Age[d]***:***	^{39}Ar %	*47.8*	*MSWD*	*1.50*	*Prob. of fit*	*0.19*	***560.4 ± 7.7 (1σ)***
Weighted Mean Age[d]***, Steps 9 to 13 (excluding Step 11):***	^{39}Ar %	*46.0*	*MSWD*	*0.93*	*Prob. of fit*	*0.42*	***560.7 ± 4.9 (1σ)***

[a] Data was corrected for mass spectrometer backgrounds, discrimination, radioactive decay and interference corrections.

[b] Interference corrections: $(^{36}Ar/^{37}Ar)_{Ca} = (2.58 \pm 0.07) \times 10^{-4}$; $(^{39}Ar/^{37}Ar)_{Ca} = (6.56 \pm 0.25) \times 10^{-4}$; $(^{40}Ar/^{39}Ar)_{K} = (1.0 \pm 5.00) \times 10^{-30}$; $(^{38}Ar/^{39}Ar)_{K} = (1.22 \pm 0.23) \times 10^{-2}$.

[c] J-value was calculated relative to an assumed age of 28.02 ± 0.14 Ma (1σ) for the Fish Canyon Tuff sanidine (Renne et al. 1998).

[d] All errors associated with the total gas, plateau and weighted mean ages are reported at the 1σ level and include the uncertainties in the J-value.

TABLE D.4 (continued): $^{40}Ar^*/^{39}Ar$ analytical data from VG3600 furnace step-heating analyses of multiple hornblende aliquots.[a]

																			Total Gas Age Calculation		
Temp (°C)	^{40}Ar (x10^{-13} moles)	± 1σ	^{39}Ar (x10^{-14} moles)[b]	± 1σ	^{38}Ar (x10^{-16} moles)	± 1σ	^{37}Ar (x10^{-16} moles)[b]	± 1σ	^{36}Ar (x10^{-16} moles)	± 1σ	Ca/K	± 1σ	%$^{40}Ar^*$	$^{40}Ar^*/^{39}Ar$	± 1σ	Cum.% ^{39}Ar	Age (Ma)	± 1σ	Included in Weighted Mean Age Calculation?	$^{39}Ar/^{39}Ar_{Total}$	Calc $(^{40}Ar^*/^{39}Ar)_{Total}$	± 1σ
Sample MF103 - 112.4 m				***J-Value =***	***0.020239***	***±***	***0.000150 (1σ)***		***0.74***	***%***[c]													
Aliquot MF103-2		**156 mg**																					
800	0.1025	0.0004	0.0338	0.0014	0.4001	0.1435	11.5502	1.0104	0.2184	0.0581	5.99	0.58	36.4	11.053	5.158	1.72	364.218	153.889		0.0172	0.1900	0.0886
1030	0.4070	0.0009	0.1548	0.0019	0.4355	0.1809	134.2892	2.9226	0.3245	0.0919	15.18	0.38	76.2	20.034	1.772	9.60	614.061	46.033		0.0788	1.5783	0.1396
1050	0.1275	0.0004	0.0520	0.0013	0.0004	0.0028	52.8284	2.1235	0.0004	0.1051	17.79	0.84	99.9	24.515	6.011	12.24	726.870	146.681		0.0264	0.6483	0.1589
1070	0.2043	0.0005	0.0978	0.0009	0.1423	0.1003	78.7355	1.7561	0.1139	0.1019	14.09	0.34	83.4	17.408	3.085	17.22	544.519	83.281		0.0498	0.8665	0.1535
1100	0.8718	0.0020	0.4532	0.0005	0.8979	0.0084	457.2190	3.0541	0.1151	0.0217	17.66	0.12	96.1	18.480	0.150	40.28	573.217	3.986	Y	0.2306	4.2624	0.0346
1130	0.3004	0.0008	0.1324	0.0005	0.4479	0.0266	146.0598	1.0137	0.2284	0.0222	19.30	0.15	77.3	17.534	0.503	47.02	547.904	13.552	Y	0.0674	1.1818	0.0339
1170	0.5960	0.0014	0.3019	0.0009	0.6133	0.0582	280.7061	3.9923	0.1742	0.0270	16.27	0.24	91.3	18.018	0.273	62.39	560.912	7.304	Y	0.1537	2.7686	0.0419
1200	0.6398	0.0015	0.3249	0.0008	0.6650	0.0148	367.3506	3.6220	0.1460	0.0159	19.78	0.20	93.2	18.348	0.158	78.93	569.703	4.219	Y	0.1654	3.0342	0.0262
1250	0.6031	0.0013	0.3036	0.0006	0.7537	0.1051	354.1092	3.3977	0.1964	0.0869	20.41	0.20	90.3	17.935	0.847	94.38	558.669	22.701	Y	0.1545	2.7710	0.1309
1350	0.2444	0.0006	0.0980	0.0007	0.0114	0.0528	102.8730	0.8834	0.0821	0.0547	18.37	0.20	90.0	22.433	1.659	99.37	675.313	41.656		0.0499	1.1191	0.0828
1450	0.1972	0.0005	0.0125	0.0008	0.0441	0.0700	10.8980	1.1123	0.5891	0.0116	15.31	1.85	10.8	17.068	2.994	100.00	535.312	81.240		0.0063	0.1082	0.0190
Total			1.9648											18.528	0.910		574.508	5.771		1.0000	18.5284	0.9100
Total Gas Age[d]:																					***574.5 ± 5.8 (1σ)***	
Plateau Age[d]:							^{39}Ar %	*100.0*		*MSWD*	*1.60*			*Prob. of fit*	*0.11*						***569.6 ± 5.0 (1σ)***	
Weighted Mean Age[d], Steps 5 to 9:							^{39}Ar %	*54.1*		*MSWD*	*1.30*			*Prob. of fit*	*0.28*						***569.2 ± 4.5 (1σ)***	

[a] Data was corrected for mass spectrometer backgrounds, discrimination, radioactive decay and interference corrections.

[b] Interference corrections: $(^{36}Ar/^{37}Ar)_{Ca} = (2.58 \pm 0.07) \times 10^{-4}$; $(^{39}Ar/^{37}Ar)_{Ca} = (6.56 \pm 0.25) \times 10^{-4}$; $(^{40}Ar/^{39}Ar)_{K} = (1.0 \pm 5.00) \times 10^{-10}$; $(^{38}Ar/^{39}Ar)_{K} = (1.22 \pm 0.23) \times 10^{-2}$.

[c] J-value was calculated relative to an assumed age of 28.02 ± 0.14 Ma (1σ) for the Fish Canyon Tuff sanidine (Renne et al. 1998).

[d] All errors associated with the total gas, plateau and weighted mean ages are reported at the 1σ level and include the uncertainties in the J-value.

TABLE D.5: *$^{40}Ar^*/^{39}Ar$ raw analytical data from VG3600 furnace step-heating analyses of multiple hornblende aliquots.*[a]

Temp	^{40}Ar	± 1σ	^{39}Ar	± 1σ	^{38}Ar	± 1σ	^{37}Ar	± 1σ	^{36}Ar	± 1σ
(°C)	(x10^{-13} moles)		(x10^{-14} moles)		(x10^{-16} moles)		(x10^{-16} moles)		(x10^{-16} moles)	
Sample MF103 - 112.4 m				***J-Value =***	***0.020239***	***±***	***0.000150 (1σ)***		***0.74 %***[a]	
Aliquot MF103-1		**184 mg**								
800	0.0532	0.0001	0.0069	0.0006	0.0059	0.0303	10.3705	0.1403	0.0156	0.0185
900	0.0512	0.0003	0.0153	0.0004	0.2371	0.0403	27.4136	0.1498	0.1376	0.0390
980	0.0903	0.0002	0.0244	0.0017	0.2356	0.0253	29.7776	1.4230	0.2514	0.0325
1010	0.1029	0.0005	0.0211	0.0003	0.1626	0.0276	35.9658	0.8137	0.2214	0.0165
1030	0.1309	0.0003	0.0225	0.0006	0.0432	0.0617	27.1422	0.4506	0.2799	0.0418
1050	0.1695	0.0003	0.0303	0.0012	0.0004	0.0012	40.2441	0.2401	0.5769	0.0952
1070	0.2517	0.0004	0.0661	0.0015	0.2534	0.2235	66.6234	1.7494	0.4861	0.0692
1100	0.6115	0.0009	0.2475	0.0008	1.0120	0.0139	266.8235	1.8394	0.7407	0.0507
1130	0.5005	0.0007	0.1782	0.0008	0.9676	0.0134	199.1510	1.1118	0.7223	0.1710
1170	0.6570	0.0011	0.2522	0.0013	0.9565	0.0437	278.3697	1.5364	0.7426	0.0211
1200	0.7343	0.0013	0.3083	0.0008	1.0449	0.0278	349.2334	1.4493	0.9079	0.0236
1250	0.8564	0.0012	0.4118	0.0008	1.4498	0.0380	457.0786	3.9290	0.5341	0.0197
1350	0.3426	0.0005	0.1240	0.0008	0.3708	0.0577	129.6314	1.0969	0.3953	0.0348
1450	0.1585	0.0002	0.0040	0.0003	0.1733	0.0235	0.0444	0.1084	0.5087	0.0138

[a] J-value was calculated relative to an assumed age of 28.02 ± 0.14 Ma (1σ) for the Fish Canyon Tuff sanidine (Renne et al. 1998).

TABLE D.5 (continued): $^{40}Ar^*/^{39}Ar$ analytical data from VG3600 furnace step-heating analyses of multiple hornblende aliquots.[a]

Temp	^{40}Ar	± 1σ	^{39}Ar	± 1σ	^{38}Ar	± 1σ	^{37}Ar	± 1σ	^{36}Ar	± 1σ
(°C)	(x10^{-13} moles)		(x10^{-14} moles)		(x10^{-16} moles)		(x10^{-16} moles)		(x10^{-16} moles)	
Sample MF103 - 112.4 m				***J-Value =***	***0.020239***	***±***	***0.000150 (1σ)***		***0.74 %***[a]	
Aliquot MF103-2		**156 mg**								
800	0.1025	0.0004	0.0338	0.0014	0.4414	0.1435	11.5502	1.0104	0.2215	0.0581
1030	0.4070	0.0009	0.1557	0.0019	0.6251	0.1809	134.2892	2.9226	0.3592	0.0919
1050	0.1275	0.0004	0.0523	0.0013	0.0004	0.0026	52.8284	2.1235	0.0047	0.1051
1070	0.2043	0.0005	0.0983	0.0009	0.2621	0.1003	78.7355	1.7561	0.1342	0.1019
1100	0.8718	0.0020	0.4562	0.0005	1.4529	0.0079	457.2190	3.0541	0.2331	0.0217
1130	0.3004	0.0008	0.1334	0.0005	0.6101	0.0266	146.0598	1.0137	0.2661	0.0222
1170	0.5960	0.0014	0.3037	0.0009	0.9830	0.0582	280.7061	3.9923	0.2467	0.0269
1200	0.6398	0.0015	0.3273	0.0008	1.0629	0.0147	367.3506	3.6220	0.2409	0.0158
1250	0.6031	0.0013	0.3059	0.0006	1.1255	0.1051	354.1092	3.3977	0.2878	0.0869
1350	0.2444	0.0006	0.0987	0.0007	0.1314	0.0528	102.8730	0.8834	0.1086	0.0547
1450	0.1972	0.0005	0.0125	0.0008	0.0594	0.0700	10.8980	1.1123	0.5919	0.0116

[a] J-value was calculated relative to an assumed age of 28.02 ± 0.14 Ma (1σ) for the Fish Canyon Tuff sanidine (Renne et al. 1998).

Appendix E

U-Pb Analytical Data

E.1 LA-ICPMS U-Pb Detrital Zircon Analytical Data

TABLE E.1: *LA-ICPMS U-Pb detrital zircon analytical data.*

Grain	U[a]	Th[a]	Pb[a]	Th/U	$^{207}Pb/^{235}U$[b]		$^{206}Pb/^{238}U$[b]		Rho[c]	$^{207}Pb/^{206}Pb$		$^{207}Pb/^{235}U$		$^{206}Pb/^{238}U$		$^{207}Pb/^{206}Pb$		Concordance[d]
	ppm	ppm	ppm	ratio	ratio	± 1σ	ratio	± 1σ	ρ	ratio	± 1σ	Ma	± 1σ	Ma	± 1σ	Ma	± 1σ	%
Sample MF23 - 44.6 m (Greywacke)																		
Concordant Analyses																		
MF23-9	112	77	24	0.688	0.8990	0.0235	0.1039	0.0023	0.2421	9.6246	0.2084	651	13	637	13	688	36	93
MF23-7	309	138	42	0.447	0.8900	0.0220	0.1043	0.0023	0.4234	9.5877	0.2068	646	12	640	13	664	31	96
MF23-115	206	107	30	0.520	0.8900	0.0140	0.1045	0.0016	0.3621	9.5694	0.1419	646	8	641	9	674	24	95
MF23-5	212	103	32	0.486	0.8940	0.0225	0.1047	0.0023	0.4171	9.5511	0.2053	649	12	642	13	657	31	98
MF23-83	480	43	12	0.090	0.8940	0.0085	0.1053	0.0013	0.4048	9.4967	0.1127	649	5	645	7	653	17	99
MF23-43	114	64	19	0.561	0.8710	0.0155	0.1054	0.0015	0.1722	9.4877	0.1350	636	8	646	9	614	39	105
MF23-36	254	122	39	0.480	0.9120	0.0110	0.1055	0.0014	0.3225	9.4787	0.1213	658	6	647	8	691	24	94
MF23-116	157	64	19	0.411	0.8980	0.0155	0.1055	0.0016	0.4348	9.4787	0.1438	651	8	647	9	671	24	96
MF23-119	91	31	10	0.344	0.9270	0.0190	0.1056	0.0017	0.2782	9.4697	0.1480	666	10	647	10	738	38	88
MF23-112	81	36	11	0.441	0.8980	0.0160	0.1058	0.0017	0.1747	9.4518	0.1519	651	9	648	10	667	33	97
MF23-1	151	64	20	0.424	0.9050	0.0225	0.1059	0.0023	0.3398	9.4429	0.2006	654	12	649	13	674	33	96
MF23-58	63	33	10	0.524	0.8670	0.0190	0.1059	0.0016	0.1233	9.4429	0.1427	634	10	649	9	589	49	110
MF23-6	970	438	138	0.452	0.9090	0.0220	0.1063	0.0023	0.4530	9.4073	0.1991	657	12	651	13	660	30	99
MF23-95	172	83	27	0.482	0.9480	0.0140	0.1064	0.0015	0.2820	9.3985	0.1281	677	7	652	8	765	21	85
MF23-2	210	93	29	0.443	0.9060	0.0225	0.1065	0.0023	0.3345	9.3897	0.2028	655	12	652	13	653	31	100
MF23-109	202	172	52	0.854	0.9060	0.0150	0.1065	0.0016	0.3402	9.3897	0.1411	655	8	652	9	657	26	99
MF23-24	94	77	23	0.819	0.9250	0.0165	0.1066	0.0016	0.2042	9.3809	0.1364	665	9	653	9	722	40	90
MF23-13	742	491	155	0.662	0.9050	0.0085	0.1067	0.0013	0.4855	9.3721	0.1142	654	5	654	8	650	16	101
MF23-19	586	296	87	0.505	0.9050	0.0105	0.1067	0.0014	0.4287	9.3721	0.1186	654	6	654	8	660	23	99
MF23-80	213	99	26	0.465	0.9080	0.0120	0.1067	0.0014	0.3279	9.3721	0.1186	656	6	654	8	657	28	100
MF23-103	400	129	39	0.323	0.9120	0.0130	0.1067	0.0015	0.5029	9.3721	0.1318	658	7	654	9	672	17	97
MF23-92	285	148	44	0.518	0.9140	0.0125	0.1068	0.0015	0.5039	9.3633	0.1271	659	7	654	8	673	16	97
MF23-98	255	123	36	0.481	0.9380	0.0165	0.1068	0.0017	0.2374	9.3633	0.1490	672	9	654	10	742	28	88
MF23-99	156	83	25	0.533	0.9110	0.0140	0.1068	0.0015	0.4406	9.3633	0.1315	658	7	654	9	667	21	98
MF23-76	109	49	15	0.450	0.8950	0.0225	0.1070	0.0016	0.2196	9.3458	0.1354	649	12	655	9	600	63	109
MF23-120	162	95	29	0.585	0.9020	0.0135	0.1071	0.0015	0.2860	9.3371	0.1308	653	7	656	9	643	23	102
MF23-26	167	72	23	0.431	0.8940	0.0125	0.1072	0.0015	0.3121	9.3284	0.1262	649	7	656	8	622	29	106
MF23-86	161	72	19	0.447	0.9110	0.0125	0.1072	0.0014	0.2350	9.3284	0.1218	658	7	656	8	639	30	103
MF23-21	129	58	17	0.450	0.9130	0.0145	0.1073	0.0016	0.2934	9.3197	0.1346	659	8	657	9	660	33	100
MF23-74	263	168	55	0.639	0.9030	0.0110	0.1076	0.0015	0.3928	9.2937	0.1252	653	6	659	8	632	25	104
MF23-77	250	151	49	0.604	0.9080	0.0115	0.1076	0.0015	0.4116	9.2937	0.1252	656	6	659	8	650	26	101
MF23-97	167	81	26	0.481	0.9330	0.0140	0.1076	0.0015	0.2774	9.2937	0.1252	669	7	659	8	688	22	96
MF23-49	489	263	77	0.538	0.9410	0.0105	0.1077	0.0014	0.4654	9.2851	0.1164	673	5	659	8	708	20	93
MF23-53	239	88	27	0.369	0.9360	0.0140	0.1077	0.0015	0.3721	9.2851	0.1293	671	7	659	9	701	20	94
MF23-44C	560	450	118	0.804	0.9250	0.0115	0.1078	0.0014	0.4104	9.2764	0.1162	665	6	660	8	674	26	98
MF23-44R	258	142	38	0.550	0.9110	0.0110	0.1078	0.0014	0.3072	9.2764	0.1205	658	6	660	8	643	25	103
MF23-22	70	65	20	0.929	0.9260	0.0180	0.1079	0.0016	0.2840	9.2678	0.1331	666	9	661	9	691	39	96
MF23-35	186	84	25	0.452	0.9220	0.0130	0.1079	0.0015	0.2465	9.2678	0.1245	663	7	661	8	691	36	96
MF23-65	156	75	24	0.481	0.9320	0.0140	0.1079	0.0016	0.3236	9.2678	0.1331	669	7	661	9	691	31	96
MF23-37	338	183	56	0.541	0.9270	0.0125	0.1080	0.0016	0.4993	9.2593	0.1329	666	7	661	9	671	24	99

Continued on next page

TABLE E.1 (continued): LA-ICPMS U-Pb detrital zircon analytical data.

Grain	U[a]	Th[a]	Pb[a]	Th/U	$^{207}Pb/^{235}U$[b]		$^{206}Pb/^{238}U$[b]		Rho[c]	$^{207}Pb/^{206}Pb$		$^{207}Pb/^{235}U$		$^{206}Pb/^{238}U$		$^{207}Pb/^{206}Pb$		Concordance[d]
	ppm	ppm	ppm	ratio	ratio	± 1σ	ratio	± 1σ	ρ	ratio	± 1σ	Ma	± 1σ	Ma	± 1σ	Ma	± 1σ	%
MF23-28	529	259	73	0.490	0.9220	0.0110	0.1081	0.0015	0.4385	9.2507	0.1241	663	6	662	8	664	26	100
MF23-105	198	108	35	0.546	0.9210	0.0140	0.1081	0.0016	0.4740	9.2507	0.1326	663	7	662	9	671	21	99
MF23-107	231	85	26	0.366	0.9070	0.0135	0.1083	0.0015	0.3888	9.2336	0.1279	655	7	663	9	629	21	105
MF23-47	228	108	33	0.474	0.9350	0.0115	0.1084	0.0015	0.2195	9.2251	0.1277	670	6	663	9	695	27	96
MF23-78	338	218	62	0.645	0.9290	0.0110	0.1084	0.0014	0.5060	9.2251	0.1191	667	6	663	8	678	22	98
MF23-31	222	74	22	0.333	0.9420	0.0110	0.1085	0.0015	0.4317	9.2166	0.1232	674	6	664	8	691	24	96
MF23-38	452	245	77	0.542	0.9290	0.0095	0.1085	0.0014	0.5274	9.2166	0.1189	667	5	664	8	674	17	99
MF23-73	160	97	31	0.606	0.9260	0.0130	0.1085	0.0015	0.3680	9.2166	0.1274	666	7	664	9	657	28	101
MF23-18	135	69	21	0.511	0.9320	0.0145	0.1086	0.0015	0.1923	9.2081	0.1229	669	8	665	8	688	34	97
MF23-10	253	148	46	0.585	0.9270	0.0115	0.1087	0.0014	0.4709	9.1996	0.1185	666	6	665	8	660	24	101
MF23-108	84	35	11	0.416	0.9270	0.0165	0.1088	0.0017	0.4255	9.1912	0.1394	666	9	666	10	657	26	101
MF23-48	339	176	51	0.519	0.9300	0.0105	0.1089	0.0014	0.3968	9.1827	0.1138	668	6	666	8	653	21	102
MF23-54	186	77	22	0.414	0.9330	0.0135	0.1089	0.0015	0.2221	9.1827	0.1223	669	7	666	8	671	31	99
MF23-59	159	91	29	0.572	0.9490	0.0125	0.1089	0.0015	0.3161	9.1827	0.1223	678	7	666	8	715	27	93
MF23-93	99	77	25	0.784	0.9620	0.0180	0.1089	0.0017	0.3222	9.1827	0.1391	684	9	666	10	758	33	88
MF23-100	228	107	34	0.471	0.9340	0.0145	0.1089	0.0016	0.4385	9.1827	0.1307	670	8	666	9	684	21	97
MF23-46	292	159	41	0.545	0.9370	0.0160	0.1090	0.0015	0.2940	9.1743	0.1263	671	8	667	9	667	36	100
MF23-60	318	140	47	0.440	0.9470	0.0115	0.1090	0.0014	0.4111	9.1743	0.1178	677	6	667	8	684	22	97
MF23-69	506	246	76	0.486	0.9420	0.0100	0.1090	0.0015	0.5259	9.1743	0.1220	674	5	667	8	701	19	95
MF23-110	223	89	28	0.398	0.9290	0.0135	0.1090	0.0015	0.3934	9.1743	0.1263	667	7	667	9	657	17	102
MF23-40	273	217	60	0.795	0.9460	0.0105	0.1091	0.0014	0.3090	9.1659	0.1134	676	5	668	8	698	22	96
MF23-68C	229	90	28	0.393	0.9350	0.0125	0.1091	0.0015	0.3921	9.1659	0.1260	670	7	668	9	660	26	101
MF23-20	318	200	58	0.629	0.9410	0.0110	0.1092	0.0015	0.4610	9.1575	0.1216	673	6	668	8	678	24	99
MF23-71	163	129	45	0.791	0.9310	0.0130	0.1092	0.0015	0.3521	9.1575	0.1258	668	7	668	9	664	28	101
MF23-87	191	92	28	0.482	0.9190	0.0115	0.1092	0.0014	0.3700	9.1575	0.1132	662	6	668	8	629	25	106
MF23-14	318	153	50	0.481	0.9450	0.0110	0.1096	0.0014	0.3619	9.1241	0.1165	675	6	670	8	681	22	98
MF23-41	88	41	12	0.466	0.9390	0.0170	0.1100	0.0016	0.2640	9.0909	0.1322	672	9	673	9	708	39	95
MF23-45	197	94	26	0.477	0.9380	0.0145	0.1101	0.0016	0.2473	9.0827	0.1320	672	8	673	9	678	33	99
MF23-72	235	88	30	0.374	0.9630	0.0125	0.1101	0.0015	0.3300	9.0827	0.1196	685	6	673	8	718	27	94
MF23-101	298	188	59	0.631	0.9820	0.0155	0.1101	0.0016	0.5650	9.0827	0.1320	695	8	673	9	761	20	88
MF23-34	193	106	34	0.549	0.9520	0.0120	0.1103	0.0015	0.3290	9.0662	0.1192	679	6	674	8	688	24	98
MF23-42	321	180	48	0.561	0.9680	0.0145	0.1103	0.0018	0.3851	9.0662	0.1438	687	7	674	10	725	32	93
MF23-55	416	85	26	0.204	0.9400	0.0110	0.1103	0.0015	0.5654	9.0662	0.1192	673	6	674	8	657	19	103
MF23-32	324	178	56	0.549	0.9470	0.0100	0.1104	0.0014	0.4169	9.0580	0.1149	677	5	675	8	667	19	101
MF23-79	257	167	46	0.650	0.9320	0.0140	0.1105	0.0016	0.4178	9.0498	0.1310	669	7	676	9	643	32	105
MF23-33	172	70	22	0.407	0.9460	0.0120	0.1106	0.0014	0.3408	9.0416	0.1145	676	6	676	8	653	24	104
MF23-27	200	125	49	0.625	0.9540	0.0195	0.1108	0.0015	0.4424	9.0253	0.1181	680	10	677	8	671	40	101
MF23-64	119	61	17	0.513	0.9640	0.0200	0.1108	0.0019	0.2950	9.0253	0.1507	685	10	677	11	735	43	92
MF23-52	486	216	62	0.444	0.9490	0.0170	0.1110	0.0023	0.5166	9.0090	0.1826	678	9	679	13	667	29	102
MF23-75	512	294	107	0.574	0.9590	0.0100	0.1110	0.0014	0.4526	9.0090	0.1136	683	5	679	8	691	19	98
MF23-84	125	58	15	0.464	0.9550	0.0400	0.1111	0.0017	0.3199	9.0009	0.1377	681	21	679	10	678	81	100
MF23-111	268	144	45	0.535	0.9340	0.0145	0.1111	0.0016	0.3988	9.0009	0.1296	670	8	679	9	643	23	106
MF23-70	172	67	22	0.390	0.9440	0.0140	0.1113	0.0016	0.3831	8.9847	0.1292	675	7	680	9	660	30	103
MF23-96	495	262	78	0.529	0.9560	0.0160	0.1113	0.0017	0.4593	8.9847	0.1332	681	8	680	10	684	22	99

Continued on next page

TABLE E.1 (continued): LA-ICPMS U-Pb detrital zircon analytical data.

Grain	U[a]	Th[a]	Pb[a]	Th/U	$^{207}Pb/^{235}U$[b]		$^{206}Pb/^{238}U$[b]		Rho[c]	$^{207}Pb/^{206}Pb$		$^{207}Pb/^{235}U$		$^{206}Pb/^{238}U$		$^{207}Pb/^{206}Pb$		Concordance[d]
	ppm	ppm	ppm	ratio	ratio	± 1σ	ratio	± 1σ	ρ	ratio	± 1σ	Ma	± 1σ	Ma	± 1σ	Ma	± 1σ	%
MF23-23	487	297	116	0.610	0.9850	0.0105	0.1114	0.0015	0.5366	8.9767	0.1209	696	5	681	9	735	17	93
MF23-106	584	143	37	0.245	0.9630	0.0195	0.1114	0.0023	0.5177	8.9767	0.1813	685	10	681	13	725	33	94
MF23-81	357	268	75	0.751	0.9490	0.0105	0.1118	0.0014	0.3408	8.9445	0.1120	678	5	683	8	646	23	106
MF23-30	211	117	37	0.555	0.9700	0.0130	0.1121	0.0014	0.3135	8.9206	0.1114	688	7	685	8	684	31	100
MF23-51	346	149	42	0.431	0.9490	0.0110	0.1122	0.0014	0.2489	8.9127	0.1072	678	6	686	8	639	23	107
MF23-57	309	197	59	0.638	0.9490	0.0175	0.1124	0.0015	0.3811	8.8968	0.1148	678	9	687	8	622	54	110
MF23-56	179	61	19	0.341	0.9770	0.0135	0.1127	0.0015	0.1996	8.8731	0.1181	692	7	688	9	712	32	97
MF23-61	364	117	37	0.321	0.9460	0.0100	0.1128	0.0015	0.4171	8.8652	0.1179	676	5	689	9	625	23	110
MF23-62	367	402	122	1.095	1.0210	0.0130	0.1130	0.0015	0.3799	8.8496	0.1136	714	7	690	8	781	23	88
MF23-16	236	102	31	0.432	1.0070	0.0135	0.1142	0.0015	0.3961	8.7566	0.1150	707	7	697	9	738	30	94
MF23-102	391	81	27	0.208	0.9920	0.0150	0.1160	0.0017	0.5302	8.6207	0.1226	700	8	707	10	674	17	105
MF23-90	380	179	65	0.471	0.9890	0.0100	0.1163	0.0015	0.5105	8.5985	0.1072	698	5	709	8	660	19	107
MF23-12	199	69	24	0.347	1.0970	0.0140	0.1237	0.0019	0.5956	8.0841	0.1209	752	7	752	11	755	28	100
MF23-8	339	251	173	0.740	3.1900	0.0800	0.2490	0.0055	0.7050	4.0161	0.0887	1455	19	1433	28	1474	26	97
MF23-91	34	21	19	0.618	3.8600	0.0550	0.2880	0.0050	0.4483	3.4722	0.0603	1605	11	1632	25	1585	31	103
MF23-29	79	129	104	1.633	3.9600	0.0430	0.2907	0.0038	0.4710	3.4400	0.0444	1626	9	1645	19	1596	17	103
MF23-89	194	112	104	0.577	5.4330	0.0420	0.3452	0.0039	0.4384	2.8969	0.0327	1890	7	1912	19	1856	11	103
MF23-50	213	77	89	0.362	5.7100	0.0550	0.3483	0.0043	0.6801	2.8711	0.0354	1933	8	1926	21	1932	11	100
Discordant Analyses																		
MF23-3	3243	2074	367	0.640	0.5370	0.0140	0.0551	0.0013	0.8648	18.1488	0.4117	436	9	346	8	931	28	37
MF23-94	3470	2030	384	0.585	0.7100	0.0120	0.0719	0.0012	0.3417	13.9082	0.2225	545	7	448	7	992	25	45
MF23-17	5700	3119	628	0.547	0.6800	0.0295	0.0738	0.0028	0.7215	13.5501	0.5049	527	18	459	17	816	27	56
MF23-67	5429	3548	491	0.654	0.7370	0.0215	0.0744	0.0011	0.5566	13.4409	0.1897	561	13	463	6	977	44	47
MF23-82	986	188	214	0.191	1.5060	0.0340	0.0809	0.0012	0.1283	12.3609	0.1757	933	14	501	7	2174	42	23
MF23-68R	2612	1427	330	0.546	0.7660	0.0075	0.0831	0.0011	0.6194	12.0337	0.1593	577	4	515	7	825	14	62
MF23-66	3756	2107	479	0.561	0.7770	0.0075	0.0835	0.0011	0.6873	11.9761	0.1506	584	4	517	6	852	15	61
MF23-117	798	91	150	0.114	1.4790	0.0285	0.0885	0.0015	0.4006	11.2994	0.1851	922	12	547	9	1965	27	28
MF23-4	1507	705	194	0.468	0.8200	0.0200	0.0917	0.0020	0.8316	10.9051	0.2378	608	11	566	12	761	28	74
MF23-39	1853	667	203	0.360	0.9120	0.0070	0.1021	0.0013	0.6043	9.7943	0.1199	658	4	627	7	746	12	84
MF23-118	112	41	14	0.369	0.9640	0.0185	0.1069	0.0016	0.4084	9.3545	0.1400	685	10	655	9	790	30	83
MF23-113	138	59	20	0.428	0.9470	0.0200	0.1075	0.0017	0.3960	9.3023	0.1471	677	10	658	10	787	37	84
MF23-104	241	164	52	0.680	1.0170	0.0175	0.1089	0.0016	0.4407	9.1827	0.1307	712	9	666	9	850	23	78
MF23-11	300	151	45	0.503	0.9000	1.3500	0.1090	0.0110	0.2949	9.1743	0.9258	652	90	667	64	674	110	99
MF23-25	274	140	42	0.511	0.9910	0.0175	0.1092	0.0018	0.5088	9.1575	0.1509	699	9	668	10	794	34	84
MF23-63	160	67	16	0.419	0.9300	0.2800	0.1095	0.0025	0.4045	9.1324	0.2085	668	152	670	15	674	456	99
MF23-85	122	58	15	0.475	1.0000	5.5000	0.1100	0.0470	0.2251	9.0909	3.8843	704	150	673	274	708	155	95
MF23-88	102	45	13	0.441	1.0880	0.0385	0.1114	0.0020	0.2013	8.9767	0.1571	748	19	681	11	957	74	71
MF23-15	5	14	8	2.685	4.4500	0.1850	0.1201	0.0045	0.0126	8.3264	0.3085	1722	35	731	26	3439	85	21
MF23-114	4	15	9	3.595	7.9300	0.4100	0.1570	0.0070	0.2117	6.3694	0.2840	2223	47	940	39	3859	100	24
Sample MF40 - 56.3 m (Greywacke)																		

Continued on next page

TABLE E.1 (continued): LA-ICPMS U-Pb detrital zircon analytical data.

Grain	U[a]	Th[a]	Pb[a]	Th/U	$^{207}Pb/^{235}U$[b]		$^{206}Pb/^{238}U$[b]		Rho[c]	$^{207}Pb/^{206}Pb$		$^{207}Pb/^{235}U$		$^{206}Pb/^{238}U$		$^{207}Pb/^{206}Pb$		Concordance[d]
	ppm	ppm	ppm	ratio	ratio	± 1σ	ratio	± 1σ	ρ	ratio	± 1σ	Ma	± 1σ	Ma	± 1σ	Ma	± 1σ	%
Concordant Analyses																		
MF40-7	1381	1169	325	0.846	0.8000	0.0130	0.0934	0.0013	0.8089	0.0621	0.0005	597	7	576	8	676	16	85
MF40-96	746	71	20	0.095	0.8090	0.0120	0.0954	0.0013	0.7335	0.0616	0.0004	602	7	587	7	659	13	89
MF40-129	172	89	26	0.520	0.8480	0.0135	0.0990	0.0013	0.4983	0.0620	0.0006	624	7	609	8	674	21	90
MF40-33	1448	85	31	0.059	0.8460	0.0130	0.0998	0.0013	0.7379	0.0613	0.0004	622	7	613	7	649	15	95
MF40-111	222	132	40	0.592	0.8640	0.0130	0.1012	0.0013	0.4104	0.0618	0.0006	632	7	621	7	667	21	93
MF40-142	356	183	54	0.514	0.8700	0.0130	0.1014	0.0014	0.5070	0.0619	0.0005	636	7	623	8	671	17	93
MF40-126	182	73	23	0.402	0.8790	0.0135	0.1018	0.0012	0.2752	0.0624	0.0006	640	7	625	7	688	21	91
MF40-25	1402	96	32	0.068	0.8700	0.0135	0.1025	0.0013	0.7780	0.0613	0.0004	636	7	629	8	648	15	97
MF40-130	192	75	22	0.392	0.8870	0.0140	0.1028	0.0013	0.4304	0.0624	0.0006	645	8	631	8	688	21	92
MF40-101	291	168	50	0.578	0.8870	0.0130	0.1031	0.0013	0.3478	0.0621	0.0006	645	7	633	7	678	19	93
MF40-120	637	375	101	0.589	0.8890	0.0150	0.1031	0.0016	0.6109	0.0625	0.0007	646	8	633	9	691	22	92
MF40-109	217	120	36	0.555	0.9100	0.0145	0.1035	0.0015	0.5812	0.0639	0.0006	657	8	635	9	738	20	86
MF40-106	350	194	54	0.555	0.9240	0.0140	0.1042	0.0015	0.3195	0.0644	0.0007	664	7	639	8	755	23	85
MF40-118	225	104	31	0.460	0.8980	0.0140	0.1044	0.0014	0.3975	0.0623	0.0007	651	7	640	8	684	22	94
MF40-123	209	112	33	0.536	0.8870	0.0135	0.1045	0.0014	0.3630	0.0618	0.0006	645	7	641	8	667	21	96
MF40-140	165	71	22	0.428	0.9130	0.0150	0.1047	0.0014	0.6078	0.0627	0.0006	659	8	642	8	698	20	92
MF40-103	510	142	47	0.278	0.9000	0.0125	0.1048	0.0013	0.4235	0.0622	0.0005	652	7	642	7	681	16	94
MF40-116	118	46	14	0.390	0.9030	0.0155	0.1050	0.0014	0.4450	0.0620	0.0007	653	8	644	8	674	24	95
MF40-122	210	124	39	0.592	0.9250	0.0150	0.1050	0.0015	0.4239	0.0638	0.0007	665	8	644	8	735	23	88
MF40-97	177	79	24	0.448	0.8890	0.0130	0.1051	0.0013	0.2109	0.0608	0.0006	646	7	644	7	632	19	102
MF40-137	119	67	21	0.566	0.8880	0.0145	0.1052	0.0014	0.2897	0.0615	0.0008	645	8	645	8	657	26	98
MF40-131	359	134	39	0.373	0.9020	0.0140	0.1055	0.0014	0.3953	0.0620	0.0006	653	7	647	8	674	21	96
MF40-134	196	84	25	0.428	0.9200	0.0130	0.1057	0.0013	0.2633	0.0625	0.0006	662	7	648	7	691	19	94
MF40-65	133	50	16	0.376	0.9050	0.0150	0.1058	0.0013	0.4547	0.0621	0.0006	654	8	648	8	678	21	96
MF40-102	1635	921	278	0.563	0.9040	0.0120	0.1059	0.0013	0.6106	0.0620	0.0003	654	6	649	7	672	12	97
MF40-127	279	164	50	0.589	0.9150	0.0130	0.1059	0.0012	0.2364	0.0626	0.0005	660	7	649	7	695	17	93
MF40-63	84	39	12	0.464	0.9020	0.0170	0.1062	0.0015	0.3935	0.0623	0.0009	653	9	651	9	684	31	95
MF40-50	592	406	128	0.686	0.9180	0.0145	0.1063	0.0015	0.6378	0.0626	0.0006	661	8	651	9	695	20	94
MF40-138	199	106	32	0.530	0.9370	0.0155	0.1064	0.0014	0.3189	0.0637	0.0008	671	8	652	8	732	25	89
MF40-46	144	53	17	0.368	0.9210	0.0155	0.1065	0.0014	0.5340	0.0627	0.0007	663	8	652	8	698	22	93
MF40-104	437	229	68	0.524	0.9040	0.0125	0.1065	0.0013	0.3951	0.0614	0.0004	654	7	652	7	652	16	100
MF40-1R	215	101	33	0.470	0.9100	0.0180	0.1066	0.0018	0.5775	0.0615	0.0009	657	10	653	10	657	30	99
MF40-26	368	216	78	0.587	0.9350	0.0165	0.1067	0.0016	0.7206	0.0636	0.0006	670	9	654	9	728	20	90
MF40-60	244	150	48	0.615	0.9330	0.0145	0.1069	0.0013	0.6185	0.0632	0.0005	669	8	655	7	715	17	92
MF40-59	196	88	27	0.449	0.9110	0.0150	0.1072	0.0016	0.5514	0.0621	0.0007	658	8	656	9	678	22	97
MF40-135	362	198	62	0.548	0.9110	0.0125	0.1072	0.0013	0.3428	0.0616	0.0005	658	7	656	8	661	16	99
MF40-78	160	100	32	0.625	0.9210	0.0145	0.1073	0.0014	0.4898	0.0628	0.0006	663	8	657	8	701	20	94
MF40-115	564	384	116	0.681	0.9200	0.0125	0.1073	0.0013	0.4662	0.0621	0.0004	662	7	657	7	676	13	97
MF40-18	762	321	102	0.421	0.9320	0.0175	0.1074	0.0020	0.6966	0.0624	0.0008	669	9	658	12	688	27	96
MF40-119	169	105	32	0.621	0.9550	0.0160	0.1075	0.0014	0.5379	0.0641	0.0007	681	8	658	8	745	21	88
MF40-35	191	89	30	0.466	0.9180	0.0150	0.1076	0.0015	0.4609	0.0622	0.0007	661	8	659	8	681	22	97
MF40-49	153	56	18	0.366	0.9220	0.0150	0.1078	0.0014	0.4810	0.0621	0.0006	663	8	660	8	678	21	97

Continued on next page

TABLE E.1 (continued): LA-ICPMS U-Pb detrital zircon analytical data.

Grain	U[a]	Th[a]	Pb[a]	Th/U	$^{207}Pb/^{235}U$[b]		$^{206}Pb/^{238}U$[b]		Rho[c]	$^{207}Pb/^{206}Pb$		$^{207}Pb/^{235}U$		$^{206}Pb/^{238}U$		$^{207}Pb/^{206}Pb$		Concordance[d]
	ppm	ppm	ppm	ratio	ratio	± 1σ	ratio	± 1σ	ρ	ratio	± 1σ	Ma	± 1σ	Ma	± 1σ	Ma	± 1σ	%
MF40-100	151	75	24	0.496	0.9270	0.0145	0.1078	0.0014	0.4535	0.0626	0.0006	666	8	660	8	695	20	95
MF40-6	113	54	18	0.478	0.9450	0.0190	0.1079	0.0017	0.5216	0.0634	0.0009	675	10	661	10	722	28	92
MF40-92	232	139	45	0.599	0.9390	0.0155	0.1079	0.0014	0.5486	0.0631	0.0006	672	8	661	8	712	20	93
MF40-32	370	218	72	0.589	0.9300	0.0155	0.1080	0.0015	0.5703	0.0625	0.0007	668	8	661	9	691	22	96
MF40-40	194	81	25	0.418	0.9190	0.0210	0.1083	0.0023	0.6394	0.0612	0.0011	662	11	663	13	646	37	103
MF40-139	333	140	43	0.420	0.9440	0.0145	0.1083	0.0014	0.2620	0.0634	0.0007	675	8	663	8	722	23	92
MF40-12	200	141	47	0.705	0.9220	0.0155	0.1084	0.0014	0.5038	0.0623	0.0007	663	8	663	8	684	22	97
MF40-37	203	100	33	0.493	0.9280	0.0150	0.1084	0.0014	0.5051	0.0623	0.0006	667	8	663	8	684	21	97
MF40-114	147	60	19	0.409	0.9290	0.0140	0.1084	0.0013	0.2592	0.0623	0.0006	667	7	663	8	684	21	97
MF40-72	754	390	127	0.517	0.9130	0.0160	0.1085	0.0018	0.7222	0.0617	0.0006	659	8	664	10	664	21	100
MF40-56	165	75	25	0.455	0.9160	0.0150	0.1087	0.0014	0.4955	0.0612	0.0007	660	8	665	8	646	23	103
MF40-3	179	84	30	0.469	0.9300	0.0155	0.1089	0.0015	0.5346	0.0623	0.0007	668	8	666	8	684	22	97
MF40-19	249	126	42	0.506	0.9390	0.0155	0.1089	0.0015	0.6290	0.0627	0.0006	672	8	666	8	698	20	95
MF40-55	231	107	35	0.463	0.9260	0.0145	0.1089	0.0014	0.5908	0.0618	0.0006	666	8	666	8	667	19	100
MF40-61	208	101	33	0.486	0.9330	0.0145	0.1089	0.0014	0.4703	0.0624	0.0006	669	8	666	8	688	19	97
MF40-62	434	221	73	0.509	0.9400	0.0145	0.1090	0.0013	0.6437	0.0623	0.0005	673	8	667	8	685	16	97
MF40-66	517	118	37	0.228	0.9370	0.0150	0.1091	0.0013	0.5979	0.0624	0.0005	671	8	668	8	688	17	97
MF40-45	183	119	38	0.650	0.9270	0.0155	0.1092	0.0014	0.5560	0.0618	0.0006	666	8	668	8	667	21	100
MF40-48	404	174	56	0.431	0.9170	0.0140	0.1092	0.0013	0.6708	0.0610	0.0005	661	7	668	8	639	16	105
MF40-73	347	185	60	0.533	0.9520	0.0145	0.1092	0.0013	0.5874	0.0634	0.0005	679	8	668	8	722	17	93
MF40-94	166	76	24	0.458	0.9310	0.0155	0.1093	0.0014	0.4507	0.0622	0.0007	668	8	669	8	681	22	98
MF40-110	602	95	26	0.158	0.9270	0.0130	0.1094	0.0014	0.6375	0.0614	0.0004	666	7	669	8	653	13	103
MF40-4	261	118	40	0.452	0.9370	0.0150	0.1096	0.0014	0.4987	0.0622	0.0006	671	8	670	8	681	21	98
MF40-16	844	362	121	0.429	0.9260	0.0145	0.1096	0.0014	0.6728	0.0610	0.0005	666	8	670	8	639	17	105
MF40-41	212	118	39	0.557	0.9350	0.0155	0.1097	0.0014	0.5669	0.0618	0.0006	670	8	671	8	667	19	101
MF40-89	297	131	42	0.441	0.9300	0.0150	0.1097	0.0014	0.5939	0.0614	0.0006	668	8	671	8	653	19	103
MF40-22	315	153	52	0.486	0.9340	0.0145	0.1098	0.0015	0.6217	0.0621	0.0006	670	8	672	8	678	19	99
MF40-58	109	42	14	0.385	0.9210	0.0160	0.1100	0.0015	0.4145	0.0613	0.0008	663	8	673	8	650	26	104
MF40-54	62	36	12	0.581	0.9230	0.0185	0.1101	0.0016	0.3741	0.0617	0.0010	664	10	673	9	664	33	101
MF40-34	220	157	53	0.714	0.9580	0.0160	0.1102	0.0015	0.6087	0.0633	0.0007	682	8	674	9	718	22	94
MF40-88	174	71	24	0.408	0.9480	0.0155	0.1102	0.0014	0.4757	0.0624	0.0007	677	8	674	8	688	22	98
MF40-64	368	184	60	0.500	0.9560	0.0150	0.1103	0.0013	0.5442	0.0624	0.0006	681	8	674	8	688	19	98
MF40-69	166	102	33	0.614	0.9550	0.0155	0.1103	0.0014	0.5267	0.0629	0.0006	681	8	674	8	705	20	96
MF40-95	260	153	49	0.588	0.9560	0.0165	0.1103	0.0016	0.5826	0.0628	0.0007	681	9	674	9	701	24	96
MF40-29	538	225	76	0.418	0.9390	0.0145	0.1104	0.0014	0.6554	0.0617	0.0005	672	8	675	8	663	17	102
MF40-57	296	168	57	0.568	0.9380	0.0150	0.1105	0.0015	0.7084	0.0616	0.0005	672	8	676	9	660	17	102
MF40-77	133	51	16	0.383	0.9500	0.0160	0.1105	0.0014	0.4230	0.0626	0.0007	678	8	676	8	695	22	97
MF40-52	530	205	69	0.387	0.9480	0.0150	0.1106	0.0015	0.7205	0.0622	0.0005	677	8	676	8	680	17	99
MF40-91	190	79	25	0.416	0.9250	0.0155	0.1108	0.0014	0.4891	0.0607	0.0006	665	8	677	8	629	21	108
MF40-93	291	155	50	0.533	0.9370	0.0150	0.1108	0.0014	0.5323	0.0617	0.0006	671	8	677	8	664	19	102
MF40-14	244	126	42	0.516	0.9540	0.0150	0.1111	0.0014	0.5720	0.0627	0.0006	680	8	679	8	698	20	97
MF40-8	317	169	56	0.533	0.9280	0.0145	0.1112	0.0015	0.6155	0.0609	0.0006	667	8	680	9	636	19	107
MF40-11	259	129	43	0.498	0.9410	0.0155	0.1112	0.0015	0.6408	0.0620	0.0006	673	8	680	8	674	19	101
MF40-82	684	275	90	0.402	0.9510	0.0140	0.1114	0.0013	0.6071	0.0619	0.0004	679	7	681	8	669	15	102

Continued on next page

TABLE E.1 (continued): LA-ICP-MS U-Pb Detrital Zircon Analytical Data

Grain	U[a]	Th[a]	Pb[a]	Th/U	$^{207}Pb/^{235}U$[b]		$^{206}Pb/^{238}U$[b]		Rho[c]	$^{207}Pb/^{206}Pb$		$^{207}Pb/^{235}U$		$^{206}Pb/^{238}U$		$^{207}Pb/^{206}Pb$		Concordance[d]
	ppm	ppm	ppm	ratio	ratio	± 1σ	ratio	± 1σ	ρ	ratio	± 1σ	Ma	± 1σ	Ma	± 1σ	Ma	± 1σ	%
MF40-21	287	173	58	0.603	0.9440	0.0150	0.1115	0.0015	0.5581	0.0617	0.0006	675	8	681	8	664	19	103
MF40-68	530	216	74	0.408	1.0090	0.0205	0.1116	0.0020	0.6457	0.0647	0.0009	708	10	682	11	765	29	89
MF40-5	165	57	21	0.345	0.9790	0.0225	0.1117	0.0026	0.6547	0.0637	0.0011	693	12	683	15	732	35	93
MF40-84	184	94	31	0.511	0.9630	0.0160	0.1117	0.0014	0.4364	0.0628	0.0007	685	8	683	8	701	22	97
MF40-39	139	77	26	0.554	0.9640	0.0165	0.1122	0.0016	0.5747	0.0627	0.0007	685	9	686	9	698	22	98
MF40-75	93	36	12	0.387	0.9570	0.0175	0.1123	0.0014	0.3245	0.0618	0.0008	682	9	686	8	667	28	103
MF40-20	164	77	27	0.470	0.9600	0.0160	0.1129	0.0014	0.4112	0.0619	0.0007	683	8	690	8	671	24	103
MF40-38	783	226	76	0.289	0.9570	0.0150	0.1129	0.0015	0.7224	0.0615	0.0005	682	8	690	9	656	16	105
MF40-81	299	196	65	0.656	0.9610	0.0150	0.1129	0.0013	0.5524	0.0617	0.0005	684	8	690	7	662	17	104
MF40-87	165	69	24	0.418	0.9500	0.0170	0.1129	0.0016	0.4568	0.0619	0.0008	678	9	690	9	671	28	103
MF40-79	100	47	15	0.470	0.9690	0.0170	0.1130	0.0014	0.4820	0.0620	0.0007	688	9	690	8	674	22	102
MF40-2	1093	622	219	0.569	0.9620	0.0145	0.1131	0.0014	0.7381	0.0618	0.0004	684	8	691	8	669	15	103
MF40-47	1453	503	176	0.346	0.9710	0.0145	0.1131	0.0015	0.7390	0.0625	0.0005	689	7	691	8	690	16	100
MF40-98	108	50	17	0.458	1.0000	0.0165	0.1132	0.0015	0.1486	0.0642	0.0008	704	8	691	8	748	26	92
MF40-42	220	113	40	0.514	0.9640	0.0150	0.1133	0.0014	0.4924	0.0616	0.0006	685	8	692	8	660	19	105
MF40-67	369	97	35	0.263	0.9770	0.0155	0.1141	0.0014	0.5922	0.0621	0.0005	692	8	697	8	678	17	103
MF40-30	525	188	67	0.358	0.9830	0.0150	0.1147	0.0014	0.6492	0.0621	0.0005	695	8	700	8	677	16	103
MF40-70	1116	513	166	0.460	0.9700	0.0160	0.1148	0.0017	0.7447	0.0610	0.0005	688	8	701	10	639	18	110
MF40-141	371	204	113	0.551	2.8290	0.0435	0.2280	0.0031	0.4150	0.0898	0.0009	1363	12	1324	16	1421	19	93
MF40-23	85	77	61	0.906	3.3000	0.0500	0.2601	0.0033	0.5478	0.0924	0.0009	1481	12	1490	17	1476	17	101
MF40-76	163	103	70	0.632	4.1000	0.0750	0.2730	0.0043	0.6691	0.1081	0.0013	1654	15	1556	22	1768	21	88
MF40-85	593	196	149	0.331	3.6900	0.0550	0.2732	0.0037	0.7849	0.0983	0.0007	1569	12	1557	18	1592	13	98
MF40-10	69	66	52	0.957	3.7900	0.0600	0.2789	0.0039	0.6523	0.0993	0.0009	1591	13	1586	19	1611	17	98
MF40-13	537	96	89	0.179	3.9500	0.0650	0.2815	0.0039	0.8048	0.1014	0.0008	1624	13	1599	20	1650	15	97
MF40-53	110	130	103	1.182	3.8000	0.0600	0.2826	0.0035	0.5634	0.0976	0.0008	1593	13	1604	18	1579	15	102
MF40-90	78	39	30	0.500	3.7200	0.0600	0.2891	0.0041	0.6713	0.0938	0.0009	1576	13	1637	20	1504	17	109
MF40-36	102	60	50	0.588	4.0300	0.0600	0.2924	0.0035	0.5591	0.1001	0.0009	1640	12	1654	17	1626	16	102
MF40-128	189	103	68	0.546	4.7090	0.0700	0.3036	0.0042	0.7441	0.1122	0.0008	1769	12	1709	21	1835	12	93
MF40-28	367	127	113	0.346	4.5400	0.0700	0.3104	0.0038	0.7404	0.1060	0.0007	1738	13	1743	19	1732	12	101
MF40-117	345	399	317	1.157	4.7000	0.0800	0.3122	0.0049	0.6148	0.1095	0.0011	1767	14	1752	24	1791	17	98
MF40-86	190	158	136	0.832	4.7200	0.0700	0.3169	0.0038	0.6567	0.1082	0.0008	1771	12	1775	19	1769	14	100
MF40-124	256	220	195	0.857	4.8020	0.0600	0.3197	0.0037	0.6424	0.1087	0.0005	1785	11	1788	18	1777	8	101
MF40-80	172	64	55	0.372	4.8700	0.0700	0.3230	0.0037	0.6625	0.1093	0.0008	1797	12	1804	18	1788	13	101
MF40-125	132	12	10	0.089	4.9710	0.0650	0.3246	0.0038	0.4607	0.1107	0.0007	1814	11	1812	18	1811	11	100
MF40-43	103	89	83	0.864	4.8900	0.0750	0.3273	0.0042	0.7161	0.1084	0.0008	1801	13	1825	20	1773	13	103
MF40-74	514	159	135	0.309	5.4900	0.0850	0.3299	0.0044	0.6721	0.1191	0.0010	1899	13	1838	21	1943	15	95
MF40-83	415	272	234	0.655	5.1700	0.0800	0.3313	0.0040	0.7821	0.1135	0.0007	1848	13	1845	19	1856	11	99
MF40-44	214	78	77	0.364	5.2400	0.0800	0.3371	0.0041	0.7226	0.1126	0.0008	1859	13	1873	20	1842	12	102
MF40-27	198	73	71	0.369	5.3300	0.0800	0.3396	0.0045	0.7408	0.1136	0.0009	1874	13	1885	21	1858	14	101
MF40-31	367	223	231	0.608	6.2500	0.1150	0.3640	0.0060	0.7726	0.1239	0.0013	2011	16	2001	28	2013	19	99
MF40-113	328	137	173	0.416	11.1400	0.1450	0.4847	0.0060	0.6328	0.1665	0.0009	2535	12	2548	26	2523	9	101
MF40-9	215	76	105	0.353	11.7400	0.1750	0.4880	0.0060	0.7947	0.1742	0.0012	2584	14	2562	26	2598	11	99
MF40-17	249	87	115	0.349	11.5300	0.1750	0.4920	0.0065	0.7992	0.1704	0.0012	2567	14	2579	28	2562	11	101
MF40-51	63	52	73	0.825	13.0100	0.2000	0.5160	0.0065	0.6837	0.1835	0.0014	2680	14	2682	28	2685	12	100

Continued on next page

TABLE E.1 (continued): LA-ICPMS U-Pb detrital zircon analytical data.

Grain	U[a]	Th[a]	Pb[a]	Th/U	$^{207}Pb/^{235}U$[b]		$^{206}Pb/^{238}U$[b]		Rho[c]	$^{207}Pb/^{206}Pb$		$^{207}Pb/^{235}U$		$^{206}Pb/^{238}U$		$^{207}Pb/^{206}Pb$		Concordance[d]
	ppm	ppm	ppm	ratio	ratio	± 1σ	ratio	± 1σ	ρ	ratio	± 1σ	Ma	± 1σ	Ma	± 1σ	Ma	± 1σ	%
Discordant Analyses																		
MF40-105	5330	5280	685	0.991	0.4127	0.0060	0.0443	0.0007	0.7763	0.0677	0.0004	351	4	280	4	860	14	33
MF40-108	1817	1026	236	0.565	0.5810	0.0085	0.0675	0.0010	0.5707	0.0622	0.0006	465	5	421	6	681	19	62
MF40-132	208	123	37	0.589	0.9690	0.0155	0.0991	0.0014	0.2750	0.0708	0.0009	688	8	609	8	952	26	64
MF40-133	181	79	23	0.438	0.9150	0.0140	0.1016	0.0014	0.3918	0.0652	0.0007	660	7	624	8	781	23	80
MF40-99	149	80	24	0.534	0.9290	0.0165	0.1036	0.0016	0.0515	0.0661	0.0013	667	9	635	9	810	40	78
MF40-136	204	135	42	0.662	1.0370	0.0190	0.1039	0.0013	0.3748	0.0718	0.0010	722	9	637	8	980	27	65
MF40-71	62	83	24	1.339	1.0280	0.0205	0.1053	0.0015	0.3424	0.0712	0.0011	718	10	645	9	963	32	67
MF40-121	138	65	20	0.472	0.9530	0.0165	0.1054	0.0014	0.2992	0.0653	0.0009	680	9	646	8	784	27	82
MF40-15	2256	630	256	0.279	1.2050	0.0215	0.1066	0.0017	0.8006	0.0823	0.0008	803	10	653	10	1253	18	52
MF40-112	213	134	44	0.628	0.9760	0.0155	0.1077	0.0014	0.3249	0.0656	0.0007	692	8	659	8	794	22	83
MF40-24	267	142	64	0.532	1.2890	0.0235	0.1098	0.0015	0.4886	0.0852	0.0011	841	10	672	9	1320	24	51
MF40-107	397	168	52	0.423	0.9990	0.0185	0.1098	0.0018	0.3353	0.0662	0.0010	703	9	672	10	813	30	83
MF40-1C	113	47	16	0.416	1.0650	0.0235	0.1111	0.0021	0.3382	0.0689	0.0014	736	12	679	12	896	42	76
Sample MF83 - 152.0 m (Greywacke)																		
Concordant Analyses																		
MF83-32	441	65	20	0.147	0.8350	0.0145	0.0970	0.0013	0.4546	0.0621	0.0008	616	8	597	8	678	28	88
MF83-38	234	183	53	0.782	0.8670	0.0145	0.0992	0.0014	0.5925	0.0628	0.0007	634	8	610	8	701	24	87
MF83-95	896	379	96	0.423	0.8660	0.0140	0.1010	0.0014	0.4967	0.0619	0.0007	633	8	620	8	671	22	92
MF83-98	277	125	35	0.451	0.8720	0.0145	0.1019	0.0013	0.4218	0.0621	0.0007	637	8	626	8	678	24	92
MF83-41	566	54	15	0.095	0.8800	0.0175	0.1020	0.0017	0.6646	0.0618	0.0009	641	9	626	10	667	29	94
MF83-19	308	179	50	0.581	0.8900	0.0135	0.1025	0.0012	0.5148	0.0625	0.0006	646	7	629	7	691	20	91
MF83-103	655	242	69	0.369	0.8790	0.0135	0.1023	0.0015	0.5152	0.0623	0.0006	640	7	628	8	684	21	92
MF83-33	522	239	67	0.458	0.9090	0.0150	0.1025	0.0015	0.6174	0.0636	0.0007	657	8	629	9	728	23	86
MF83-55	312	284	76	0.910	0.8910	0.0160	0.1027	0.0015	0.5830	0.0626	0.0008	647	9	630	8	695	26	91
MF83-94	489	234	72	0.478	0.8680	0.0120	0.1031	0.0013	0.4400	0.0611	0.0005	634	7	633	7	644	17	98
MF83-92	166	93	31	0.561	0.8820	0.0160	0.1033	0.0015	0.2832	0.0620	0.0009	642	9	634	8	674	31	94
MF83-105	323	198	56	0.611	0.8710	0.0140	0.1037	0.0014	0.3822	0.0610	0.0007	636	8	636	8	639	23	100
MF83-85	173	79	24	0.455	0.8900	0.0150	0.1039	0.0014	0.4423	0.0622	0.0007	646	8	637	8	681	24	94
MF83-97	304	137	42	0.450	0.9220	0.0135	0.1042	0.0013	0.2205	0.0641	0.0006	663	7	639	8	745	20	86
MF83-49	216	152	45	0.704	0.8690	0.0140	0.1048	0.0014	0.6184	0.0600	0.0006	635	8	642	8	604	22	106
MF83-83	364	226	69	0.620	0.8970	0.0130	0.1050	0.0013	0.3743	0.0618	0.0005	650	7	644	7	665	17	97
MF83-87	748	918	253	1.227	0.9130	0.0145	0.1056	0.0015	0.6257	0.0628	0.0006	659	8	647	9	701	20	92
MF83-91	275	149	45	0.540	0.9000	0.0130	0.1056	0.0013	0.3947	0.0618	0.0005	652	7	647	8	667	17	97
MF83-45	255	135	41	0.529	0.9270	0.0140	0.1057	0.0013	0.4471	0.0632	0.0006	666	7	648	7	715	20	91
MF83-96	243	147	45	0.606	0.9220	0.0135	0.1059	0.0013	0.3477	0.0629	0.0006	663	7	649	7	705	19	92
MF83-88	96	48	15	0.497	0.9050	0.0165	0.1059	0.0014	0.3605	0.0623	0.0009	654	9	649	8	684	29	95
MF83-21	345	175	52	0.507	0.8970	0.0130	0.1061	0.0013	0.5029	0.0614	0.0006	650	7	650	8	653	21	100
MF83-36	427	200	58	0.468	0.9270	0.0160	0.1064	0.0015	0.6604	0.0629	0.0007	666	8	652	9	705	24	92
MF83-82	157	58	18	0.369	0.9390	0.0145	0.1063	0.0012	0.2666	0.0636	0.0010	672	8	651	7	728	32	89

Continued on next page

TABLE E.1 (continued): LA-ICPMS U-Pb detrital zircon analytical data.

Grain	U[a]	Th[a]	Pb[a]	Th/U	$^{207}Pb/^{235}U$[b]		$^{206}Pb/^{238}U$[b]		Rho[c]	$^{207}Pb/^{206}Pb$		$^{207}Pb/^{235}U$		$^{206}Pb/^{238}U$		$^{207}Pb/^{206}Pb$		Concordance[d]
	ppm	ppm	ppm	ratio	ratio	± 1σ	ratio	± 1σ	ρ	ratio	± 1σ	Ma	± 1σ	Ma	± 1σ	Ma	± 1σ	%
MF83-90	118	61	19	0.519	0.9150	0.0165	0.1065	0.0014	0.4009	0.0622	0.0008	660	9	652	8	681	27	96
MF83-23	424	239	73	0.564	0.9130	0.0140	0.1067	0.0014	0.6153	0.0617	0.0006	659	7	654	8	664	19	98
MF83-81	257	104	31	0.405	0.8970	0.0170	0.1072	0.0014	0.4065	0.0612	0.0010	650	9	656	8	646	35	102
MF83-31	256	169	50	0.660	0.9270	0.0140	0.1076	0.0013	0.5334	0.0620	0.0006	666	7	659	8	674	21	98
MF83-1	120	98	30	0.817	0.9620	0.0175	0.1075	0.0014	0.4605	0.0649	0.0009	684	9	658	8	771	28	85
MF83-53	88	40	13	0.455	0.9550	0.0290	0.1075	0.0022	0.3394	0.0643	0.0019	681	15	658	13	752	61	88
MF83-25	186	94	29	0.505	0.9020	0.0140	0.1077	0.0014	0.3772	0.0607	0.0007	653	7	659	8	629	23	105
MF83-46	381	140	44	0.367	0.9360	0.0145	0.1078	0.0014	0.5077	0.0630	0.0007	671	8	660	8	708	24	93
MF83-28	212	120	38	0.566	0.9510	0.0150	0.1079	0.0013	0.4744	0.0635	0.0007	679	8	661	8	725	22	91
MF83-18	453	236	73	0.521	0.9130	0.0130	0.1079	0.0013	0.5642	0.0611	0.0005	659	7	661	7	643	18	103
MF83-84	184	92	28	0.501	0.9150	0.0140	0.1081	0.0014	0.4208	0.0614	0.0006	660	7	662	8	653	21	101
MF83-3	246	150	45	0.610	0.9430	0.0150	0.1082	0.0014	0.5416	0.0634	0.0007	674	8	662	8	722	22	92
MF83-79	138	61	19	0.442	0.9170	0.0140	0.1085	0.0014	0.3755	0.0618	0.0009	661	7	664	8	667	31	100
MF83-13	296	153	49	0.517	0.9280	0.0145	0.1089	0.0014	0.5653	0.0618	0.0006	667	8	666	8	667	21	100
MF83-34	351	236	72	0.672	0.9270	0.0135	0.1090	0.0013	0.5216	0.0616	0.0006	666	7	667	8	660	19	101
MF83-8	172	87	27	0.506	0.9270	0.0150	0.1092	0.0014	0.4272	0.0617	0.0007	666	8	668	8	664	24	101
MF83-5	419	280	83	0.668	0.9360	0.0165	0.1095	0.0016	0.4846	0.0617	0.0008	671	9	670	9	664	26	101
MF83-11	106	43	14	0.406	0.9530	0.0160	0.1094	0.0015	0.4668	0.0634	0.0008	680	8	669	9	722	25	93
MF83-77C	231	126	39	0.545	0.9220	0.0145	0.1095	0.0013	0.4088	0.0610	0.0007	663	8	670	8	639	23	105
MF83-64	408	234	74	0.574	0.9410	0.0135	0.1097	0.0013	0.4311	0.0622	0.0006	673	7	671	8	681	19	99
MF83-6	72	36	11	0.500	0.9190	0.0170	0.1101	0.0016	0.4284	0.0612	0.0009	662	9	673	9	646	32	104
MF83-15	213	74	24	0.347	0.9490	0.0145	0.1101	0.0014	0.2641	0.0627	0.0007	678	8	673	8	698	24	96
MF83-77R	190	86	27	0.453	0.9270	0.0145	0.1100	0.0013	0.4762	0.0614	0.0007	666	8	673	8	653	23	103
MF83-4	281	126	40	0.448	0.9440	0.0145	0.1103	0.0014	0.4714	0.0621	0.0007	675	8	674	8	678	22	100
MF83-2	260	103	32	0.396	0.9300	0.0140	0.1105	0.0013	0.5288	0.0610	0.0006	668	7	676	8	639	19	106
MF83-39	164	81	25	0.494	0.9370	0.0145	0.1104	0.0013	0.4901	0.0612	0.0007	671	8	675	8	646	23	104
MF83-78	306	191	59	0.624	0.9430	0.0140	0.1104	0.0013	0.4102	0.0622	0.0006	674	7	675	8	681	21	99
MF83-93	565	479	146	0.848	0.9790	0.0180	0.1105	0.0017	0.5719	0.0644	0.0008	693	9	676	10	755	25	90
MF83-73	338	201	60	0.595	0.9860	0.0215	0.1104	0.0023	0.4922	0.0649	0.0013	697	11	675	13	771	41	88
MF83-24	190	94	30	0.495	0.9250	0.0145	0.1107	0.0014	0.4318	0.0607	0.0007	665	8	677	8	629	23	108
MF83-76	102	40	12	0.392	0.9200	0.0155	0.1108	0.0014	0.2653	0.0606	0.0008	662	8	677	8	625	27	108
MF83-16	281	155	51	0.552	0.9990	0.0160	0.1106	0.0014	0.5320	0.0654	0.0007	703	8	676	8	787	22	86
MF83-30	90	35	11	0.389	0.9740	0.0165	0.1110	0.0014	0.3634	0.0631	0.0008	691	8	679	8	712	27	95
MF83-63	368	183	56	0.497	0.9390	0.0140	0.1109	0.0014	0.5383	0.0612	0.0006	672	7	678	8	646	19	105
MF83-68	321	189	60	0.589	0.9470	0.0145	0.1109	0.0013	0.4769	0.0619	0.0006	677	8	678	8	671	21	101
MF83-12	151	89	29	0.589	0.9730	0.0170	0.1112	0.0016	0.5475	0.0633	0.0008	690	9	680	9	718	25	95
MF83-7	195	76	23	0.390	0.9360	0.0150	0.1113	0.0015	0.4707	0.0613	0.0007	671	8	680	8	650	25	105
MF83-47	415	83	25	0.200	0.9450	0.0160	0.1110	0.0016	0.5763	0.0611	0.0007	675	8	679	9	643	25	106
MF83-17	617	201	66	0.326	0.9590	0.0140	0.1118	0.0014	0.6944	0.0624	0.0005	683	7	683	8	688	17	99
MF83-9	251	90	28	0.359	0.9550	0.0145	0.1121	0.0015	0.5998	0.0620	0.0006	681	8	685	8	674	21	102
MF83-66	269	70	23	0.260	0.9510	0.0135	0.1122	0.0013	0.3928	0.0615	0.0006	679	7	686	7	657	19	104
MF83-69	472	292	93	0.619	0.9390	0.0135	0.1121	0.0013	0.5316	0.0608	0.0005	672	7	685	8	632	18	108
MF83-70	173	87	27	0.503	0.9220	0.0145	0.1121	0.0013	0.5102	0.0598	0.0006	663	8	685	8	596	22	115
MF83-26	55	24	6	0.436	0.9780	0.0340	0.1126	0.0024	0.2898	0.0634	0.0022	693	17	688	14	722	72	95

Continued on next page

TABLE E.1 (continued): LA-ICPMS U-Pb detrital zircon analytical data.

Grain	U[a]	Th[a]	Pb[a]	Th/U	$^{207}Pb/^{235}U$[b]		$^{206}Pb/^{238}U$[b]		Rho[c]	$^{207}Pb/^{206}Pb$		$^{207}Pb/^{235}U$		$^{206}Pb/^{238}U$		$^{207}Pb/^{206}Pb$		Concordance[d]
	ppm	ppm	ppm	ratio	ratio	± 1σ	ratio	± 1σ	ρ	ratio	± 1σ	Ma	± 1σ	Ma	± 1σ	Ma	± 1σ	%
MF83-20	141	60	20	0.426	0.9750	0.0160	0.1130	0.0015	0.4575	0.0627	0.0007	691	8	690	8	698	24	99
MF83-67	826	308	100	0.373	0.9620	0.0135	0.1140	0.0013	0.6097	0.0611	0.0005	684	7	696	7	644	17	108
MF83-58	560	197	64	0.352	0.9690	0.0140	0.1144	0.0014	0.5330	0.0611	0.0006	688	7	698	8	643	19	109
MF83-65	148	67	22	0.453	0.9680	0.0180	0.1151	0.0018	0.4842	0.0611	0.0009	687	9	702	10	643	32	109
MF83-62	55	69	40	1.255	2.2110	0.0370	0.2026	0.0027	0.4293	0.0791	0.0010	1185	12	1189	14	1175	24	101
MF83-74	293	142	95	0.485	4.0300	0.0550	0.2850	0.0033	0.6114	0.1028	0.0008	1640	11	1616	17	1675	14	96
MF83-61	559	106	82	0.190	4.3800	0.0700	0.2872	0.0039	0.6961	0.1102	0.0011	1709	13	1628	20	1803	17	90
MF83-27	128	45	37	0.352	3.9100	0.0550	0.2900	0.0035	0.5336	0.0973	0.0009	1616	11	1642	17	1573	17	104
MF83-35	719	269	205	0.374	4.5400	0.0800	0.3000	0.0048	0.7043	0.1097	0.0012	1738	15	1691	24	1794	20	94
MF83-48	193	145	87	0.751	4.7200	0.0700	0.3033	0.0040	0.5966	0.1128	0.0011	1771	12	1708	20	1845	17	93
MF83-102	139	70	59	0.508	4.4550	0.0600	0.3049	0.0036	0.5220	0.1059	0.0007	1723	11	1716	18	1730	11	99
MF83-104	154	118	102	0.767	4.7270	0.0650	0.3163	0.0039	0.5219	0.1083	0.0008	1772	12	1772	19	1771	13	100
MF83-72	94	98	83	1.043	4.7400	0.0700	0.3239	0.0039	0.4998	0.1064	0.0010	1774	12	1809	19	1739	16	104
MF83-75	273	75	67	0.275	5.0500	0.0700	0.3321	0.0039	0.7241	0.1106	0.0008	1828	12	1849	19	1809	13	102
MF83-71	459	145	122	0.316	5.2100	0.0750	0.3368	0.0045	0.6464	0.1123	0.0011	1854	12	1871	22	1837	17	102
MF83-51	570	187	209	0.328	8.0200	0.1150	0.3970	0.0048	0.7146	0.1456	0.0012	2233	13	2155	22	2295	14	94
MF83-101	388	232	277	0.598	10.0400	0.1350	0.4611	0.0055	0.6759	0.1578	0.0008	2438	12	2444	24	2432	8	101
MF83-10	235	222	278	0.945	11.6100	0.1700	0.4990	0.0065	0.7611	0.1687	0.0014	2573	14	2609	28	2545	14	103
Discordant Analyses																		
MF83-80	3771	2211	427	0.586	0.7390	0.0095	0.0726	0.0012	0.6881	0.0720	0.0005	562	6	452	7	985	13	46
MF83-14	2226	803	234	0.361	0.8210	0.0135	0.0880	0.0014	0.7529	0.0676	0.0007	609	8	544	8	856	22	63
MF83-43	81	42	15	0.519	0.9960	0.0195	0.0956	0.0015	0.3064	0.0746	0.0013	702	10	589	9	1058	34	56
MF83-50	118	71	19	0.602	0.9170	0.0175	0.0981	0.0015	0.4285	0.0677	0.0011	661	9	603	9	859	32	70
MF83-54	175	97	28	0.554	0.8830	0.0155	0.0984	0.0013	0.5010	0.0647	0.0008	643	8	605	7	765	26	79
MF83-40	177	130	39	0.734	0.9830	0.0160	0.1006	0.0013	0.4968	0.0704	0.0008	695	8	618	7	940	23	66
MF83-57	115	60	18	0.522	0.9220	0.0155	0.1018	0.0014	0.4033	0.0653	0.0009	663	8	625	8	784	27	80
MF83-56	159	171	46	1.075	0.9680	0.0160	0.1022	0.0013	0.2801	0.0687	0.0009	687	8	627	8	890	26	71
MF83-99	125	64	19	0.514	0.9030	0.0190	0.1017	0.0017	0.3611	0.0645	0.0012	653	10	624	10	758	39	82
MF83-22	71	34	13	0.479	1.1790	0.0225	0.1032	0.0015	0.2855	0.0822	0.0013	791	10	633	8	1250	31	51
MF83-44	109	84	20	0.771	1.0450	0.0275	0.1045	0.0020	0.3383	0.0729	0.0018	726	14	641	11	1011	49	63
MF83-29	187	96	32	0.513	0.9710	0.0175	0.1064	0.0015	0.5274	0.0661	0.0009	689	9	652	9	810	28	81
MF83-100	85	47	15	0.553	0.9550	0.0215	0.1066	0.0017	0.2852	0.0650	0.0013	681	11	653	10	774	40	84
MF83-52	176	91	31	0.517	1.0070	0.0160	0.1069	0.0015	0.3137	0.0689	0.0009	707	8	655	8	896	25	73
MF83-60	214	102	33	0.477	0.9950	0.0170	0.1076	0.0014	0.4670	0.0675	0.0009	701	9	659	8	853	26	77
MF83-86	235	115	35	0.489	0.9870	0.0195	0.1086	0.0018	0.3277	0.0660	0.0010	697	10	665	10	806	32	82
MF83-37	50	24	8	0.480	1.0450	0.0230	0.1109	0.0018	0.3463	0.0688	0.0013	726	11	678	10	893	39	76
MF83-59	112	59	30	0.527	1.6290	0.0345	0.1110	0.0014	0.4024	0.1056	0.0017	981	13	679	8	1725	30	39
MF83-42	348	64	26	0.184	2.6500	0.0550	0.1971	0.0038	0.7476	0.0966	0.0013	1315	15	1160	20	1559	24	74

[a] U, Th and Pb concentrations were calculated relative to ziron standard 91500 (Wiedenbeck et al. 1995).

[b] Zircon standard 91500 (Wiedenbeck et al. 1995) was used as the primary standard for the correction of $^{206}Pb/^{238}U$ and $^{207}Pb/^{235}U$ ratios; Temora 2 (Black et al. 2004) and Plesovice (Sláma et al. 2008) were used as secondary zircon standards.

[c] Rho (ρ) is the error correlation coefficient.

[d] Degree of concordance is expressed as a percentage of the $^{206}Pb/^{238}U$ age divided by the $^{207}Pb/^{206}Pb$ age, with a perfectly concordant analysis equal to 100% (Gehrels 2011); concordance cut-off is set at ± 15% of a perfectly concordant analysis.

Bibliography

Adabi M. 1997. Application of carbon isotope chemostratigraphy to the Renison dolomites, Tasmania: A Neoproterozoic age. *Australian Journal of Earth Sciences* **44(6)**, 767–775. URL http://dx.doi.org/10.1080/08120099708728353.

Arndt N., Lesher C. & Czamanske G. 2005. Mantle-derived magmas and magmatic Ni-Cu-(PGE) deposits. *In:* J. Hedenquist, J. Thompson, R. Goldfarb & J. Richards, eds., *Economic Geology, 100th Anniversary Volume*, pp. 2–33. Society of Economic Geologists.

Banks M., Baillie P., Brown A., Burrett C., Calver C., Carey S., Hills P., Jago J., Kennedy D., Powell C., Rao C. & Taylor S. 1989. Late Cambrian to Devonian. *In:* C. Burrett & E. Martin, eds., *Geology and Mineral Resources of Tasmania: Geological Society of Australia, Special Publication 15*, pp. 182–273. Geological Society of Australia (Tasmania Division).

Berry R. & Bull S. 2012. The pre-Carboniferous geology of Tasmania. *Episodes: International Geoscience Newsmagazine* **35(1)**, 195–204.

Berry R. & Crawford A. 1988. The tectonic significance of Cambrian allochthonous mafic-ultramafic complexes in Tasmania. *Australian Journal of Earth Sciences* **35(4)**, 523–533. URL http://dx.doi.org/10.1080/08120098808729467.

Black L., Kamo S., Allen C., Davis D., Aleinikoff J., Valley J., Mundil R., Campbell I., Korsch R., Williams I. & Foudoulis C. 2004. Improved 206Pb/238U microprobe geochronology by the monitoring of a trace-element-related matrix effect; SHRIMP, ID-TIMS, ELA-ICP-MS and oxygen isotope documentation for a series of zircon standards. *Chemical Geology* **205(1-2)**, 115–140. URL http://dx.doi.org/10.1016/j.chemgeo.2004.01.003.

Blissett A. 1962. Zeehan One Mile Geological Map Series K55-5-50. *Tasmania Department of Mines, Geological Survey Explanatory Report* pp. 1–258.

Blundy J. & Wood B. 2003. Partitioning of trace elements between crystals and melts. *Earth and Planetary Science Letters* **210(3–4)**, 383–397. URL http://dx.doi.org/10.1016/S0012-821X(03)00129-8.

Brown A. 1986. Geology of the Dundas-Mt Lindsay-Mt Youngbuck region. *Tasmania Department of Mines, Geological Survey Bulletin 62* pp. 1–221.

Brown A. 1991. Revocation report on the Melba Flats Exempt Area, SR 1987. *Unpublished report for Tasmania Department of Resources and energy, Division of Mines and Mineral Resources* pp. 1–63.

Brown A., Jago J., Williams P., Calver C. & Turner N. 1989. Eo-Cambrian-Cambrian. *In:* C. Burrett & E. Martin, eds., *Geology and Mineral Resources of Tasmania: Geological Society of Australia, Special Publication 15*, pp. 47–83. Geological Society of Australia (Tasmania Division).

Brown A. & Jenner G. 1989. Geological setting, petrology and chemistry of Cambrian boninite and low Ti tholeiite lavas in western Tasmania. *In:* A. Crawford, ed., *Boninites and related rocks*, pp. 232–263. Unwin Hyman, London.

Calver C. 1998. Isotope stratigraphy of the Neoproterozoic Togari Group, Tasmania. *Australian Journal of Earth Sciences* **45(6)**, 865–874. URL `http://dx.doi.org/10.1080/08120099808728441`.

Calver C., Black L., Everard J. & Seymour D. 2004. U-Pb zircon age constraints on late Neoproterozoic glaciation in Tasmania. *Geology* **32(10)**, 893–896. URL `http://dx.doi.org/10.1130/G20713.1`.

Calver C., Everard J., Berry R., Bottrill R. & Seymour D. 2014. Proterozoic Tasmania. *In:* K. Corbett, P. Quilty & C. Calver, eds., *Geological Evolution of Tasmania: Geological Society of Australia, Special Publication 24*, pp. 33–94. Geological Society of Australia (Tasmania Division).

Cawood P., Wang Y., Xu Y. & Zhao G. 2013. Locating south china in rodinia and gondwana: A fragment of greater india lithosphere? *Geology* **41(8)**, 903–906. URL `http://dx.doi.org/10.1130/G34395.1`.

Corbett K. 2014. A summary of Tasmania's geology and geological history. *In:* K. Corbett, P. Quilty & C. Calver, eds., *Geological Evolution of Tasmania: Geological Society of Australia, Special Publication 24*, pp. 1–12. Geological Society of Australia (Tasmania Division).

Corbett K., Berry R., Everard J., Calver C., Crawford A., Vicary M., Bottrill R. & McNeill A. 2014a. Cambrian Tasmania. *In:* K. Corbett, P. Quilty & C. Calver, eds., *Geological Evolution of Tasmania: Geological Society of Australia, Special Publication 24*, pp. 95–240. Geological Society of Australia (Tasmania Division).

Corbett K., Calver C., Bacon C., Bottrill R., Dickens G., Mazengarb C., Stevenson M. & Houshold I. 2014b. Geology and Tasmania's Development. *In:* K. Corbett, P. Quilty & C. Calver, eds., *Geological Evolution of Tasmania: Geological Society of Australia, Special Publication 24*, pp. 549–574. Geological Society of Australia (Tasmania Division).

Cox K., Bell J. & Pankhurst R. 1979. *The Interpretation of Igneous Rocks*. Allen & Unwin, London, 450 pp.

Crawford A. & Berry R. 1992. Tectonic implications of Late Proterozoic-Early Palaeozoic igneous rock associations in western Tasmania. *Tectonophysics* **214(1-4)**, 37–56. URL http://dx.doi.org/10.1016/0040-1951(92)90189-D.

Crawford A., Corbett K. & Everard J. 1992. Geochemistry of the Cambrian volcanic-hosted massive sulfide-rich Mount Read Volcanics, Tasmania, and some tectonic implications. *Economic Geology* **87(3)**, 597–619. URL http://dx.doi.org/10.2113/gsecongeo.87.3.597.

Crawford A. & Keays R. 2010. Magmatic Ni-Cu sulfides in mafic sills at Melba Flats, Western Tasmania - a geochemical investigation. *Unpublished report for Allegience Mining Pty Ltd* pp. 1–34.

Dalrymple G. & Lanphere M. 1969. *Potassium-Argon Dating: Principles, Techniques and Applications to Geochronology*. W.H. Freeman, San Francisco, 258 pp.

Dickinson W. & Gehrels G. 2009. Use of U–Pb ages of detrital zircons to infer maximum depositional ages of strata: A test against a Colorado Plateau Mesozoic database. *Earth and Planetary Science Letters* **288(1-2)**, 115–125. URL http://dx.doi.org/10.1016/j.epsl.2009.09.013.

Direen N. & Crawford A. 2003. Fossil seaward-dipping reflector sequences preserved in south-eastern Australia: a 600 Ma volcanic passive margin in eastern Gondwanaland. *Journal of the Geological Society, London* **160(6)**, 985–990. URL http://dx.doi.org/10.1144/0016-764903-010.

Do Campo M. & Ribeiro Guevara S. 2005. Provenance analysis and tectonic setting of late Neoproterozoic metasedimentary successions in NW Argentina. *Journal of South American Earth Sciences* **19(2)**, 143–153. URL http://dx.doi.org/10.1016/j.jsames.2005.01.003.

Dodson M. 1973. Closure Temperature in Cooling Geochronological and Petrological Systems. *Contributions to Mineralogy and Petrology* **40(3)**, 259–274. URL http://dx.doi.org/10.1007/BF00373790.

Eckstrand O., Grinenko L., Krouse H., Paktunc A., Schwann P. & Scoates R. 1989. Preliminary data on sulphur isotopes and Se/S ratios, and the source of sulphur in magmatic sulphides from the Fox River Sill, Molson Dykes and Thompson nickel deposits, northern Manitoba. *Current Research Part C, Geological Survey of Canada, Paper* pp. 235–242.

Eckstrand O. & Hulbert L. 1987. Selenimum and the source of sulphur in magmatic nickel and platinum deposits. *Geol. Assoc. Canada/Mineral Assoc. Canada: Program with Abstracts* **12**, 40.

Eckstrand O. & Hulbert L. 2007. Magmatic nickel-copper-platinum group element deposits. *In:* W. Goodfellow, ed., *Mineral Deposits of Canada: A Synthesis of Major Deposit Types, District Metallogeny, the Evolution of Geological Provinces and Exploration Methods: Geological Association of Canada, Special Publication 5*, pp. 205–222. Geological Association of Canada (Mineral Deposits Division).

Eggins S., Woodhead J., Kinsley L., Mortimer G., Sylvester P., McCulloch M., Hergt J. & Handler M. 1997. A simple method for the precise determination of $\geqslant 40$ trace elements in geological samples by icpms using enriched isotope internal standardisation. *Chemical Geology* **134(4)**, 311–326. URL `http://dx.doi.org/10.1016/S0009-2541(96)00100-3`.

Ely K.S., Sandiford M., Phillips D. & Boger S.D. 2014. Detrital zircon U-Pb and 40Ar/39Ar hornblende ages from the Aileu Complex, Timor-Leste: provenance and metamorphic cooling history. *Journal of the Geological Society* **171(2)**, 299–309. URL `http://dx.doi.org/10.1144/jgs2012-065`.

Evans-Lamswood D., Butt D., Jackson R., Lee D., Muggridge M., Wheeler R. & Wilton D. 2000. Physical controls associated with the distribution of sulfides in the voisey's bay ni-cu-co deposit, labrador. *Economic Geology* **95(4)**, 749–769. URL `http://dx.doi.org/10.2113/gsecongeo.95.4.749`.

Faure G. & Mensing T. 2005a. The 40Ar*/39Ar Method. *In: Isotopes: Principles and Applications*, chapter 7, pp. 144–179. John Wiley & Sons, New Jersey, 3rd edition.

Faure G. & Mensing T. 2005b. The K-Ar Method. *In: Isotopes: Principles and Applications'*, chapter 6, pp. 113–143. John Wiley & Sons, New Jersey, 3rd edition.

Faure G. & Mensing T. 2005c. The U-Pb, Th-b, and Pb-Pb Methods. *In: Isotopes: Principles and Applications*, chapter 10, pp. 214–255. John Wiley & Sons, New Jersey, 3rd edition.

Fedo C., Sircombe K. & Rainbird R. 2003. Detrital Zircon Analysis of the Sedimentary Record. *Reviews in Mineralogy and Geochemistry* **53(1)**, 277–303. URL `http://dx.doi.org/10.2113/0530277`.

Fiorentini M., Barnes S., Lesher C., Heggie G., Keays R. & Burnham O. 2010. Platinum group element geochemistry of mineralized and nonmineralized komatiites and basalts. *Economic Geology* **105(4)**, 795–823. URL http://dx.doi.org/10.2113/gsecongeo.105.4.795.

Fleck R., Sutter J. & Elliot D. 1977. Interpretation of discordant 40Ar/39Ar age-spectra of mesozoic tholeiites from antarctica. *Geochimica et Cosmochimica Acta* **41(1)**, 15–32. URL http://dx.doi.org/10.1016/0016-7037(77)90184-3.

Floyd P., Shail R., Leveridge B. & Franke W. 1991. Geochemistry and provenance of Rhenohercynian synorogenic sandstones: implications for tectonic environment discrimination. *Geological Society, London, Special Publications* **57(1)**, 173–188. URL http://dx.doi.org/10.1144/GSL.SP.1991.057.01.14.

Floyd P. & Winchester J. 1975. Magma type and tectonic setting discrimination using immobile elements. *Earth and Planetary Science Letters* **27(2)**, 211–218. URL http://dx.doi.org/10.1016/0012-821X(75)90031-X.

Floyd P. & Winchester J. 1978. Identification and discrimination of altered and metamorphosed volcanic rocks using immobile elements. *Chemical Geology* **21(3–4)**, 291–306. URL http://dx.doi.org/10.1016/0009-2541(78)90050-5.

Gehrels G. 2011. Detrital zircon U-Pb geochronology: current methods and new opportunities. *In:* C. Busby & A. Pérez, eds., *Tectonics of Sedimentary Basins: Recent Advances*, pp. 47–62. John Wiley & Sons, New Jersey.

Gélinas L., Mellinger M. & Trudel P. 1982. Archean mafic metavolcanics from the Rouyn–Noranda district, Abitibi Greenstone Belt, Quebec. 1. Mobility of the major elements. *Canadian Journal of Earth Sciences* **19(12)**, 2258–2275. URL http://dx.doi.org/10.1139/e82-199.

Godel B., Barnes S. & Maier W. 2007. Platinum-group elements in sulphide minerals, platinum-group minerals, and whole-rocks of the Merensky Reef (Bushveld Complex, South Africa): Implications for the formation of the reef. *Journal of Petrology* **48(8)**, 1569–1604. URL http://dx.doi.org/10.1093/petrology/egm030.

Godel B., Seat Z., Maier W. & Barnes S. 2011. The Nebo-Babel Ni-Cu-PGE Sulfide Deposit (West Musgrave Block, Australia): Pt. 2. Constraints on Parental Magma and Processes, with Implications for Mineral Exploration. *Economic Geology* **106(4)**, 557–584. URL http://dx.doi.org/10.2113/econgeo.106.4.557.

Greenhill P. 1995. The Geological Setting and Mineralisation of the CUNI Cu/Ni Deposits. *Unpublished B.Sc.(Honours) Thesis, University of Tasmania* pp. 1–84.

Groves D. & Bierlein F. 2007. Geodynamic settings of mineral deposit systems. *Journal of the Geological Society, London* **164(1)**, 19–30. URL http://dx.doi.org/10.1144/0016-76492006-065.

Haines P., Turner S., Kelley S., Wartho J. & Sherlock S. 2004. 40Ar–39Ar dating of detrital muscovite in provenance investigations: a case study from the Adelaide Rift Complex, South Australia. *Earth and Planetary Science Letters* **227(3-4)**, 297–311. URL http://dx.doi.org/10.1016/j.epsl.2004.08.020.

Hallberg J. 1984. A geochemical aid to igneous rock type identification in deeply weathered terrain. *Journal of Geochemical Exploration* **20(1)**, 1–8. URL http://dx.doi.org/10.1016/0375-6742(84)90085-2.

Harrison T. 1981. Diffusion of 40Ar in hornblende. *Contributions to Mineralogy and Petrology* **78(3)**, 324–331. URL http://dx.doi.org/10.1007/BF00398927.

Harrison T., Célérier J., Aikman A., Hermann J. & Heizler M. 2009. Diffusion of 40Ar in muscovite. *Geochimica et Cosmochimica Acta* **73(4)**, 1039–1051. URL http://dx.doi.org/10.1016/j.gca.2008.09.038.

Hoatson D., Jaireth S. & Jaques A. 2006. Nickel sulfide deposits in Australia: Characteristics, resources, and potential. *Ore Geology Reviews* **29(3-4)**, 177–241. URL http://dx.doi.org/10.1016/j.oregeorev.2006.05.002.

Hodges K., Ruhl K., Wobus C. & Pringle M. 2005. 40Ar/39Ar Thermochronology of Detrital Minerals. *Reviews in Mineralogy and Geochemistry* **58(1)**, 239–257. URL http://dx.doi.org/10.2138/rmg.2005.58.9.

Holwell D., Keays R., Firth E. & Findlay J. 2014. Geochemistry and mineralogy of platinum group element mineralization in the river valley intrusion, ontario, canada: A model for early-stage sulfur saturation and multistage emplacement and the implications for "contact-type" ni-cu-pge sulfide mineralization. *Economic Geology* **109(3)**, 689–712. URL http://dx.doi.org/10.2113/econgeo.109.3.689.

Hynes A. 1980. Carbonatization and mobility of Ti, Y, and Zr in Ascot Formation Metabasalts, SE Quebec. *Contributions to Mineralogy and Petrology* **75**, 79–87. URL http://dx.doi.org/10.1007/BF00371891.

Irvine T. & Baragar W. 1971. A Guide to the Chemical Classification of the Common Volcanic Rocks. *Canadian Journal of Earth Sciences* **8(5)**, 523–548. URL http://dx.doi.org/10.1139/e71-055.

Jacques R. & Galeotti S. 2008. *Stratigraphy: Terminology and Practice*. Editions OPHRYS, 163 pp.

Kattenhorn S. 1994. Mechanisms of Sill and Dyke Intrusion. *Unpublished M.Sc. Thesis, University of Natal (Durban)* pp. 1–152.

Keays R. 1995. The role of komatiitic and picritic magmatism and S-saturation in the formation of ore deposits. *Lithos* **34(1-3)**, 1–18. URL http://dx.doi.org/10.1016/0024-4937(95)90003-9.

Keays R. & Jowitt S. 2013. The Avebury Ni deposit, Tasmania: A case study of an unconventional nickel deposit. *Ore Geology Reviews* **52**, 4–17. URL http://dx.doi.org/10.1016/j.oregeorev.2012.07.001.

Keays R. & Lightfoot P. 2010. Crustal sulfur is required to form magmatic Ni-Cu sulfide deposits: Evidence from chalcophile element signatures of Siberian and Deccan Trap basalts. *Mineralium Deposita* **45(3)**, 241–257. URL http://dx.doi.org/10.1007/s00126-009-0271-1.

Kelley S. 2002. K-Ar and Ar-Ar Dating. *Reviews in Mineralogy and Geochemistry* **47(1)**, 785–818. URL http://dx.doi.org/10.2138/rmg.2002.47.17.

Kerr A. & Leitch A. 2005. Self-destructive sulfide segregation systems and the formation of high-grade magmatic ore deposits. *Economic Geology* **100(2)**, 311–332. URL http://dx.doi.org/10.2113/gsecongeo.100.2.311.

Le Bas M., Le Maitre R. & Woolley A. 1992. The construction of the Total Alkali-Silica chemical classification of volcanic rocks. *Mineralogy and Petrology* **46(1)**, 1–22. URL http://dx.doi.org/10.1007/BF01160698.

Lee J., Marti K., Severinghaus J., Kawamura K., Yoo H., Lee J. & Kim J. 2006. A redetermination of the isotopic abundances of atmospheric Ar. *Geochimica et Cosmochimica Acta* **70(17)**, 4507–4512. URL http://dx.doi.org/10.1016/j.gca.2006.06.1563.

Ludwig K. 2012. User's Manual for Isoplot 3.75: A Geochronological Tool for Microsoft Excel. *Berkeley Geochronology Center Special Publication No. 5* pp. 1–75.

Maas R. & McCulloch M. 1991. The provenance of Archean clastic metasediments in the Narryer Gneiss Complex, Western Australia: Trace element geochemistry, Nd isotopes, and U-Pb ages for detrital zircons. *Geochimica et Cosmochimica Acta* **55(7)**, 1915–1932. URL http://dx.doi.org/10.1016/0016-7037(91)90033-2.

MacLean W. & Barrett T. 1993. Lithogeochemical techniques using immobile elements. *Journal of Geochemical Exploration* **48(2)**, 109–133. URL http://dx.doi.org/10.1016/0375-6742(93)90002-4.

Maier W. & Barnes S. 2010. The Kabanga Ni sulfide deposits, Tanzania: II. Chalcophile and siderophile element geochemistry. *Mineralium Deposita* **45(5)**, 443–460. URL http://dx.doi.org/10.1007/s00126-010-0283-x.

Maier W. & Groves D. 2011. Temporal and spatial controls on the formation of magmatic PGE and Ni-Cu deposits. *Mineralium Deposita* **46(8)**, 841–857. URL http://dx.doi.org/10.1007/s00126-011-0339-6.

McDonough W., Sun S., Ringwood A., Jagoutz E. & Hofmann A. 1992. Potassium, rubidium, and cesium in the Earth and Moon and the evolution of the mantle of the Earth. *Geochimica et Cosmochimica Acta* **56(3)**, 1001–1012. URL http://dx.doi.org/http://dx.doi.org/10.1016/0016-7037(92)90043-I.

McDougall I. & Harrison T. 1999. *Geochronology and Thermochronology by the 40Ar/30Ar Method*. Oxford University Press, New York, 2nd edition, 269 pp.

Meffre S., Direen N., Crawford A. & Kamenetsky V. 2004. Mafic volcanic rocks on King Island, Tasmania: Evidence for 579 Ma break-up in east Gondwana. *Precambrian Research* **135(3)**, 177–191. URL http://dx.doi.org/10.1016/j.precamres.2004.08.004.

Merrihue C. & Turner G. 1966. Potassium-argon dating by activation with fast neutrons. *Journal of Geophysical Research* **71(11)**, 2852–2857. URL http://dx.doi.org/10.1029/JZ071i011p02852.

Middlemost E. 1994. Naming materials in the magma/igneous rock system. *Earth-Science Reviews* **37(3–4)**, 215–224. URL http://dx.doi.org/http://dx.doi.org/10.1016/0012-8252(94)90029-9.

Moore D., Betts P. & Hall M. 2015. Fragmented Tasmania: the transition from Rodinia to Gondwana. *Australian Journal of Earth Sciences* **62(1)**, 1–35. URL http://dx.doi.org/10.1080/08120099.2014.966757.

Mulder J., Halpin J. & Daczko N. 2015. Mesoproterozoic tasmania: Witness to the east antarctica–laurentia connection within nuna. *Geology* **43(9)**, 759–762. URL http://dx.doi.org/10.1130/G36850.1.

Najman Y., Pringle M., Johnson M., Robertson A. & Wijbrans J. 1997. Laser 40Ar/39Ar dating of single detrital muscovite grains from early foreland-basin sedimentary deposits in India: Implications for early Himalayan evolution. *Geology* **25(6)**, 535. URL http://dx.doi.org/10.1130/0091-7613(1997)025<0535:LAADOS>2.3.CO;2.

Naldrett A. 1999. World-class Ni-Cu-PGE deposits: Key factors in their genesis. *Mineralium Deposita* **34(3)**, 227–240. URL http://dx.doi.org/10.1007/s001260050200.

Naldrett A. 2004a. Introduction. *In:* A. Naldrett, ed., *Magamtic Sulfide Deposits: Geology, Geochemistry and Exploration*, pp. 1–20. Springer-Verlag, Heidelberg.

Naldrett A. 2004b. Summary and use of genetic concepts in exploration. *In:* A. Naldrett, ed., *Magamtic Sulfide Deposits: Geology, Geochemistry and Exploration*, pp. 613–668. Springer-Verlag, Heidelberg.

Noda A. 2015. Python functions for U–Pb data analysis. URL `https://staff.aist.go.jp/a.noda/memo/UPbage/UPbage.html`.

Nye P. & Blake F. 1938. The Geology and Mineral Deposits of Tasmania. *Tasmania Department of Mines, Geological Survey Bulletin 44* pp. 1–109.

O'Nions R., Hamilton P. & Hooker P. 1983. A nd isotope investigation of sediments related to crustal development in the british isles. *Earth and Planetary Science Letters* **63(2)**, 229–240. URL `http://dx.doi.org/10.1016/0012-821X(83)90039-0`.

Paton C., Hellstrom J., Paul B., Woodhead J. & Hergt J. 2011. Iolite: Freeware for the visualisation and processing of mass spectrometric data. *Journal of Analytical Atomic Spectrometry* **26(12)**, 2508. URL `http://dx.doi.org/10.1039/c1ja10172b`.

Paton C., Woodhead J., Hellstrom J., Hergt J., Greig A. & Maas R. 2010. Improved laser ablation U-Pb zircon geochronology through robust downhole fractionation correction. *Geochemistry, Geophysics, Geosystems* **11(3)**, 1–36. URL `http://dx.doi.org/10.1029/2009GC002618`.

Peach C., Mathez E. & Keays R. 1990. Sulfide melt-silicate melt distribution coefficients for noble metals and other chalcophile elements as deduced from MORB: Implications for partial melting. *Geochimica et Cosmochimica Acta* **54(12)**, 3379–3389. URL `http://dx.doi.org/10.1016/0016-7037(90)90292-S`.

Peach C., Mathez E., Keays R. & Reeves S. 1994. Trace-element Partitioning with Application to Magmatic Processes Experimentally determined sulfide melt-silicate melt partition coefficients for iridium and palladium. *Chemical Geology* **117(1)**, 361–377. URL `http://dx.doi.org/http://dx.doi.org/10.1016/0009-2541(94)90138-4`.

Pearce J. 1996. A User's Guide to Basalt Discrimination Diagrams. *In:* D. Wyman, ed., *Trace Elment Geochemistry of Volcanic Rocks: Applications for Massive Sulphide Exploration: Geological Association of Canada, Short Course Notes*, volume 12, pp. 79–113. Geological Association of Canada.

Pearce J. & Cann J. 1973. Tectonic setting of basic volcanic rocks determined using trace element analyses. *Earth and Planetary Science Letters* **19(2)**, 290–300. URL `http://dx.doi.org/10.1016/0012-821X(73)90129-5`.

Peck D. & Keays R. 1990. Insights into the Behaviour of Precious Metals in Primitive, S-undersaturated Magmas: Evidence from the Heazlewood River Complex, Tasmania. *Canadian Mineralogist* **28**, 553–577.

Phillips D. & Matchan E. 2013. Ultra-high precision 40Ar/39Ar ages for Fish Canyon Tuff and Alder Creek Rhyolite sanidine: New dating standards required? *Geochimica et Cosmochimica Acta* **121**, 229–239. URL http://dx.doi.org/10.1016/j.gca.2013.07.003.

Phillips G., Wilson C., Phillips D. & Szczepanski S. 2007. Thermochronological (40Ar/39Ar) evidence of Early Palaeozoic basin inversion within the southern Prince Charles Mountains, East Antarctica: implications for East Gondwana. *Journal of the Geological Society* **164(4)**, 771–784. URL http://dx.doi.org/10.1144/0016-76492006-073.

Queffurus M. & Barnes S. 2015. A review of sulfur to selenium ratios in magmatic nickel–copper and platinum-group element deposits. *Ore Geology Reviews* **69**, 301–324. URL http://dx.doi.org/10.1016/j.oregeorev.2015.02.019.

Reid A. 1925. The Dundas Mineral Field. *Tasmania Department of Mines, Geological Survey Bulletin 36* pp. 1–98.

Renne P., Swisher C., Deino A., Karner D., Owens T. & DePaolo D. 1998. Intercalibration of standards, absolute ages and uncertainties in 40Ar/39Ar dating. *Chemical Geology* **145(1-2)**, 117–152. URL http://dx.doi.org/10.1016/S0009-2541(97)00159-9.

Ripley E. 1999. Systematics of sulfur and oxygen isotopes in mafic igneous rocks and related Cu-Ni-PGE mineralization. *In:* R. Keays, C. Lesher, P. Lightfoot & C. Farrow, eds., *Dynamic processes in magmatic ore deposits and their application in mineral exploration.*, pp. 133–158. Geol. Assoc. Can. Short Course Notes 13.

Rollinson H. 1993. *Using Gechemical Data: Evaluation, Presentation, Interpretation*. Taylor & Francis Ltd, London, 384 pp.

Schoene B. 2014. U-Th-Pb Geochronology. *In:* D. Holland & K. Turekian, eds., *Treatise on Geochemistry*, volume 4, chapter 10, pp. 341–378. Elsevier, Oxford, 2nd edition. URL http://dx.doi.org/10.1016/B978-0-08-095975-7.00310-7.

Seat Z., Mary Gee M., Grguric B., Beresford S. & Grassineau N. 2011. The Nebo-Babel Ni-Cu-PGE Sulfide Deposit (West Musgrave, Australia): Pt. 1. U/Pb Zircon Ages, Whole-Rock and Mineral Chemistry, and O-Sr-Nd Isotope Compositions of the Intrusion, with Constraints on Petrogenesis. *Economic Geology* **106(4)**, 527–556. URL http://dx.doi.org/10.2113/econgeo.106.4.527.

Seymour D. & Calver C. 1995. Explanatory notes for the Time–Space Diagram and Stratotectonic Elements Map of Tasmania. *Tasmanian Geological Survey Record 1995/01* pp. 1–62.

Seymour D., Green G. & Calver C. 2013. The Geology and Mineral Deposits of Tasmania: a summary. *Mineral Resources Tasmania, Geological Survey Bulletin 72* pp. 1–29.

Seymour D., McClenaghan M., Green G., Everard J., Berry R., Callaghan T., Davidson G. & Hills P. 2014. Mid-Palaeozoic orogenesis, magmatism and minerlization. *In:* K. Corbett, P. Quilty & C. Calver, eds., *Geological Evolution of Tasmania: Geological Society of Australia, Special Publication 24*, pp. 273–362. Geological Society of Australia (Tasmania Division).

Simon A. & Ripley E. 2011. The Role of Magmatic Sulfur in the Formation of Ore Deposits. *Reviews in Mineralogy and Geochemistry* **73(1)**, 513–578. URL `http://dx.doi.org/10.2138/rmg.2011.73.16`.

Sircombe K. & Hazelton M. 2004. Comparison of detrital zircon age distributions by kernel functional estimation. *Sedimentary Geology* **171(1–4)**, 91–111. URL `http://dx.doi.org/10.1016/j.sedgeo.2004.05.012`.

Sláma J., Košler J., Condon D., Crowley J., Gerdes A., Hanchar J., Horstwood M., Morris G., Nasdala L., Norberg N., Schaltegger U., Schoene B., Tubrett M. & Whitehouse M. 2008. Plešovice zircon - A new natural reference material for U-Pb and Hf isotopic microanalysis. *Chemical Geology* **249(1-2)**, 1–35. URL `http://dx.doi.org/10.1016/j.chemgeo.2007.11.005`.

Stacey A. & Berry R. 2004. The structural history of Tasmania, a review for petroleum explorers. *In:* P. Boult, D. Johns & S. Lang, eds., *Petroleum Exploration Society Australia Special Publication: Eastern Australasian Basins Symposium II, Adelaide*, pp. 151–162. Petroleum Exploration Society Australia.

Steiger R. & Jäger E. 1977. Subcommission on geochronology: Convention on the use of decay constants in geo- and cosmochronology. *Earth and Planetary Science Letters* **36(3)**, 359–362. URL `http://dx.doi.org/10.1016/0012-821X(77)90060-7`.

Sun S. & McDonough W. 1989. Chemical and isotopic systematics of oceanic basalts: implications for mantle composition and processes. *Geological Society, London, Special Publications* **42(1)**, 313–345. URL `http://dx.doi.org/10.1144/GSL.SP.1989.042.01.19`.

Taylor B. & Burger D. 1952. The Five-mile copper-nickel deposits. *Unpublished report for Department of Mines, Tasmania* pp. 72–97.

Thériault R. & Barnes S. 1998. Compositional variations in Cu-Ni-PGE sulfides of the Dunka Road deposit, Duluth Complex, Minnesota: the importance of combined assimilation and magmatic processes. *Canadian Mineralogist* **36**, 869–886.

Turner N., Boulter C., Calver C., Cox S., Gee R., Komyshan P., McNeill A. & Weatherstone N. 1989. Precambrian. *In:* C. Burrett & E. Martin, eds., *Geology and Mineral Resources of Tasmania: Geological Society of Australia, Special Publication 15*, pp. 5–46. Geological Society of Australia (Tasmania Division).

Varne R. & Foden J. 1987. Tectonic setting of cambrian rifting, volcanism and ophiolite formation in western tasmania. *Tectonophysics* **140(2-4)**, 275–295. URL `http://dx.doi.org/10.1016/0040-1951(87)90235-6`.

Vermeesch P. 2004. How many grains are needed for a provenance study? *Earth and Planetary Science Letters* **224(3–4)**, 441–451. URL `http://dx.doi.org/10.1016/j.epsl.2004.05.037`.

Vermeesch P. 2012. On the visualization of detrital age distributions. *Chemical Geology* pp. 190–194. URL `http://dx.doi.org/10.1016/j.chemgeo.2013.01.010`.

Vermeesch P. & Garzanti E. 2015. Making geological sense of 'big data' in sedimentary provenance analysis. *Chemical Geology* **409**, 20–27. URL `http://dx.doi.org/10.1016/j.chemgeo.2015.05.004`.

Villa I.M., Grobety B., Kelley S.P., Trigila R. & Wieler R. 1996. Assessing Ar transport paths and mechanisms in the McClure Mountains hornblende. *Contributions to Mineralogy and Petrology* **126(1-2)**, 67–80. URL `http://dx.doi.org/10.1007/s004100050236`.

Vogel D. & Keays R. 1997. The petrogenesis and platinum-group element geochemistry of the Newer Volcanic Province, Victoria, Australia. *Chemical Geology* **136(3–4)**, 181–204. URL `http://dx.doi.org/10.1016/S0009-2541(96)00142-8`.

Wiedenbeck M., Allé P., Corfu F., Griffin W., Meier M., Oberli F., Quadt A., Roddick J. & Spiegel W. 1995. Three Natural Zircon Standards for U-Th-Pb, Lu-Hf, Trace Element and Ree Analyses. *Geostandards and Geoanalytical Research* **19(1)**, 1–23. URL `http://dx.doi.org/10.1111/j.1751-908X.1995.tb00147.x`.

Williams E., McClenaghan M., Collins P., Brown S., Camacho A., Dronseika E., Higgins N., Morland R., Reid E. & Seymour D. 1989. Mid-Palaeozoic Deformation, Granitoids and Ore Deposits. *In:* C. Burrett & E. Martin, eds., *Geology and Mineral Resources of Tasmania: Geological Society of Australia, Special Publication 15*, pp. 238–292. Geological Society of Australia (Tasmania Division).

Wilson M. 1989. *Igneous Petrogenesis*. Unwin Hyman, London, 466 pp.

Winchester J. & Floyd P. 1977. Geochemical discrimination of different magma series and their differentiation products using immobile elements. *Chemical Geology* **20**, 325–343. URL `http://dx.doi.org/10.1016/0009-2541(77)90057-2`.

Winchester J. & Max M. 1989. Tectonic setting discrimination in clastic sequences: an example from the Late Proterozoic Erris Group, NW Ireland. *Precambrian Research* **45(1-3)**, 191–201. URL `http://dx.doi.org/10.1016/0301-9268(89)90039-9`.

Wood D. 1980. The application of a Th-Hf-Ta diagram to problems of tectonomagmatic classification and to establishing the nature of crustal contamination of basaltic lavas of the British Tertiary Volcanic Province. *Earth and Planetary Science Letters* **50(1)**, 11–30. URL `http://dx.doi.org/10.1016/0012-821X(80)90116-8`.

Woodhead J., Hergt J., Shelley M., Eggins S. & Kemp R. 2004. Zircon Hf-isotope analysis with an excimer laser, depth profiling, ablation of complex geometries, and concomitant age estimation. *Chemical Geology* **209(1-2)**, 121–135. URL `http://dx.doi.org/10.1016/j.chemgeo.2004.04.026`.